



**University of
Nottingham**

UK | CHINA | MALAYSIA

**Modelling of Ultrasonic Wave Propagation for
Industrial Sonoreactor Design and Optimisation**

CHU JIN KIAT

Department of Chemical and Environmental
Engineering

Thesis submitted to the University of Nottingham for the degree of

Doctor of Philosophy

September 2022

I declare that this thesis had been produced solely by myself and that it had not been submitted, in whole or in part, in any previous application for a degree. Except stated otherwise by reference or acknowledgment, the work presented is entirely my own.

A handwritten signature in black ink, consisting of a large, stylized initial 'C' followed by a horizontal line that extends to the right.

Abstract

The development of power ultrasound technology had raised interest in the design of sonoreactors. Numerical simulations were identified as a promising tool for tackling the challenges involved in scaling up and optimisation. The development of simulation strategies for sonoreactor acoustics had mainly focused on horn-type configurations, and little information was available for bath-type systems. This work evaluated the performance of three popular frequency-domain models for the prediction of acoustic pressure in bath-type configurations. The results of the pure-liquid, linear Commander and Prosperetti (CP), and nonlinear Helmholtz (NH) models were verified against hydrophone measurements and antinode characterisation results obtained from experiments. Emphasis was placed on the evaluation of the linear CP model, as it was hypothesised to best characterise the acoustic behaviour of the studied systems. In accordance with the objectives of this work, seven case studies were carried out.

Case Study 1 explored the suitability of frequency-domain solutions for the characterisation of acoustic pressure fields. Predictions of frequency-domain solutions compared well with time-domain models and experimental observations, notably in terms of antinode locations. The results justified the use of frequency-domain models to characterise sonoreactors. Case Study 2 explored the acoustic boundary conditions used in the modelling strategies of this work. The test cases showed that Dirichlet pressure boundaries can be used to represent the vibrating walls of studied sonoreactors. Numerical aspects of other boundary conditions were also identified to improve confidence in the simulation results.

Case Study 3 presented a pressure validation study using a 252 L ultrasonic bath to evaluate the performance of selected acoustic pressure models. The pure-liquid model was found to yield good agreements for lower-frequency cases (35 and 72 kHz, but failed to account for increased attenuation at higher-frequency cases (110 and 170 kHz). The linear CP model showed mixed results and performance was strongly affected by wall reflection. The results were found to depend on the bubble density magnitude. Empirically tuned bubble densities significantly improved the performance of the linear CP model for the 35 and 72 kHz cases. Preliminary studies for the nonlinear CP and NH models resulted in strong deviations from hydrophone measurements, which suggested an overtuned attenuation mechanism.

Case Study 4 presented a novel investigation on the effect of geometry on qualitative antinode validation methods. Heuristic and theoretical analysis supported the hypothesis which stated that the value of the effective-geometry-to-wavelength ratio, D_s/λ , affects the confidence in the antinode validation results. A simplified standing wave model was developed and proposed to show that wavelength-shortening effects can only be detected above a certain D_s/λ threshold. The findings of the case study were found to strongly influence current interpretations of antinode validation in sonoreactors and outlined the effect sonoreactor geometry on the validity of antinode verification results.

Antinode validation was performed for the pure-liquid, linear CP, and NH models in Case Study 5, using SCL images of a hexagonal sonoreactor. The performance of the selected models in terms of phase-speed prediction was evaluated. The pure-liquid model consistently predicted wavelengths longer than those of SCL observations. The

outputs of the linear CP model once again showed strong sensitivity to the bubble density parameter. The results suggested that the best agreement with the SCL standing wave patterns could be obtained using a bubble density magnitude between $1 \times 10^{10} - 1 \times 10^{11} \text{ m}^{-3}$. The NH model also yielded mixed results. The phase speed prediction mechanism of the NH model was found to depend on many factors, in which a detailed analysis could not be completed within the scope of this work.

Case Study 6 served to demonstrate and discuss the proposed semi-empirical wavelength tuning approach for the characterisation of the bubble density in a sonoreactor. The novel method was developed based on the linear CP model to address the uncertainties regarding bubble field characterisation in sonoreactor simulations. The method allowed the bubble density parameter to be tuned against wavelength measurements which led to remarkable improvements for antinode characterisation results using the linear CP model.

Case Study 7 presents an exploratory study on the use of frequency-domain modelling strategies for multi-frequency sonoreactors. Based on Parseval's theorem, the CP model was modified to account for multi-frequency harmonics. The antinode verification of the simulation results suggested that the use of linear wave superposition was a promising approach for simplifying the characterisation of multi-frequency acoustic fields. The remarkable agreement with SCL images also further supported the viability of the linear CP model.

List of Publications

Refereed Journals

Tiong, T.J., Chu, J.K., Lim, L.Y., Tan, K.W., Hong Yap, Y., Asli, U.A., 2019. A computational and experimental study on acoustic pressure for ultrasonically formed oil-in-water emulsion. *Ultrasonics Sonochemistry* 56, 46–54.

Chu, J.K., Tiong, T.J., Chong, S., Asli, U.A., Yap, Y.H., 2021. Multi-frequency sonoreactor characterisation in the frequency domain using a semi-empirical bubbly liquid model. *Ultrasonics Sonochemistry* 80, 105818.

Chu, J.K., Tiong, T.J., Chong, S., Asli, U.A., 2022. Investigation on different time-harmonic models using FEM for the prediction of acoustic pressure fields in a pilot-scale sonoreactor. *Chemical Engineering Science* 247, 116912.

Acknowledgement

First, I express my utmost gratitude to my main supervisor, Dr. Tiong Timm Joyce, for her guidance, insight, and patience throughout all these years. She has allowed me much freedom in following my own initiative to pursue my (sometimes very off-topic) ideas, and provided much guidance and continual support. I would also like to thank my co-supervisor, Dr. Faye Chong Siew Hui, for her input and support for my work. Furthermore, I am very grateful for Dr. Umi Aisah Asli for her support and simulation software (COMSOL), and also Dr. Hii Ching Lik for the constructive feedback which led to key improvements in this work. I am grateful to my senior, Derick Liew Khong Lit, for his contribution in the form of a comprehensive dataset used in parts of this work.

I would like to express my gratitude to the University of Nottingham Malaysia which made this research project possible. I also wish to thank the laboratory technicians and faculty staff for the support and assistance given to me throughout these years. I would also like to express my thanks to fellow researchers at the 17th Meeting of the European Society of Sonochemistry (ESS 2022). I have gained very valuable experiences that greatly added to my growth as a researcher.

I would like to express my gratitude to my parents, grandparents, and sister for their love and support throughout this long journey. I thank my family and friends for their care and encouragement. I would like to thank God, and my church community for their support. Last but not least, a very special thank you to my online friends from all over the world, in the group '*Didn't Expectus*' on the online platform Discord, for their companionship throughout these years.

Table of Contents

Chapter 1: Background	1
1.1 Introduction	1
1.1.1 Power Ultrasound and Acoustic Cavitation	1
1.1.2 Workings of a Sonoreactor	3
1.2 Literature Review	6
1.2.1 Numerical Simulations for Sonoreactor Modelling	6
1.2.2 Sonoreactor Characterisation and Model Validation	8
1.2.3 Review of Acoustic Pressure Modelling and Validation Works	13
1.3 Notable Knowledge Gaps	22
1.3.1 Modelling Strategies for Bath-Type Configurations	23
1.3.2 Large-Scale Validation Studies	23
1.3.3 Inter-Model Comparison and Discussion	24
1.3.4 Bubble Field Characterisation in Sonoreactor Acoustics	24
1.4 Problem Statement	25
1.5 Aims and Objectives	25
1.5.1 Research Timeline	27
1.6 Thesis Structure and Case Studies	28
Chapter 2: Theory	31
2.1 The Wave Equation	31
2.2 The Helmholtz Equation	33
2.3 Pure-Liquid vs Bubbly-Liquid Models	34
2.3.1 Pure-Liquid Approach	34
2.3.2 Bubbly-Liquid Approach	35
2.4 The Cafilisch Equation for Bubbly-Liquid Acoustics	36
2.4.1 Mathematical Formulation	36

2.4.2	Important Assumptions	38
2.4.3	Practical Limitations.....	40
2.5	The Commander and Prosperetti (CP) Model.....	43
2.5.1	Formulation of the CP Model.....	43
2.5.2	Variations of the CP model	45
2.5.3	Comments on the CP Model	46
2.6	The Nonlinear Helmholtz Model.....	48
2.6.1	Formulation of the NH Models	48
2.6.2	Comments on the NH Model	53
2.7	Bubble Field Characterisation and Bubble Dynamics	54
2.7.1	Specification of Bubble Field Parameters	54
2.7.2	Bubble Dynamics.....	56
2.8	Mesh and Solver Considerations in FEM	60
2.8.1	Meshing Considerations in Sonoreactor Acoustics.....	61
2.8.2	Convergence Criteria and Solver Framework	61
2.9	Acoustic Boundary Conditions and Perfectly Matched Layers (PML).....	64
2.9.1	Acoustic Boundary Conditions	64
2.9.2	Perfectly Matched Layers (PML)	67
Chapter 3:	Fundamental Modelling Strategies in FEM	68
3.1	Case Study 1: Time- and Frequency-Domain Acoustic Simulations.....	68
3.1.1	Methodology.....	68
3.1.2	Results and Discussion	70
3.2	Case Study 2: Investigating the Suitability of Boundary Conditions.....	83
3.2.1	Dirichlet vs. Neumann Transducer Boundary Condition for Horns	83
3.2.2	Dirichlet vs. Neumann Transducer Boundary Condition for Baths.....	87
3.2.3	Dynamics of a Plate-Transducer Assembly	89

3.2.4	Auxiliary Study: Numerical Effects and Level of Constraint.....	94
3.3	Concluding Remarks for Chapter 3	98
Chapter 4:	Validation of Acoustic Pressure Models	100
4.1	Case Study 3: Pressure Magnitude Prediction in Large Sonoreactors.....	100
4.1.1	Methodology.....	100
4.1.2	Results and Discussion	104
4.2	Case Study 4: The Effect of Geometry on Antinode Characterisation.....	133
4.2.1	Defining the DS/λ Parameter.....	133
4.2.2	Heuristic Approach: Revisiting the Klíma et al. (2007) Validation Study	134
4.2.3	Analysis of the DS/λ Parameter	136
4.2.4	Compilation of the DS/λ Parameter in Past Studies.....	143
4.3	Case Study 5: Antinode Prediction in Large Sonoreactor	146
4.3.1	Methods: Experimental Data	146
4.3.2	Methods: Numerical Simulation	149
4.3.3	Results and Discussion	152
4.4	Concluding Remarks for Chapter 4	174
Chapter 5:	Bubble Field and Multi-Frequency Considerations	178
5.1	Literature Review on Bubble Characterisation Strategies	179
5.1.1	Experimental Measurements for Sonoreactor Bubble Fields.....	179
5.1.2	Bubble Field Characterisation Strategies in Past Works.....	183
5.2	Derivation of the Semi-Empirical CP Method	194
5.2.1	Reviewing Empirical Tuning Practices in Sonoreactor Acoustics.....	194
5.2.2	Establishing the Basis of the Semi-Empirical Characterisation Approach	196
5.3	Case Study 6: Demonstrating the Semi-Empirical Tuning Approach.....	201
5.3.1	Methodology.....	201
5.3.2	Results and Discussion	202

5.4	Case Study 7: Preliminary Investigation for Multi-Frequency Systems	210
5.4.1	Theoretical Derivation	213
5.4.2	Modification of the CP Model for Multi-Frequency Considerations	214
5.4.3	Methodology.....	218
5.4.4	Results and Discussion	222
5.5	Concluding Remarks for Chapter 5	240
Chapter 6:	Conclusions and Future Work	242
6.1	Key Contributions.....	242
6.2	Summary of Case Studies.....	244
6.3	Future Work.....	248

List of Figures

<i>Figure 1.1: Graphical depiction of acoustic cavitation and its effects.</i>	<i>2</i>
<i>Figure 1.2: (a) Transducer cross-section; (b) Sonotrode (Hielscher Ultrasonics) for horn-type configurations; (c) Wall transducer (Sonictron Malaysia) for bath-type sonoreactors.</i>	<i>4</i>
<i>Figure 1.3: Schematic drawing describing: (a) a probe-beaker system; (b) an ultrasonic flow cell.</i>	<i>5</i>
<i>Figure 1.4: Example of: (a) ultrasonic bath with wall transducers; (b) ultrasonic bath with a transducer array module (KSONIC, Malaysia).</i>	<i>6</i>
<i>Figure 1.5: Validation methods for acoustic pressure models listed based on validation quality.</i>	<i>9</i>
<i>Figure 1.6: Validation result of Klíma et al. (2007) showing that the antinode locations coincide with the cavitation bubbles.</i>	<i>14</i>
<i>Figure 1.7: Summary of the thesis structure.</i>	<i>28</i>
<i>Figure 1.8: Summary of Case Studies 1 – 4 presented in this work.</i>	<i>29</i>
<i>Figure 1.9: Summary of Cast Studies 5 – 7 presented in this work.</i>	<i>30</i>
<i>Figure 2.1: Numerical blow-up of the Caflisch solution during preliminary testing. (a) – (d) shows the evolution of the acoustic pressure field over time, where the red region shows unrealistic pressures.</i>	<i>41</i>
<i>Figure 2.2: Summary of bubbly-liquid models and common bubble field assumptions.</i>	<i>54</i>
<i>Figure 2.3: The numerical solver set-up in COMSOL. The Damped Newton Method (MUMPS) was the main numerical method used in this work.</i>	<i>63</i>
<i>Figure 3.1: The simulation geometry for: (a) the 1D study; (b) the 2D asymmetric study of Klíma et al. (2007).</i>	<i>69</i>

<i>Figure 3.2: The meshes used for the 2D asymmetric case: (a) frequency-domain simulation; (b) time-domain simulation.</i>	<i>70</i>
<i>Figure 3.3: Acoustic pressure plot P for the 1D frequency-domain simulation.</i>	<i>71</i>
<i>Figure 3.4: Absolute acoustic pressure plot P for the 1D frequency-domain result.</i>	<i>71</i>
<i>Figure 3.5: Evolution of the 1D time-domain acoustic pressure.</i>	<i>72</i>
<i>Figure 3.6: Depiction of the half-cycle of the transient standing wave; note that pressures at the antinodes oscillate as the waveform evolved from (a) to (d).</i>	<i>72</i>
<i>Figure 3.7: Comparison between the: (a) validation result of Klíma et al. (2007); (b) frequency-domain simulation results; (c) time-domain simulation result. The colour scale is normalised, based on the original work.</i>	<i>74</i>
<i>Figure 3.8: Numerical dispersion error in the 1D time-domain results: (a) the loss of sinusoidal behaviour; (b) reduced error after mesh refining.</i>	<i>75</i>
<i>Figure 3.9: Time evolution of acoustic pressure at $x = 40$ mm from simulation T2. The phase mismatch formed multiple levels of constructive and destructive interference between the incident and reflecting waves.</i>	<i>76</i>
<i>Figure 3.10: Spectral decomposition of time-dependent acoustic pressure at $x = 40$ mm (T2) obtained using FFT.</i>	<i>78</i>
<i>Figure 3.11: Simulation results for the 1D system with a specified attenuation of 5 Np/m: (a) acoustic pressure, P; (b) absolute pressure, P.</i>	<i>80</i>
<i>Figure 3.12: Simulation results for the 1D system with a non-reflecting right boundary: (a) acoustic pressure, P; (b) absolute pressure, P.</i>	<i>82</i>

<i>Figure 3.13: The mesh model used to study the numerical behaviour of Dirichlet and Neumann active boundaries. PML was used to eliminate reflection effects on the results.....</i>	<i>84</i>
<i>Figure 3.14: Absolute pressure profile of the active boundary: (a) Dirichlet pressure condition; (b) Neumann displacement condition.</i>	<i>85</i>
<i>Figure 3.15: Plots of the pressure and absolute pressure solved using Dirichlet (a and c) and Neumann (b and d) active boundaries for the horn-type configuration.....</i>	<i>85</i>
<i>Figure 3.16: Propagation pattern and absolute pressure profile on the boundary, solved for increasing sonotrode width using the Neumann boundary.</i>	<i>87</i>
<i>Figure 3.17: Effect of discretisation order on the Neumann boundary condition. Horizontal linear regression lines visualised the average magnitude across the investigated boundary.</i>	<i>87</i>
<i>Figure 3.18: Plots of pressure and absolute pressure solved using the Dirichlet (a and c) and Neumann (b and d) active boundaries for the bath-type test case.</i>	<i>88</i>
<i>Figure 3.19: Absolute pressure magnitude at for each boundary condition.</i>	<i>89</i>
<i>Figure 3.20: Schematics of the plate-transducer system and the boundary conditions.....</i>	<i>90</i>
<i>Figure 3.21: (a) Total displacement magnitude with deformation magnified 40000x; (b) 1D plot of normal displacement magnitude at the top surface.</i>	<i>91</i>
<i>Figure 3.22: Acoustic pressure $P(r)$ simulated for three different methods of representing the vibrating wall: (a) solid-acoustic simulation; (b) Dirichlet pressure boundary; (c) Neumann pressure boundary.</i>	<i>92</i>

Figure 3.23: (a) Depiction of the transducers fitted for the hexagonal sonoreactor featured in this work; (b) Acoustic pressure simulation from full solid acoustics; (c) Acoustic pressure simulation using simplified Dirichlet boundary condition.93

Figure 3.24: Graphical depiction of the simulation geometry for the boundary condition test.94

Figure 3.25: Simulation results when (a) Dirichlet and (b) Neumann transducer boundaries are paired with the sound-soft wall boundary.95

Figure 3.26: Methods to reduce discontinuity numerical error using: (a) mesh refinement; (b) higher-order shape functions.....96

Figure 3.27: Simulation results when: (a) Dirichlet; (b) Neumann transducer boundaries are paired with the sound-hard wall boundary.97

Figure 3.28: Results for the non-reflecting case. The Neumann pressure boundary resulted in a peak magnitude of nearly 5 Pa.....97

Figure 4.1: Bisection of the model for the physical system studied by Son et al. (2009).101

Figure 4.2: 2D representation of the simulated system taken as a horizontal cross-section of the sonoreactor.103

Figure 4.3: (a) Example of the triangular element mesh generated for the 35 kHz case; (b) Close-up of the mesh matrix.104

Figure 4.4: Comparison between power input calculation and hydrophone measurements for: (a) 35 kHz; (b) 72 kHz.107

Figure 4.5: Mesh refinement results for the pure-liquid and linear CP model (35 kHz).109

Figure 4.6: Maximum mesh sizes against the number of elements per wavelength (35 kHz).109

<i>Figure 4.7: Absolute pressure for the four frequencies solved using the pure-liquid model.....</i>	<i>110</i>
<i>Figure 4.8: Pure-liquid model 35 kHz solution: (a) Acoustic pressure; (b) Pressure magnitude.</i>	<i>111</i>
<i>Figure 4.9: 35 kHz simulation using fully sound-hard and fully sound-soft boundary conditions: (a and c) acoustic pressure plot; (b and d) acoustic pressure magnitude plot.</i>	<i>111</i>
<i>Figure 4.10: Compilation of the acoustic pressure magnitude plots P for the linear CP model.</i>	<i>113</i>
<i>Figure 4.11: 72 kHz CP model with $n = 1 \times 10^{10} \text{ m}^{-3}$: (a) Absolute acoustic pressure; (b) Acoustic pressure; (c) Regions above the pressure magnitude threshold.</i>	<i>116</i>
<i>Figure 4.12: (a) Simulation geometry for the PML case; (b) Mesh generation for PML.....</i>	<i>117</i>
<i>Figure 4.13: 72 kHz CP model with $n = 1 \times 10^{10} \text{ m}^{-3}$ simulated using perfectly matched layers (PML): (a) Acoustic pressure magnitude plot; (b) Acoustic pressure plot.</i>	<i>118</i>
<i>Figure 4.14: Comparison of acoustic pressure magnitude profiles for three boundary conditions against hydrophone measurements, solved for CP, $n = 1 \times 10^{10} \text{ m}^{-3}$.....</i>	<i>119</i>
<i>Figure 4.15: The results of the 35 kHz pure-liquid case simulated using PML to represent the absorbent boundaries against hydrophone measurements.</i>	<i>120</i>
<i>Figure 4.16: Absolute pressure comparison for the 35 kHz case against hydrophone measurements.</i>	<i>123</i>
<i>Figure 4.17: Absolute pressure comparison for the 72 kHz case against hydrophone measurements.</i>	<i>125</i>

<i>Figure 4.18: Absolute pressure comparison for the 110 kHz case against hydrophone measurements.</i>	<i>126</i>
<i>Figure 4.19: Absolute pressure comparison for the 170 kHz case against hydrophone measurements.</i>	<i>126</i>
<i>Figure 4.20: Results of the linear CP model solved with tuned bubble density parameters from attenuation measurements, compared against hydrophone measurements.</i>	<i>129</i>
<i>Figure 4.21: Absolute pressure profiles predicted by the nonlinear CP and NH ($1 \times 10^{10} \text{ m}^{-3}$) models and the empirical measurements, compared against hydrophone measurements.</i>	<i>131</i>
<i>Figure 4.22: The antinode validation results of Klíma et al. (2007), compared against a series of simulation results using arbitrary phase speeds.</i>	<i>135</i>
<i>Figure 4.23: Depiction of an ideal standing wave model with constant wavelength, validation points numbered in red: (a) Pure node at boundary; (b) Pure antinode at boundary; (c) Neither a pure node nor pure antinode at the boundary.</i>	<i>138</i>
<i>Figure 4.24: Graphical explanation on the effect of larger effective geometry on the detectability of 'wavelength-shortening' in the form of an extra validation point.</i>	<i>140</i>
<i>Figure 4.25: The relation between the DS/λ parameter and its corresponding threshold to successfully capture wavelength-shortening effects in the form of a validation point.</i>	<i>141</i>
<i>Figure 4.26: (a) Physical representation of the dimensions of the hexagonal sonoreactor; (b) Top view schematic showing the orientation of the transducers corresponding to each frequency.</i>	<i>147</i>
<i>Figure 4.27: (a) Image showing the physical sonoreactor; (b) The schematic describing the method by which the SCL images were captured.</i>	<i>148</i>

Figure 4.28: (a) Mesh for the pure liquid of the 28 kHz simulation with 229,241 degrees of freedom; (b) Orientation of the boundary conditions of single-frequency operations.....151

Figure 4.29: Effect of boundary conditions on predicted standing wave characteristics: (a) Sound-hard; (b) Sound-soft; (c) Impedance of stainless steel. Arrows represent the emitting walls.153

Figure 4.30: SCL results used in this work: (a) 28 kHz; (b) 40 kHz; (c) 70 kHz. Design power of 300 W and arrows show the ultrasound emitting walls.....154

Figure 4.31: Example of possible visual errors metal wall reflection, and the region of interest used for antinode validation.155

Figure 4.32: The absolute acoustic pressure fields predicted by the pure-liquid model for the three studied frequencies.....158

Figure 4.33: Absolute acoustic pressure fields predicted by the linear CP model for three frequencies at different bubble density magnitudes.159

Figure 4.34: (a) Semi-log plot of the real and imaginary parts of the analytical wavenumber against bubble density; (b) Variation of the phase speed ratio against bubble fraction. Obtained using linear CP model with 5 μm equilibrium radius and 40 kHz.161

Figure 4.35: (a) Semi-log plot of attenuation as a function of dimensionless pressure for 28, 40 and 70 kHz; (b) Semi-log plot of 28 kHz attenuation as a function of dimensionless pressure at studied bubble densities. Vertical line represents Blake threshold at 1.05 bar.....162

Figure 4.36: The absolute acoustic pressure fields predicted by the NH model for three frequencies at different bubble density magnitudes.163

Figure 4.37: Three convergence plots of the nonlinear solver, for the NH simulations for the 70 kHz case with $n = 1 \times 10^{10} \text{ m}^{-3}$. The degree of freedom

<i>(mesh fineness), solution time, and number of iterations are shown for each case.</i>	<i>165</i>
<i>Figure 4.38: (a) Graphical description of the defined region of interest; (b) Example of the region of interest in the 40 kHz SCL image.</i>	<i>165</i>
<i>Figure 4.39: Qualitative comparison for the 28 kHz standing wave characteristics between the SCL image (a) and the investigated simulations (b) - (h).....</i>	<i>166</i>
<i>Figure 4.40: Real and imaginary parts of kc^2 predicted by the NH model for the 70 kHz case, at $n = 1 \times 10^{10} \text{ m}^{-3}$.</i>	<i>167</i>
<i>Figure 4.41: Qualitative comparison for the 40 kHz standing wave characteristics between the SCL image (a) and the investigated simulations (b) - (h).....</i>	<i>169</i>
<i>Figure 4.42: Normalised luminance profile plotted for the centre of the regions of interest for the 40 kHz case. Dashed lines mark the approximated locations of the SCL antinodes.</i>	<i>170</i>
<i>Figure 4.43: Qualitative comparison for the 70 kHz standing wave characteristics between the SCL image (a) and the investigated simulations (b) - (h).....</i>	<i>171</i>
<i>Figure 4.44: Normalised luminance profile plotted for the centre of the regions of interest for the 70 kHz case. Dashed lines mark the approximate locations of the SCL antinodes.</i>	<i>172</i>
<i>Figure 5.1: Graphical explanation depicting the similarities between the constant polydisperse approach and the monodisperse approach.</i>	<i>190</i>
<i>Figure 5.2: Representation of the dependencies within an acoustic pressure simulation framework.....</i>	<i>196</i>

Figure 5.3: Relationship between the phase speed and wavelength as a function of the uniform bubble density, plotted at 40 kHz and bubble radius of 5 μm.200

Figure 5.4: Graphical description of the proposed semi-empirical approach to characterise the hexagonal sonoreactor using SCL image data.202

Figure 5.5: The wavelength measurement process: (a) Distinct and uniform standing waves for the 40 and 70 kHz case; (b) Normalised luminosity plots.203

Figure 5.6: The effect of different equilibrium bubble radii on the relationship between the bubbly-liquid phase speed and the bubble density.....205

Figure 5.7: The comparison of the antinode prediction of the monodisperse linear CP model using a tuned bubble parameter of $n = 6.04 \times 10^{10} \text{ m}^{-3}$ for the 40 kHz case.207

Figure 5.8: The comparison of the antinode prediction of the monodisperse linear CP model using a tuned bubble parameter of $n = 4.31 \times 10^{10} \text{ m}^{-3}$ for the 70 kHz case.207

Figure 5.9: (a) Visual representation of the hexagonal sonoreactor dimensions; (b) Orientation of the frequencies involved.218

Figure 5.10: Graphical representation of the nonlinear CP iteration loop.221

Figure 5.11: SCL images of multi-frequency combinations; with design power of 600 W for dual-frequency and 900 W for tri-frequency.223

Figure 5.12: RMS acoustic pressure solved using the linear CP approach.....224

Figure 5.13: Plots of the root-mean-squared acoustic pressure solved for the four multi-frequency cases using the nonlinear CP approach.226

Figure 5.14: Bubble density (left axis) and its associated attenuation magnitude (right axis) plotted as a function of root-mean-squared pressure for the harmonic fields of 28 and 40 kHz.227

<i>Figure 5.15: Attenuation mechanism of the linear and nonlinear approach in this investigation.....</i>	<i>227</i>
<i>Figure 5.16: (a) Comparison between $Prms(r)$ predicted from simulation and SCL data for the 28 – 40 kHz case, (b) Region of interest showing the agreement of the 40 kHz standing wave.</i>	<i>229</i>
<i>Figure 5.17: (a) Comparison between $Prms(r)$ predicted from simulation and SCL data for the case of 28-40 kHz case; (b) Region of interest showing the agreement of the 28 kHz standing wave.....</i>	<i>229</i>
<i>Figure 5.18: (a) Comparison between $Prms(r)$ predicted from simulation and SCL data for the 40 – 70 kHz case; (b) Region of interest showing the weak agreement of the 40 kHz standing wave.....</i>	<i>230</i>
<i>Figure 5.19: (a) Comparison between $Prms(r)$ predicted from simulation and SCL data for the 28 – 70 kHz case superimposed along the 28 kHz standing wave; (b) Region of interest showing very good agreement.....</i>	<i>231</i>
<i>Figure 5.20: (a) Comparison between $Prms(r)$ predicted from simulation and SCL data for the 28 – 70 kHz case; (b) Region of interest showing very good agreement for the fine 70 kHz wave patterns.</i>	<i>231</i>
<i>Figure 5.21: (a) Comparison between $Prms(r)$ predicted from simulation and SCL data for the tri-frequency case; (b) Region of interest comparing the 40 kHz standing wave.</i>	<i>232</i>
<i>Figure 5.22: (a) Comparison between $Prms(r)$ predicted from simulation and SCL data for the tri-frequency case; (b) Region of interest comparing the 28 kHz standing wave.</i>	<i>232</i>
<i>Figure 5.23: Illustration comparing $Prms(r)$ (horizontal solid line) and $Pmax(r)$ (horizontal dotted line). The fine-dotted curves represent different frequencies oscillating at magnitudes $P1(r)$, $P2(r)$ and $P3(r)$, and $p_{total}(r, t)$ is the sum of pressure (solid curve).</i>	<i>235</i>

Figure 5.24: The graphical representation in Figure 5.23 plotted in terms of absolute pressure.236

Figure 5.25: Case study on two different interpretations of the acoustic pressure magnitude for the tri-frequency case: Pressure field characterised using $P_{rms}(\mathbf{r})$ (a and c); Pressure field characterised using $P_{max}(\mathbf{r})$ (b and d).237

Figure 5.26: Simulated single frequency components for the triple frequency case. Image (a), (b) and (c) represents the 28, 40 and 70 kHz frequency-domain absolute pressure. Results are plotted using a shared colour legend.238

Figure 5.27: Peak absolute pressure for 28, 40 and 70 kHz with increasing hexagonal sonoreactor sizes. The physical sonoreactor used in this work has a side length of 140 mm, marked as the vertical line.239

List of Tables

<i>Table 2.1: Assumptions for the derivation of the Caflisch model.</i>	<i>38</i>
<i>Table 2.2: Complex wavenumber calculation for the CP model.</i>	<i>44</i>
<i>Table 2.3: Summary of wavenumber formulation for NH models.</i>	<i>49</i>
<i>Table 2.4: Louisnard's (2010) formulation of the NH model.</i>	<i>50</i>
<i>Table 2.5: Jamshidi and Brenner (2013) formulation of the NH model.</i>	<i>51</i>
<i>Table 2.6: Trujillo's (2020) formulation of the NH model.</i>	<i>52</i>
<i>Table 2.7: Common boundary conditions in acoustic simulations.</i>	<i>64</i>
<i>Table 3.1: Computational resource requirements for each test simulation.</i>	<i>76</i>
<i>Table 4.1: Physical properties (25°C) used in Case Study 3.</i>	<i>102</i>
<i>Table 4.2: Dirichlet boundary condition magnitudes for each frequency.</i>	<i>102</i>
<i>Table 4.3: Summary of mesh information for four studied frequencies (pure-liquid simulations).</i>	<i>108</i>
<i>Table 4.4: Solution times and memory requirements for simulated cases.</i>	<i>108</i>
<i>Table 4.5: Bubbly-liquid phase speed and attenuation compared with calculated attenuation values of Son. et al. (2009).</i>	<i>114</i>
<i>Table 4.6: Effective bubbly-liquid density for each bubble density.</i>	<i>115</i>
<i>Table 4.7: Experimentally tuned bubble density magnitude determined from reported attenuation values, using the linear CP model with $R_0 = 5 \text{ um}$.</i>	<i>128</i>
<i>Table 4.8: Compilation of past antinode validation works and their calculated DS/λ values.</i>	<i>145</i>
<i>Table 4.9: Physical properties (25°C) used in Case Study 5.</i>	<i>150</i>

<i>Table 4.10: Calorimetry data for the calculation of Dirichlet transducer boundary condition for single-frequency simulations (Tiong et al., 2017a).</i>	150
<i>Table 5.1: Compilation of bubble measurements reported for cavitating systems in past works.</i>	180
<i>Table 5.2: Compilation of bubble field parameters used in past numerical investigations.</i>	184
<i>Table 5.3: Averaged wavelength measurements from SCL images compared to theoretical pure-liquid wavelength.</i>	204
<i>Table 5.4: Calorimetry data for the calculation of Dirichlet transducer boundary condition for multi-frequency simulations (Tiong et al., 2017a).</i>	219
<i>Table 5.5: Physical properties (25°C) used in Case Study 7.</i>	220
<i>Table 5.6: Bubble field parameters used for each harmonic in the multi-frequency simulation.</i>	224
<i>Table 5.7: Comparison between peak values of RMS pressure and Maximum pressure for frequency combinations.</i>	236

Nomenclature

*Variables in **bold** are vector fields.

Abbreviations and Acronyms

CFL	Courant-Friedrichs-Lewy
FEM	Finite Element Method
FDM	Finite Difference Method
FVM	Finite Volume Method
CP	Commander and Prosperetti (model)
NH	Nonlinear Helmholtz (model)
R-P	Rayleigh-Plesset (bubble dynamics)
K-M	Keller-Miksis (bubble dynamics)
PML	Perfectly Matched Layer

Mathematical operators and physical quantities

$\langle \rangle$	Period averaged properties
$f_G ()$	Generalised Gaussian function
$\Im ()$	Imaginary-part of complex-valued expression
$\Re ()$	Real-part of complex-valued expression
B	Arbitrary coefficients for the Helmholtz solution
$c. c.$	Complex conjugate
∇	Nabla operator, partial derivative in space
∂	Partial derivative
E	Notation for exponent ($\times 10^n$), e.g., 1E5 is equivalent to 1×10^5
e	Exponential constant
i	Imaginary constant
\mathbf{n}	Normal vector
π	Pi constant
\mathbf{r}	Spatial coordinate, (m)
t	Time dimension, (s)

τ	Dimensionless time, (-)
\mathcal{A}	Trujillo's NH model real part parameter
α	Attenuation coefficient, (Np/m)
α'	Modified time-domain attenuation coefficient, (Np/m)
\mathcal{B}	Trujillo's NH model imaginary part parameter
β	Bubble fraction, (m^3/m^3)
γ_g	Ratio of specific heats for gas in bubble, (-)
Δt_{max}	Solver time-stepping interval limit, (s)
κ	Propagation wavenumber, (1/m)
λ	Wavelength, (m)
λ_{min}	Smallest wavelength in the system, (m)
λ_{SCL}	Empirically determined wavelength [SCL], (m)
μ_l	Liquid dynamic viscosity, (Pa.s)
Π_{dis}	Total dissipation density, (W/m^3)
Π_{th}	Thermal dissipation density, (W/m^3)
Π_r	Radiation dissipation density, (W/m^3)
Π_v	Viscous dissipation density, (W/m^3)
ρ_0	Mean density, (kg/m^3)
ρ_{bd}	Boundary density, (kg/m^3)
ρ_{eff}	Effective bubbly-liquid density, (kg/m^3)
ρ_g	Gas density, (kg/m^3)
ρ_l	Liquid density, (kg/m^3)
ρ_{PU}	Polyurethane density, (kg/m^3)
ρ_s	Solid density, (kg/m^3)
σ_B	Bubble radii standard deviation, (m)
σ_l	Liquid surface tension, (N/m)
Φ	Dimensionless CP bubble parameter, (-)
Φ_h	Dimensionless Preston's heat coefficient, (-)

χ	Dimensionless CP thermal diffusion term, (-)
ω	Angular frequency, (rad/s)
ω_0	Bubble resonance angular frequency, (rad/s)
A_{bd}, a_{bd}	Specified boundary acceleration, (m/s ²)
A_{tr}	Transducer surface area, (m ²)
b	CP damping term, (-)
C_b	Tuning parameter for truncated Gaussian radii relation, (-)
C_v	Specific heat capacity of gas, (J/mol.K)
c_{bd}	Phase speed at boundary, (m/s)
c_{bl}	Bubbly-liquid phase speed, (m/s)
c_{bd}	Phase speed at boundary, (m/s)
c_{eff}	Effective phase speed, (m/s)
c_l	Phase speed in liquid, (m/s)
c_{PU}	Phase speed in polyurethane, (m/s)
c_{SCL}	Empirically measured phase speed [SCL], (m/s)
D_{bd}, d_{bd}	Specified boundary displacement, (m)
D_g	Gas diffusivity in bubble, (m ² /s)
D_S	Effective length of sonoreactor, (m)
E	Error estimate of solver
E_A	Acoustic energy, (J)
f	Frequency, (Hz)
f_B	Acoustic body forces, (N/m ³)
f_e	Wavelength reduction factor, (-)
f_{max}	Maximum frequency in simulation, (Hz)
G	Foldy's bubble dissipation per volume
h	Half-wavelength, (m)
h_{SCL}	Empirically measured half-wavelength [SCL], (m)
h_T	Heat transfer coefficient, (W/m ² .K)

h_{vap}	Latent heat of vaporisation of water, (J/mol)
I_{ac}	Acoustic pressure intensity, (W/m ²)
K_T	Gas thermal conductivity, (1/m)
k	Wavenumber, (1/m)
k_c	Complex-valued wavenumber, (1/m)
k_{real}	Wavenumber [real part, see also: κ], (1/m)
k_{imag}	Wavenumber [imaginary part, see also: α], (1/m)
l_{th}	Diffusion penetration depth, (m)
M	Foldy's bubble scattering function
N	Foldy's bubble distribution function
\dot{N}_{H_2O}	Vapour rate of change, (mol/s)
N_{mesh}	Number of mesh per wavelength, (-)
N_T	Molecular density, (1/m ³)
n	Bubble density, (1/m ³)
O_m	Transducer power measure from calorimetry, (W)
P	Spatial acoustic pressure, (Pa)
P^*	Spatial acoustic pressure (complex conjugate), (Pa)
P_B	Blake's cavitation threshold, (Pa)
Pe	Peclet number, (-)
P_{bd}, p_{bd}	Specified boundary pressure, (Pa)
P_{g0}	Initial bubble pressure, (Pa)
P_m	Helmholtz spatial pressure for m th harmonic, (Pa)
P_{max}	Maximum spatial acoustic pressure in a multi-harmonic field, (Pa)
P_{rms}	Root-mean-squared acoustic pressure, (Pa)
P_{Tr}	Transducer surface pressure, (Pa)
$ P $	Acoustic pressure magnitude, (Pa)
$ P _{ant}$	Antinodal pressure magnitude, (Pa)
$ P _{nod}$	Nodal pressure magnitude, (Pa)

p	Transient acoustic pressure, (Pa)
p^*	Dimensionless pressure amplitude, (-)
p'	Transient acoustic pressure (perturbation form), (Pa)
p_∞	Mean (far-field) pressure around bubble, (Pa)
p_{bd}	Boundary acoustic pressure, (Pa)
p_F	Acoustic forcing on bubble, (Pa)
p_g	Bubble pressure, (Pa)
\dot{p}_g	Rate of change in bubble pressure, (Pa/s)
p_T	Total acoustic pressure, (Pa)
$\overline{p_T}$	Averaged total pressure, (Pa)
p_v	Bubble vapour pressure, (Pa)
p_w	Composite bubble wall pressure, (Pa)
\dot{Q}	First time derivative of heat transfer, (W/s)
R	Bubble wall radius, (m)
R_0	Equilibrium bubble radius, (m)
R_{ac}	Reflection coefficient, (-)
R_{gas}	Gas constant, (J/mol.K)
R_m, R_{mean}	Mean equilibrium bubble radii, (m)
R_t, \dot{R}	Bubble wall velocity, (m/s)
R_{tt}, \ddot{R}	Bubble wall acceleration, (m/s ²)
S_{mesh}	Upper limit of mesh size, (m)
T_∞	Temperature of bubble surroundings, (K)
T_B	Uniform bubble internal temperature, (K)
U	Spatial acoustic velocity, (m/s)
U^*	Spatial acoustic velocity (complex conjugate), (m/s)
u	Acoustic velocity, (m/s)
u_{bd}	Boundary acoustic velocity, (m/s)
u'	Acoustic velocity [perturbation form], (m/s)

\mathbf{u}_B	Bubble velocity, (m/s)
V	Bubble volume, (m ³)
\dot{V}	Rate of change of bubble volume, (m ³ /s)
V_{bd}, v_{bd}	Specified boundary velocity, (m/s)
X	Nonlinear bubble density scaling parameter, (1/Pa)
x	Estimated solution
x_0	Exact solution
Z	Specific acoustic impedance, (kg/m ² .s)

Chapter 1: Background

The technology of power ultrasound and sonoreactors became increasingly popular in recent years. The simulation of acoustic pressure fields within the working fluid was noted to be an important aspect of sonoreactor design. Simulation results were found to be useful for design and optimisation purposes (Sutkar et al., 2010). Currently, there are many knowledge gaps to be explored, notably concerning the modelling of acoustic pressure in large-scale ultrasonic baths.

1.1 Introduction

1.1.1 Power Ultrasound and Acoustic Cavitation

Ultrasound refers to acoustic waves above 20 kHz (Leighton, 1994), and the technology of power ultrasound involves the high-intensity application of ultrasonic energy (Yao et al., 2020). The driving force behind power ultrasound is acoustic cavitation. Acoustic cavitation generally occurs when a liquid medium is subjected to high-amplitude ultrasonic waves (Noltingk and Neppiras, 1950). Figure 1.1 provides a graphical description of the acoustic cavitation process. Compression and rarefaction pressure cycles cause bubbles to grow in a process called rectified diffusion (Ashokkumar et al., 2007). Eventually, the bubbles collapse and release a large amount of energy (Flynn, 1964). This can theoretically generate local pressures and temperatures up to 500 bar and 5000 K (Leighton, 1994).

Acoustic cavitation can be used to achieve various physiochemical effects such as micromixing, particle size reduction, and radical generation (Lorimer and Mason, 1987; Ley and Low, 1989; Pandit et al., 2021). Lower-frequency power ultrasound (20 – 100

kHz) had been reported to be more suitable for applications that require mechanical effects; while higher frequencies (100 – 1 MHz) were known to perform better in chemical applications (Kiss et al., 2018). To date, power ultrasound technology had been studied for various applications such as chemical synthesis (Gholami et al., 2019; Islam et al., 2019a), nanotechnology (Islam et al., 2019b; Modarres-Gheisari et al., 2019), separation processes (Chen et al., 2020; Wang et al., 2020), biotechnology (Yin et al., 2004; Arefi-Oskoui et al., 2019), food processing (Huang et al., 2020), textile treatment (Perincek et al., 2009) and metal melt processing (Lebon et al., 2018).

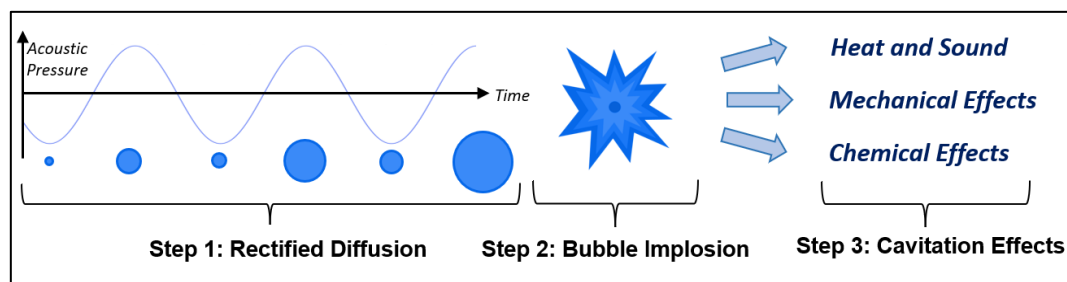


Figure 1.1: Graphical depiction of acoustic cavitation and its effects.

A strong indicator of cavitation performance is the acoustic intensity, which in turn is related to the acoustic pressure magnitude (Pandit et al., 2021). The cavitation threshold refers to the acoustic pressure at which cavitation begins to occur. This threshold had been noted to depend on multiple factors such as operating frequency, working fluid properties, and bubble properties (Sutkar and Gogate, 2009). Other factors that affect cavitation performance include the effects of temperature and pressure in relation to the vapour pressure of the liquid. Conditions that favour lower vapour pressures will decrease the cavitation threshold; at the cost of reduced cavitation intensities due to condensation losses (Lorimer and Mason, 1987).

1.1.2 Workings of a Sonoreactor

Sonoreactors, or 'sound reactors' are set-ups that are used to generate acoustic cavitation within a volume of liquid. This can range from laboratory configurations with beakers to large industrial vessels. In its simplest form, the basic components of a sonoreactor consist of the transducers, the propagation medium, and the mechanical vessel.

1.1.2.1 Ultrasonic Transducers

Ultrasonic transducers provide the main driving force for a sonoreactor. Transducers generally consist of metal fittings, electrodes, and piezoceramic stacks (Iula et al., 2002). The property of piezoelectric materials causes them to mechanically displace in response to changes in electric fields (DeAngelis and Schulze, 2016). In sonoreactors, the mechanical vibration generated by one or more transducers is used to emit ultrasonic waves into the working fluid.

Figure 1.2 (a) shows a simplified schematic of a transducer assembly. The mechanical energy generated by the piezoelectric stack is transmitted into the working fluid through the front mass/coupling head. Figure 1.2 (b) shows an example of a sonotrode, also known as an ultrasonic horn. The ultrasonic horn is designed to generate strong acoustic intensities at the tip of the front mass, which is usually immersed in the working fluid. Figure 1.2 (c) shows the image of a wall transducer. These transducers are generally attached to the walls of a sonoreactor vessel; for which a common example is an ultrasonic cleaning bath (Tangsopa and Thongsri, 2019). An interesting caveat of ultrasonic transducers is the need to tune their geometric parameters to

achieve optimal performance (Chen, 2011). This is a challenge when scaling up sonoreactors. A common workaround is to modify the number of transducers instead of changing its size. One such example is the use of a transducer array (Asakura et al., 2008).

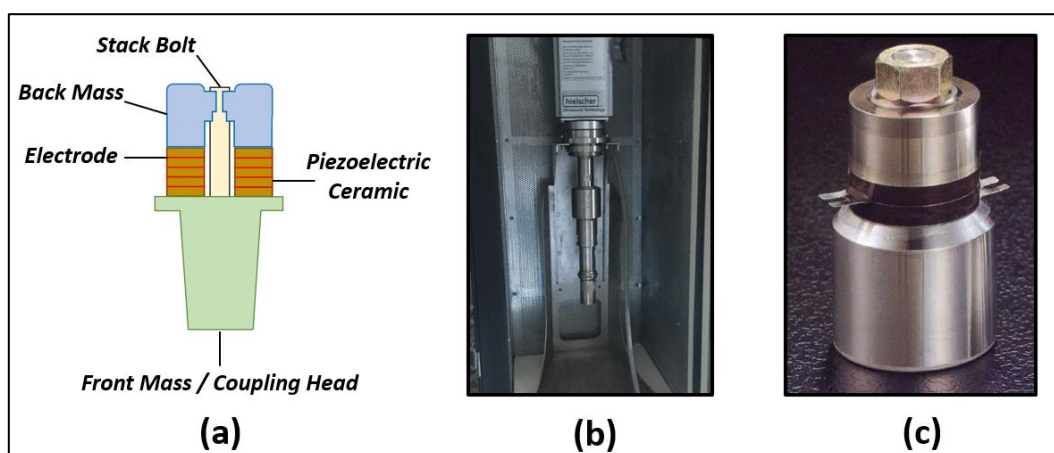


Figure 1.2: (a) Transducer cross-section; (b) Sonotrode (Hielscher Ultrasonics) for horn-type configurations; (c) Wall transducer (Sonictron Malaysia) for bath-type sonoreactors.

1.1.2.2 Horn- and Bath-Type Sonoreactors

Conventional sonoreactor designs are categorised into two configurations: horn-type and bath-type. The horn-type configuration refers to systems that use an ultrasonic horn or sonotrode. An important characteristic of the horn-type configuration is the direct contact between the ultrasonic transducer and the working fluid. This design allows mechanical energy to be directly transmitted into a small effective volume to generate intense cavitation effects (Dahlem et al., 1999). The most common example is a probe-beaker system described in Figure 1.3 (a). The probe-beaker system is widely used in laboratorial sonochemical research due to its operational simplicity (Pokhrel et al., 2016; Modarres-Gheisari et al., 2019; Singla and Sit, 2021). Sonotrodes

can also be fitted to ultrasonic flow cells; for which an example configuration is shown in Figure 1.3 (b). These configurations attempt to maximise cavitation activity by confining acoustic waves within a small volume (Guo et al., 2019). The schematics shown are inspired by the sonoreactor studied by Hussain and Janajreh (2017).

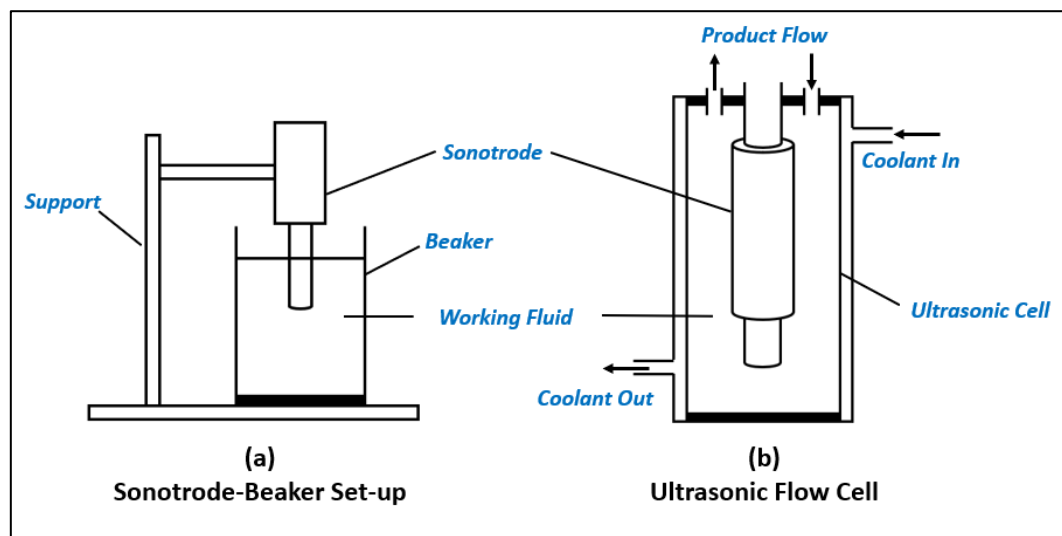


Figure 1.3: Schematic drawing describing: (a) a probe-beaker system; (b) an ultrasonic flow cell.

In bath-type configurations, the acoustic waves are generally emitted into the working fluid from large vibrating surfaces, on which wall transducers are attached. Figure 1.4 (a) shows two example designs for a typical ultrasonic bath. Mechanical energy from transducers is transmitted into the working fluid through the solid walls or the floor of the vessel (Tangsopa and Thongsri, 2019). Another common design for ultrasonic baths uses a transducer array module shown in Figure 1.4 (b). This configuration generates ultrasonic waves by submerging the transducer array module into the working fluid (Son et al., 2009).

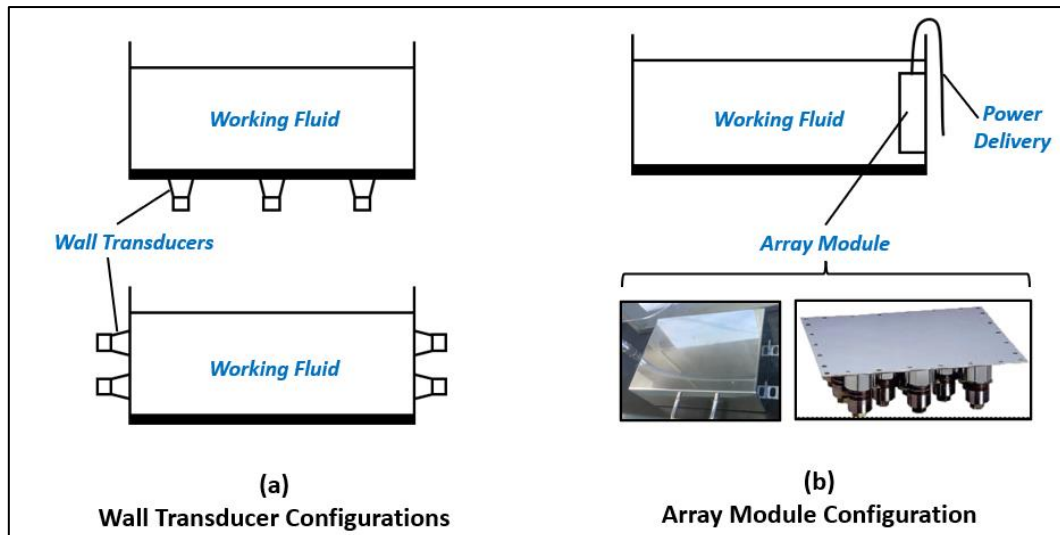


Figure 1.4: Example of: (a) ultrasonic bath with wall transducers; (b) ultrasonic bath with a transducer array module (KSONIC, Malaysia).

Horn-type and bath-type sonoreactors have different characteristics. Horn-type systems generate high acoustic intensities in a conical region under the sonotrode (Dahlem et al., 1999; Campos-Pozuelo et al., 2005; Jamshidi et al., 2012), but have limited effective volume due to a smaller emission area and the "shielding effect" caused by dense bubble clouds (Moussatov et al., 2003). In contrast, bath-type systems have larger effective volumes and a more uniform distribution of acoustic energy, but lower acoustic intensities at the same input power (Son et al., 2009; Tangsopa and Thongsri, 2019). Bath-type systems can also be scaled through the use of transducer arrays (Gogate et al., 2011).

1.2 Literature Review

1.2.1 Numerical Simulations for Sonoreactor Modelling

Sonoreactor scale-up was found to be a challenging process due to the need to consider many interlinked factors such as geometry, transducer designs, operating

frequencies, power intensity, and propagation medium (Gogate et al., 2011). Changing certain parameters would often interfere with other aspects of the design (Romdhane et al., 1997; Asakura and Yasuda, 2021). Difficulties in achieving controlled design environments often led to resource-intensive design methods (Gogate et al., 2011) or a strong reliance on trial and error (Liu et al., 2008; Sutkar and Gogate, 2009; Bandelin et al., 2020).

The prospects of numerical simulation for sonoreactor design and optimisation had caught the attention of researchers since the twentieth century (Ando and Kagawa, 1989). On paper, well-developed simulation methods can solve complex design problems in place of physical experiments. This led to acoustic pressure models becoming a major focus in the study of sonoreactor acoustics. The models were used to predict cavitation regions (Klíma et al., 2007; Tangsopa and Thongsri, 2019), acoustic streaming (Louisnard, 2017), and heat transfer (Chen et al., 2021).

Early studies mainly focused on simple acoustic models that considered the working fluid as a pure liquid (Sáez et al., 2005; Klíma et al., 2007). However, it soon became apparent that the presence of bubbles should not be ignored (Servant et al., 2000). This led to the adoption of bubbly-liquid acoustic pressure models, henceforth referred to as bubbly-liquid models, to model sonoreactor acoustics (Tudela et al., 2014). Two prominent bubbly-liquid models are the Commander and Prosperetti (CP) model (Commander and Prosperetti, 1989) and the nonlinear Helmholtz (NH) model (Louisnard, 2012a; Jamshidi and Brenner, 2013; Trujillo, 2018). These frequency-domain models were shown to provide better predictions compared to pure-liquid models (Louisnard, 2012a; Sarac et al., 2020).

1.2.2 Sonoreactor Characterisation and Model Validation

Validation of mathematical models is crucial to evaluate and enhance the performance of numerical simulations. The performance of acoustic pressure models was often verified and validated using data obtained from experiments (Klíma et al., 2007; Yasuda et al., 2018). A straightforward method was to compare it to the pressure measurements of a hydrophone (Campos-Pozuelo et al., 2005; Sarac et al., 2020). Some researchers also performed validation using proxy measurements that relied on well-understood relations between the acoustic pressure field and the measured quantity (Sutkar et al., 2010). Examples include cavitation intensity measurements (Yasuda et al., 2018), acoustic streaming analysis (O'Sullivan et al., 2018), temperature distribution measurements (Chen et al., 2021), and chemical reaction rates (Son et al., 2020). Figure 1.5 provides a summary of the various validation methods in literature. Some methods allow for a more specific validation quality, while others only provide rough estimations on the model performance.

This work focused on verifying two key mechanisms of the acoustic pressure model: phase speed prediction and attenuation prediction. The former was studied using antinode validation methods, and the latter required hydrophone data. The prediction of phase speed is crucial for the identification of effective/dead zones in the sonoreactor, while accurate attenuation modelling is important for energy balance calculations (e.g., cooling and rate of reaction).

Validation Quality	Empirical Method	Studied Physical Phenomena	Relation to Acoustic Pressure Field	Validated Quantity
Specific ↓	Hydrophone Measurement	Pressure Distribution	Direct	Pressure Magnitude, *Antinode Prediction
	Foil Mapping	Mechanical Force Distribution	Cavitation Intensity	Antinode Prediction *Relative Pressure Magnitude
	Sonochemiluminescence (SCL) Imaging	Chemical Reaction and Bubble Field	Sonochemistry and Bjerknes Force	Antinode Prediction *Relative Pressure Magnitude
	Bubble Structure Imaging	Bubble Field	Bjerknes Force	Antinode Prediction
	Particle Image Velocimetry	Fluid Flow Field	Acoustic Radiation Forcing and Pressure Gradients	Acoustic Streaming Forces
	Calorimetry	Bulk Temperature	Acoustic Energy Dissipation	Active Power
	General	Dosimetry	Sonochemical Reaction Rates	Sonochemistry

* Depends on the studied system.

Figure 1.5: Validation methods for acoustic pressure models listed based on validation quality.

1.2.2.1 Antinode Characterisation and Validation Methods

In classical acoustics, the term ‘antinode’ describes the peaks of a standing wave. In this work, the definition was relaxed to refer to regions in the sonoreactor with high local pressure magnitudes. The characterisation of antinodes in sonoreactors involved visual methods such as sonochemiluminescence (SCL) or foil erosion mapping (Sutkar and Gogate, 2009). In foil mapping, the antinodes are inferred from regions that exhibit significant foil erosion. On the other hand, the SCL approach identifies antinodes as regions that exhibit sonochemiluminescence. Thus, it is imperative to note that antinode characterisation methods are often strongly qualitative, and resulting interpretations hold an inherent degree of subjectivity.

Foil mapping had been reported to be a cheap and simple method for characterising the antinodal regions (Sutkar and Gogate, 2009). The main limitation of the method is that it is invasive, as the presence of the foil in the working fluid could alter the pressure field. Additionally, mechanical structures may need to be used to ensure that

the foil remains static during testing (Tangsopa and Thongsri, 2019). In contrast, SCL is non-invasive and provides information on the relative cavitation intensities in the studied system. SCL is also easily scalable for large sonoreactor volumes. The main drawbacks of SCL are its relatively higher costs of materials and the need to capture optical data under low light conditions.

1.2.2.2 Direct Acoustic Pressure Measurements

On paper, validating acoustic pressure models against pressure measurements would be preferable, as it offers a direct comparison. However, this method can be challenging as pressure measurements were found to be highly transient and noisy due to the generation of broadbands by the cavitating bubbles (Avvaru and Pandit, 2009; Moholkar et al., 2000). This led to the need for additional signal processing to identify and isolate the required data. Furthermore, acoustic pressure measurements were found to depend on many factors such as geometry, reflection surfaces, wave interference, calibration data, and equipment condition (Leighton, 1994; Dähnke et al., 1999b; Son et al., 2009). Difficulties in maintaining a controlled environment further complicate the validation process. Lastly, the risk of cavitation damage also limits the range of applicable hydrophones. In light of these limitations, a direct pressure verification study is the only way to properly investigate the attenuation prediction mechanism of the acoustic pressure model.

1.2.2.3 Other Characterisation and Validation Methods

While not the main focus of this work, the author finds it instructive to discuss some other methods used to evaluate the performance of acoustic pressure models. Data gathered from calorimetry is often used in the study of sonoreactor acoustics. The calorimetric method quantifies the active power of the sonoreactor, which is the energy received by the working fluid minus environmental losses (Louisnard et al., 2009). The method generally assumes that all the acoustic energy is eventually converted into heat and that the temperature change over time is used to calculate the active power. In sonoreactor acoustics, calorimetry measurements were often used to approximate the effective pressure intensity at the vibrating boundaries of the simulation model (Tiong et al., 2019).

In addition to calorimetry, acoustic streaming data was also often analysed along the acoustic behaviour of sonoreactors. Acoustic radiation forces in a sonoreactor can generate flow fields, and researchers had attempted to verify the acoustic pressure model using streaming characteristics (Louisnard, 2017; Fang et al., 2018). The flow fields predicted from the acoustic pressure model were compared with data from characterisation techniques such as particle image velocimetry (Barthès et al., 2015; Lebon et al., 2019). It can be argued that this validation method is less suitable for bath-type configurations because the acoustic radiation forces are much weaker. This can be shown using simple radiation force calculations (Eckart, 1948), but was omitted in this work.

Last but not least, chemical dosimetry methods often serve as an integral indicator for sonochemical efficiency within a sonoreactor based on the change in concentration of

a chemical species (Lorimer and Mason, 1987). A comprehensive review on this matter can be found in the work of (Sutkar and Gogate, 2009). In the field of sonochemistry, chemical dosimetry provides a valuable means to study chemical mechanisms and reaction pathways; however, its use for the verification of acoustic pressure models is limited.

1.2.3 Review of Acoustic Pressure Modelling and Validation Works

This section reviews past works involving acoustic pressure simulation using pure-liquid, CP, and NH models. The focus is placed on simulation strategies, mathematical implementations, and the performance of the studied models. Comments are provided for notable contributions and uncertainties. The main objective is to consolidate the available information on the matter and identify key knowledge gaps to be addressed in this research.

1.2.3.1 Studies Involving the Pure-Liquid Model

Before the popularity of the pure-liquid approach, time-domain bubbly-liquid models had been used by research groups to study acoustic pressure fields in sonoreactors (Dähnke et al., 1999a, 1999b; Servant et al., 2000, 2001, 2002; Vanhille et al., 2004, 2005). These works involved time-domain simulations solved using FDM. Interestingly, these bubbly-liquid methods did not gain significant traction until much later, presumably due to the complexity of the methods involved.

The studies of Sáez et al. (2005) and Klíma et al. (2007) reported promising prospects for the pure-liquid approach solved in FEM. Their results led to an increase in interest within the community on the topic of sonoreactor modelling. Figure 1.6 shows a commonly cited verification result reported by Klíma et al. (2007). The result showed strong agreement between the experimentally observed antinodal bubbles and the high-pressure regions predicted by the numerical simulation.

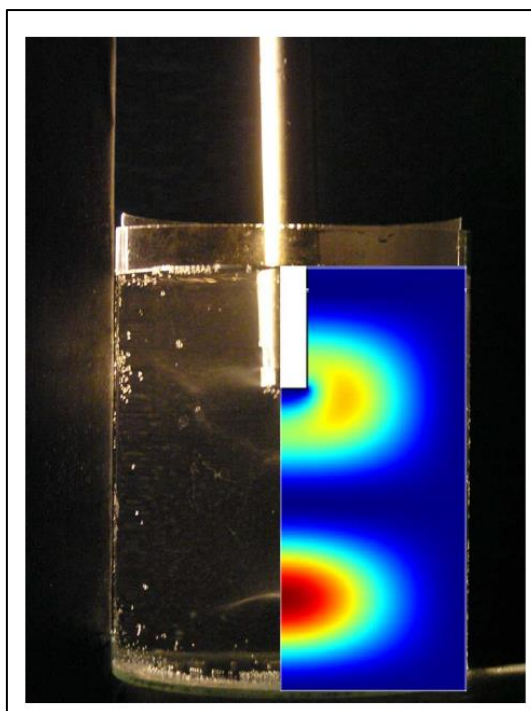


*Figure 1.6: Validation result of Klíma et al. (2007) showing that the antinode locations coincide with the cavitation bubbles. [Reprinted from: *Ultrasonics Sonochemistry* 14, Klíma, J., Frias-Ferrer, A., González-García, J., Ludvík, J., Sáez, V., Iniesta, J., Optimisation of 20 kHz sonoreactor geometry on the basis of numerical simulation of local ultrasonic intensity and qualitative comparison with experimental results. 19–28, Copyright (2007), with permission from Elsevier]*

Although the effect of bubbles on the acoustic pressure field was known (Wilson et al., 2005), the pure-liquid approach remains one of the most used modelling strategies to date. It was speculated that this was due to the simplicity and accessibility of the model. The Helmholtz equation was integrated into many commercial numerical solvers, which allowed researchers to easily set up a well-posed simulation. On the topic of bubble effects, Sáez et al. (2005) briefly commented on the importance of including cavitation in future works, while Klíma et al. (2007) explained that bubble attenuation was omitted in their work to reduce model complexity. It was also commented that the results should only be taken as rough qualitative estimates.

In their study, Yasui et al. (2007) tested several arbitrary attenuation values using the pure-liquid model to study the acoustic pressure field of a 100 kHz cylindrical sonoreactor. Their simulations considered wall vibrations modelled using solid mechanics. They compared the predicted acoustic pressure fields using several attenuation values with experimental observations and reported that a value of 5 m^{-1} provided the best qualitative agreement with SCL images. In another study, Shao et al. (2010) used the pure-liquid model to study ultrasonic melt treatment. They fully adopted the methodology of Klíma et al. (2007) but did not further address the issue of bubble effects.

The study of Louisnard et al. (2009) referenced the methods of Yasui et al. (2007) and used arbitrary attenuation values to study the effect of solid vibrations in sonoreactor design. They stated that the effect of bubbly liquids was excluded from their simulation due to difficulties in implementation. A similar study was also reported by Tudela et al. (2011) who also provided little discussion on bubbly-liquid effects.

A series of studies attempted to incorporate viscous attenuation into the pure-liquid approach using the dispersion relation presented in Eqn. (1) to better model the behaviour of the working fluid (Sutkar et al., 2010; Sutkar and Gogate, 2010; Csoka et al., 2011):

$$k_c = \frac{\omega}{c_l} \frac{1}{\sqrt{1 + (i\omega\mu_l/\rho_l c_l^2)}} \quad (1)$$

Sutkar et al. (2010) argued that cavitation effects can be neglected in their investigation, as they were assumed to be insignificant for the studied range of intensities. A scrutiny of the dispersion relation in Eqn. (1) revealed that the

attenuation was found to be virtually zero. Since the parameters used in their simulation were not specified, common values for pure water were used to support this claim ($c_l = 1500$ m/s; $\mu_l = 0.001$ Pa.s; $f = 20$ kHz; and $\rho_l = 1000$ kg/m³). A simple calculation using Eqn. (1) resulted in a complex-valued wavenumber of $83.7 - 2.3E-6i$, where the attenuation coefficient was calculated to be 2.3×10^{-6} Np/m. For reference, the attenuation values reported by Son et al. (2009) measured for an ultrasonic tank were reported to be around 2 Np/m. This showed that viscous attenuation alone is not sufficient to characterise the cavitating system.

Xu et al. (2013) used the pure-liquid model to investigate acoustic streaming using an arbitrary attenuation of 1 Np/m and did not comment on bubbly-liquid contributions. Wang and Yao (2013) extended the investigations of Klíma et al. (2007) by incorporating contributions of solid mechanics and attenuation. They recognised the importance of bubble effects, but considered it to be out of scope. Instead, they used attenuation values determined by Kinsler et al. (1982). Recently, Wei and Weavers (2016) used the pure-liquid approach for the characterisation of a stepped-horn vessel, using a similar approach as Tudela et al. (2011) but on a larger scale. The study by Yasuda et al. (2018) reported remarkable agreement between their simulation results and hydrophone measurements. However, some of their simulation methods were omitted, notably the specification of the transducer boundary condition, which limits the reproducibility of their results. Tiong et al. (2019) used the pure-liquid approach to analyse the ultrasonic mixing of oil-water emulsions. Tangsopa and Thongsri (2019, 2021) used the model in a comprehensive FEM study for the design of ultrasonic cleaning tanks. Rashwan et al. (2020, 2021) also adopted the pure-liquid approach in

a theoretical investigation to determine the best sonoreactor geometry for their hydrogen reactor.

A common observation regarding the pure-liquid model was found to be the prevalence of antinode verification (foil mapping and SCL). Interestingly, most studies reported good agreement between simulation and experiments. The study of Lewis et al. (2007) for an ultrasonic bath showed that the antinode prediction agrees well with foil mapping data. Xu et al. (2013) also noted that their simulation managed to correctly predict the location of four antinodes in a beaker. More recently, foil mapping results of Tangsopa and Thongsri, (2019) also agreed well with their simulations. This was noted to be interesting because it was established that the presence of bubbles alters the phase speed (Servant et al., 2001b). Thus, the change in phase speed should be reflected in the antinode verification results, which contradicts the above findings. This led to two possible explanations. It was first hypothesised that the changes in phase speeds in the studied sonoreactors were negligible. However, Case Study 6 [Section 5.3] showed that the phase-speed reduction measured for an investigated sonoreactor was calculated to be around 15 %, which contradicts the first hypothesis. This led to a second hypothesis, which states that the small geometries studied in past investigations were not able to provide sufficient resolution to capture this reduction in phase speed. This matter was investigated in Case Study 4 and led to interesting results.

1.2.3.2 Studies Involving the CP Model

The CP model and its variations had a prominent presence in sonoreactor simulations prior to the rise of FEM methods. Its earliest documented use in sonoreactor acoustics was published by Dähnke et al. (1999a, 1999b) where the model was incorporated into a modified wave equation:

$$\frac{\partial^2 p}{\partial t^2} + 2\alpha' \frac{\partial p}{\partial t} - \left(\frac{\alpha'^2 + \omega^2}{k_c^2} \right) \nabla^2 p = 0 \quad (2)$$

Their study proposed two key ideas, which is the nonlinear n approach and the piecewise bubble density assumption. These ideas would later be adopted in subsequent bubbly-liquid studies (Jamshidi and Brenner, 2012; Hussain and Janajreh, 2017, 2018). A series of sonoreactor simulation works used a similar approach by approximating the bubbly-liquid contributions using the linearised Keller-Miksis bubble dynamics (Servant et al., 2000, 2001a, 2003). Their studies solved the first-order Caflisch mass and momentum equations using FDM¹, and validation results using foil mapping were reported to be promising. The authors also commented on the uncertainties related to bubble field parameters and discussed the validity of the Caflisch model for sonoreactor acoustics.

The CP model re-emerged more than a decade later as the importance of bubbly-liquid contributions was realised. Jamshidi et al. (2012) showed that pure-liquid models were not reliable for the prediction of attenuation in cavitating systems and proposed the CP model as an alternative to address bubbly-liquid effects. However, their

¹ While their study did not explicitly include the CP model, their model showed many similarities.

justification for the suitability of the CP model was lacking. Notably, the fact that the CP model was derived for steady bubble fields was not discussed. The study also did not consider any form of empirical validation, which made it difficult to assess the accuracy of the simulations. A similar work by Jordens et al. (2013) also used the exact methodology. The CP model was used to predict the chemical activity in a sonoreactor, but the study focused on the aspects of sonochemistry and briefly commented on sonoreactor acoustics.

Several important issues for the linear CP model were noted by Dogan and Popov (2016) who performed a simple theoretical comparison against the NH model proposed by Jamshidi and Brenner (2013). Both models were studied under controlled conditions for a custom sonoreactor in 2D. They noted that the linear CP model suffered from unrealistic standing wave predictions that were not found in the NH model. They suggested that this was caused by the sensitivity of the phase-speed prediction to the bubble density parameter. Similar to Jamshidi et al. (2012), their work only involved theoretical discussion and lacked empirical validation.

Hussain and Janajreh (2017, 2018) adopted the methodologies of Jamshidi et al. (2012) to study the design and optimisation of a pilot-scale sonoreactor. Their study briefly discussed the aspect of acoustic pressure modelling and focused more on sonoreactor design. They justified the use of the nonlinear CP model by validating the simulation results against an empirical observation reported by Servant et al. (2001a). Their study extended the use of the validated model to design and optimise a much larger industrial sonoreactor. It was noted that their simulations predicted a wavelength slightly shorter than experimental observations, which was not addressed. Most

recently, Fang et al. (2018) used a nonlinear CP model for their study on acoustic streaming. They solved the model in OpenFOAM and commented on the difficulties in specifying the bubble field parameters. They also noted a surprising result where nonlinear n assumption seemed to yield bubble fraction values that showed good agreement with data reported by Burdin et al. (1999). Since their study focused on streaming fields for a very small geometry, the results did not yield any conclusive insights on the performance of the CP model.

1.2.3.3 Studies Involving the NH Model

As a recent addition to the field of sonoreactor acoustics, the NH model had yet to be extensively studied in literature. Louisnard (2012a) numerically compared the performance of the model against the pure-liquid and linear CP model in 1D, and claimed that it provided better attenuation predictions above the Blake threshold; however, this claim was made based on a qualitative comparison to the pressure measurements of Mettin (2005). In a subsequent study, Louisnard (2012b) showed that the NH model was able to correctly predict the ‘bubble cone’ streaming structure reported by Moussatov et al. (2003). This was done by coupling the NH model to the governing equations for bubble motion. While the results are impressive, they do not serve to validate the phase speed or the pressure magnitude prediction of the NH model. In the same study, it was also reported that the NH model managed to roughly provide pressure magnitudes that agreed with the measurements of Campos-Pozuelo et al. (2005).

The study by Dogan and Popov (2016) claimed that the NH model is capable of predicting the performance of the sonoreactor with greater accuracy compared to the linear CP model. However, this claim was based on numerical observations without experimental verification. An unexpected area of study that has seen considerable adoption of the NH model is ultrasonic melt processing (Beckwith et al., 2021; Subroto et al., 2021) where it was used to study power ultrasound technology in metal processing. Lebon et al. (2018, 2019a; 2019b) reported extensive investigations on the matter. Their studies provided important information on the implementation of the NH model; however, most of their validation results were performed at small scales using streaming fields measured from PIV.

One of the most prominent developments of the NH model is the work of Trujillo (2020). Not only does it serve as a very good technical documentation for the model, but an attempt to validate the model against the measurements of Campos-Pozuelo et al. (2005) yielded some interesting insights. Although a good agreement against the experimental pressure measurements was achieved, the author reported the need to parametrically vary the bubble density parameter. Additionally, the results also suggested that the NH model may have overpredicted bubble attenuation. This claim was made on the finding that very low bubble densities were required to match the experimental measurements.

Chen et al. (2021) used the NH model to study mass and heat transfer within a sonoreactor and reported promising results based on temperature measurements. Little can be derived for the performance of the NH model from their study. The study of Sarac et al. (2020) showed that Louisnard's (2012a) NH formulation compared well

with hydrophone measurements. However, the methods used to determine the bubble field parameters were not discussed. Interestingly, they noted that the NH model gave similar antinode predictions to the pure-liquid model. Similar methods were used by Delacour et al. (2020) to study a microreactor. They commented that their bubble fraction was tuned against hydrophone measurements, and the simulations showed good agreement in terms of pressure field distribution and maximum pressure magnitudes. Based on recent studies, the use of empirical tuning to address uncertainties in bubble field parameters seemed to be a rising trend. This matter shall be the focus of Chapter 5 as it was found to be an important topic to address current uncertainties for the bubbly-liquid models.

1.3 Notable Knowledge Gaps

Knowledge about sonoreactor modelling was found to be unconsolidated and lacking in terms of streamlined modelling strategies. Additionally, most validation studies only considered probe-beaker systems (Tudela et al., 2014) or very small (< 1L) ultrasonic baths (Delacour et al., 2020; Sarac et al., 2020). For this work, a large sonoreactor was defined as having a working volume of at least 10 L. The need to extend current knowledge to larger bath-type systems was driven by two key motivations. First, the results of the investigation would greatly contribute to the ongoing effort to develop a robust modelling strategy for the purpose of sonoreactor design and optimisation. Second, the knowledge generated would open up the possibility of using the bubbly-liquid models as a scale-up tool. This section discusses the knowledge gaps used to form the objectives of this work.

1.3.1 Modelling Strategies for Bath-Type Configurations

Sonoreactor acoustic studies were dominated by horn-type configurations, especially for the study of bubbly-liquid models (Jamshidi et al., 2012; Fang et al., 2018; Trujillo 2020). In contrast, studies involving ultrasonic baths were rare. Since the modelling strategies required for bath-type configurations can be drastically different, this presented to be an interesting knowledge gap. Current evidence suggests that uniform working fluid properties (Lewis et al., 2007; Tangsopa and Thongsri, 2019) in bath-type configurations can be sufficiently modelled using a simpler approach, such as the linear CP model. Additionally, while bubble clouds generated under sonotrodes had been observed to be dense and highly transient² (Dahlem et al., 1999; Moussatov et al., 2003), bath-type configurations had shown more uniform bubble fields (Tiong et al., 2017b). This further suggested that quasi-static methods could be sufficient. Based on these differences, a comprehensive investigation was carried out to confirm the viability of simpler bubbly-liquid models (linear CP) for the characterisation of bath-type sonoreactors.

1.3.2 Large-Scale Validation Studies

There was little evidence in literature to extend the insights gained from small-scale validation studies to large-scale systems. Thus, the difference in size between bath-type sonoreactors and previous horn-type configurations should be considered in the

² The strong nonlinear relation between the acoustic and bubble field near the tips of the sonotrodes often result in rapidly changing acoustic bubble structures. This highly transient behavior makes presents a challenging problem when attempting to model the behavior using current models that rely on quasistatic (steady-state) analysis.

modelling strategies. Model size also affects the simulation in terms of memory and computational costs, due to strict mesh requirements for acoustic problems (Ihlenburg and Babuška, 1995). Furthermore, it was hypothesised that certain aspects such as the wavelength-shortening effect cannot be clearly detected if the investigated geometry is small relative to the wavelength. Therefore, this work also focused on the validation of sonoreactor simulation strategies at large scales.

1.3.3 Inter-Model Comparison and Discussion

Current knowledge suggested that there is no 'one size fits all' approach, and therefore the selection of an appropriate acoustic model based on the studied system was found to be crucial. The selection process was impeded by the lack of information on how different mathematical models perform under different conditions. Most studies only considered one model, with little consideration for alternative strategies. Additionally, studies that considered inter-model comparison focused on theoretical discussion and lack empirical validation (Jamshidi et al., 2012; Louisnard, 2012a; Dogan and Popov, 2016). While this work mainly focused on the applicability of the linear CP model in ultrasonic baths, an effort was also made to consider the performance of the pure-liquid and NH models to serve as a point of comparison.

1.3.4 Bubble Field Characterisation in Sonoreactor Acoustics

Several studies have highlighted uncertainties related to the specification of bubble field parameters required for bubbly-liquid models (Servant et al., 2000; Fang et al., 2018). During the course of this work, it was noted that uncertainties related to the

bubble-field parameters interfered with the quality of the investigation. To thoroughly explore this limitation, Chapter 5 was dedicated to reviewing and discussing this matter with the aim of developing a potential solution to address this issue.

1.4 Problem Statement

This work considered the following research question:

How does the linear CP model (and, by extension, the pure-liquid and NH model) perform for the characterisation of acoustic pressure fields in large ultrasonic baths, in terms of predicting the phase speed and attenuation of the system?

1.5 Aims and Objectives

In this work, the aim is to identify, validate, and improve the modelling strategies for large-scale sonoreactors. This work focused on the linear CP model; however, the pure-liquid and NH models were also studied to serve as a point of comparison and to generate insight on their respective performance at large scales. The main hypothesis investigated in this study is that the linear CP model would be able to characterise the acoustic pressure field of bath-type sonoreactors. This hypothesis was investigated by evaluating the performance of the models in terms of phase speed and attenuation predictions against empirical measurements. To increase confidence in the validation results, preliminary and auxiliary investigations were also conducted to eliminate key uncertainties that affect the main findings. The numerical method used to solve the acoustic pressure simulations is the finite element method (FEM). The main expected outcome of this work is a comprehensive understanding of the performance of linear

CP model for the characterisation of large ultrasonic baths. This includes the strengths, limitations, and potential improvements for the model. The key objectives proposed to study this matter are as follows:

1. Establishing the foundational aspects of the modelling framework

To ensure the accuracy of the empirical verification studies, several foundational aspects of the modelling strategy were addressed. This includes investigating:

- How should frequency-domain simulations be interpreted and compared with experimental measurements [Case Study 1].
- The suitability of acoustic boundary conditions for the systems of interest, notably the vibrating walls in the hexagonal sonoreactor [Case Study 2].

2. Evaluating the performance of the pure-liquid, linear CP and NH models for the characterisation of bath-type sonoreactors

This objective addressed the main research problem, where acoustic pressure models were tested for bath-type sonoreactors in two verification studies:

- To investigate the pure-liquid, linear CP, and NH models in terms of pressure magnitude predictions against hydrophone measurements [Case Study 3].
- To investigate the pure-liquid, CP, and NH models in terms of phase speed predictions (antinode) against SCL imaging data [Case Study 4 and 5].

3. Improving the applicability of the linear CP model

This objective targeted several knowledge gaps identified for the linear CP model. The lack of reliable methods to characterise the bubble field and the consideration of multi-frequency sonoreactors were addressed:

- To develop and demonstrate an empirical λ -tuning approach to address uncertainties in bubble field characterisation [Case Study 6].
- To extend frequency-domain strategies for multi-frequency acoustic pressure fields in sonoreactors, based on linear superposition [Case Study 7].

1.5.1 Research Timeline

This work focused on theoretical and numerical investigations based on the research question in four phases. The literature review in **Phase 1** established a strong theoretical foundation and identified knowledge gaps. **Phase 2** investigated the foundational elements that were crucial for subsequent simulation strategies. **Phase 3** evaluated the governing equations against experimental data in large ultrasonic baths. Lastly, **Phase 4** proposed and explored improvements for the linear CP model to address uncertainties related to bubble field characterisation and multi-frequency systems.

1.6 Thesis Structure and Case Studies

Figure 1.7 presents a summary of the thesis chapters. Investigative work carried out during the course of this project is reported in the form of case studies. A total of seven case studies shall be discussed. Figure 1.8 and Figure 1.9 provide a brief summary of the objective and key findings of the seven case studies presented within this work.

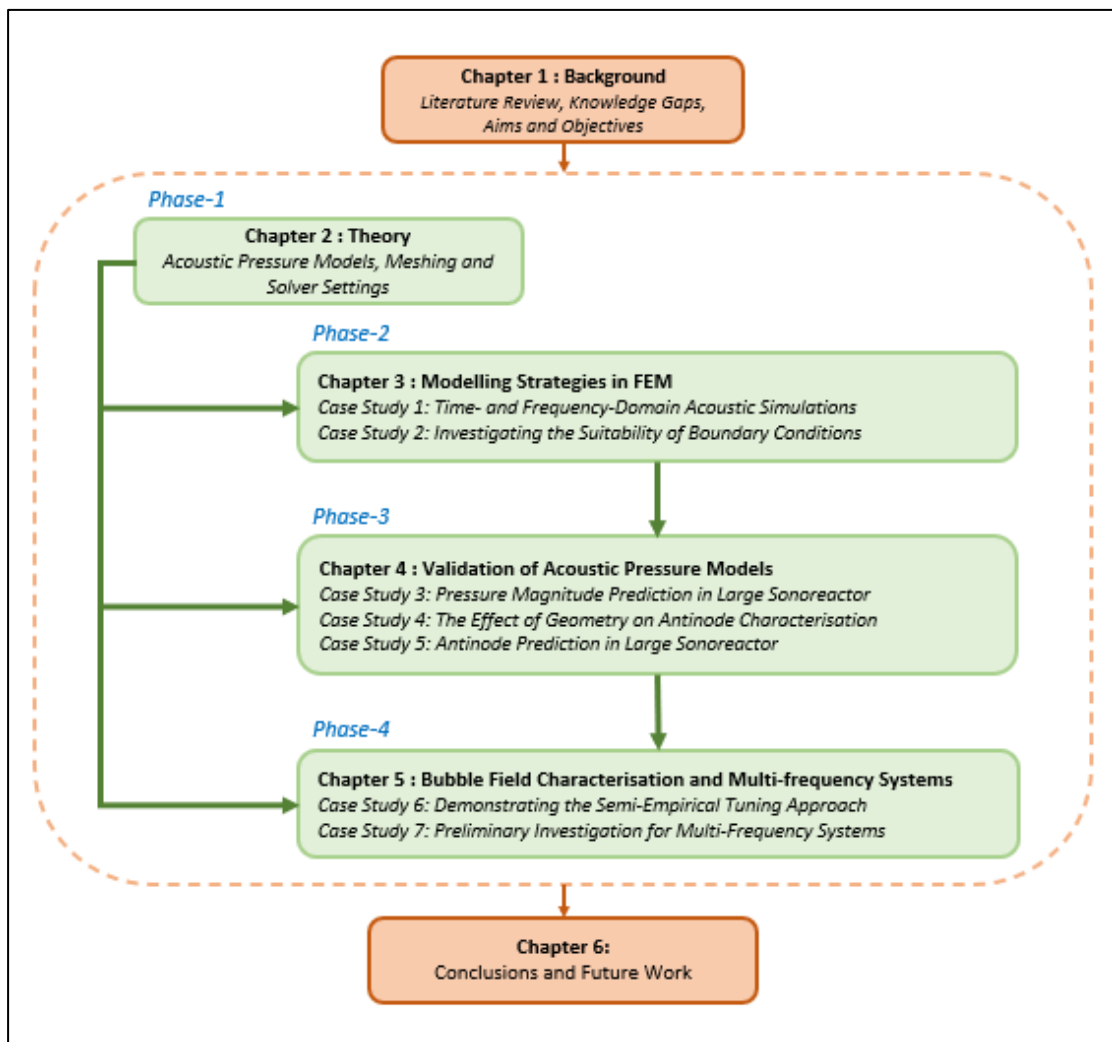


Figure 1.7: Summary of the thesis structure.

Outline of Case Studies in This Work

Case Study 1: Time- and Frequency-Domain Acoustic Simulations

To investigate the nature of frequency-domain acoustic pressure solutions in FEM from the perspective of sonoreactor acoustics.

- Discussed the key differences between time- vs frequency-domain solutions and showed that the latter are sufficient to characterise sonoreactors in this work.
- Highlighted the importance of pressure magnitude plots in sonoreactor acoustics

Case Study 2: Investigating the Suitability of Boundary Conditions

To discuss and investigate the suitability of boundary conditions used in sonoreactor acoustics modelling.

- Critically discussed the choice of boundary conditions in past literature.
- Outlined the numerical behaviour of Dirichlet and Neumann active boundary conditions and its impact on the acoustic pressure solution.
- Results show that the approximation of vibrating walls in the studied sonoreactors are justifiable for the intended region of interest in Case Study 5.

Case Study 3: Pressure Magnitude Prediction in Large Sonoreactor

To investigate the performance of popular acoustic pressure models on the aspect of pressure magnitude/attenuation prediction.

- Results outlined the impact of acoustic reflection on the acoustic pressure field.
- Pure-liquid model is relatively accurate in the absence of strong reflections.
- The performance of the linear CP model is inconsistent and sensitive to bubble field parameters.
- The nonlinear models were noted to perform poorly, suggesting a large overprediction of attenuation.

Case Study 4: The Effect of Geometry on Antinode Characterisation

To investigate the effects of sonoreactor geometry on the accuracy of antinode characterisation methods.

- The effect of geometry on the uncertainties in the results was demonstrated both heuristically and theoretically.
- The proposal of a dimensionless parameter D_s/λ to estimate the quality of antinode characterisation studies.
- Critically reviewed the D_s/λ values used in literature.

Figure 1.8: Summary of Case Studies 1 – 4 presented in this work.

Case Study 5: Antinode Prediction in Large Sonoreactor

To investigate the performance of popular acoustic pressure models on the aspect of phase speed/antinode prediction using SCL images.

- The large investigated D_s/λ outlined the phenomena of phase speed reduction which was often omitted in past studies.
- The limitations of the pure-liquid model in approximating bubbly-liquid phase speeds are outlined.
- The strong sensitivity of the linear CP model to bubble field parameters is highlighted.
- The NH model yielded rather ambiguous results in terms of phase speed prediction, while results also strongly suggests the possibility of overpredicting the attenuation.

Case Study 6: Demonstrating the Semi-Empirical Tuning Approach

To demonstrate the semi-empirical approach developed in Chapter 6 using a hexagonal sonoreactor.

- The proposed semi-empirical tuning method for the bubble density parameter was found to yield good agreement against experimental observations.
- Results suggests the applicability of the approach for bath-type configurations given that several key prerequisites are met.

Case Study 7: Preliminary Investigation for Multi-frequency Systems

To discuss and investigate a novel approach of extending frequency-domain models for multi-frequency systems using Parseval's theorem.

- RMS pressure fields yielded promising agreement against multi-frequency SCL data.
- The semi-empirical approach demonstrated in Case Study 6 once again is shown clearly to be able to circumvent uncertainties in bubble field characterisation even under a multi-frequency setting.
- A large knowledge gap was identified for the modelling of multi-frequency attenuation in bubbly-liquids.

Figure 1.9: Summary of Cast Studies 5 – 7 presented in this work.

Chapter 2: Theory

2.1 The Wave Equation

Sonoreactor acoustics is essentially a wave propagation problem and can be modelled using the wave equation (Ginsberg, 2018). The wave equation is fundamentally a balance of mass and momentum in a fluid. Assuming no source terms, the mass conservation is written as:

$$\frac{\partial \rho_l}{\partial t} + \nabla(\rho_l \mathbf{u}) = 0 \quad (3)$$

while the momentum equation is Newton's second law written in terms of density:

$$\rho_l \left(\frac{\partial \mathbf{u}}{\partial t} + \mathbf{u} \cdot \nabla \mathbf{u} \right) = -\nabla p + f_B \quad (4)$$

Vector fields are represented in bold. The left-hand side of the equation is the mass times acceleration for a unit volume of liquid, whereas the right-hand side consists of force terms. It is generally useful to write the equation in terms of pressure when discussing acoustics. The density can be related to the pressure using:

$$p = c_l^2 \rho_l \quad (5)$$

The linear wave equation is a result of applying several simplifying assumptions (Pierce, 1989):

1. No body / volume forces (e.g., gravity) and viscous forces.
2. Negligible relative motion (zero mean velocity) and shear stress.
3. Homogeneous medium with constant liquid density and compressibility.
4. First-order linearisation assuming small perturbations for the density, velocity, and pressure fields (ρ_l' , u' , p') relative to mean values (ρ_0 , u_0 , p_0).

The last assumption allows the system of equations to be written in terms of linear perturbations, while ignoring higher-order terms:

$$\frac{\partial p'}{\partial t} = -c_l^2 \rho_0 \nabla \mathbf{u} \quad (6)$$

$$-\nabla p' = \rho_0 \frac{\partial \mathbf{u}'}{\partial t} \quad (7)$$

Eliminating the velocity field yields the well-known linear wave equation:

$$\frac{\partial^2 p'}{\partial t^2} - c_l^2 \nabla^2 p' = 0 \quad (8)$$

It is also common to preserve the density term to allow for source-term considerations:

$$\frac{1}{\rho_l} \frac{\partial^2 p}{\partial t^2} - \frac{c_l^2}{\rho_l} \nabla^2 p = 0 \quad (9)$$

Subsequent references to the acoustic pressure variables are written without an apostrophe. The variable p is used for the time-dependent acoustic pressure, and P for the time-harmonic acoustic pressure. The acoustic pressure should not be confused with other forms of pressure, such as static or hydrodynamic pressure. The acoustic pressure is the result of acoustic waves, and thus a region with zero acoustic pressure should be interpreted as lacking pressure oscillations instead of being a vacuum. A similar case can be made for the acoustic velocity, which is essentially a particle velocity associated with the acoustic vibrations (Ginsberg, 2018).

2.2 The Helmholtz Equation

The wave equation in Eqn. (9) can be simplified by assuming that the acoustic pressure field is a sinusoidal periodic quantity (Pierce, 1989). Mathematically, this assumption can be written in complex-exponential form in terms of the angular frequency ω :

$$p(\mathbf{r}, t) = \Re[P(\mathbf{r})e^{-i\omega t}] = \frac{1}{2}[P(\mathbf{r})e^{i\omega t} + P^*(\mathbf{r})e^{-i\omega t}] \quad (10)$$

The real part of the complex-exponential expression, $\Re[P(\mathbf{r})e^{-i\omega t}]$, represents the physical pressure $p(\mathbf{r}, t)$. The variable $P(\mathbf{r})$ is the spatial, complex-valued pressure amplitude. It is evident from Eqn. (10) that the model describes a monoharmonic system. This simplifies the wave propagation problem by only requiring the spatial acoustic pressure, $P(\mathbf{r})$, to be solved. The spatial acoustic pressure can be obtained as a solution of the Helmholtz equation:

$$\nabla^2 P(\mathbf{r}) + k^2 P(\mathbf{r}) = 0 \quad (11)$$

The solution of Eqn. (11) depends on the wavenumber k and the boundary conditions (Ginsberg, 2018). The wavenumber can be real- or complex-valued and is related to the physical properties of the medium. The simplest wavenumber is:

$$k = \omega/c_l \quad (12)$$

The wavenumber in Eqn. (12) describes an unattenuated wave with the phase speed c_l . The term 'phase speed' refers to the sound speed at a certain frequency. Wave attenuation can be modelled using a complex-valued k :

$$k = k_{real} + ik_{imag} \quad (13)$$

Mathematically, the effect of attenuation is clear if one substitutes Eqn. (13) into Eqn. (10), giving:

$$p(x, t) = |P|e^{-(k_{imag})x} \cos(k_{real}x - \omega t) \quad (14)$$

As shown in Eqn. (14), the attenuation factor $e^{-(k_{imag})x}$ reduces the amplitude of the wave as a function of distance travelled, x .

2.3 Pure-Liquid vs Bubbly-Liquid Models

In Eqn. (14), the acoustic pressure field $p(x, t)$ depends on the phase speed and the attenuation. In sonoreactor acoustics, an accurate representation of the phase speed and attenuation of the working fluid is important to correctly characterise the antinode locations and pressure magnitudes (Servant et al., 2001b). Rewriting Eqn. (13) in the form:

$$k_c = \kappa - i\alpha \quad (15)$$

The variable κ is the propagation wavenumber (Ginsberg, 2018) which is related to the phase speed, while α is the attenuation coefficient.

2.3.1 Pure-Liquid Approach

Modelling efforts can be categorised into those that considered the working fluid as a pure liquid or as a bubbly liquid. In this work, the term ‘pure-liquid model’ refers to modelling strategies that do not explicitly consider the effect of the bubble field. In works that considered the pure-liquid model, some used the simple wavenumber in Eqn. (12) (Sáez et al., 2005; Klíma et al., 2007), while others specified attenuation values that were arbitrary (Yasui et al., 2007; Louisnard et al., 2009) or based on

empirical models (Rashwan et al., 2020). In their study, Sutkar et al. (2010) considered viscous dissipation of pure liquid using Eqn. (1):

$$k_c = \frac{\omega}{c_l} \frac{1}{\sqrt{1 + (i\omega\mu_l/\rho_l c_l^2)}} \quad (1)$$

Other formulations had also been developed for various energy losses (Fox and Rock, 1941; Markham et al., 1951; Wijngaarden, 1972). The main concern of omitting bubbly-liquid effects is the issue of incorrectly predicting the acoustic properties of the working fluid (Jamshidi et al., 2012). These effects can cause significant errors in acoustic pressure predictions if not properly modelled (Chu et al., 2022).

2.3.2 Bubbly-Liquid Approach

Realistically, the working fluid within a sonoreactor should be considered a bubbly liquid (Dähnke and Keil, 1999). Theoretically, one can accurately simulate sonoreactor acoustics if the behaviour of every single bubble within the medium is specified. However, this is practically impossible given that the acoustic-bubble interaction is very complex (Servant et al., 2003). To simplify the problem, researchers assumed that the working fluid can be approximated using existing bubbly-liquid models (Dähnke et al., 1999a; Servant et al., 2000; Jamshidi et al., 2012; Louisnard, 2012a; Fang et al., 2018; Trujillo, 2018).

Specifically, continuum-based models for bubbly-liquid acoustics had been receiving attention (Tudela et al., 2014). Developed in the works of Carstensen and Foldy (1947), Wijngaarden (1968), and Caflisch et al. (1985a), the continuum-based approach treats the bubbly liquid as a single phase. The bubbly liquid can then be characterised using

averaged properties, rather than modelling the gas and liquid phases separately (Žnidarčič et al., 2015). Adoption of this class of bubbly-liquid models was reported to yield improvements in terms of accuracy for sonoreactor simulations (Tudela et al., 2014). Developments have also been made to modify existing formulations to better suit sonoreactor conditions (Louisnard, 2010, 2012a).

Despite promising results, it should not be overlooked that bubbly-liquid models were originally developed for systems that contain stable and uniform bubble fields (Caflich et al., 1985a). The bubble field of a sonoreactor had been shown to consist of both stable and transient bubbles depending on the cavitation regime (Church and Carstensen, 2001). Therefore, the use of the aforementioned models in sonoreactor simulations carries an inherent degree of error, based on the deviation from the stable bubble field assumption. Naturally, this deviation is more prominent in systems that are strongly cavitating, such as horn-type sonoreactors.

2.4 The Caflich Equation for Bubbly-Liquid Acoustics

The development of the CP and NH model (Commander and Prosperetti, 1989; Louisnard, 2010) is based on the Caflich equation. Caflich et al. (1985a) proposed the equation upon performing rigorous derivations based on the idea presented in the previous works of Wijngaarden (1968) and (Foldy, 1945).

2.4.1 Mathematical Formulation

The Caflich equation is a modified wave equation derived on the basis of bubbly-liquid acoustics (Caflich et al., 1985a). The principal assumption treats the

propagation medium as a single continuum. This assumption can be argued to be valid if the length scales for the state variables (pressure, temperature, etc.) are large compared to inter-bubble distances and bubble sizes. This allows for a quasi-static analysis of the bubbly-liquid, making it possible to relate averaged acoustic properties to averaged bubble parameters (Wijngaarden, 1968). Caflisch et al. (1985a) based their model on the first-order mass and momentum balances proposed by Wijngaarden (1970), also known as the Wijngaarden-Papanicolaou model:

$$\frac{\partial \rho_l}{\partial t} + \nabla(\rho_l \mathbf{u}) = \rho_l \frac{\partial \beta}{\partial t} \quad (16)$$

$$\rho_l \left(\frac{\partial \mathbf{u}}{\partial t} \right) = -\nabla p \quad (17)$$

Similar to the wave equation in Eqn. (9), the velocity term can be eliminated and Caflisch et al. (1985a) rigorously showed that the model can be written as:

$$\frac{\partial^2 p}{\partial t^2} - c_l^2 \nabla^2 p = \rho_l \frac{\partial^2 \beta}{\partial t^2} \quad (18)$$

Eqn. (18) is an inhomogeneous wave equation with a source term containing the second time derivative of the bubble fraction, β . To solve the equation, the time-derivative $\frac{\partial^2 \beta}{\partial t^2}$ would have to be specified. Based on the assumption that all bubbles are spherical, monodisperse, and uniformly distributed, Caflisch et al. (1985a) approximated the source term as:

$$\frac{\partial^2 \beta}{\partial t^2} = \frac{4}{3} n \pi \frac{\partial^2 R}{\partial t^2} \quad (19)$$

From Eqn. (19) it is evident that a description of the evolution of bubble radius R in the time domain is required to close the model. This can be achieved using bubble dynamics, such as the Rayleigh-Plesset equation (Rayleigh, 1917; Plesset, 1949).

2.4.2 Important Assumptions

Table 2.1 lists the assumptions involved in the derivation of the Caflisch equation. This section shall discuss these assumptions within the context of sonoreactor acoustics with the intent of identifying the limitations of the model.

Table 2.1: Assumptions for the derivation of the Caflisch model.

Num.	Assumptions	Remarks
1.	Constant liquid density, sound speed, and irrotational flow.	Inherited from Wijngaarden-Papanicolaou model
2.	Bubbly liquid is treated as a continuum.	
3.	Constant bubble fraction (mass of gas in liquid is constant).	
4.	Bubbles are fully spherical and have a uniform internal pressure.	Inherited from bubble dynamics
5.	Incompressible liquid, negligible heat conduction for bubbles.	
6.	No bubble fragmentation or coalescence.	Rigorously shown in Caflisch et al. (1985a)
7.	No bubble convection (no bubble velocity field).	
8.	Small bubble fractions and neglect inter-bubble interactions.	
9.	No bubble resonance effects.	

Assumption 1 is inherited from the derivation of the linearised wave equation, while Assumptions 2 and 3 serve as the basis for treating the acoustic medium as a continuum outlined in the study of Wijngaarden (1968). These assumptions allow the pressure experienced by the bubbles to be written as the ensemble-averaged pressure.

Instead of treating bubbles as individual dissipators (Foldy, 1945), averaged values are used to characterise the bulk dissipating fluid. Caflisch et al. (1985b) argued that Assumption 2 is valid as long as the wavelength is significantly larger than the bubbles. In the context of sonoreactors, bubble measurements generally reported bubble sizes in the range of 1-50 μm (Section 5.1). The wavelengths involved in power ultrasound tend to be significantly larger (e.g., wavelength of 100 kHz ultrasound is around 15 mm in pure water), and thus this assumption can be argued to be valid for conventional sonoreactors. Possible exceptions include local regions under very strong ultrasonic horns, where large air pockets had been reported to form (Žnidarčič et al., 2014). In such situations, the assumption of continuum is challenged.

Assumptions 4 and 5 are inherited from the bubble dynamics model used by Caflisch et al. (1985a), which is the Rayleigh-Plesset equation (Rayleigh, 1917; Plesset, 1949). Caflisch et al. (1985a) dedicated a larger part of their work to argue the applicability of Assumptions 6 and 7. These assumptions allow the bubble density n to be treated as a constant in time. Assumption 6 enforces bubble conservation, written as:

$$\frac{dn}{dt} + n(\nabla \cdot \mathbf{u}_B) = 0 \quad (20)$$

Assumption 7 causes the bubble velocity field \mathbf{u}_B to vanish, thus making n a constant.

$$\frac{dn}{dt} = 0 \quad (21)$$

These assumptions allow the model to be closed by simply specifying R . It is evident that when applied to sonoreactor acoustics, Assumption 6 oversimplifies the behaviour of the bubble field since bubble generation, coalescence, and fragmentation is definitely present in cavitating systems (Ashokkumar, 2011). A case

can be made that the deviation from this assumption is smaller in sonoreactors with weaker cavitation regimes, such as low-power ultrasonic baths; however, this claim is largely anecdotal and lacks supporting evidence.

The Caflisch model also neglects inter-bubble effects (Assumption 8) and does not consider bubble resonance effects (Assumption 9). Assumption 8 simplifies the model by limiting the forces experienced by the bubbles to only the fundamental harmonic (pressure generated by the transducer). Assumption 8 is clearly violated in sonoreactors, as a defining characteristic of cavitating liquids is the strong broadband of acoustic pressure generated by transient cavitation (Campos-Pozuelo et al., 2005; Avvaru and Pandit, 2009). Regarding Assumption 9, bubble sizes from empirical measurements are generally reported to be within the range of 1 – 50 μm [Section 5.1]. A simple approximation using the Minnaert resonance relation (Minnaert, 1933) for ideal gas bubbles yields a resonance radius of c.a. 163 μm for a 20 kHz system. Thus, the resonance condition is generally avoided unless the frequencies are high, or the bubbles are very large.

2.4.3 Practical Limitations

The Caflisch equation had been reported to be notoriously difficult to solve for cavitating systems (Louisnard, 1998; Vanhille and Campos-Pozuelo, 2009a). Preliminary tests involving a simplified variation of the model revealed that it is prone to numerical errors and requires a rigorous meshing process. Additionally, the full model requires bubble dynamics to be solved for each single point in space, which is unpractical outside of 1D simulations (Lebon et al., 2017). Prevalent numerical

instabilities also led to frequent numerical ‘blow-up’ (Glasse, 1981). The term numerical blow-up refers to a phenomenon in which the solution to a mathematical model becomes infinite or unbounded as the simulation progresses. This often results in extremely large solution values which is unrealistic, and is often caused by an ill-posed model or inherent instabilities in certain mathematical models.

An example of a numerical blow-up when solving a variation of the Caflisch equation during preliminary testing is presented in Figure 2.1. For yet-to-be-determined reasons, the transient solution was found to ‘blow up’ at the corners of the geometry and spread to the entire domain. While unproven, the observation was thought to be caused by numerical errors in gradient calculations due to the drastic changes in acoustic properties. Studies have noted that steep gradients in bubble dynamic equations (notably the bubble fraction term) can cause problems during numerical differentiation and integration (Trujillo, 2020).

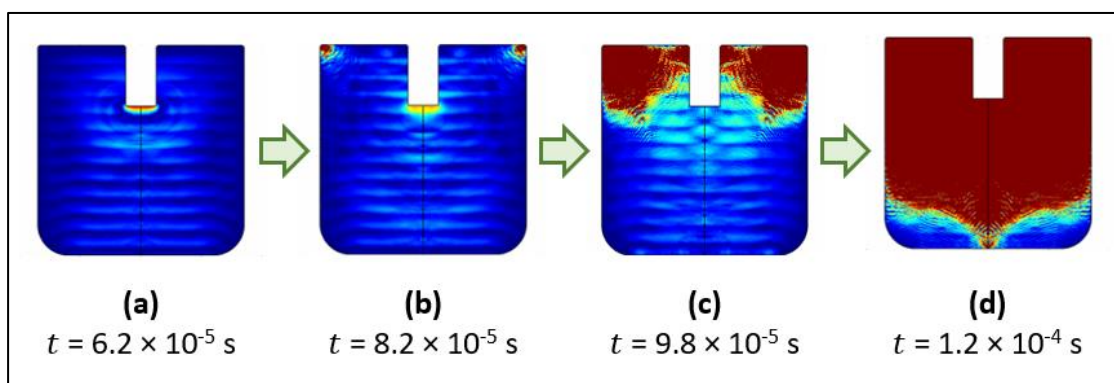


Figure 2.1: Numerical blow-up of the Caflisch solution during preliminary testing. (a) – (d) shows the evolution of the acoustic pressure field over time, where the red region shows unrealistic pressures.

The Caflisch model had been subsequently simplified to improve its practicality, leading to the development of the Commander and Prosperetti (CP) model and the nonlinear Helmholtz (NH) model. The CP and NH approach simplified the Caflisch model by reducing it to a frequency-domain model. Both models were reported to offer a better prediction of bubbly-liquid attenuation (Louisnard, 2010; Jamshidi et al., 2012) while being more practical to solve. However, such Caflisch-based models should strictly be considered as an approximation in sonoreactor acoustics due to the deviations from the intended assumptions identified in Section 2.4.2.

2.5 The Commander and Prosperetti (CP) Model

The Commander and Prosperetti (CP) model was developed by Commander and Prosperetti (1989) to study the Cafilich model for linearised bubble dynamics. In the original study, the model was well validated against experimental benchmarks measured for stable bubble field experiments. This section reviews the formulation of the CP model with a focus on the associated simplifying assumptions.

2.5.1 Formulation of the CP Model

Commander and Prosperetti (1989) used Keller-Miksis bubbly dynamics (Keller and Miksis, 1998) to close the Cafilich equation. This inherently assumed that the liquid around the bubbles is weakly compressible and introduced radiation damping into the attenuation mechanism (Jamshidi and Brenner, 2013). A more robust energy balance was also considered using the linearised heat transfer model of Prosperetti (1977). The CP model was derived on the basis of three important assumptions. First, the bubble source term in Eqn. (18) can be approximated as:

$$\frac{\partial^2 \beta}{\partial t^2} \approx 4\pi \int_0^\infty R_0^2 n R_{tt} dR_0 \quad (22)$$

Second, all fields were assumed to be periodic, and transient fields were incorporated as period-averaged values. Lastly, the model assumed that the bubble dynamics is linear. The result is a dispersion relation for the bubbly-liquid, which can be written for the monodisperse case as:

$$k_c^2 = \frac{\omega^2}{c_l^2} + \frac{4\pi\omega^2 n R_0}{\omega_0^2 - \omega^2 + 2ib\omega} \quad (23)$$

At first glance, the expression shares similarities with classical linear oscillator systems (Ginsberg, 2018), notably the parameter b which represents the damping term. Once the liquid-gas properties, the frequency, and the two bubble field parameters n and R_0 are specified, the complex-valued k_c^2 can be calculated from a series of parameters listed in Table 2.2. The damping factor b describes the energy loss calculated from linearised bubble dynamics. The three terms on the right-hand-side of Eqn. (28) represent the viscous, thermal, and radiation damping terms.

Table 2.2: Complex wavenumber calculation for the CP model.

Parameter	Expression	
Initial Bubble Pressure, P_{g0}	$P_{g0} = p_\infty + \frac{2\sigma_l}{R_0}$	(24)
Dimensionless Thermal Diffusion, χ	$\chi = D_g/\omega R_0^2$	(25)
Dimensionless Complex-valued Parameter, Φ	$\Phi = \frac{3\gamma_g}{1 - 3(\gamma_g - 1)i\chi[(i/\chi)^{1/2} \coth(i/\chi)^{1/2} - 1]}$	(26)
Resonance Frequency Squared, ω_0^2	$\omega_0^2 = \frac{P_{g0}}{2\rho_l R_0^2} \left(\Re\{\Phi\} - \frac{2\sigma_l}{R_0 P_{g0}} \right)$	(27)
Damping Factor, b	$b = \frac{2\mu_l}{\rho_l R_0^2} + \frac{P_{g0}}{2\rho_l \omega R_0^2} \Im\{\Phi\} + \frac{\omega^2 R_0}{2c_l}$	(28)

2.5.2 Variations of the CP model

The CP model had been implemented using two main strategies in sonoreactor acoustics, henceforth referred to as the linear CP model and the nonlinear CP model.

The linear CP model assumes that the bubble field does not depend on the acoustic pressure field. This was usually implemented by assuming that the bubble density or bubble fraction is constant and uniform in the working fluid. The method was considered in the work of Jamshidi et al. (2012), as well as Dogan and Popov (2016).

The linear CP model was selected as the main focus of this work, as it was hypothesised that the acoustic behaviour predicted by the model resembles that of conventional bath-type sonoreactors. In contrast, the nonlinear CP model is formulated using a bubble density or bubble fraction that depends on the local acoustic pressure. It was first proposed by Dähnke et al. (1999a) and was adopted in several subsequent studies (Jamshidi et al., 2012; Hussain and Janajreh, 2017; Fang et al., 2018). In this work, the nonlinear CP model was only considered as a simplified alternative to the NH model in Case Study 7.

Other improvements of the CP model were also proposed in literature, mainly to address extreme or fringe conditions. Kargl (2002) proposed that the linearised bubble dynamics in the CP model should be written in terms of effective mixture properties to provide a better approximation for radiation damping. They reported that improvements are only significant for near-resonance systems. Ando et al. (2009) also addressed near-resonance behaviour, where some assumptions of the Caflisch model were violated. They noted that radiation and compressibility losses become important near resonance and showed that very high frequencies (>1 MHz) violate the assumption of continuum for the Caflisch model. Fuster et al. (2014) attempted to

relax Assumption 8 of the Caflisch equation by modifying the CP model using a bubble cluster modelling approach. Their model characterised bubble behaviour as groups rather than individual scatterers.

Other studies considered more robust gas- and vapour-transfer models. Fuster and Montel (2015) claimed that the inclusion of vapour transfer resulted in higher attenuation and lower phase speed predictions in their modified CP model. Prosperetti (2015) also reported similar results when considering the transfer of gasses across the bubble boundaries. These observations were restricted to cases where the operating frequency is very low and the bubble fraction is very large; which allowed more time and surface area for diffusion effects to be significant.

2.5.3 Comments on the CP Model

The CP model is significantly simpler in terms of formulation and implementation than the Caflisch model. When considering the use of the CP model in sonoreactor acoustics, the main consideration is the validity of the linearised bubble dynamics in representing the effect of the bubble field. This work argues that the CP model can be used to approximate the acoustic pressure field of weakly cavitating regimes such as bath-type systems. The use of linearised bubble dynamics had been noted to show good agreement in low-amplitude applications (Servant et al., 2001b; Vanhille et al., 2004). Furthermore, measurements had shown that ultrasonic baths can operate at pressures lower than the Blake threshold (Moholkar et al., 2000; Tangsopa and Thongsri, 2019). The results suggest that the working fluid can be characterised by stable cavitation (Leighton, 1994; Young, 1989), which better conformed to linear

bubble dynamics (Prosperetti, 1975). Commander and Prosperetti (1989) reported an applicable range of bubble conditions for their model. Based on their validation studies using stable bubble fields, the CP model was reported to be applicable for bubble fractions up to 1-2 %. This condition is usually obeyed in sonoreactor acoustics, with reference to bubble fraction measurements that lie well below this threshold for horn-type configurations (Burdin et al., 1999).

2.6 The Nonlinear Helmholtz Model

Trujillo (2018) coined the term ‘nonlinear Helmholtz model’ to refer to a specific class of bubbly-liquid models applying the strategy proposed by Louisnard (2010, 2012a). NH models were mainly developed to address the issue of predicting bubbly-liquid attenuation for strongly cavitating systems (Louisnard, 2010), notably for regimes above the Blake threshold (Blake et al., 1999).

2.6.1 Formulation of the NH Models

The formulation of NH models shares similarities with the CP model, notably for its early variations (Jamshidi and Brenner, 2013; Louisnard, 2010). Instead of modelling bubble effects from linearised bubble dynamics, the NH model relies on solving full bubble dynamics to calculate the wavenumber. Developed on the foundations of the Caflisch model, the implementation of the NH model is a two-step process. The first step involves solving bubble dynamics to obtain bubble dissipation data as a function of acoustic pressure magnitude; while the second step solves a nonlinear Helmholtz equation by incorporating dissipation data as an interpolation curve. The model was reported to predict much higher attenuation than the linear CP model when the acoustic pressure exceeds the cavitation threshold (Louisnard, 2012a).

Unlike the CP model, which uses a single dispersion relation to determine k_c^2 , the NH models were historically derived to have separate expressions for the real and imaginary parts of the wavenumber squared (Trujillo, 2018):

$$k_c^2 = \text{real}(k_c^2) + i[\text{imag}(k_c^2)] = \Re(k_c^2) + \Im(k_c^2)i \quad (29)$$

To date, three variations had been proposed by different authors. Table 2.3 summarises their similarities and differences compared to the CP model. Louisnard (2010) derived bubble dissipation from Rayleigh-Plesset bubble dynamics (Rayleigh, 1917; Plesset, 1949). Subsequently, the work of Jamshidi and Brenner (2013) rederived the bubble dissipation by considering a weakly-compressible fluid using the Keller-Miksis bubble dynamics (Keller and Miksis, 1998). In both works, the real part of the wavenumber squared was directly adopted from the CP model, while the imaginary part was determined from period-averaged dissipation terms calculated from bubble ODEs. Recently, Trujillo (2018) reported a rigorous re-derivation of the NH model from fundamental energy balances and proposed a new expression for $\Re(k_c^2)$.

Table 2.3: Summary of wavenumber formulation for NH models.

Model	Real Part, $\Re(k_c^2)$	Imaginary Part, $\Im(k_c^2)$
CP	Linearised Caflisch Model (Keller-Miksis Bubble Dynamics)	
NH (Louisnard)	Adapted from CP Dispersion Relation	Derived from Rayleigh-Plesset Bubble Dynamics
NH (Jamshidi and Brenner)		Derived from Keller-Miksis Bubble Dynamics
NH (Trujillo)	Rigorously Derived from the Caflisch Model and Keller-Miksis Bubble Dynamics	

2.6.1.1 Review of Louisnard's Formulation

The initial work of Louisnard (2010) considered isothermal Rayleigh-Plesset bubble dynamics. They included the effects of viscosity and surface tension, and the formulation of the dissipation terms are summarised in Table 2.4. The two period-averaged dissipation terms Π_{th} and Π_v were calculated from period-averaged expressions derived from energy balances. Once the dissipation terms were determined, the imaginary part of the wavenumber squared was specified as a function of the local acoustic pressure magnitude $|P|$. Louisnard (2012a) assumed that the real part can be approximated using the CP model based on the hypothesis that its effect is negligible compared to the imaginary part. This hypothesis was later confirmed by Trujillo (2020) who numerically investigated the matter.

Table 2.4: Louisnard's (2010) formulation of the NH model.

Formulation of Louisnard's NH Model

*Rayleigh-Plesset bubble dynamics is used to solve R, \dot{R}, \ddot{R}, V and \dot{V} .

$$\text{Thermal dissipation term :} \quad \Pi_{th} = \langle -p_g \dot{V} \rangle \quad (30)$$

$$\text{Viscous dissipation term :} \quad \Pi_v = \langle 16\pi\mu_l R \dot{R}^2 \rangle \quad (31)$$

$$\text{Imaginary } k\text{-squared:} \quad \Im(k_c^2) = -2\rho_l\omega n \frac{\Pi_{th} + \Pi_v}{|P|^2} \quad (32)$$

$$\text{Real } k\text{-squared :} \quad \Re(k_c^2) = \frac{\omega^2}{c_l^2} + \frac{4\pi R_o \omega^2 n}{\omega_0^2 - \omega^2} \quad (33)$$

2.6.1.2 Review of Jamshidi's Formulation

Jamshidi and Brenner (2013) considered the Keller-Miksis equation for the bubble dissipation calculations, which is summarised in Table 2.5. They also considered a more comprehensive energy balance around the acoustic bubble using the approach of Toegel et al. (2000). Their bubble dynamics considered a weakly-compressible liquid coupled with heat transfer effects, in contrast to the inviscid and isothermal assumptions of the predecessor. The main contribution of their work is the extra dissipation term that corresponds to radiation losses, Π_r .

Table 2.5: Jamshidi and Brenner (2013) formulation of the NH model.

Formulation of Jamshidi's NH Model

*Keller-Miksis bubble dynamics is used to solve R, \dot{R}, \ddot{R}, V and \dot{V} .

**Real part of k_c^2 follows Eqn. (33).

$$\text{Viscous dissipation term:} \quad \Pi_v = \langle 16\pi\mu_l R \dot{R}^2 + \frac{16\pi\mu_l}{c_l} R^2 \dot{R} \ddot{R} \rangle \quad (34)$$

$$\text{Viscous dissipation term:} \quad \Pi_v = \langle 16\pi\mu_l R \dot{R}^2 + \frac{16\pi\mu_l}{c_l} R^2 \dot{R} \ddot{R} \rangle \quad (35)$$

$$\text{Radiation dissipation term:} \quad \Pi_r = \left\langle \frac{4\pi}{c_l} R^2 \dot{R}^2 p + \frac{4\pi}{c_l} R^3 \dot{R} \dot{p} - \frac{2\pi\rho_l}{c_l} R^2 \dot{R}^4 - \frac{4\pi\rho_l}{c_l} R^3 \dot{R}^2 \ddot{R} \right\rangle \quad (36)$$

$$\text{Imaginary } k\text{-squared:} \quad \Im(k_c^2) = -2\rho_l\omega n \frac{\Pi_{th} + \Pi_v + \Pi_r}{|P|^2} \quad (37)$$

2.6.1.3 Review of Trujillo's Formulation

The latest development for the NH model was published by Trujillo (2018, 2020) who rigorously rederived a new set of expressions for the real and imaginary parts of k_c^2 as shown in Table 2.6. The more generalised expressions allow the dispersion relation to be obtained directly from bubble dynamics without the need to calculate individual dissipation terms, making the adoption of the NH model more efficient. Unlike previous variations, the generalised formulations are also independent of the bubble dynamics, which allows for increased flexibility for the modelling of bubble behaviour.

Table 2.6: Trujillo's (2020) formulation of the NH model.

Formulation of Trujillo's NH Model

*Keller-Miksis bubble dynamics is used to solve R, \dot{R}, \ddot{R}, V and \dot{V} .

$$\mathcal{A} = -2\rho_l\omega^2 \left\langle \frac{\partial^2 \beta}{\partial \tau^2} \cos\left(\tau + \frac{\pi}{2}\right) \right\rangle \quad (38)$$

or

Real-part variable:

$$\mathcal{A} = \frac{4\rho_l\omega^2}{|P|} \langle E_A \rangle + \frac{\rho_l\omega}{|P|} [\Im(P^*\nabla \cdot \mathbf{U} + \mathbf{U}^* \cdot \nabla P)] \quad (39)$$

$$\mathcal{B} = 2\rho_l\omega^2 \left\langle \frac{\partial^2 \beta}{\partial \tau^2} \sin\left(\tau + \frac{\pi}{2}\right) \right\rangle \quad (40)$$

or

Imaginary-part variable:

$$\mathcal{B} = \frac{2\rho_l\omega}{|P|} \langle \Pi_{dis} \rangle \quad (41)$$

Imaginary k -squared:

$$\Im(k_c^2) = -\frac{\mathcal{B}}{|P|} \quad (42)$$

Real k -squared:

$$\Re(k_c^2) = \frac{\omega^2}{c_l^2} - \frac{\mathcal{A}}{|P|} \quad (43)$$

2.6.2 Comments on the NH Model

It can be argued that the interpolation curve approach is the key novelty of the NH model. Although this approach incurs a slight loss of accuracy (depending on the resolution of the interpolation curve), it is balanced by the much-needed boost in performance. This feature improves the modelling strategy in two ways. First, the local wavenumber can be specified as a function of local pressure, which allows for a more comprehensive prediction of the wavenumber. Second, it allows rigorous bubble data to be practically incorporated into the acoustic pressure model. The latter opens up the possibility of archiving existing bubble data for future simulations.

From the standpoint of sonoreactor acoustics, the NH model is a practical solution for modelling strongly cavitating systems or systems that exhibit strong inhomogeneity such as horn-type sonoreactors. In the context of this work, while the model is more comprehensive, it is debatable whether the additional complexity is necessary for the modelling of ultrasonic baths. Furthermore, unlike the CP model, which had been extensively validated (Commander and Prosperetti, 1989), the development of the NH models remains in its early stages. Thus, the approach still requires further studies to determine its reliability. Recently, validation results reported by Trujillo (2020) suggest that the model may overpredict bubbly-liquid attenuation. They also reported convergence issues under certain conditions.

2.7 Bubble Field Characterisation and Bubble Dynamics

2.7.1 Specification of Bubble Field Parameters

When applying the CP and NH bubbly-liquid models, one would need to describe the bubble equilibrium radius R_0 and the bubble density n . The equilibrium bubble fraction β can then be determined using:

$$\beta = \frac{4}{3} n \pi R_0^3 \quad (44)$$

Figure 2.2 summarises the Caflisch class of bubbly-liquid models, as well as the available strategies for characterising the bubble field. Currently, there are two main strategies to characterise the equilibrium bubble radius and the bubble density, respectively. The following section reviews these methods. In Chapter 5, the topic of bubble field characterisation will be comprehensively revisited to address an important knowledge gap that was identified during the course of this work.

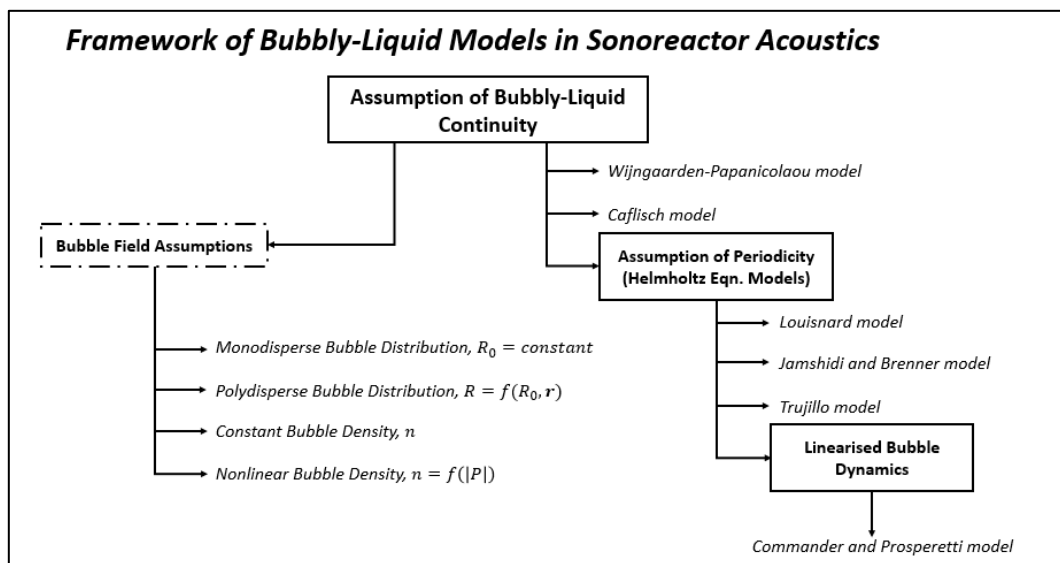


Figure 2.2: Summary of bubbly-liquid models and common bubble field assumptions.

2.7.1.1 Bubble Equilibrium Radius

Past studies characterised the bubble equilibrium radius R_0 using two methods. The simpler approach is the monodisperse assumption where all bubbles were assumed to have the same equilibrium radius (Jamshidi et al., 2012; Dogan and Popov, 2016; Sarac et al., 2020).

$$R_0(\mathbf{r}) = \text{constant} \quad (45)$$

The second approach characterised R_0 as a distribution of radii sizes, also known as the polydisperse approach (Commander and Prosperetti, 1989). A common method of implementing a polydisperse R_0 is to assume that the radii distribution follows a Gaussian curve (Dähnke et al., 1999a):

$$f_G(R_0) = \frac{1}{\sqrt{2\pi\sigma_B^2}} e^{-\frac{(R_0-R_m)^2}{2\sigma_B^2}} \quad (46)$$

2.7.1.2 Bubble Density

The bubble density parameter n represents the number of bubbles per unit volume of bubbly liquid. Recent studies assumed that the bubble density is spatially constant and uniform (Delacour et al., 2020; Sarac et al., 2020; Trujillo, 2020):

$$n(\mathbf{r}) = \text{constant} \quad (47)$$

The second approach specified n as a spatial variable. Studies had used the acoustic pressure field to map the bubble population in sonoreactors (Servant et al., 2001b; Vanhille and Campos-Pozuelo, 2009b). Another common method was proposed by Dähnke et al. (1999a), who used a nonlinear relation between bubble density and the

acoustic pressure magnitude. Henceforth referred to as the nonlinear n approach, the relationship can be mathematically described as:

$$n(\mathbf{r}) = X|P(\mathbf{r})| \quad (48)$$

The parameter X depends on the linear scaling relation between the bubble density and the pressure magnitude.

2.7.1.3 *Bubble Field Characterisation Strategies*

Bubble field characterisation was found to vary between studies that used the CP and NH models. The CP model had been solved using more varied methods, such as monodisperse - constant n (Dogan and Popov, 2016), polydisperse - constant n (Lebon et al., 2017), and monodisperse - nonlinear n (Jamshidi et al., 2012; Fang et al., 2018), and polydisperse - nonlinear n (Dähnke, et al. 1999a; Servant et al. 2000). Interestingly, the factors that influence these choices remain under-discussed. For the nonlinear Helmholtz model, most works considered a monodisperse constant n formulation (Louisnard, 2012b; Dogan and Popov, 2016; Sarac et al., 2020; Trujillo, 2020). It was speculated that this is because the NH model is relatively new, leaving other formulations yet to be explored in literature.

2.7.2 *Bubble Dynamics*

Ordinary differential equation (ODE) systems for bubble dynamics were solved to obtain the dissipation curves for the NH models. The system of ODEs can be broken down into several parts, namely:

- 1) Bubble External Pressure, $p_\infty(t)$
- 2) Bubble Radius, $R(t)$
- 3) Bubble Internal Gas and Vapour Pressure $p_g(t)$ and $p_v(t)$
- 4) Bubble Internal Temperature, $T_B(t)$

2.7.2.1 Bubble External Pressure (Acoustic Forcing)

The bubble external pressure $p_\infty(t)$ includes the steady-state hydrodynamic pressure p_0 as well as the pressure generated by the transducers. For monoharmonic cases, the pressure field surrounding the bubble is written as (Louisnard, 2012a):

$$p_F = p_\infty(1 - p^* \sin(2\pi ft)) = p_\infty - p_\infty p^* \sin(2\pi ft) \quad (49)$$

The term p^* is the ratio between the driving amplitude and the steady-state pressure p_∞ . Other potential pressure sources, such as broadbands generated by nearby cavitation activity or multi-frequency irradiation (Moholkar et al., 2000; Avvaru and Pandit, 2009), were not considered in this work.

2.7.2.2 Bubble Radius

The two main bubble dynamics equations described in this work are the Rayleigh-Plesset equation (Rayleigh, 1917; Plesset, 1949):

$$\rho_l \left[RR_{tt} + \frac{3}{2} R_t^2 \right] = p_v + p_g - p_F - \frac{2\sigma_l}{R} - \frac{4\mu_l R_t}{R} \quad (50)$$

and the Keller-Miksis equation (Keller and Miksis, 1998):

$$\rho_l \left[\left(1 - \frac{R_t}{c_l}\right) RR_{tt} + \left(1 - \frac{R_t}{3c_l}\right) \frac{3}{2} R_t^2 \right] = \left(1 + \frac{R_t}{c_l}\right) p_w + \left(\frac{R}{c_l}\right) \frac{dp_w}{dt} \quad (51)$$

(52)

$$p_w = p_v + p_g - \frac{2\sigma_l}{R} - \frac{4\mu_l}{R} R_t - p_\infty - p_F$$

Both were derived on the basis of spherical symmetry, shape stability, and uniform bubble pressure. The key difference between the two is that the latter includes a weak contribution of liquid compressibility in the form of a compressibility factor $\left(1 - \frac{R_t}{c_l}\right)$ which incorporates radiation damping into the system.

2.7.2.3 Bubble Internal Pressure

The internal pressure of the bubble depends on its vapour and gas content which can be represented by the vapour pressure p_v and the gas pressure p_g respectively. This work neglects the vapour pressure contributions based on the reasoning provided by Toegel et al. (2000). They argued that cavitation dynamics is much faster than diffusion and phase change, and thus the latter can be omitted. The same reasoning was applied for gas diffusion across the bubble boundary. With these simplifying assumptions, the internal pressure of a bubble can be represented using equations of state for a closed system, such as the ideal gas equation of state:

$$p_g = p_{g0} \left(\frac{T}{T_\infty}\right) \left(\frac{R_0}{R}\right)^{3j} \quad (53)$$

where the exponent j is 1 for isothermal cases and γ for adiabatic cases.

2.7.2.4 Bubble Internal Temperature

Outside of the isothermal assumption, the internal temperature has to be described using an energy balance. Assuming that the internal temperature is uniform, the uniform bubble temperature T_B can be written as (Toegel et al., 2000):

$$\frac{dT_B}{dt} = \frac{\dot{Q}}{N_T C_v} + \frac{\dot{N}_{H_2O} h_{vap}}{N_T C_v} - \frac{p_g \dot{V}}{N_T C_v} \quad (54)$$

The right-hand-side source terms describe heat transfer across the boundary, enthalpy of vaporisation, and work done from gas expansion, respectively. The work done can be calculated from the equation of state, whereas the enthalpy of vaporisation is omitted on prior reasoning in Section 2.7.2.3. Therefore, only the heat transfer across the bubble, \dot{Q} needs to be specified. Trujillo (2020) outlined two useful methods for this purpose. The first is the formulation of Toegel et al. (2000) who proposed a diffusion penetration depth to validate the homogeneous temperature assumption and the ODE formulation:

$$l_{th} = \min\left(\frac{R}{\pi}, \sqrt{\frac{RD_g}{|\dot{R}|}}\right) \quad (55)$$

The bubble temperature is assumed to be uniform, and the energy balance is:

$$\dot{Q} = \frac{4\pi R^2 K_T}{l_{th}} (T_\infty - T_B) \quad (56)$$

The method of Preston et al. (2007) was also studied by Trujillo (2020). The model uses a heat transfer coefficient which was determined from the dimensionless Peclet number:

$$\Phi_h = \left\{ \left[\sqrt{i\omega(Pe)} \coth \sqrt{i\omega(Pe)} - 1 \right]^{-1} - \frac{3}{i\omega(Pe)} \right\}^{-1} \quad (57)$$

where the Peclet number for heat transfer is:

$$Pe = R_0^2/D_g \quad (58)$$

The variable heat transfer coefficient h_T can be expressed using the real part of the complex-valued transfer function:

$$h_T = \frac{K_T \Re(\Phi_h)}{R_0} \quad (59)$$

The imaginary part of the transfer function represents the phase difference between heat transfer and bubble oscillations and can be safely neglected in most ultrasound applications, as argued by Trujillo (2020). Finally, the energy transfer can be expressed as:

$$\dot{Q} = 4\pi R^2 h_T (T_\infty - T_B) \quad (60)$$

2.8 Mesh and Solver Considerations in FEM

Early simulations for sonoreactors can be traced back to the late 1990s, where the finite difference method (FDM) was primarily used (Dähnke and Keil, 1999a; Servant et al., 2000; Vanhille et al., 2004). FEM later became a popular alternative as key disadvantages of FDM, such as the modelling of complex geometries, can be easily addressed (Louisnard et al., 2009). In this work, the acoustic pressure simulations were solved using the commercial FEM software, COMSOL Multiphysics (version 4.2). The hardware specifications of the machine used consists of an *AMD Ryzen 7 3700X* CPU (3593 MHz, 8 cores) with 64 GB of available physical memory (RAM).

2.8.1 Meshing Considerations in Sonoreactor Acoustics

The work of Thompson (2006) was used as the main reference for the meshing strategies in this work. In acoustic simulations, mesh requirements are commonly defined in terms of elements per wavelength:

$$S_{mesh} = \frac{\lambda_{min}}{N_{mesh}} \quad (61)$$

The upper limit of the mesh size, S_{mesh} can be obtained for the shortest wavelength to be simulated. The software manual recommends N_{mesh} values of 6 to 10 for acoustic problems, while Moser et al. (1999) argued that an N_{mesh} up to 20 is recommended. These values were used for initial mesh estimates and subsequently revised using mesh refinement to satisfy accuracy requirements. The temporal mesh in transient simulations also followed software recommendations where estimates were obtained based on the Courant–Friedrichs–Lewy (CFL) criterion (Courant et al., 1928):

$$\Delta t_{max} = \frac{CFL}{10f_{max}} \quad (62)$$

Lebon et al. (2017) claimed that a CFL value of 0.2 is sufficient. The parameter f_{max} represents the maximum frequency to be solved. Similarly, time-stepping refinements were performed to ensure the accuracy of the results.

2.8.2 Convergence Criteria and Solver Framework

The convergence of the numerical solvers can be characterised using relative tolerance ($R.tol$) and absolute tolerance ($A.tol$). Consider two values X and Y , the definitions of $R.tol$ and $A.tol$ are as follows (Helton, 2012):

$$R.tol = \frac{abs(X - Y)}{\min(abs(X), abs(Y))} \quad (63)$$

$$A.tol = abs(X - Y) \quad (64)$$

The relation between *R.tol* and *A.tol* is also clear:

$$R.tol = \frac{A.tol}{\min(abs(X), abs(Y))} \quad (65)$$

Both *R.tol* and *A.tol* were used to specify the convergence criteria in the solvers. For a numerical problem with an exact solution x_0 and an estimated solution x , the absolute error can be written as $E = abs(x - x_0)$. In this work, a value of *R.tol* of 0.001 was used for all acoustic pressure simulations, corresponding to a maximum estimated deviation of 0.1%. Unless stated otherwise, the solver configuration used for the simulations in this work used the Damped Newton method (Deuflhard, 1974) using the MUMPS solver. Figure 2.3 shows a graphical breakdown of the relevant solver types available in the software based on the software manual (COMSOL AB, 2018). The linear models solved in this work simply used the default configurations, while the settings for nonlinear models were tuned to ensure numerical stability and accuracy.

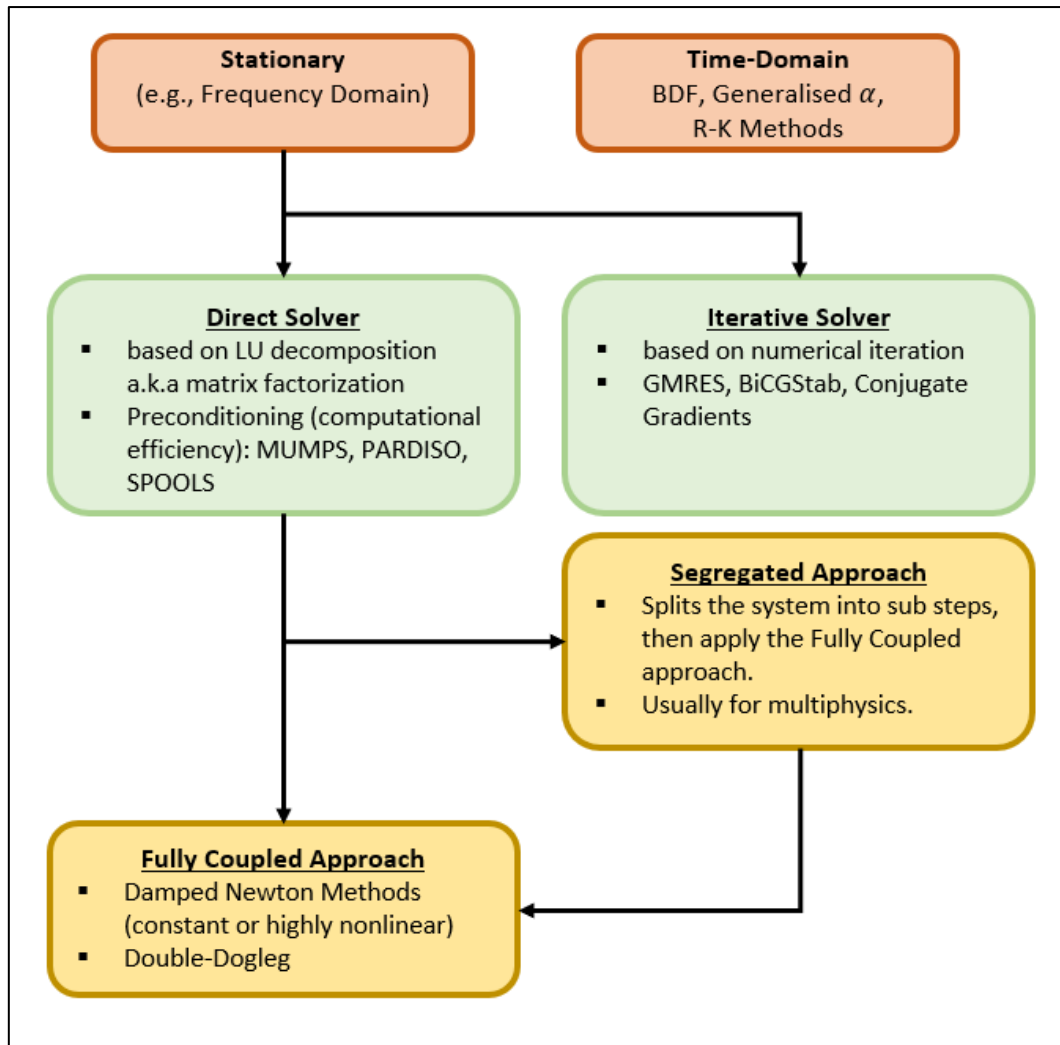


Figure 2.3: The numerical solver set-up in COMSOL. The Damped Newton Method (MUMPS) was the main numerical method used in this work.

2.9 Acoustic Boundary Conditions and Perfectly Matched Layers (PML)

2.9.1 Acoustic Boundary Conditions

The boundary conditions used in sonoreactor acoustics can be categorised into active (e.g., transducers) and passive (e.g., walls and water-air interfaces) boundaries. The boundary conditions can be categorised into Dirichlet, Neumann, and Robin type boundaries (Miles, 2020) as shown in Table 2.7.

Table 2.7: Common boundary conditions in acoustic simulations.

B.C. (Type)	Time-Domain	Frequency-Domain
Active Boundaries		
Pressure (Dirichlet)	$p = p_{bd}$ (66)	$P = P_{bd}$ (67)
Pressure (Neumann)	$\mathbf{n} \cdot \left(\frac{\nabla p}{\rho_l} \right) = \frac{1}{\rho_l c_l} \left(\frac{\partial p_{bd}}{\partial t} \right)$ (68)	$\mathbf{n} \cdot \left(\frac{\nabla P}{\rho_l} \right) = \frac{i\omega P_{bd}}{\rho_l c_l}$ (69)
Normal Acceleration (Neumann)	$\mathbf{n} \cdot \left(\frac{\nabla p}{\rho_l} \right) = a_{bd}$ (70)	$\mathbf{n} \cdot \left(\frac{\nabla P}{\rho_l} \right) = A_{bd}$ (71)
Normal Velocity (Neumann)	$\mathbf{n} \cdot \left(\frac{\nabla p}{\rho_l} \right) = \frac{\partial v_{bd}}{\partial t}$ (72)	$\mathbf{n} \cdot \left(\frac{\nabla P}{\rho_l} \right) = i\omega V_{bd}$ (73)
Normal Displacement (Neumann)	$\mathbf{n} \cdot \left(\frac{\nabla p}{\rho_l} \right) = \frac{\partial^2 d_{bd}}{\partial t^2}$ (74)	$\mathbf{n} \cdot \left(\frac{\nabla P}{\rho_l} \right) = -\omega^2 D_{bd}$ (75)
Passive Boundaries		
Impedance (Robin)	$\mathbf{n} \cdot \left(\frac{\nabla p}{\rho_l} \right) = \frac{1}{\rho_{bd} c_{bd}} \left(\frac{\partial p}{\partial t} \right)$ (76)	$\mathbf{n} \cdot \left(\frac{\nabla P}{\rho_l} \right) = \frac{i\omega P}{\rho_{bd} c_{bd}}$ (77)
Sound-Soft (Dirichlet)	$p = 0$ (78)	$P = 0$ (79)
Sound-Hard (Neumann)	$\frac{\partial p}{\partial t} = 0$ (80)	$i\omega P = 0$ $\mathbf{n} \cdot \left(\frac{\nabla P}{\rho_l} \right) = 0$ (81)

2.9.1.1 Boundary Conditions for Passive Walls

Literature review revealed an interesting inconsistency among the research community on the choice of boundary condition for solid walls in a sonoreactor. Some studies opted for the sound-hard boundary condition (Servant et al., 2000; Sáez et al., 2005; Shao et al., 2010); while others specified the walls as sound-soft (Klíma et al., 2007; Sutkar et al., 2010; Vanhille and Campos-Pozuelo, 2011; Delacour et al., 2020; Sarac et al., 2020). This was found to be interesting, as the numerical and physical implications for both specifications are markedly different. Researchers argued that the sound-hard boundary should be used if the sonoreactor walls are rigid and do not deform. On the other hand, those who selected the sound-soft boundary assumed that the walls are thin enough to deform freely. The study of Yasui et al. (2007) shed some light on this matter using fully-coupled-solid-acoustics simulations, and reported that glass and steel walls with thickness of 2 mm approached that of a free (sound-soft) boundary, while a 7 mm thick wall approximated a rigid (sound-hard) boundary. From their finding, it was clear that the material and thickness of the wall play an important role in this decision.

It is imperative to comment that both sound-hard and sound-soft boundary conditions are idealised, and should be used as simplified approximations. The sound-hard and sound-soft conditions do not account for energy loss through the walls, which is obviously unrealistic. Nonetheless, past studies showed that they are applicable if properly understood and applied (Tudela et al., 2014). Recently, Robin-type impedance boundary condition saw increased adoption in simulation studies (Xu et al., 2013; Tiong et al., 2019). The condition is essentially a generalised formulation for both hard and soft boundaries, and can be specified from acoustic properties of the

boundary. The advantage of the impedance boundary is to be able to partly model energy loss through walls (Ginsberg, 2018). In this work, sound-hard, sound-soft, and impedance passive boundary conditions were used depending on the studied system and the required numerical behaviour. Extensive justification on this topic will be given in the respective studies.

2.9.1.2 *Boundary Conditions for Vibrating Surfaces*

Active boundary conditions simplify vibrating surfaces when modelling a sonoreactor, which is an alternative to fully simulating the solid mechanics (Wei and Weavers, 2016; Tangsopa and Thongsri, 2019). Past studies had used a Dirichlet pressure formulation (Sutkar et al., 2010; Tudela et al., 2011; Jamshidi et al., 2012; Xu et al., 2013) or a Neumann formulation (Louisnard, 2012a; Dogan and Popov, 2016; Lebon et al., 2017). Unlike passive boundaries, the physical significance between the two types of active boundaries is less distinct.

Conventional wisdom suggests that the appropriate boundary should be chosen based on available information (Miles, 2020). For example, a Dirichlet pressure specification is preferred if pressure measurements at the transducer surface are available. Likewise, if displacement data at the surface can be obtained, then a Neumann boundary condition can be easily implemented. It is also possible to convert between pressure and the normal velocity at the surface using the impedance relation:

$$\mathbf{u}_{bd} = \frac{p_{bd}}{\rho_l c_l} \quad (82)$$

2.9.2 Perfectly Matched Layers (PML)

Perfectly Matched Layers (PML) was used to address the issue of truncating discretised waves (Johnson, 2010). PML is a numerical technique used to artificially enforce a non-reflecting condition. It will be shown in Case Study 1, Figure 3.12, that a 1D non-reflecting boundary can be achieved using a matched-impedance boundary. However, the same approach is not effective for 2D and 3D domains due to discretisation (Johnson, 2010). To circumvent this problem, researchers explored various strategies from analytical impedance matching algorithms (Hunt et al., 1974) to absorbing layers that artificially attenuated the waves (Berenger, 1994). PML is part of the latter and became a very common feature in commercial FEM software. The use of PML generally involves the generation of an artificial domain at the boundary, which would be designated as the PML region. The PML region is then meshed and solved along with the acoustic domain. In this work, PML was frequently used for numerical analyses, specifically to examine the acoustic pressure solution in the absence of reflection behaviour.

Chapter 3: Fundamental Modelling Strategies in FEM

This chapter presents two case studies that focused on exploring the numerical properties of acoustic solutions. In Case Study 1, frequency-domain solutions were evaluated against a corresponding time-domain approach to investigate their viability for sonoreactor acoustics. In Case Study 2, a series of short test cases were conducted to investigate the effect of acoustic boundary conditions on the final solutions. The findings from the two case studies served as the cornerstone for developing the fundamental modelling approaches in this work.

3.1 Case Study 1: Time- and Frequency-Domain Acoustic Simulations

Case Study 1 investigated the quality of frequency-domain solutions against time-domain solutions to justify their adoption in this project. Additionally, the interpretation of frequency-domain solutions in relation to sonoreactor acoustics and experimental data was discussed. It was hypothesised that the frequency-domain solution provides sufficient information to characterise a sonoreactor within the scope of study, specifically in terms of antinode and acoustic pressure prediction. This hypothesis was tested by comparing the solution of a time- and frequency-domain solution in a 1D and an asymmetrical 2D model. Further validation against experimental observations by Klíma et al. (2007) were also presented.

3.1.1 Methodology

The time- and frequency-domain solutions were compared in 1D and asymmetric 2D by solving the same physical system using the wave equation in Eqn. (9) and the

Helmholtz equation in Eqn. (11) respectively. Figure 3.1 depicts the model geometries used in this investigation. For the 1D study in Figure 3.1 (a), the left edge was specified as a 20 kHz Dirichlet pressure boundary with an arbitrary magnitude of 1 bar. The right boundary was specified as a perfectly reflecting sound-hard boundary. The propagation medium was treated as a pure liquid ($\rho_l = 1000 \text{ kg/m}^3$ and $c_l = 1500 \text{ m/s}$) with no explicit attenuation. The asymmetric 2D simulation was modelled using the set-up of Klíma et al. (2007) shown in Figure 3.1 (b). The simulation parameters also followed the original study. Quadratic Lagrange elements were used for the simulation mesh. The mesh of the 1D model was set at 10 nodes per wavelength. For the asymmetric 2D study, different meshes were required for the frequency- and time-domain cases, as shown in Figure 3.2. The mesh sizes were significantly overtuned to minimise the impact of numerical uncertainties on the solutions. The frequency-domain mesh requirements were set at $N = 70$, while the time-domain mesh had to be refined until $N = 85$ to properly eliminate numerical errors in transient solutions.

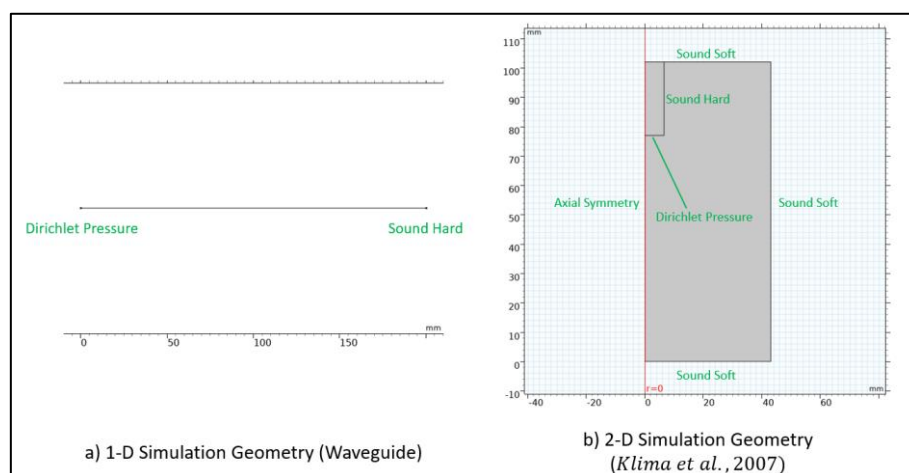


Figure 3.1: The simulation geometry for: (a) the 1D study; (b) the 2D asymmetric study of Klíma et al. (2007).

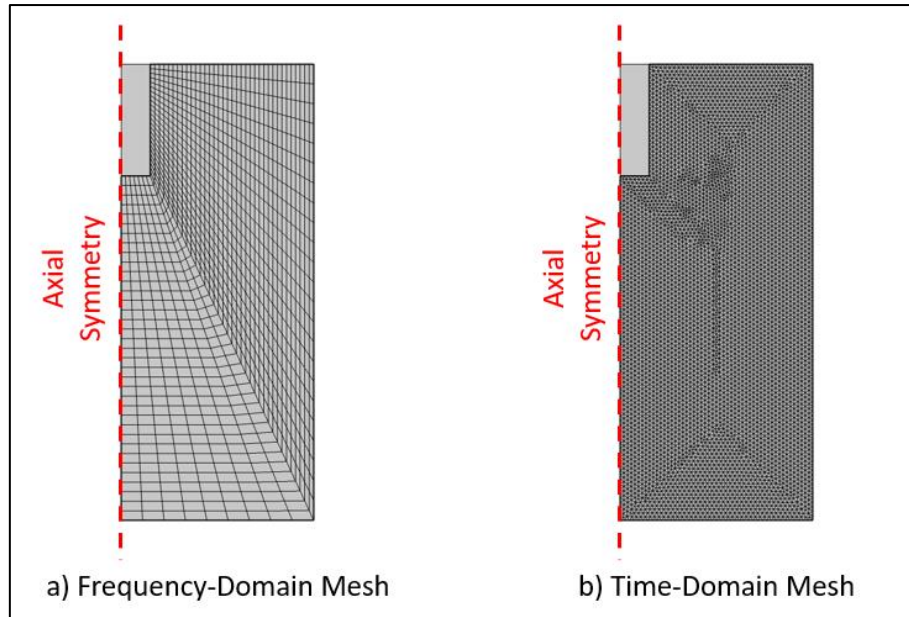


Figure 3.2: The meshes used for the 2D asymmetric case: (a) frequency-domain simulation; (b) time-domain simulation.

3.1.2 Results and Discussion

3.1.2.1 1D Simulation Results

Pure-liquid models were used to avoid uncertainties related to attenuation, since establishing the same dispersion relation for both frequency- and time-domain models was found to be challenging (Ginsberg, 2018). The arbitrary value specified for the Dirichlet boundary condition did not affect the findings as the investigated models are linear. Figure 3.3 shows the spatial pressure $P(\mathbf{r})$ from the frequency-domain solution. A total of six antinodes and five nodes were observed. The antinodes predicted highly cavitating regions, while the nodes were interpreted as ‘dead zones’ (Tudela et al., 2014; Tangsopa and Thongsri, 2019). Since the solution was inherently time-harmonic, it was useful to analyse the results using the absolute acoustic pressure $|P|(\mathbf{r})$, as plotted in Figure 3.4. The prediction of nonzero pressure at the

nodes was found to be reduced upon refinement of the mesh, which suggested that this was the consequence of discretisation resolution.

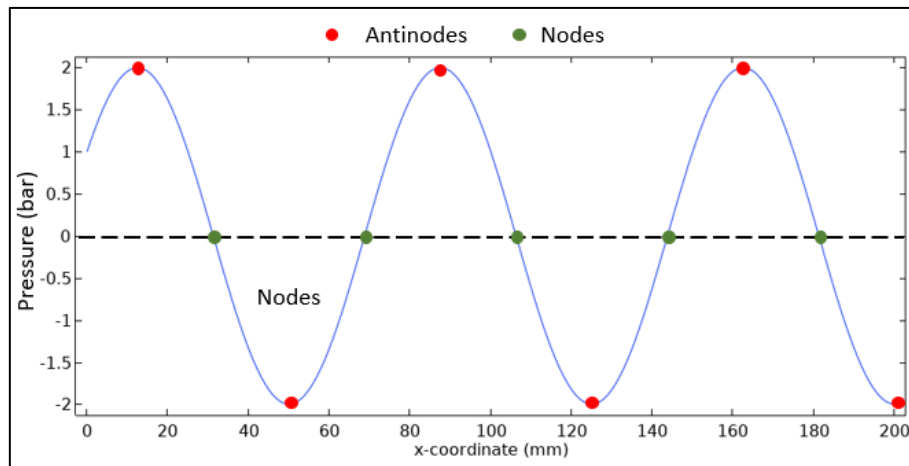


Figure 3.3: Acoustic pressure plot P for the 1D frequency-domain simulation.

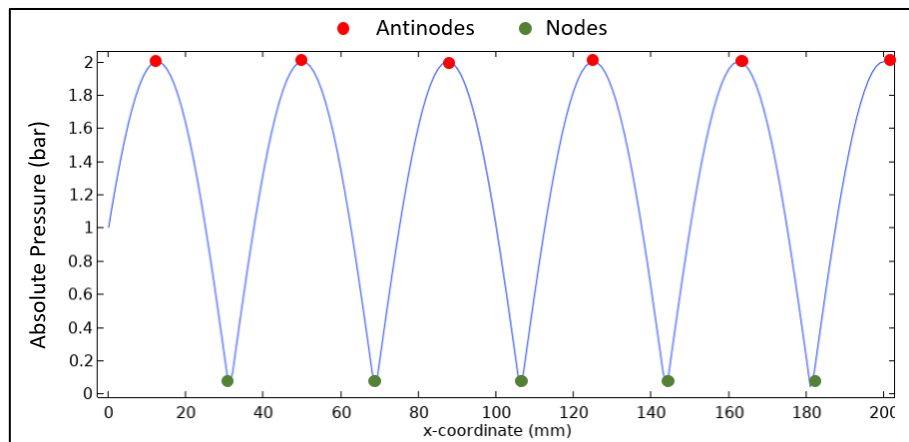


Figure 3.4: Absolute acoustic pressure plot $|P|$ for the 1D frequency-domain result.

The results of the time-domain solution are shown in Figure 3.5. Figure 3.5 (a) and Figure 3.5 (b) show the initial waveform propagating to the right, before fully reflecting at the sound-hard boundary in Figure 3.5 (c). Figure 3.5 (d) shows the start of standing wave formation ($t = 3E-4$ s) as the two opposing waves superimposed.

Figure 3.6 shows the oscillating behaviour of the transient standing wave, which was comparable to the frequency-domain result in Figure 3.4. Interestingly, there was a notable difference in terms of pressure magnitude prediction. This is obvious in Figure 3.6 (d), where the first antinode on the left reached a pressure magnitude of -2.5 bar, which was 0.5 bar lower than the frequency-domain solution in Figure 3.3.

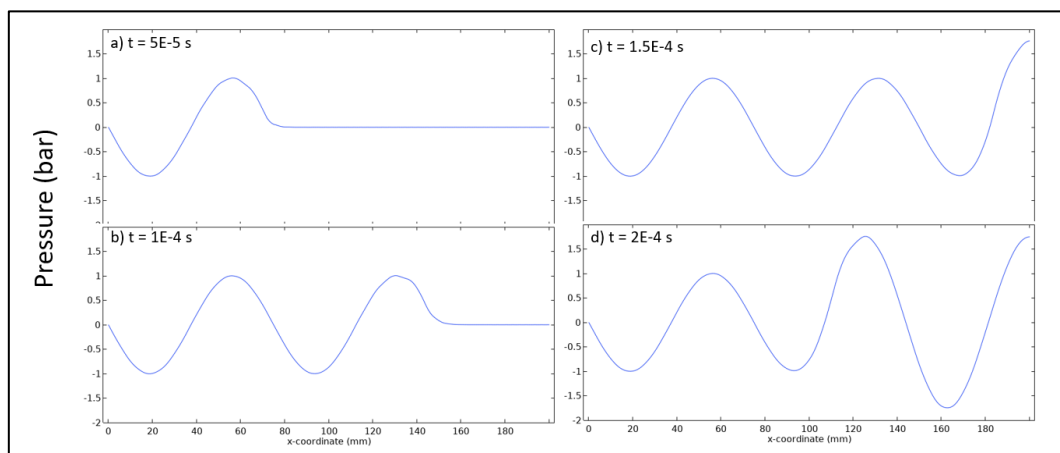


Figure 3.5: Evolution of the 1D time-domain acoustic pressure.

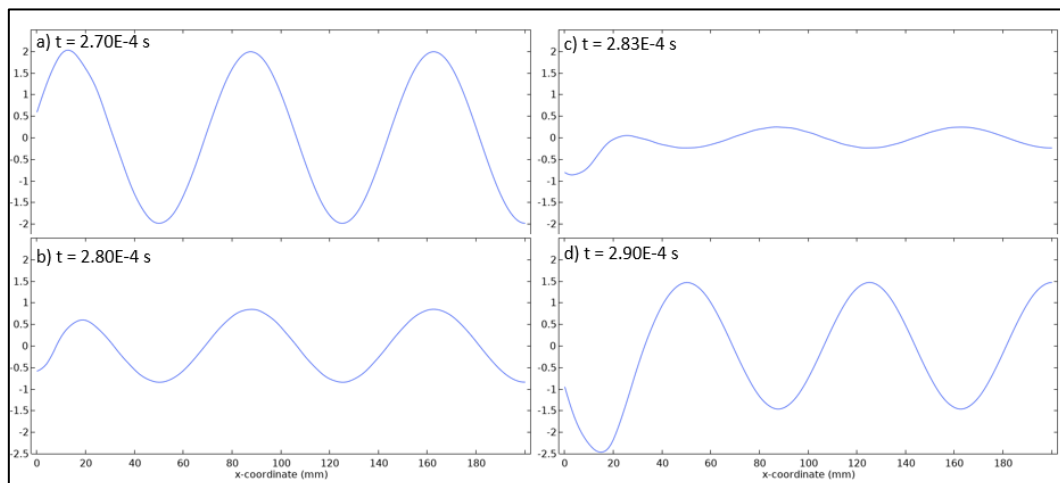


Figure 3.6: Depiction of the half-cycle of the transient standing wave; note that pressures at the antinodes oscillate as the waveform evolved from (a) to (d).

3.1.2.2 2D Asymmetric Simulation Results

The results of a 2D asymmetric simulation for both the time- and frequency-domain models were compared with the experimental observations of Klíma et al. (2007). The original study only considered the frequency-domain result, and it was hypothesised that the time-domain simulation would also produce similar results. Figure 3.7 compares the frequency-domain solution reported in the original study (Klíma et al., 2007), as well as the frequency- and time-domain solutions obtained in this investigation. In terms of antinode predictions, both the time- and frequency-domain results showed good agreement with empirical observations. The two antinodal bubble structures in Figure 3.7 (a) correspond to the antinodal locations predicted by both solutions. On the other hand, the comparison for the acoustic pressure prediction results was not straightforward. Similar to the 1D investigation in the previous section, the time-domain result once again predicted differences in terms of acoustic pressure magnitude compared to frequency-domain results. This is clear in Figure 3.7 (c), where the magnitudes predicted at the antinodal regions are lower compared to the frequency-domain results.

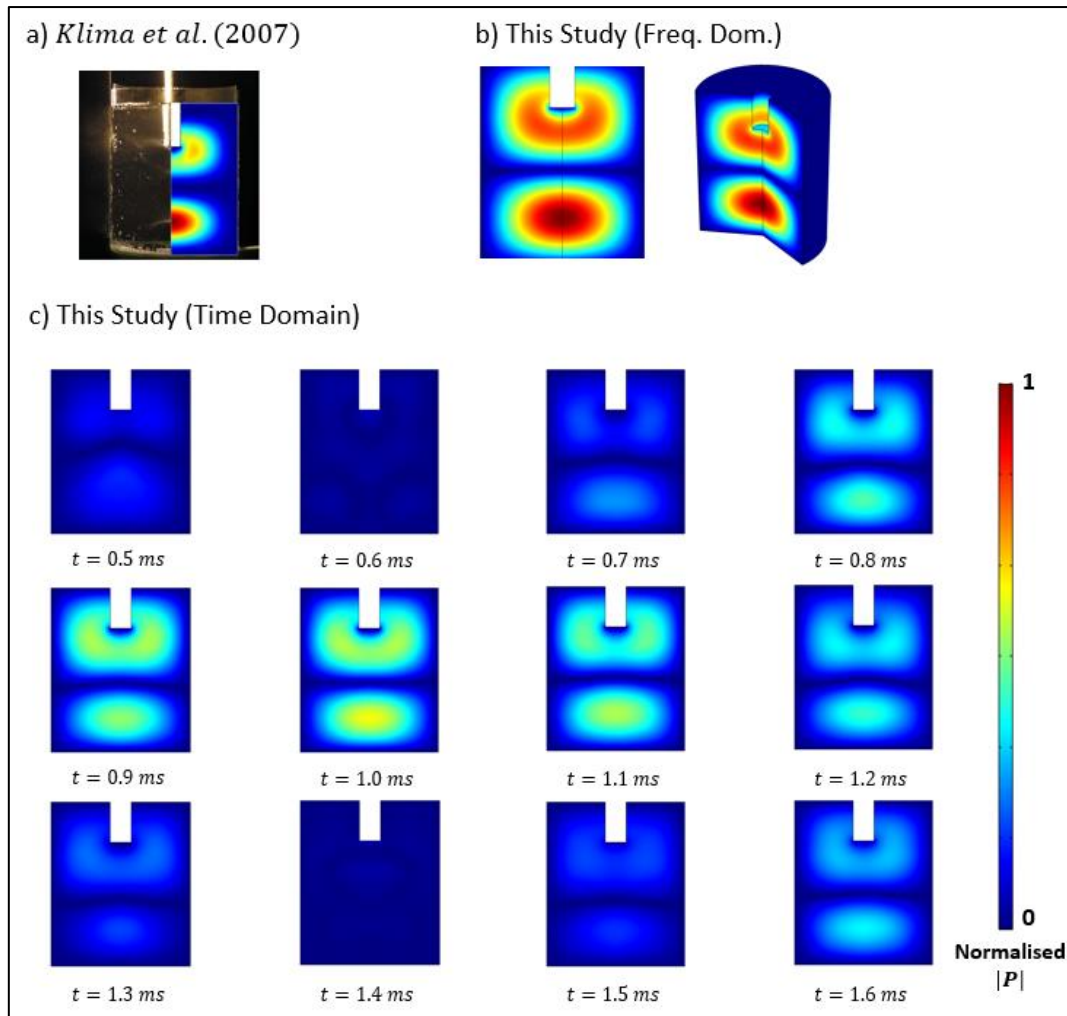


Figure 3.7: Comparison between the: (a) validation result of Klíma et al. (2007); (b) frequency-domain simulation results; (c) time-domain simulation result. The colour scale is normalised, based on the original work.

3.1.2.3 Discussing the Difference in Acoustic Pressure Predictions

Initial postulations suggested that the differences in pressure magnitudes predicted in the two simulations were caused by numerical errors based on the loss of sinusoidal behaviour in Figure 3.5 and Figure 3.6. A clearer example is shown in Figure 3.8 (a). It was argued that this was the result of numerical dispersion, which often manifests itself as a deterioration of the signal shape (Prikšaitis et al., 2015). Numerical errors were prominent in time-domain simulations (Chai and Bathe, 2020; Chai and Zhang, 2020) and can generate numerical artifacts that do not have physical significance.

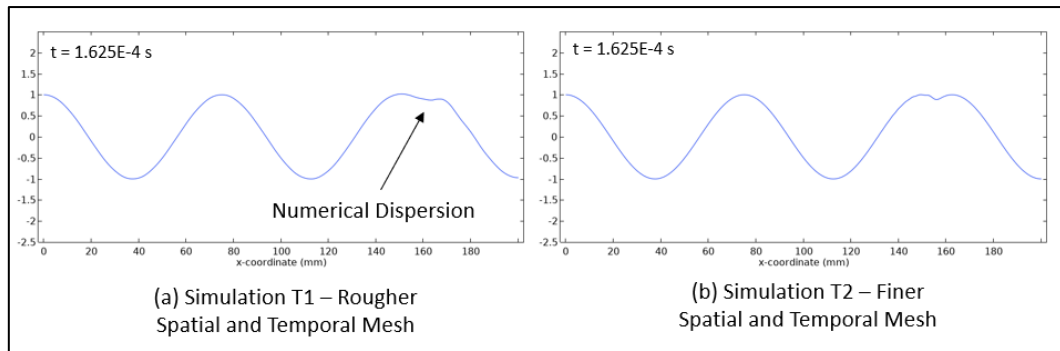


Figure 3.8: Numerical dispersion error in the 1D time-domain results: (a) the loss of sinusoidal behaviour; (b) reduced error after mesh refining.

The numerical artifact was found to be reduced by refining the spatial and temporal meshes. This is shown using another simulation, T2, which was carried out using a spatial mesh that is 4 times finer and a temporal mesh that is 100 times smaller. The result for the same time stamp is shown in Figure 3.8 (b), where it can be seen that the sinusoidal shape of the reflected wave was better preserved. This is clear evidence that the distortion observed in Figure 3.8 (a) was caused by numerical error. This was a costly solution as shown in Table 3.1 which compares the resource usage of the frequency-domain simulation (F1) and the two time-domain simulations (T1 and T2). It is imperative to state that the refined mesh used in T2 was arbitrarily decided. In practice, a comprehensive mesh refinement study would yield a more efficient and practical refinement. Compared to a full sonoreactor simulation, the values tabulated in Table 3.1 were found to be relatively small since only a 1D linear model was considered. The increase in resource requirements was calculated to be exponentially larger when considering additional space dimensions and more complex nonlinear models.

Table 3.1: Computational resource requirements for each test simulation.

Ref.	Simulation Type	Degrees of Freedom	Solver Time Step (s)	Memory Req. (MB)	Solution Time (s)
F1	Frequency-Domain	101	N / A	810 MB	1
T1	Time-Domain	101	8.33E-7	1540 MB	5
T2	Time-Domain	401	8.33E-9	1720 MB	241

Interestingly, differences in predicted pressure magnitudes persisted after mesh refinement. It was hypothesised that the deviation was caused by transient behaviour that was not captured in the frequency-domain solutions. Further testing conducted by extending the transient simulation yields an interesting result, as shown in Figure 3.9. Analysis showed that the transient acoustic pressure at a fixed point in space ($x = 40$ mm) experienced different magnitudes in time that appeared to be periodic.

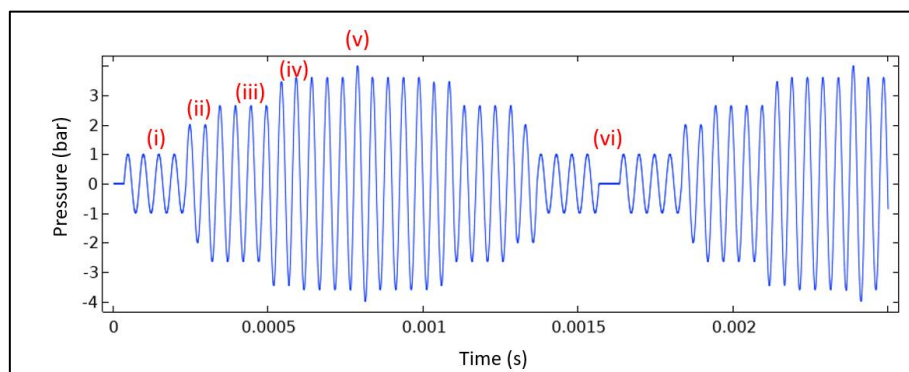


Figure 3.9: Time evolution of acoustic pressure at $x = 40$ mm from simulation T2. The phase mismatch formed multiple levels of constructive and destructive interference between the incident and reflecting waves.

Further analysis of the results in Figure 3.9 strongly suggested that it was caused by a unique combination of simulation geometry and perfectly reflecting boundary conditions. It was postulated that the observation was caused by the mismatch between the simulated frequency and the resonance frequency of the geometry. In cases where the simulated frequency was resonant, the phase of the reflected wave would match the phase of the emitted wave, leading to large accumulation of energy at the antinodes. Instead, the simulated frequency was slightly off-resonant, evident by the fact that the left boundary in Figure 3.4 was neither a pure node nor an antinode. Thus, each time an emitted wave was reflected at the boundaries, it experienced a slight phase difference. Referring to Figure 3.9, (i) represents the magnitude when the first travelling wave is emitted, while (ii) shows the magnitude of the first standing wave. As multiple reflection cycles accumulate with different phases within the geometry, the composite pressure magnitude gradually increases, as seen in (iii) and (iv). Eventually, after the (v) mode, some phases coincided and destructively interfered with each other. The strongest destructive interference is observed at (vi), where all phases of the travelling waves were temporarily cancelled out by their counterparts. The cycle was then repeated in a periodic manner. Interestingly, this behaviour can only be observed in an unattenuated system in a perfectly reflecting geometry. This is an interesting finding from an acoustic standpoint. The finding was noted to be relevant when analysing solutions of the pure-liquid model which was noted to be a popular choice in sonoreactor acoustics [Section 1.2.3.1].

The pressure profile in Figure 3.9 was also converted into a spectral distribution using the fast Fourier transform (FFT) in MATLAB. Using a sampling rate of 200 kHz for a sample size of 16384 (the sample was truncated to reduce spectral leakage), the

single-sided spectra depicting the amplitudes for each involved harmonic is plotted in Figure 3.10. The resolution was coarse as the sampled signal was short. Expectedly, the primary harmonic of interest (20 kHz) was dominant, with a spectral magnitude that was slightly higher than 2 bar, which slightly deviated from the results of the frequency-domain analysis. The result clearly showed the presence of other harmonics, which could be linked to the deviation in terms of pressure magnitude predictions between the time- and frequency-domain solutions. However, there was no confirmation whether these harmonics were of numerical origin or caused by the nonlinear interaction between travelling waves.

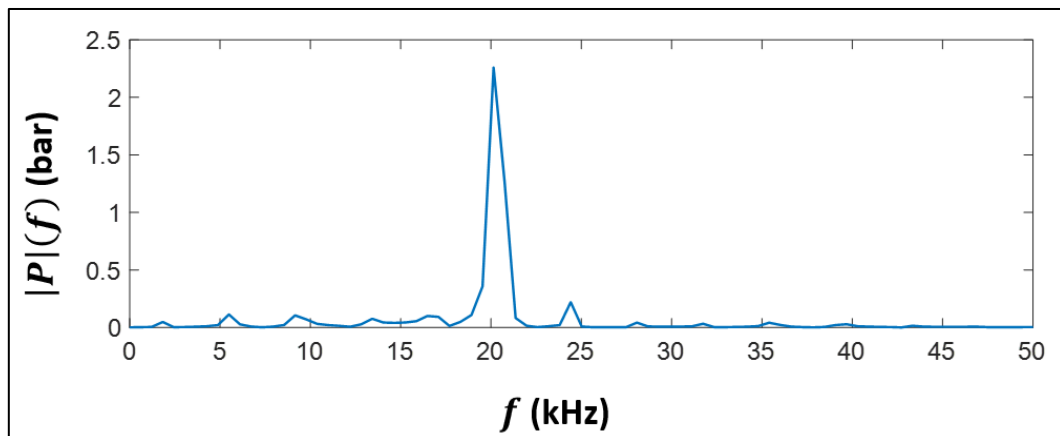


Figure 3.10: Spectral decomposition of time-dependent acoustic pressure at $x = 40$ mm (T_2) obtained using FFT.

3.1.2.4 Justifying the Use of Frequency-Domain Solutions

Frequency-domain models had been known to be much more efficient for sonoreactor acoustics. The main benefit of using frequency-domain models is its cost efficiency and the lower risk of numerical error. Tangsopa and Thongsri (2021) reported that their time-domain model took 16 times longer to solve when simulating the same

system. The benefits of using frequency-domain models are further amplified when considering systems with high operating frequencies. The use of time-domain models becomes increasingly resource intensive upon considering higher operating frequencies due to the stricter temporal and spatial meshing requirements. This would lead to not only longer solution times, but also greater memory requirement to store the solution. In contrast, frequency-domain solutions would only need to consider the effect of frequency on the wavelength for spatial mesh generation. A similar discussion can be made when considering working fluids with different physical properties. Notably, working fluids with lower phase speeds would also affect the solution time and memory requirements of both time- and frequency-domain simulations. This is due to the shorter wavelength, which results in a higher mesh count per unit length with reference to Eqn. (61).

Based on the above findings, it was suggested that frequency-domain solutions can be a reliable way to characterise the antinodes, but pressure magnitude predictions should be treated as an approximation. Exceptions can be made for cases where very accurate pressure magnitude prediction is crucial, or when studying acoustic phenomena which are highly transient in nature. For example, it was known that acoustic phenomena such as shock waves (Seung and Kwak, 2017), nonlinear harmonics (Vanhille and Campos-Pozuelo, 2011), and cavitation broadbands (Moholkar et al., 2000; Avvaru and Pandit, 2009) cannot be adequately captured by a single frequency-domain simulation.

3.1.2.5 Interpretation of Frequency-Domain Results

The interpretation of the frequency-domain results was also discussed. Literature review revealed that some studies only analysed acoustic pressure using spatial pressure P instead of absolute pressure $|P|$ (Sutkar et al., 2010; Wei and Weavers, 2016; Tonry et al., 2020). It was argued that this could be misleading and that absolute pressure plots should be used as they provide a better representation for the acoustic behaviour. This is because the frequency-domain solutions can be complex-valued. Prior discussions omitted the complex-valued P because the imaginary part of a pure attenuated standing wave is zero. A complex-valued P indicates the presence of travelling wave contributions which manifests when attenuation is considered. Figure 3.11 shows the same 1D simulation model used in Section 3.1.2.1 with an added arbitrary attenuation of 5 Np/m throughout the domain. It can be observed in Figure 3.11 (a) that the waveform loses amplitude while oscillating around zero.

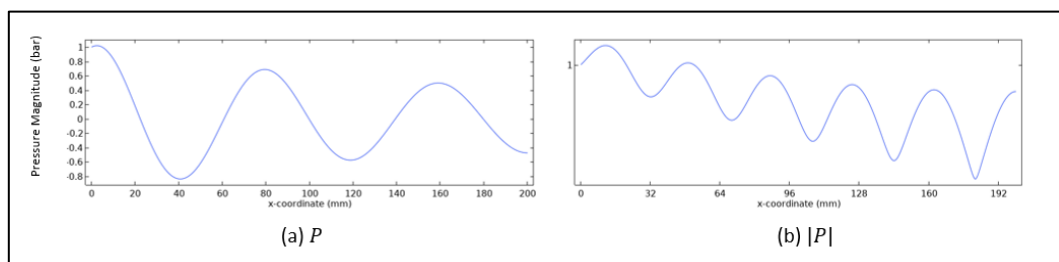


Figure 3.11: Simulation results for the 1D system with a specified attenuation of 5 Np/m: (a) acoustic pressure, P ; (b) absolute pressure, $|P|$.

A better representation of the acoustic behaviour can be shown using a plot of $|P|$ in Figure 3.11 (b), where the nodal regions near the left of the geometry show significantly higher magnitudes above zero. This can be explained if one considers that

a pure standing wave is the result of two opposing travelling waves. When both travelling waves have equal amplitudes, destructive interference would perfectly cancel out any pressure signal at the nodes (e.g., Figure 3.4). This changes in the presence of attenuation, since the amplitudes of the travelling waves decrease with propagation distance. For Figure 3.11, the left-propagating reflected waves would have a lower amplitude than their right-propagating counterpart. This results in weaker destructive interferences near the left of the geometry, and a pure standing wave is no longer observed. Some authors referred to this observation as a damped standing wave (Yasui, 2018). Leighton (1994) suggested that this phenomenon can be characterised in terms of its local standing wave component and its travelling wave component, where the standing wave contribution can be calculated from the magnitude of the local node $|P|_{nod}$ and antinode $|P|_{ant}$:

$$\text{Standing Wave Contribution} = \frac{|P|_{ant} - |P|_{nod}}{|P|_{ant} + |P|_{nod}} \times 100\% \quad (83)$$

The numerical result of Figure 3.11 (b) explains the weak standing wave characteristics observed in the simulation of certain systems, such as in ultrasonic horns, where the attenuation was reported to be strong (Jamshidi et al., 2012; Louisnard, 2012b). It is also instructive to demonstrate the effect of boundary conditions on the travelling wave contribution. The pure standing wave in Figure 3.3 was caused by the perfectly reflecting right boundary. In contrast, Figure 3.12 shows the pressure plots when the unattenuated case was simulated using a perfectly non-reflecting right boundary. This was achieved using an impedance boundary that was matched to the acoustic properties of the medium [Eqn. (77)]. The right boundary essentially acts as an unbounded edge through which the acoustic waves can propagate. Naturally, no

standing wave formation was observed. This was confirmed in the absolute pressure plots in Figure 3.12 (b), where $|P|$ is spatially constant, which indicates a pure travelling wave. Similarly, if one were to analyse this result using a plot of P , the observation would not be obvious. Based on the above discussion, the frequency-domain solution should primarily be analysed using the absolute pressure $|P|(\mathbf{r})$.

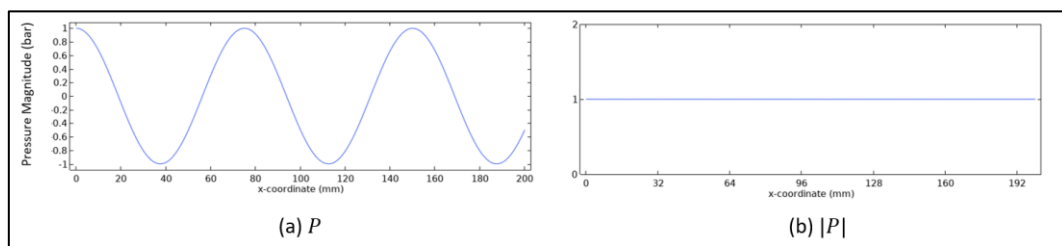


Figure 3.12: Simulation results for the 1D system with a non-reflecting right boundary: (a) acoustic pressure, P ; (b) absolute pressure, $|P|$.

3.2 Case Study 2: Investigating the Suitability of Boundary Conditions

The solution of the Helmholtz equations depends on both the boundary conditions and the wavenumber (Ginsberg, 2018). While the choice of common boundary conditions in sonoreactor acoustics was summarised in literature (Tudela et al., 2014), several key uncertainties remained to be addressed. A series of short numerical tests were carried out to investigate the suitability of frequency-domain Dirichlet and Neumann active boundaries for the representation of vibrating surfaces in a sonoreactor. Additionally, the performance of boundary conditions compared to full solid-acoustic simulations was also compared and discussed.

3.2.1 Dirichlet vs. Neumann Transducer Boundary Condition for Horns

The numerical behaviour of Dirichlet and Neumann active boundaries for horn-type configurations was investigated using an arbitrary 2D frequency-domain simulation model presented in Figure 3.13. The arbitrary rectangular geometry (20 x 10 mm) was used to represent a simple sonotrode in a square acoustic domain (100 x 100 mm). The mesh for the domain was drastically overtuned to eliminate mesh refinement errors. The model was solved using a Dirichlet pressure specification [Eqn.(67)] and a Neumann displacement specification [Eqn. (75)] as the active boundary condition, respectively. An arbitrary 1 bar was used for the Dirichlet condition, while an equivalent normal displacement of 0.266 μm was used for the Neumann condition.

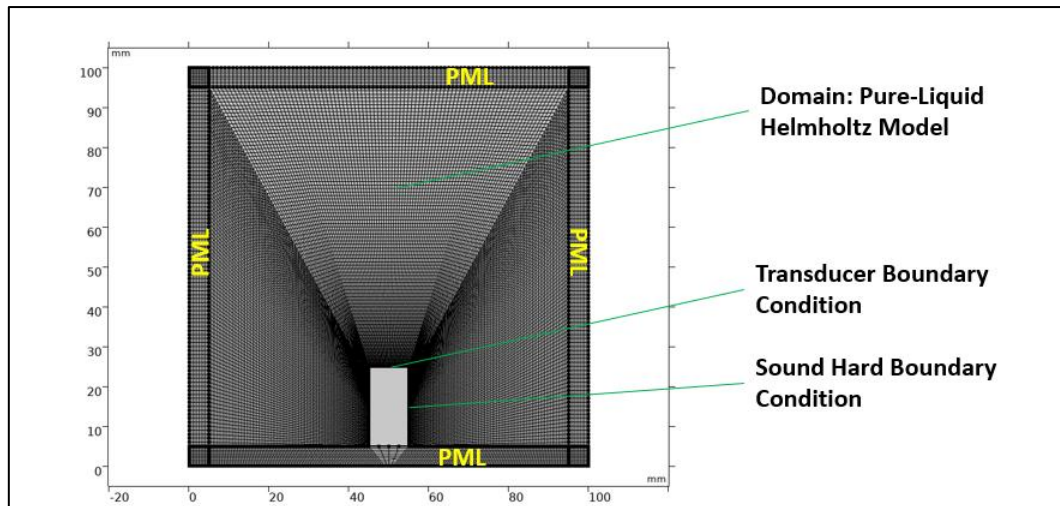


Figure 3.13: The mesh model used to study the numerical behaviour of Dirichlet and Neumann active boundaries. PML was used to eliminate reflection effects on the results.

The plot of absolute pressure along the investigated boundary is shown in Figure 3.14. Since the models did not consider attenuation, the values specified for the active boundaries do not impact the result and can be normalised. A stark difference was observed between the two specifications. The Dirichlet specification strongly constrained the entire 10 mm boundary to a magnitude of 1 bar, while the Neumann specification resulted in a curved profile. Figure 3.15 plots the pressure field P and the absolute pressure field $|P|$ for each case. The P plots in (a) and (b) clearly showed that both cases exhibited similar propagation behaviour in the non-reflecting domain. Another important observation is the difference in the phase of the solution. In Figure 3.15 (a), the transducer surface is at positive pressure, while the opposite is observed in Figure 3.15 (b). This is a consequence of the constraint imposed by the Dirichlet boundary. Another difference was observed in Figure 3.15 (c) and (d), where the pressure magnitude $|P|$ for the Dirichlet case resulted in a slightly larger region of high acoustic pressure.

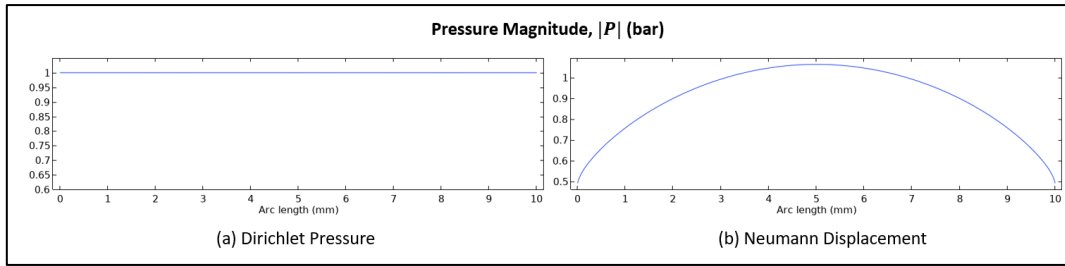


Figure 3.14: Absolute pressure profile of the active boundary: (a) Dirichlet pressure condition; (b) Neumann displacement condition.

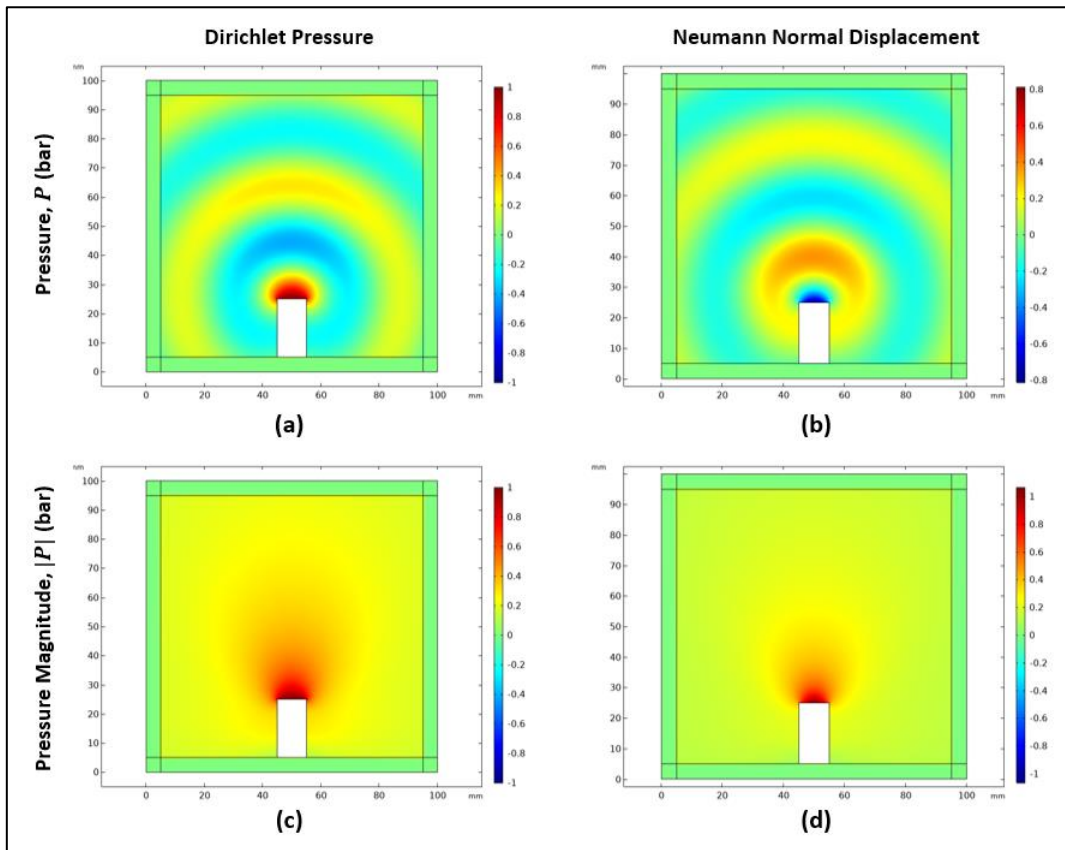


Figure 3.15: Plots of the pressure and absolute pressure solved using Dirichlet (a and c) and Neumann (b and d) active boundaries for the horn-type configuration.

The results strongly suggest that there is a distinct difference between the Dirichlet and Neumann active boundaries when used to represent a harmonically vibrating surface of a sonotrode. In particular, several studies that closely studied the surface dynamics of sonotrodes reported observations similar to the curved pressure profile

generated by the Neumann boundary condition in Figure 3.14 (b) (Campos-Pozuelo et al., 2005; Tian et al., 2018). These findings suggest that the use of a Dirichlet boundary specification for a sonotrode surface slightly overpredicts the pressure field.

The behaviour of Neumann active boundaries was also affected by the width of the sonotrode. As the size of the boundary was increased, the numerical behaviour of the Neumann boundary condition approached a uniform distribution, similar to the Dirichlet specification. This result is shown in Figure 3.16. The test results showed that by increasing the dimensions of the sonotrode by one wavelength, the number of 'peaks' predicted by the Neumann boundary condition doubled. Furthermore, the results were affected by the quality of the shape function and the mesh, which is shown in Figure 3.17. The quality of the Neumann boundary gradually approximated a uniform 1 bar specification when the order of the shape functions was increased. This sensitivity was not observed for the Dirichlet boundaries, which consistently constrained the pressure magnitude to specified values. Currently, there is yet to be a satisfactory explanation for the discretisation sensitivity observed for the Neumann boundary condition. A hypothesis can be made suggesting that this was caused by the mathematical implementations of the discretisation scheme. An in-depth study of this matter was left for future work.

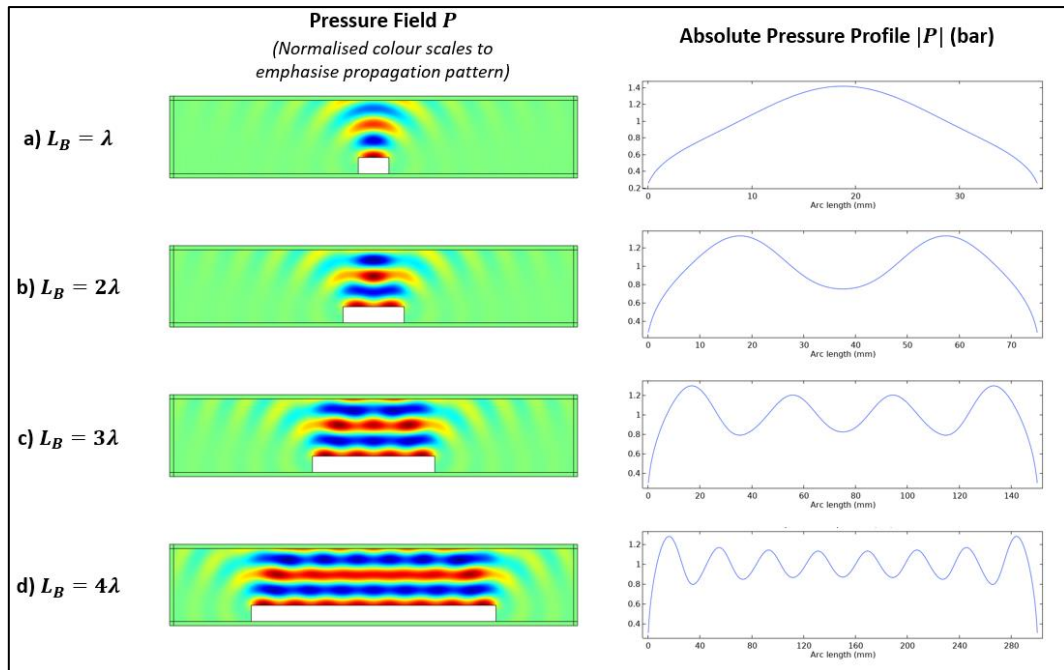


Figure 3.16: Propagation pattern and absolute pressure profile on the boundary, solved for increasing sonotrode width using the Neumann boundary.

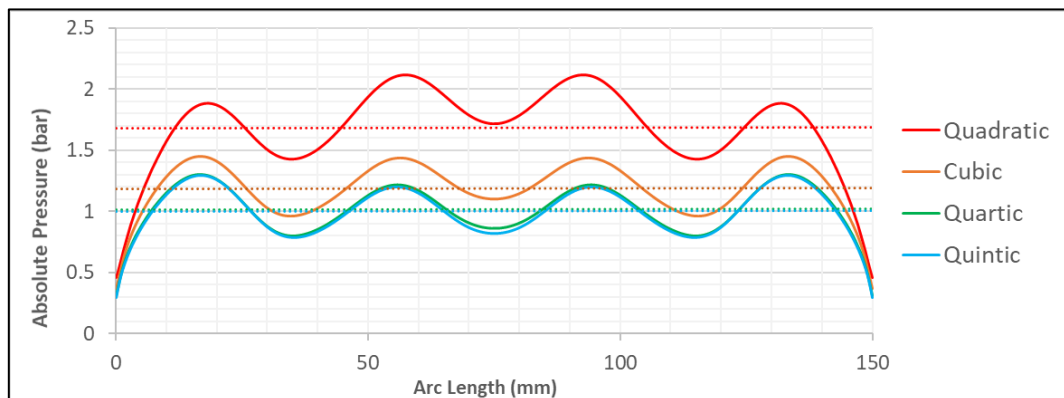


Figure 3.17: Effect of discretisation order on the Neumann boundary condition. Horizontal linear regression lines visualised the average magnitude across the investigated boundary.

3.2.2 Dirichlet vs. Neumann Transducer Boundary Condition for Baths

Ultrasonic baths generally rely on the vessel walls to transmit mechanical vibrations into the fluid, leading to a larger surface. These aspects need to be considered in the modelling strategies of this work. The differences between the Dirichlet and Neumann active boundary conditions were tested in an arbitrary simulation domain (600 x 600

mm). The entire bottom boundary was specified as the active boundary, and the sides of the domain were modelled as sound-hard passive walls, while PML was used at the opposite boundary. The results in Figure 3.18 show strongly planar waves with negligible reflection at the side walls for both boundary conditions. The region at the top of the square test geometry (green) with zero acoustic pressure is the PML region. Interestingly, the differences between the Dirichlet and Neumann specifications were small, with the only notable difference being the phase of the pressure field. The $|P|$ plots in Figure 3.18 (c) and (d) are 2D representations of the travelling wave profile previously shown in Figure 3.12, which was caused by the use of PML.

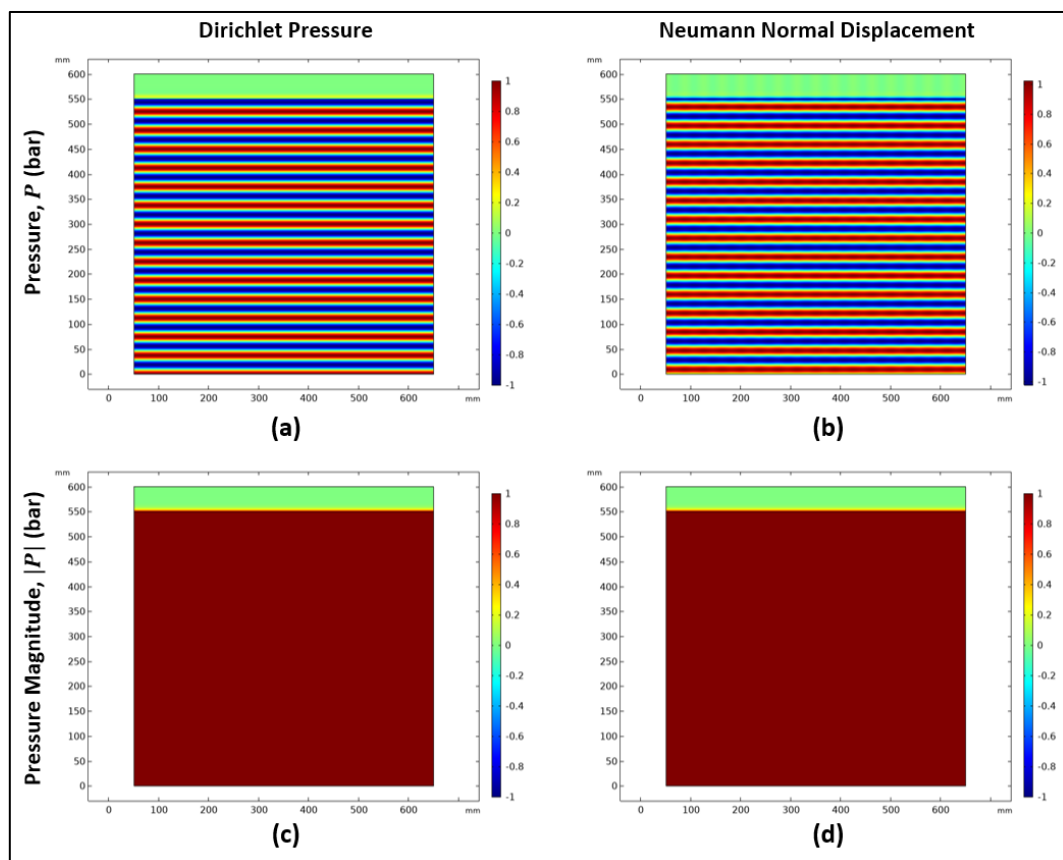


Figure 3.18: Plots of pressure and absolute pressure solved using the Dirichlet (a and c) and Neumann (b and d) active boundaries for the bath-type test case.

Figure 3.19 plots the acoustic pressure magnitude across the bottom boundary. As expected, the Dirichlet boundary condition was strongly constrained in Figure 3.19 (a). The effect of the shape function was again observed for the Neumann boundary condition, and is shown in Figure 3.19 (b) and (c). The observations are consistent with the findings of the previous sonotrode test in Section 3.2.1.

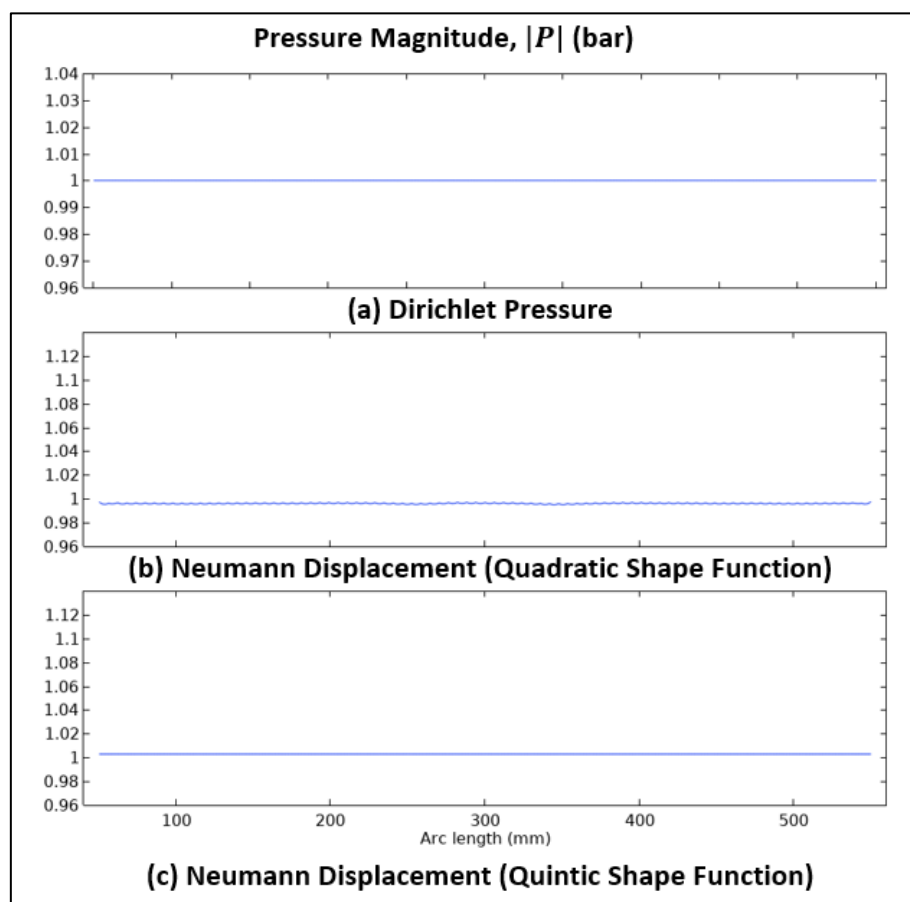


Figure 3.19: Absolute pressure magnitude at for each boundary condition.

3.2.3 Dynamics of a Plate-Transducer Assembly

It can be argued that the active boundary conditions should only be used if the vibration across the entire sonoreactor wall is uniform. Past studies either did not comment on this matter (Delacour et al., 2020; Sarac et al., 2020) or opted to fully

simulate the solid walls (Wei and Weavers, 2016; Tangsopa and Thongsri, 2019). However, the latter was found to be challenging for larger systems or when accurate mechanical data is limited. An investigation was conducted to compare the results solved for a solid-acoustic system with the simplified representation provided by boundary conditions. The modelling of solid vibrations followed the methods reported by Louisnard et al. (2009). A simplified plate-transducer system was simulated to generate preliminary insights. The model represents a 2 mm thick stainless-steel plate with a wall transducer (*Sonictron, Malaysia*) attached at the centre as shown in Figure 3.20. The ends of the plate were set as fixed constraints to represent welded edges. A normal displacement boundary of $0.1 \mu\text{m}$ was specified at the surface contacting the main piezoelectric stack, while other edges were left as free boundaries. Linear elastic constitutive equations were assumed, and the model was solved at 40 kHz.

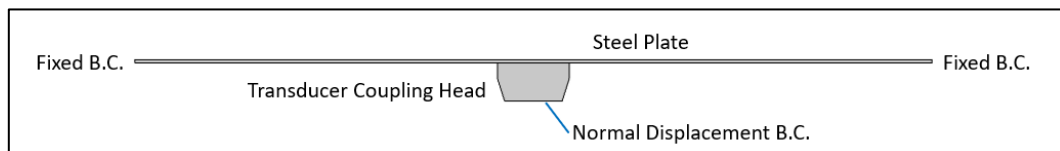


Figure 3.20: Schematics of the plate-transducer system and the boundary conditions.

The displacement of the steel plate is shown in Figure 3.21 (a) with 40000x scale for deformation. The left- and right-most boundaries exhibited zero displacement due to the fixed constraints. Figure 3.21 (b) clearly showed flexural Lamb wave characteristics. The displacement was uniformly distributed across the plate at c.a. $1 \mu\text{m}$, except for the centre which was 20% greater in magnitude. An acoustic pressure domain of length 1000 mm was coupled to the plate surface and solved using a pure-liquid model

(water). The result of the solid-acoustic coupled simulation is shown in Figure 3.22 (a). For comparison, Figure 3.22 (b) and (c) plot the results when Dirichlet and Neumann active boundaries were used to replace the vibrating plate³. The colour contours of the plots were normalised to better compare the propagation behaviour and wave characteristics. The differences between the modelling strategies are clear. Both Figure 3.22 (b) and (c) resulted in strong plane waves, while Figure 3.22 (a) behaves like a point source near the vibrating plate and approximates a plane wave with increasing distance.

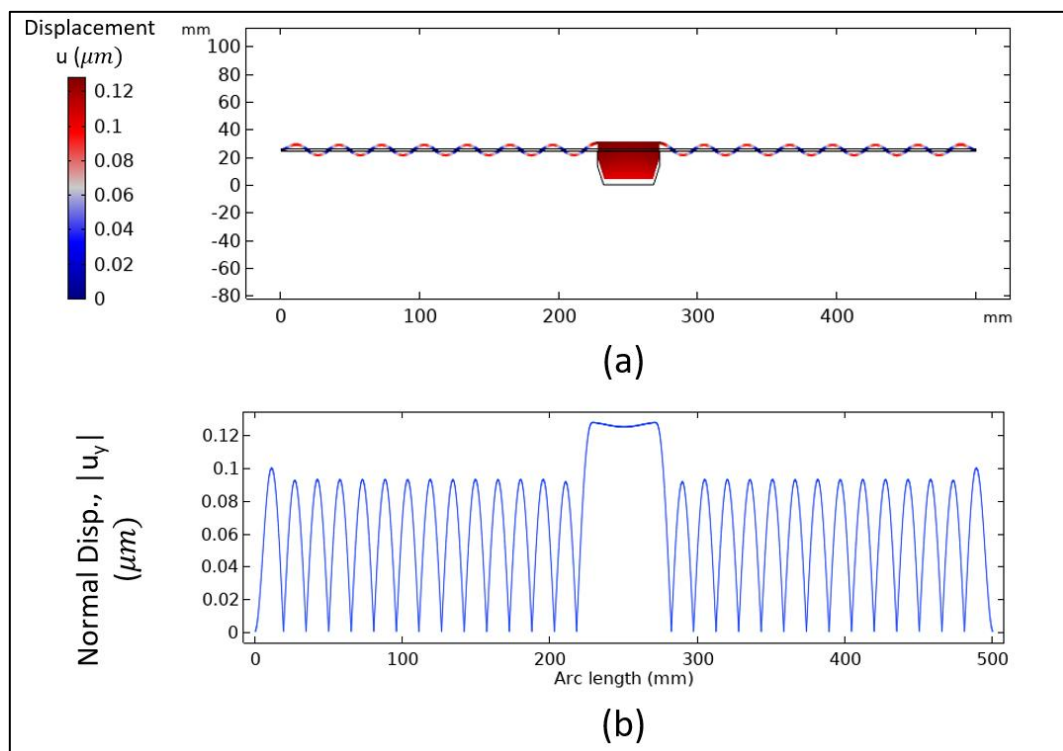


Figure 3.21: (a) Total displacement magnitude with deformation magnified 40000x; (b) 1D plot of normal displacement magnitude at the top surface.

³ For all intents and purposes, this value specified for the boundary condition can be regarded as arbitrary since it is assumed that energy is equally distributed.

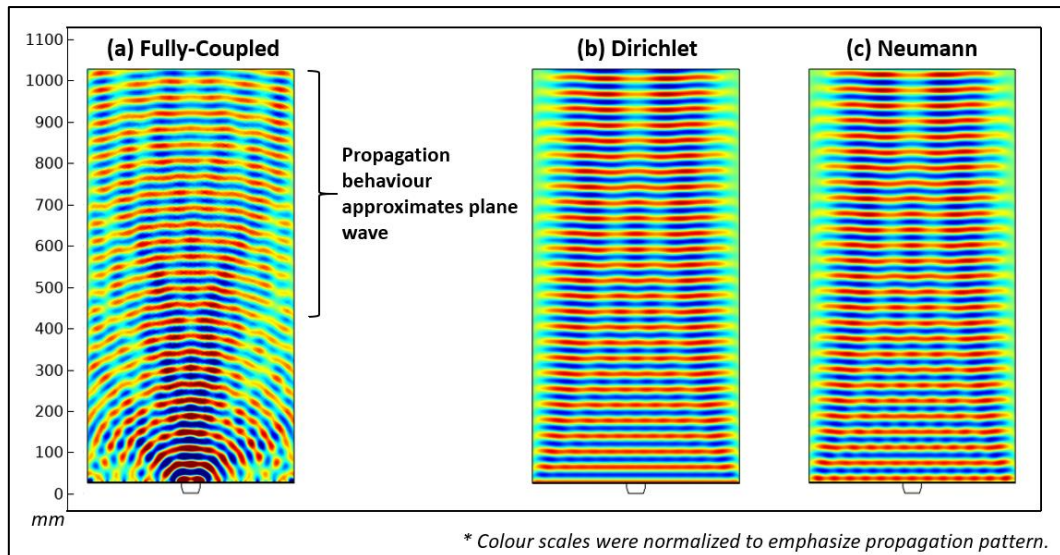


Figure 3.22: Acoustic pressure $P(r)$ simulated for three different methods of representing the vibrating wall: (a) solid-acoustic simulation; (b) Dirichlet pressure boundary; (c) Neumann pressure boundary.

The finding highlights the shortcoming of using boundary conditions. In particular, the cone-like propagation due to imbalances in displacement magnitude near the centre of the plate was not captured by the boundary conditions. Nevertheless, the result in Figure 3.22 considered a very specific plate-transducer configuration. Much of the research conducted within this work revolved around an ultrasonic bath with a hexagonal geometry. All six faces of the hexagonal sonoreactor used in this work were fitted with a transducer array. The investigation was extended to consider the suitability of boundary conditions for the hexagonal sonoreactor. The six walls of the hexagonal sonoreactor were measured to be exactly 140 mm in length. The orientation of the wall transducers was noted to be arranged with two units along the length, as shown in Figure 3.23 (a). The previous 2D plate-transducer model was modified to represent the wall of the sonoreactor, and the suitability of the Dirichlet boundary condition was studied by comparing the solution obtained from a full solid-acoustic coupling [Figure 3.23 (b)] to the simplified representation [Figure 3.23 (c)].

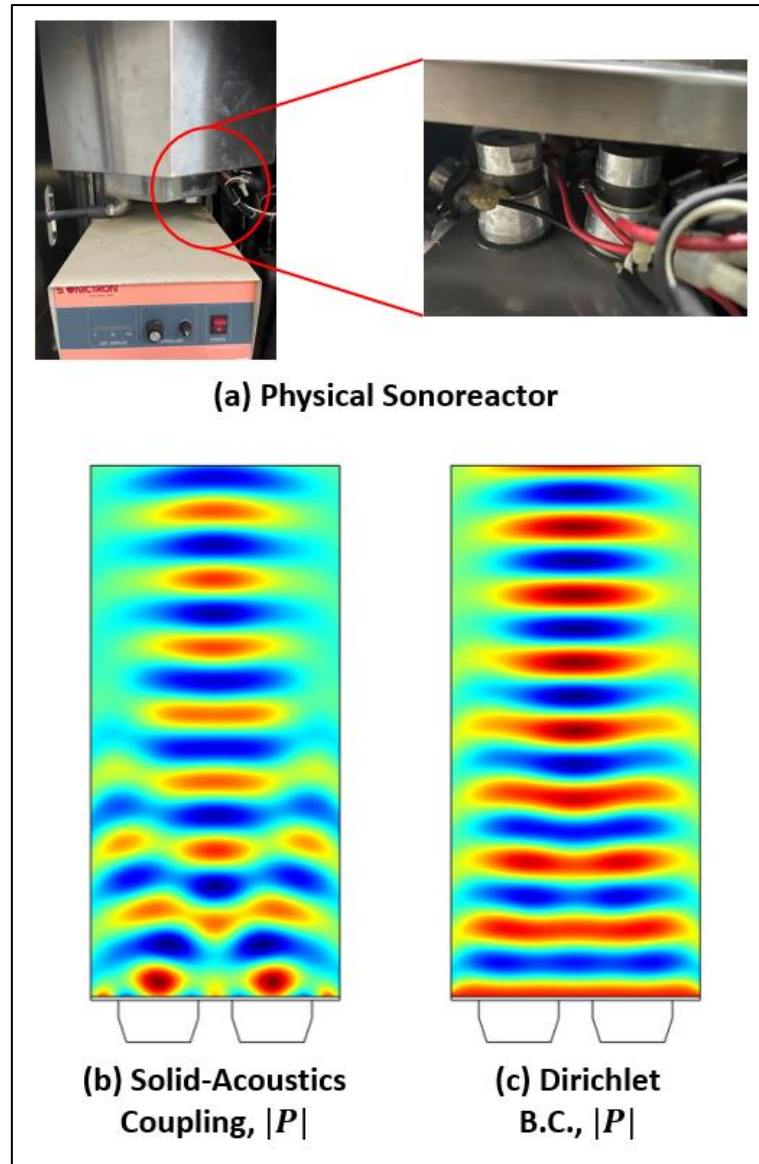


Figure 3.23: (a) Depiction of the transducers fitted for the hexagonal sonoreactor featured in this work; (b) Acoustic pressure simulation from full solid acoustics; (c) Acoustic pressure simulation using simplified Dirichlet boundary condition.

The comparison between Figure 3.23 (b) and (c) revealed similar characteristics in the predicted acoustic pressure field. This finding suggests that the Dirichlet boundary condition provides a good approximation of the propagation behaviour in the hexagonal sonoreactor, especially at the centre of the geometry. Based on this finding, the use of Dirichlet boundary condition to represent the vibrating wall in subsequent simulations can be justified.

3.2.4 Auxiliary Study: Numerical Effects and Level of Constraint

A short study was conducted to investigate the numerical behaviour of an edge shared by two different boundary conditions. A test geometry of a 2D square (30 mm sides) was solved using the pure-liquid Helmholtz model. The bottom boundary was partitioned into three 10 mm sections. The middle section was specified as an active boundary, with passive boundaries specified at the sides, as shown in Figure 3.24. Several permutations of boundary conditions were studied, and the numerical outcome was documented. An overtuned mesh was used similar to previous cases.

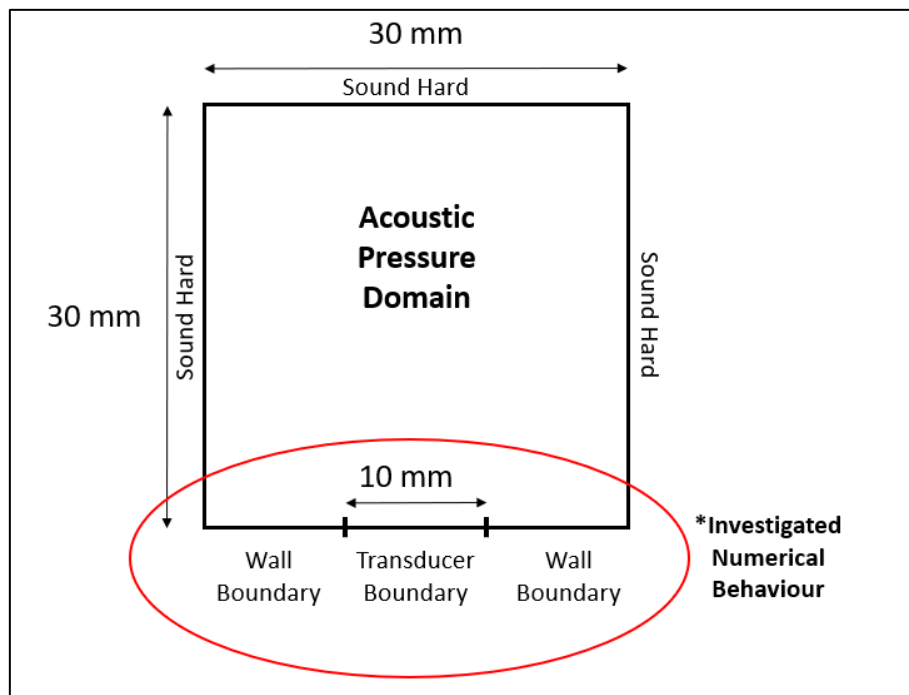


Figure 3.24: Graphical depiction of the simulation geometry for the boundary condition test.

The first combination considered the Wall Boundary as Dirichlet sound-soft conditions [Eqn. (79)] and the Transducer Boundary as Dirichlet pressure [Eqn. (67)] or Neumann displacement [Eqn. (75)] boundaries. An arbitrary pressure magnitude of 5 Pa was

used for the pressure specification. The pressure magnitude profile across the bottom boundary is plotted in Figure 3.25. In Figure 3.25 (a) and (b) the Wall Boundaries were strictly constrained to zero because of the constraint imposed by the sound-soft condition. The Neumann active boundary yielded a bell-shaped pressure distribution. Figure 3.25 (a), showed that the combination of two Dirichlet specifications resulted in numerical artifacts, which was hypothesised to be a discretisation error caused by numerical discontinuity. To test the claim, both the mesh and shape function were refined, and the results are plotted in Figure 3.26. The finer mesh reduced the size of the artifact [Figure 3.26 (a)], while the higher-order shape function (quintic) led to curve smoothing [Figure 3.26 (a)]. These observations confirmed the above hypothesis.

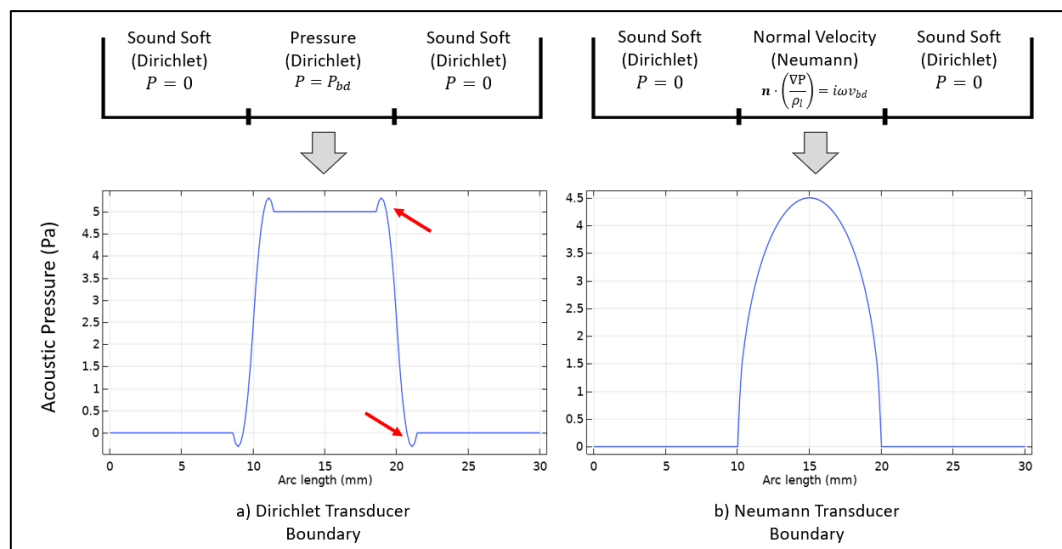


Figure 3.25: Simulation results when (a) Dirichlet and (b) Neumann transducer boundaries are paired with the sound-soft wall boundary.

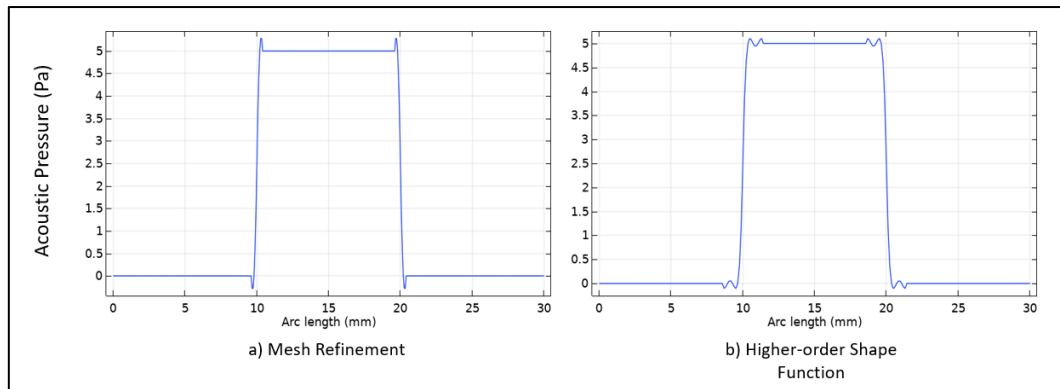


Figure 3.26: Methods to reduce discontinuity numerical error using: (a) mesh refinement; (b) higher-order shape functions.

A second permutation used sound-hard (Neumann) boundaries for the Wall Boundaries. Figure 3.27 (a) and (b) showed the less constrained sound-hard boundaries exhibiting nonzero acoustic pressure. Interestingly, the Neumann active boundary in Figure 3.27 (b) showed much lower magnitude than 5 Pa. It was hypothesised that this was the result of destructive interference by reflected waves. This was tested by simulating the test case using PML, eliminating internal reflection. The results in Figure 3.28 confirmed the hypothesis, and the peak was noted to be approximately 5 Pa. This result showed that the Neumann active boundaries can be affected by factors such as wave reflection.

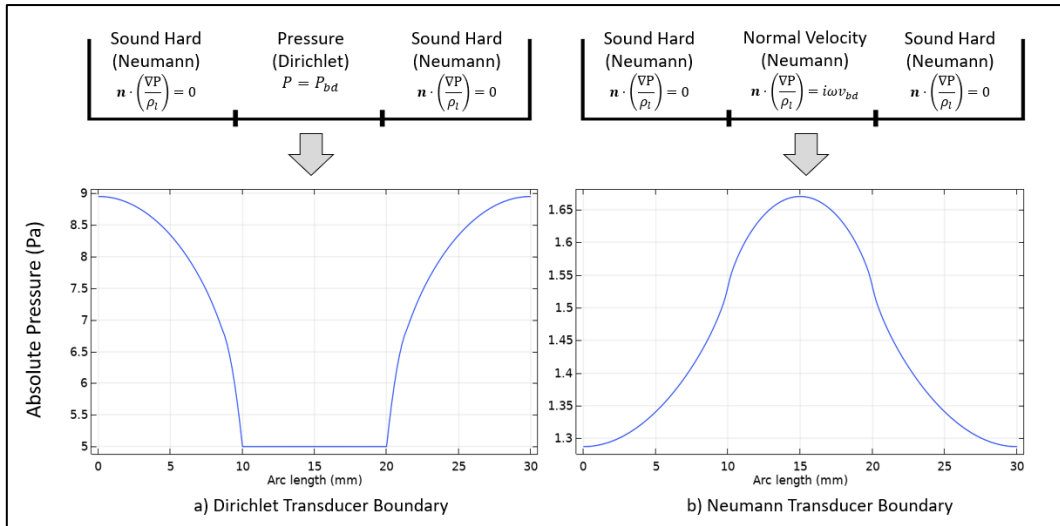


Figure 3.27: Simulation results when: (a) Dirichlet; (b) Neumann transducer boundaries are paired with the sound-hard wall boundary.

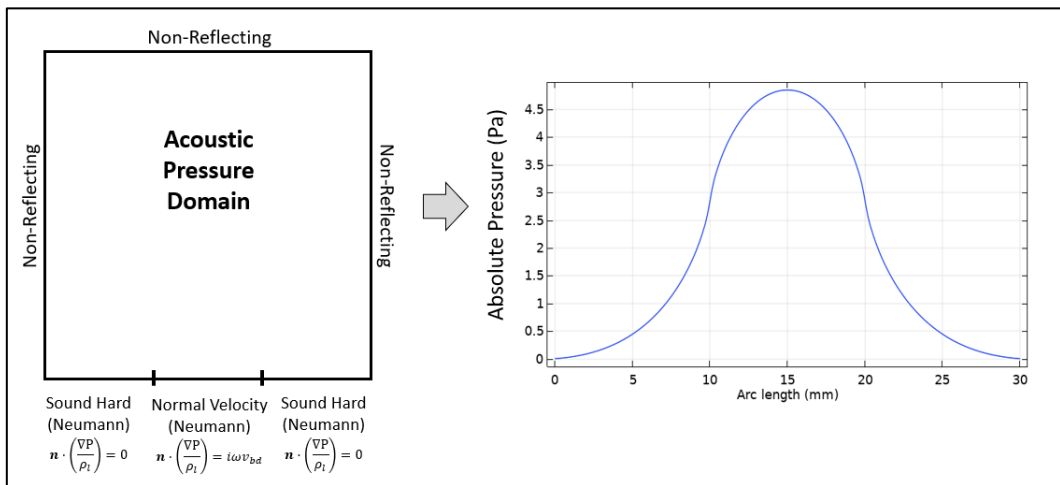


Figure 3.28: Results for the non-reflecting case. The Neumann pressure boundary resulted in a peak magnitude of nearly 5 Pa.

3.3 Concluding Remarks for Chapter 3

Chapter 3 presented two short case studies to address several uncertainties regarding the foundational aspects of sonoreactor acoustics modelling in FEM. The results were used to form the foundational aspects of subsequent simulation strategies.

In **Case Study 1**, the viability of frequency-domain acoustic solutions was investigated in terms of sonoreactor acoustics. In both the 1D and asymmetric 2D cases, frequency-domain solutions predicted similar antinode locations compared to time-domain models. However, slight differences in acoustic pressure magnitude prediction were observed. Further investigation confirmed that the differences were not caused by numerical error, but were instead the result of idealised simulation conditions. The results of Case Study 1 justified the use of frequency-domain models for sonoreactor acoustics. However, it was noted that only pure-liquid models were used in the comparisons. Future works should consider conducting the comparison using attenuated acoustic models and extend investigations to larger geometries in 3D. Another limitation of the current study was the lack of pressure magnitude validation. This should be addressed in future work using experimental measurements (e.g., hydrophone readings).

Case Study 2 presented a series of short investigations to address the selection of acoustic boundary conditions. Results showed that a full solid-acoustic coupling can result in significantly different solutions compared to the use of active boundary conditions. For the hexagonal sonoreactor used in this work, test cases had shown that the Dirichlet pressure boundary condition can be used to simplify the vibrating walls, and its effect on the solution is small if the region of interest was kept near the

centre of the geometry. The investigations also showed that the degree of constraint is a major consideration in the selection of boundary conditions. Dirichlet boundaries were able to strongly enforce specified conditions at the expense of limiting the solution space. On the contrary, the Neumann boundaries were found to be less constrained. Interestingly, test cases also showed that results solved using the Neumann active boundary exhibit inconsistent predictions based on the length of the geometry and discretisation parameters. The reason for this remains unclear and was left for future work.

Chapter 4: Validation of Acoustic Pressure Models

This chapter addresses the main research question by evaluating the performance of acoustic pressure models. Case Study 3 served as a pressure validation study for the pure-liquid and linear CP model in a bath-type sonoreactor. Case Study 4 investigated the effect of the geometry-wavelength ratio on qualitative antinode validation results. Lastly, an antinode validation study was conducted in Case Study 5 for the pure-liquid, linear CP and NH models using SCL images for a hexagonal bath-type sonoreactor.

4.1 Case Study 3: Pressure Magnitude Prediction in Large Sonoreactors

This case study evaluated the performance of acoustic pressure models for predicting the pressure magnitude in large ultrasonic baths. The results of the pure-liquid and linear CP models were compared with hydrophone measurements for a 252 L ultrasonic bath reported by Son et al. (2009). Due to difficulties in numerical convergence, only preliminary tests were done for the nonlinear CP and NH models.

4.1.1 Methodology

4.1.1.1 Acoustic Pressure Models

The pure-liquid model [Eqn. (12)] and the monodisperse linear CP model [Eqn. (23)] were used. The CP model was solved using an assumed equilibrium bubble radius of $R_0 = 5 \mu\text{m}$, based on past studies (Dogan and Popov, 2016; Louisnard, 2017). Three magnitudes of bubble density n of 1×10^{10} , 1×10^{11} , and $1 \times 10^{12} \text{ m}^{-3}$ were investigated to study their effects on the prediction of acoustic pressure. The range of investigated magnitudes also referenced past works (Jamshidi et al., 2012; Trujillo, 2020).

4.1.1.2 Description of the Physical System

The sonoreactor used for this study was modelled after the work of Son et al. (2009). Figure 4.1 illustrates the vertical bisection of the model. The system is an acrylic tank with dimensions of 1.2 m x 0.6 m x 0.4 m, fitted with a transducer array module (0.2 m x 0.2 m x 0.07 m). The inner walls were layered with polyurethane acoustic absorbents. During the experiment, a water level of 350 mm was maintained. With this information, a 3D representation shown in Figure 4.1 was constructed to serve as a reference for the simulation domain.

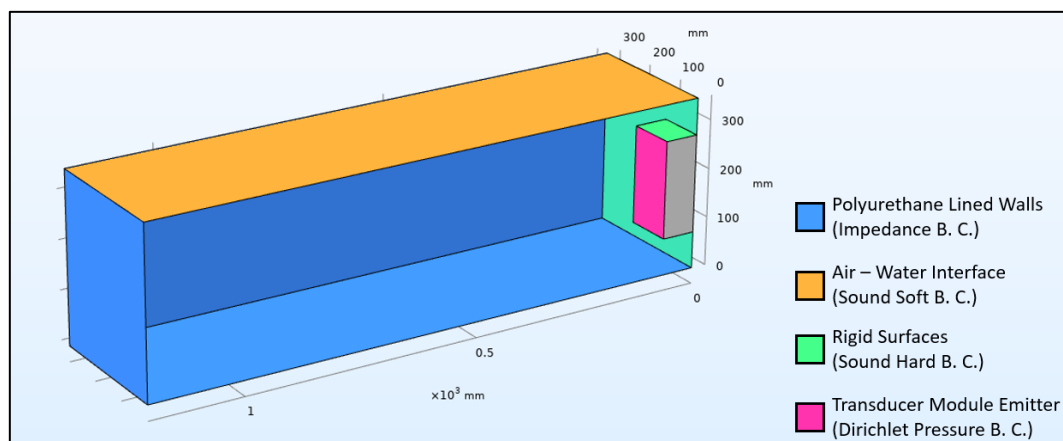


Figure 4.1: Bisection of the model for the physical system studied by Son et al. (2009).

The physical properties of water were assumed to be at standard values (25°C). The effect of temperature on the physical properties of the fluids was assumed to be negligible. The main reason lies with the large working volume (and thus heat capacity) of the sonoreactor. Properties of air were used to represent the gas content within the cavitation bubbles for the bubbly-liquid models. The relevant simulation parameters used in this study are summarised in Table 4.1. Based on extensive testing,

impedance boundary conditions were used to represent the polyurethane acoustic absorbers. The similar acoustic properties between polyurethane and water were used to numerically approximate the acoustic absorption. For the transducer pressure boundary, a Dirichlet pressure specification was used by taking the hydrophone reading 4 cm from the emitting surface. The Dirichlet transducer boundary condition differed for each frequency and is summarised in Table 4.2.

Table 4.1: Physical properties (25°C) used in Case Study 3.

Parameter	Value	Unit	Description
D_g	2.19×10^{-5}	m ² /s	Diffusivity of gas
c_l	1481	m/s	Speed of sound in water
c_{PU}	1520	m/s	Speed of sound in polyurethane
γ_g	1.41	-	Adiabatic index for air
μ_l	0.001	Pa.s	Dynamic viscosity of liquid
p_∞	101325	Pa	Ambient pressure around bubble
R_{gas}	8.3145	J/mol.K	Gas constant
ρ_l	997	kg/m ³	Density of liquid
ρ_{PU}	1050	kg/m ³	Density of polyurethane
σ_l	0.0725	N/m	Surface tension of liquid

Table 4.2: Dirichlet boundary condition magnitudes for each frequency.

Frequency (kHz)	35	72	110	170
Dirichlet Pressure Magnitude (bar)	2.71	3.87	1.98	0.46

4.1.1.3 2D Simulation Set-up

Preliminary simulations revealed that a full 3D investigation was not possible for the studied system, as memory requirements vastly exceeded the limitations of the computational set-up. Thus, 2D simulations were used to model the horizontal cross section of the sonoreactor. Figure 4.2 shows the simulation domain used in the 2D simulations and the corresponding boundary conditions. In terms of mesh considerations, default free-triangular meshes were used due to their flexibility and the well-optimised mesh generation algorithm. Default quadratic Lagrange shape functions were used, and adaptive meshing algorithms were not considered since wavenumbers are analytical for the linear models. The maximum mesh size was set to satisfy the condition in Eqn. (61). Based on the mesh refinement results, the restriction of 10 elements per wavelength was imposed. Figure 4.3 shows an example of the simulation mesh generated for the 35 kHz case.

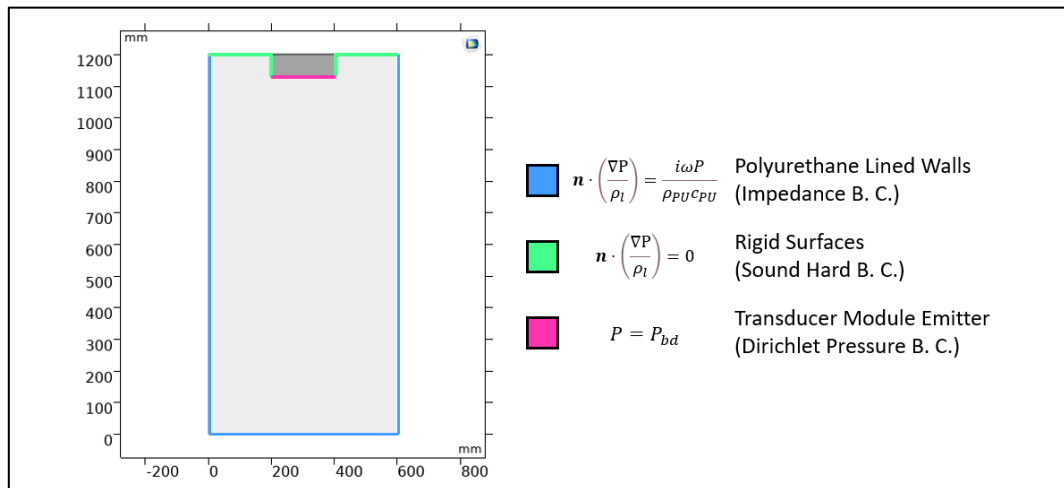


Figure 4.2: 2D representation of the simulated system taken as a horizontal cross-section of the sonoreactor.

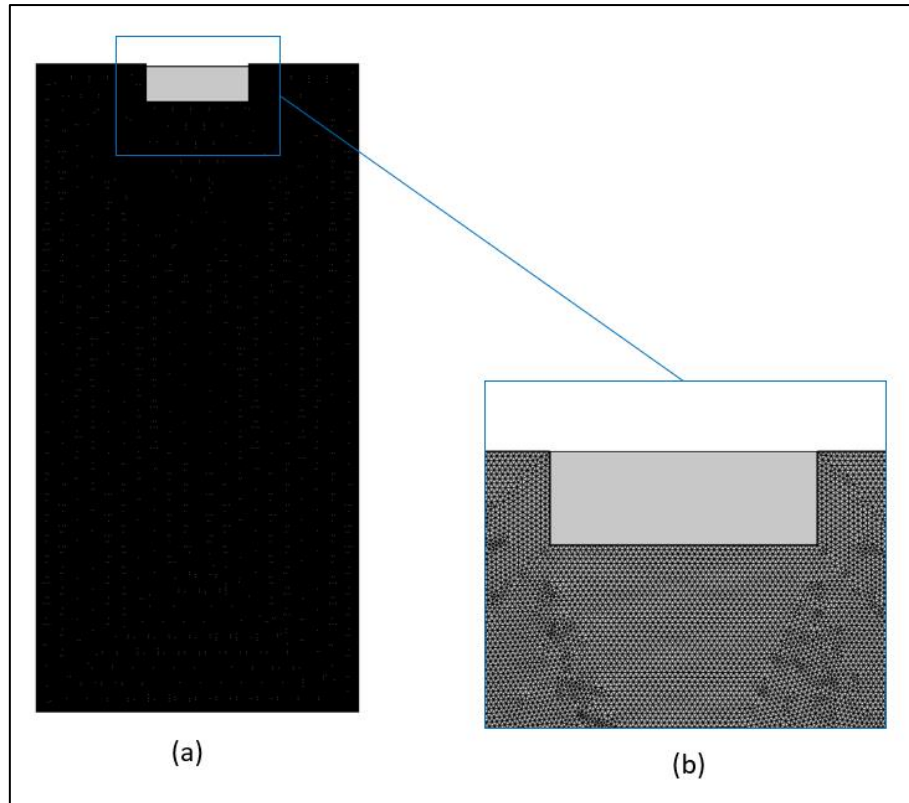


Figure 4.3: (a) Example of the triangular element mesh generated for the 35 kHz case; (b) Close-up of the mesh matrix.

4.1.2 Results and Discussion

For this study, it was observed that the RAM requirements for a full 3D simulation exceeded machine limits (64 GB) due to the very small mesh size and the large simulation geometry. Compared to published works in literature, the system involved in this validation study was noted to be the largest sonoreactor to be simulated. The largest reported 3D simulation conducted in literature was found to be a 10 L ultrasonic bath operating at 28 kHz (Tangsopa and Thongsri, 2019, 2021). In comparison, the system considered in this study was found to be approximately 252 L with frequencies up to 170 kHz. Even with conservative mesh settings and geometry optimisation measures, it was noted that there is insufficient RAM for the generation and storage of the meshed 3D model.

To represent the simulated system as a 2D model, it was assumed that the acoustic behaviour in the sonoreactor can be represented as plane waves. A notable limitation of this assumption is the loss of information by omitting a space dimension, notably the water-air interface and the floor boundary in Figure 4.1. However, the analyses in Figure 4.8 were used to support the plane-wave assumption. The results in Figure 4.8 showed that the reduced geometric reflection in the simulated geometry resulted in strong plane wave characteristics. Thus, it was assumed that a 2D simulation is sufficient to characterise the studied system.

It is imperative to comment on the data reported by Son et al. (2009). A detailed description allowed the system to be modelled with minimal uncertainties. The sonoreactor geometry also approximated a 1D waveguide; coupled with the use of acoustic absorbents, this reduced the effect of internal acoustic reflection. This was noted to be important, as it was known to cause uncertainties in hydrophone validation studies (Trujillo, 2020). Lastly, they provided comprehensive and uniformly spaced pressure readings that allowed a proper evaluation of the attenuation mechanisms in the acoustic pressure models.

4.1.2.1 Transducer Boundary Specification

The transducer module in the study by Son et al. (2009) was reported to consist of nine transducers in a square array with a total emitting area of 0.04 m^2 . The design power was reported to be 400 W while the experiments were carried out at 240 W. Initially, the transducer boundary condition was specified from the reported input power (240 W) using the acoustic intensity relation (Tiong et al., 2019):

(84)

$$P_{Tr} = \sqrt{\frac{2\rho_l c_l O_M}{A_{tr}}}$$

The parameter O_M represents the power input and A_{tr} is the total surface area of the pressure-emitting surface; both values were reported in the original study. The value of P_{Tr} was specified as the Dirichlet pressure boundary condition. However, a significant deviation from the experimental data was observed when following this approach. The method resulted in a pressure magnitude profile that was markedly lower than hydrophone measurements, even for the unattenuated pure-liquid model. This result showed that the boundary specification was inaccurate. The outcome was found to be plausible since the effects of resonance on the transducers, as well as mechanical and mismatch losses, were not considered in Eqn. (84). Therefore, it was decided that the Dirichlet boundary should instead be specified as the pressure magnitude that was measured 4 cm from the transducer surface. This required the assumption that the difference between the two is negligible. Figure 4.4 compares the 1D pressure field profile projected along the bisecting line for the 35 and 72 kHz cases solved using the pure-liquid model. The difference between the first approach (dashed line) and the second approach (solid line) was found to be obvious. The latter approach was chosen to circumvent any errors related to energy transfer between the transducer and the working fluid.

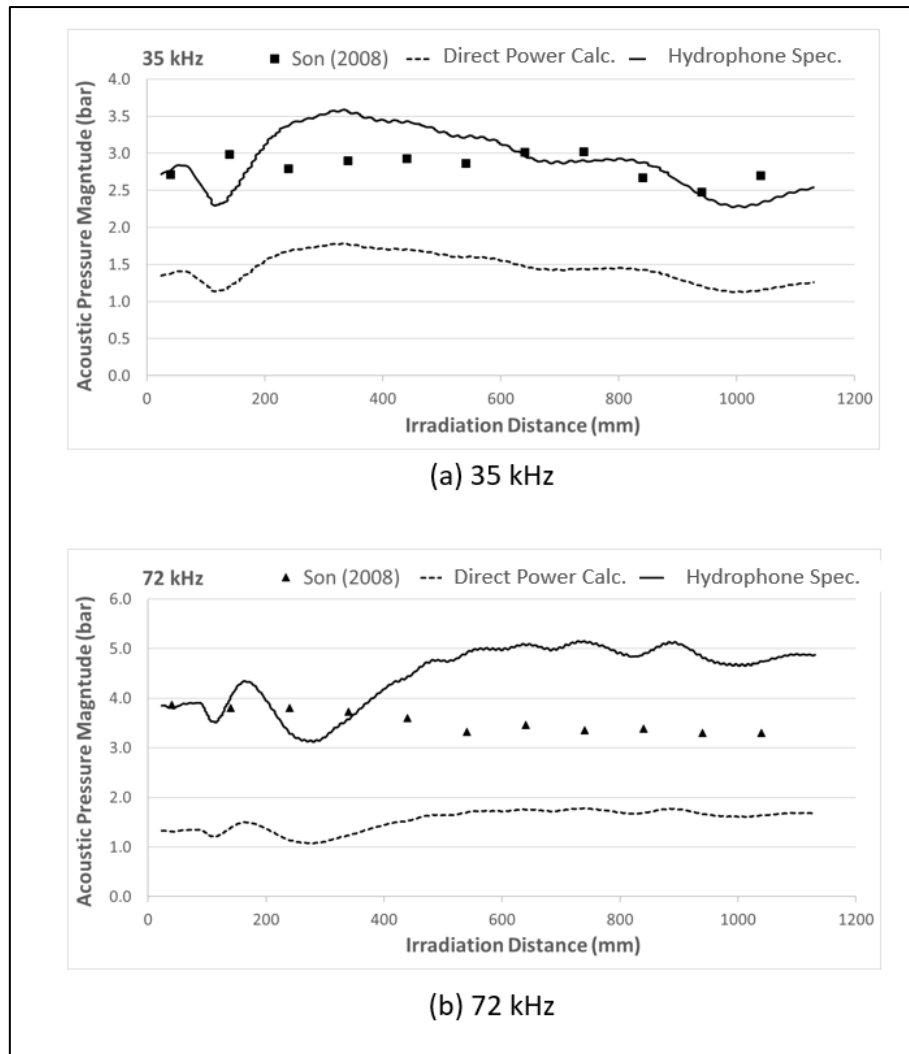


Figure 4.4: Comparison between power input calculation and hydrophone measurements for: (a) 35 kHz; (b) 72 kHz.

4.1.2.2 Mesh and Resource Requirements

Table 4.3 summarises the 2D meshes used for the four simulated frequencies. Mesh restrictions were specified based on acoustic properties of a pure liquid. For the same geometry, increasing the frequency by a factor of x was found to roughly increase the elements by a factor of x^2 in 2D and by x^3 in 3D. Considering that sonochemical research can reach frequencies up to 1 MHz (Leighton, 1994), this outlined a potential problem concerning mesh generation for high-frequency ultrasonic baths.

Table 4.4 compiles the time and memory requirements for several simulated cases. As expected, resource requirements increased with frequency as a result of finer meshes. It was also noted that the mesh generation algorithm was more resource intensive compared to the solvers for high-frequency cases (110 and 170 kHz).

Table 4.3: Summary of mesh information for four studied frequencies (pure-liquid simulations).

Frequency (kHz)	S_{mesh} [$N_{mesh} = 10$] (mm)	Num. of Elements	Min. Element Quality
35	4.23	100094	0.6127
72	2.06	450996	0.5773
110	1.35	1078087	0.5608
170	0.87	2643031	0.5454

Table 4.4: Solution times and memory requirements for simulated cases.

Model	Frequency (kHz)	Solution Time (s)	Physical Memory (GB)
Pure-Liquid Model	35	3	1.35
	72	15	3.31
	110	38	6.58
	170	106 [1m 46s]	14.31
CP Model ($n = 1 \times 10^{10}$)	35	3	1.49
	72	16	3.59
	110	41	6.8
	170	113 [1m 53s]	15.57

Figure 4.5 and Figure 4.6 show the results of mesh refinement for four bubble densities at 35 kHz (the pure liquid case has a bubble density of zero). The same study was repeated for all frequencies and yielded similar observations. The relative error converged around six elements per wavelength, coinciding with software recommendations that suggested a range of 6 – 10 for linear acoustics (COMSOL AB, 2018). For this study, 10 elements were used per wavelength. The linear CP model required a new mesh for each magnitude of bubble density because of a change in the effective phase speed c_{eff} . The meshing process was simple since the effective phase speed can be determined before the model was solved.

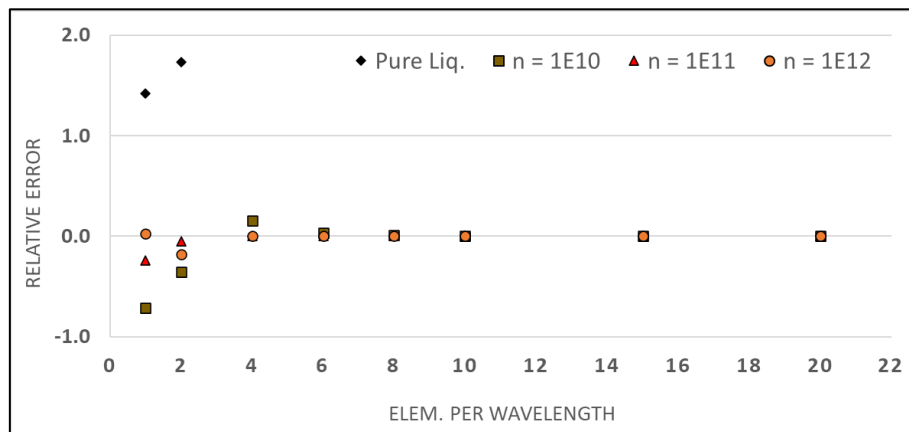


Figure 4.5: Mesh refinement results for the pure-liquid and linear CP model (35 kHz).

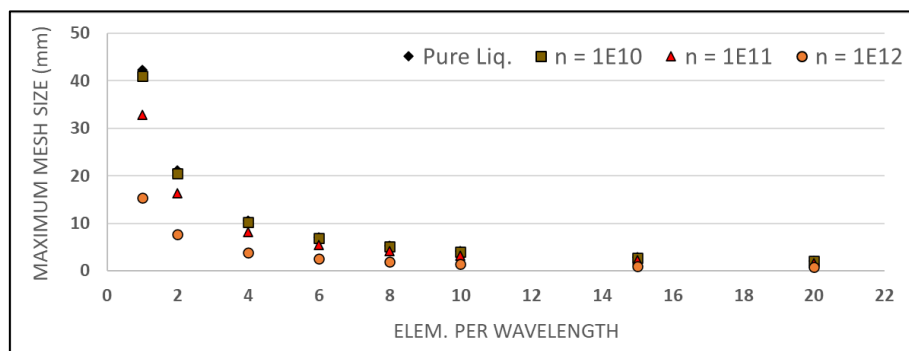


Figure 4.6: Maximum mesh sizes against the number of elements per wavelength (35 kHz).

4.1.2.3 Acoustic Pressure Field Results

The simulated pressure fields were analysed to investigate the behaviour of wave propagation and the distribution of acoustic magnitude. The former was evaluated using pressure plots $P(\mathbf{r})$, and the latter was evaluated using the pressure magnitude $|P(\mathbf{r})|$. Figure 4.7 shows the absolute pressure fields solved from the pure-liquid model for the four studied frequencies.

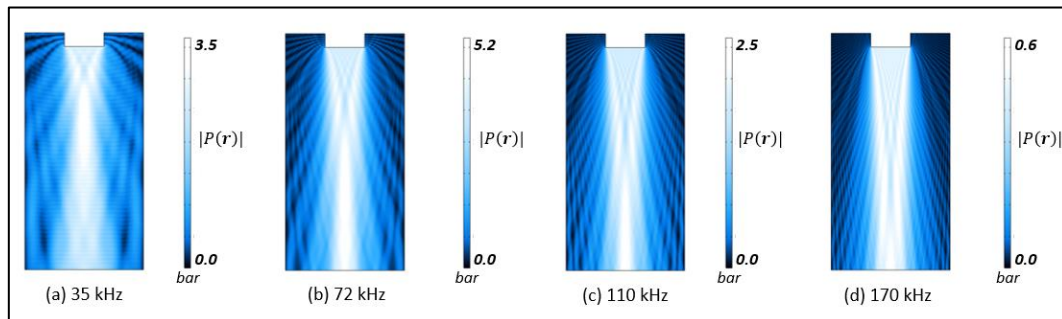


Figure 4.7: Absolute pressure for the four frequencies solved using the pure-liquid model.

Across all frequencies, a narrow, high-pressure region was observed along the centre of sonoreactor. Side-wall reflection was found to be weakly noticeable, especially for the two lower frequencies of 35 and 72 kHz. The short wavelengths relative to the geometry and the inhibition of standing waves by the impedance boundaries resulted in the lack of distinct standing wave formation. To further analyse the behaviour of the simulated wave, Figure 4.8 shows the plot of $P(\mathbf{r})$ and $|P(\mathbf{r})|$ for the 35 kHz case of the pure-liquid model. In Figure 4.8 (a), the propagation of the wave in the geometry was found to behave like a point source near the transducer and approximate a plane wave near the middle of the geometry. Figure 4.8 (b) shows that reflections near the side walls are discernible but not significant.

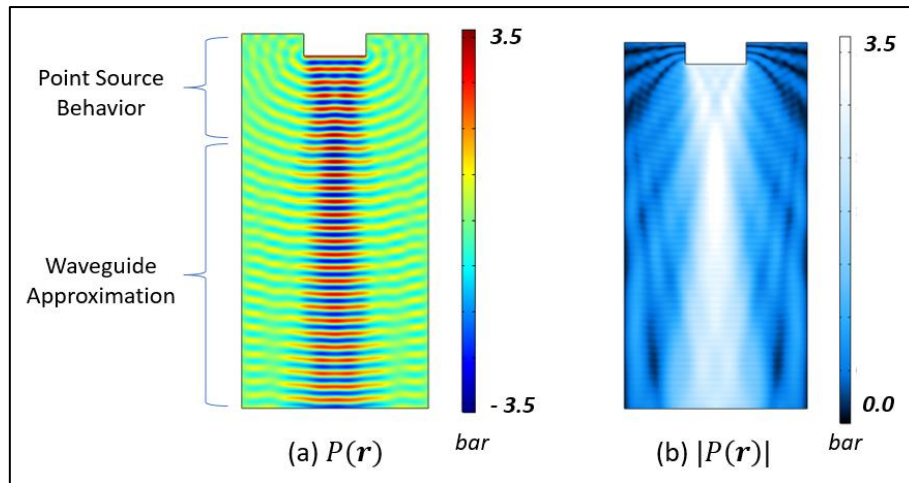


Figure 4.8: Pure-liquid model 35 kHz solution: (a) Acoustic pressure; (b) Pressure magnitude.

For comparison, the solutions obtained using idealised and perfectly reflecting wall boundaries are shown in Figure 4.9. Figure 4.9 shows the plot of $P(r)$ and $|P(r)|$ of the 35 kHz case, when the boundary conditions at the walls were replaced with the sound-hard and sound-soft boundary conditions, respectively. As expected, the sound-hard walls resulted in a drastic overprediction of the acoustic pressure magnitude (25 bar) in addition to exaggerated internal reflections, forming a highly geometric pressure field pattern.

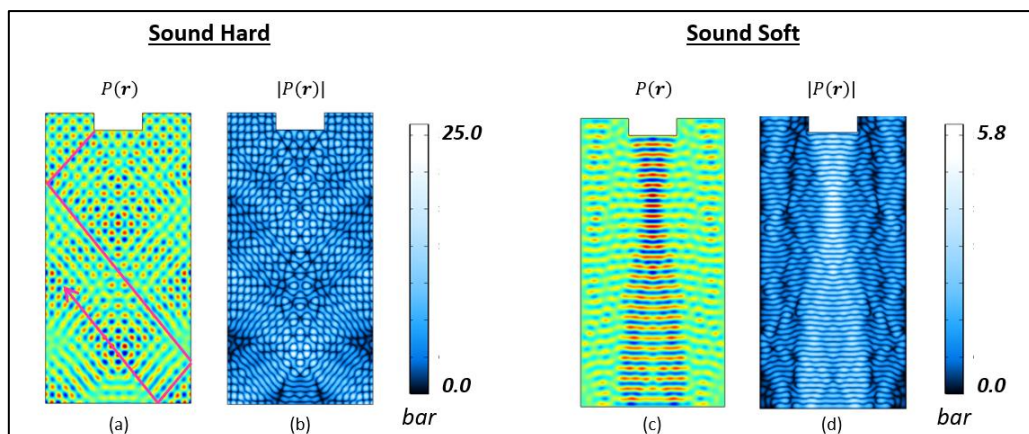


Figure 4.9: 35 kHz simulation using fully sound-hard and fully sound-soft boundary conditions: (a and c) acoustic pressure plot; (b and d) acoustic pressure magnitude plot.

Figure 4.9 highlighted potential errors when combining the unattenuated model with fully reflecting boundaries, which essentially resulted in waves that reflect internally without energy loss. Nonetheless, the sound-hard simulation was useful for visualising propagation patterns, depicted by the pink arrow in Figure 4.9 (a). This can be useful when analysing reflection effects. The reflection behaviour of the sound-soft walls was markedly different, despite also being a perfectly reflecting boundary. Surprisingly, the result solved using the sound-soft boundaries yielded a pressure field pattern similar to those in Figure 4.8. The sound-soft results also predicted higher maximum pressure compared to the impedance boundaries, albeit much less drastic than in the sound-hard case. Current observations suggest that this was caused by standing wave formation, as inferred from the more distinct antinode bands.

For the case of the linear CP model, Figure 4.10 shows the absolute acoustic pressure fields $|P(r)|$ for each frequency and bubble density. Several interesting observations were found. As expected, pressure magnitudes became increasingly attenuated with increasing bubble density. Attenuation also increased with frequency because bubbly liquids are dispersive mediums. However, the pressure fields of Figure 4.10 (b), (c), and (e) showed rather unexpected results. The simulations showed unrealistic pressure peaks, particularly in Figure 4.10(b) where the peak pressure magnitude is almost 30 bar. The prediction of such a large pressure magnitude was noted to be an interesting finding, since the linear CP model was expected to yield lower pressure magnitudes than those of the pure-liquid model, because of the consideration of bubbly-liquid attenuation. It was hypothesised that this was caused by the interaction between the effective phase speed, the geometry, and the wall reflections. To confirm the hypothesis, several tests were performed and discussed in the following section.

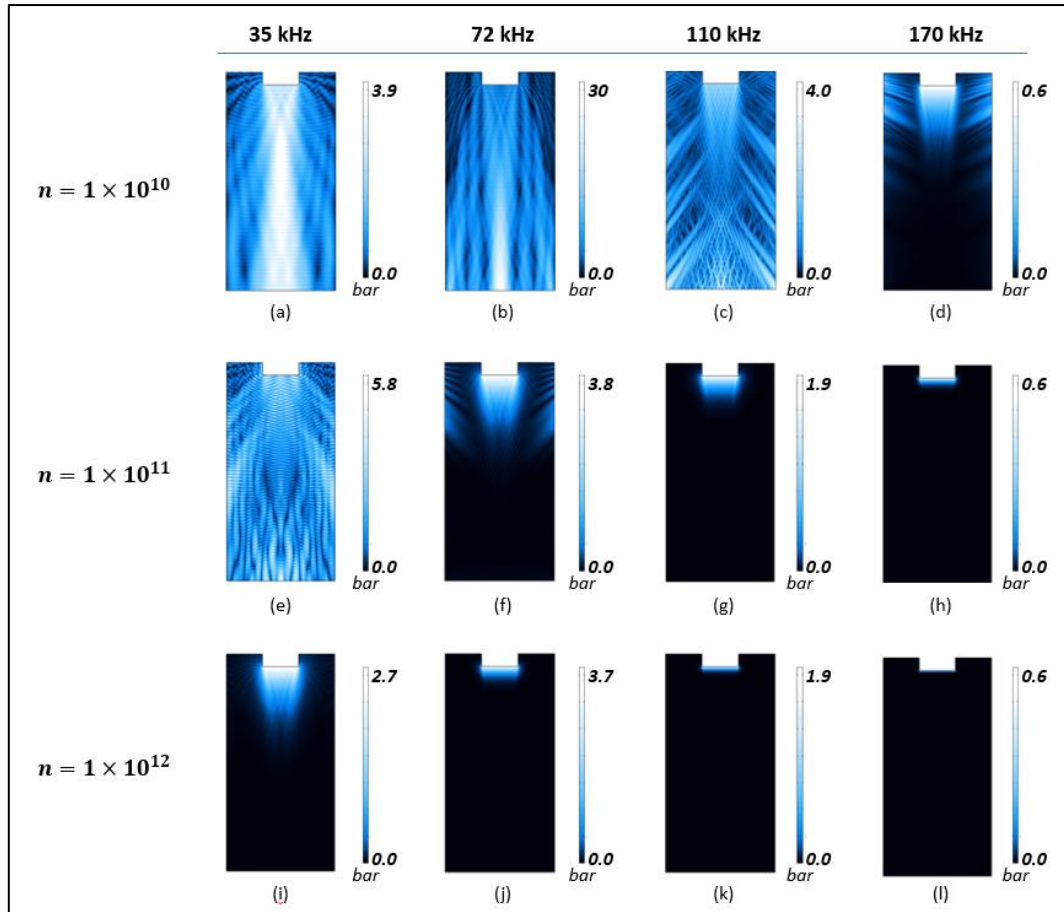


Figure 4.10: Compilation of the acoustic pressure magnitude plots $|P|$ for the linear CP model.

4.1.2.4 Effect of Reflection on Acoustic Pressure Prediction

The abnormal results in Figure 4.10 suggested that wave reflection may have been incorrectly modelled. This brought the suitability of the boundary conditions into consideration. The impedance boundary condition was used to model the acoustic absorbers because it was able to account for weak reflection effects. In classical acoustics, the energy transmission of an incident wave at an interface between two acoustic mediums can be described using the reflection coefficient R_{ac} calculated from the specific acoustic impedance Z (Ginsberg, 2018):

$$R_{ac} = \left(\frac{Z_2 - Z_1}{Z_2 + Z_1} \right)^2 = \left(\frac{\rho_2 c_2 - \rho_1 c_1}{\rho_2 c_2 + \rho_1 c_1} \right)^2 \quad (85)$$

For a pure liquid, the reflection coefficient calculated from the properties listed in Table 4.1 yielded $R_{ac} = 0.15$, which suggests a weakly-reflecting boundary. However, an important caveat of using the impedance representation is that changes in the acoustic properties of the working fluid would change the reflection coefficient. Since the linear CP model is analytical, the effective phase speed for bubbly liquids modelled using different bubble densities was directly tabulated in Table 4.5. With reference to the predicted c_{eff} , it can be shown that the effective phase speeds decreased with increasing bubble densities and frequencies. This would increase the reflection coefficient calculated from Eqn. (85), which was noted to be a plausible explanation for the increased reflection behaviour observed in Figure 4.10 (b) and (e).

Table 4.5: Bubbly-liquid phase speed and attenuation compared with calculated attenuation values of Son. et al. (2009).

n (m^{-3})	35 kHz		72 kHz		110 kHz		170 kHz	
	c_{eff} (m/s)	α (Np/m)	c_{eff} (m/s)	α (Np/m)	c_{eff} (m/s)	α (Np/m)	c_{eff} (m/s)	α (Np/m)
1×10^{10}	1434.5	0.25	1434.1	1.12	1433.5	2.86	1432.1	8.86
1×10^{11}	1149.6	2.02	1147.2	8.97	1142.7	22.84	1129.7	70.24
1×10^{12}	537.1	9.46	533.7	41.84	527.56	106.00	507.9	321.79
Son et al.	-	0.10	-	0.18	-	0.23	-	-

Results also showed that the maximum pressure predicted by the case with $n = 1 \times 10^{11} \text{ m}^{-3}$ in Figure 4.10 (e) was higher than the case with $n = 1 \times 10^{10} \text{ m}^{-3}$ in Figure 4.10 (a). The result contradicted expectations as higher bubble densities would yield greater attenuation and thus lower pressure magnitudes. It was suggested that the increase in pressure magnitude due to magnified reflection effects was more dominant than the increased attenuation in Figure 4.10 (e). This would mean that the effect of impedance mismatch may also be present in other cases; however, due to the much larger attenuation, the acoustic wave lost most of its energy before wall reflection and constructive interference effects can become significant.

The effect of bubble density on effective density was also considered. Theoretical estimates suggested insignificant differences since the bubble fractions were low. The effective medium density can be approximated from mixture laws assuming that the bubble distribution is uniform (Wijngaarden, 1972):

$$\rho_{eff} = \rho_l(1 - \beta) + \rho_g\beta \quad (86)$$

Table 4.6 plots the change in bubble density for the investigated cases. It is shown that bubbly-liquid density was virtually unchanged for all cases.

Table 4.6: Effective bubbly-liquid density for each bubble density.

$n \text{ (1/m}^3\text{)}$	Bubble vol. fraction, $\beta \text{ (m}^3\text{/m}^3\text{)}$	Effective liq. Density, $\rho_{eff} \text{ (kg/m}^3\text{)}$	$\frac{\rho_l - \rho_{eff}}{\rho_l} \times 100 \text{ (\%)}$
1×10^{10}	4.191×10^{-8}	9.971×10^2	4.181×10^{-6}
1×10^{11}	4.191×10^{-7}	9.971×10^2	4.181×10^{-5}
1×10^{12}	4.191×10^{-6}	9.971×10^2	4.181×10^{-4}

To confirm that the deviation in Figure 4.10 was a consequence of wall reflection and not caused by the acoustic pressure model, additional simulations were solved for the 72 kHz, $n = 1 \times 10^{10} \text{ m}^{-3}$ case [Figure 4.10(b)]. In one simulation, the impedance boundary conditions were specified to match the acoustic properties of the medium calculated in Table 4.5 and Table 4.6. Theoretically, this would yield no reflection with $R_{ac} = 0\%$ [Eqn. (85)], and minimise the impedance mismatch to eliminate reflection problems. The result of this simulation is shown in Figure 4.11. Interestingly, it was observed that even with a perfectly matched impedance, the simulation still predicted an unrealistic maximum acoustic magnitude prediction of 16 bar. Scrutiny of the high-magnitude regions in Figure 4.11 (c) revealed that the highest pressures were found near the opposing wall. This result suggested that there is a local standing wave caused by wave reflections. Furthermore, the conical shape of the high-pressure region and the distinct wall reflection identified in Figure 4.11 (c) strongly showed that perfectly tuning the impedance did not result in fully eliminating the reflection effects.

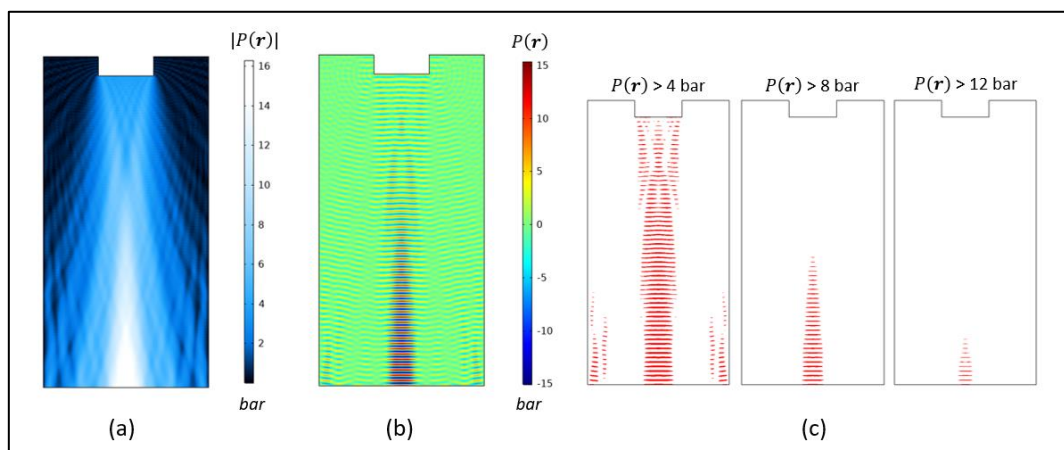


Figure 4.11: 72 kHz CP model with $n = 1 \times 10^{10} \text{ m}^{-3}$: (a) Absolute acoustic pressure; (b) Acoustic pressure; (c) Regions above the pressure magnitude threshold.

This finding suggested that Eqn. (85) is not an accurate measure for reflecting walls in the numerical solution. Findings in literature confirmed this claim, as the problem of acoustic scattering in unbounded (non-reflecting) domains remains one of the largest challenges in numerical wave modelling in the past few decades (Thompson, 2006). It was found that the use of impedance matching in numerical models is not an effective strategy to eliminate boundary reflection effects in 2D problems (Johnson, 2010). This explains the results observed in Figure 4.11.

This study also considered PML to model idealised non-reflecting behaviour at the absorbent boundaries. The PML region was specified as a 10 cm thick layer on the inner surface of the reactor walls to represent perfect acoustic absorbents. The modified simulation domain and the resulting mesh are shown in Figure 4.12. The PML mesh was set at 10 layers as shown in Figure 4.12 (b). Default PML settings were found to be sufficient based on the software manual for frequency-domain solutions (COMSOL AB, 2018). The polynomial coordinate stretching method was selected and the PML scaling factor and curvature parameter were set to 10 and 1 respectively.

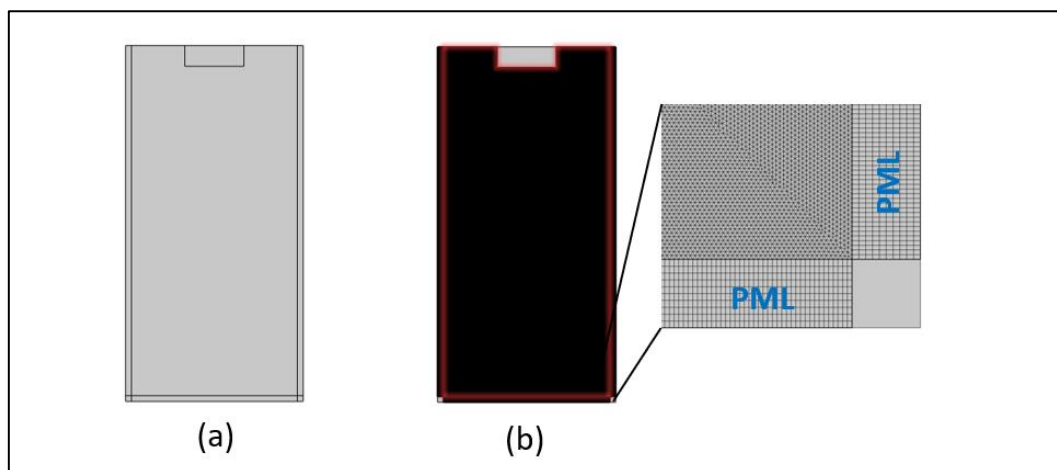


Figure 4.12: (a) Simulation geometry for the PML case; (b) Mesh generation for PML.

Figure 4.12 shows the results of simulating the 72 kHz, $n = 1 \times 10^{10} \text{ m}^{-3}$ CP model using PML. The resulting pressure field was markedly different from the previous approaches. The PML completely eliminated the problem of unrealistic pressure magnitudes and managed to produce a propagation pattern comparable to that of a point source in an infinitely far field, as shown in Figure 4.12 (b). The unrealistic pressure magnitude from previous predictions was not observed. This strongly proves that previous deviations were caused by reflection phenomena. Scrutiny on Figure 4.13(b) revealed that only the rigid back wall shows slight reflection.

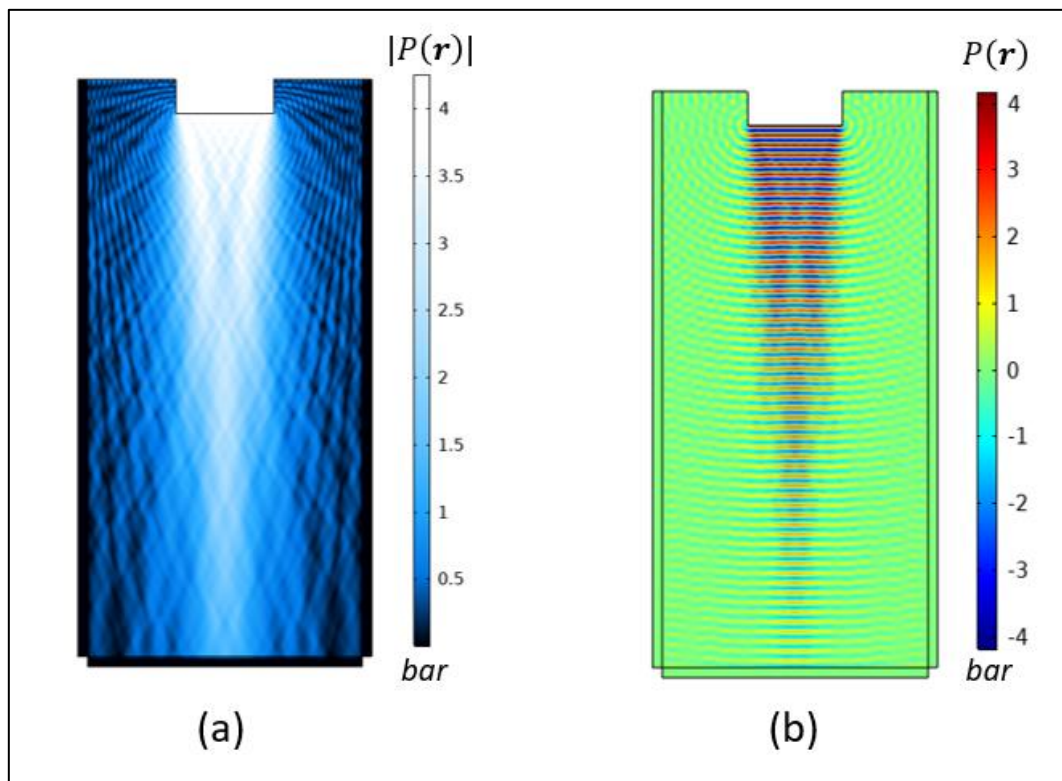


Figure 4.13: 72 kHz CP model with $n = 1 \times 10^{10} \text{ m}^{-3}$ simulated using perfectly matched layers (PML): (a) Acoustic pressure magnitude plot; (b) Acoustic pressure plot.

Figure 4.14 compares the axial acoustic pressure magnitude profile bisecting the geometry for the PU-impedance case, the impedance matching case (tuned

impedance), and the PML case with the empirical measurements. The circled region denotes the artificial attenuation of the PML region. Although it can be argued that the PML case best agreed with empirical measurements, it should be noted that the y-axis was skewed by the unrealistic values predicted by the other two cases. An interesting observation was noted when analysing the pressure profiles predicted by the PU-impedance case and the tuned impedance case in Figure 4.14. Both profiles were noted to be similar, but with an increasing deviation with distance travelled. This result showed that the effects of boundary reflection ‘accumulate’ along the geometry with increasing distance from the transducer. This can be used to explain the observation presented in Figure 4.11 (c), which showed that the highest pressure regions were found near the end of the geometry. With reference to Figure 4.14, the tuned-impedance case exhibited a lower reflection coefficient than the PU-impedance case, which led to a lower accumulation of reflection effects along the geometry.

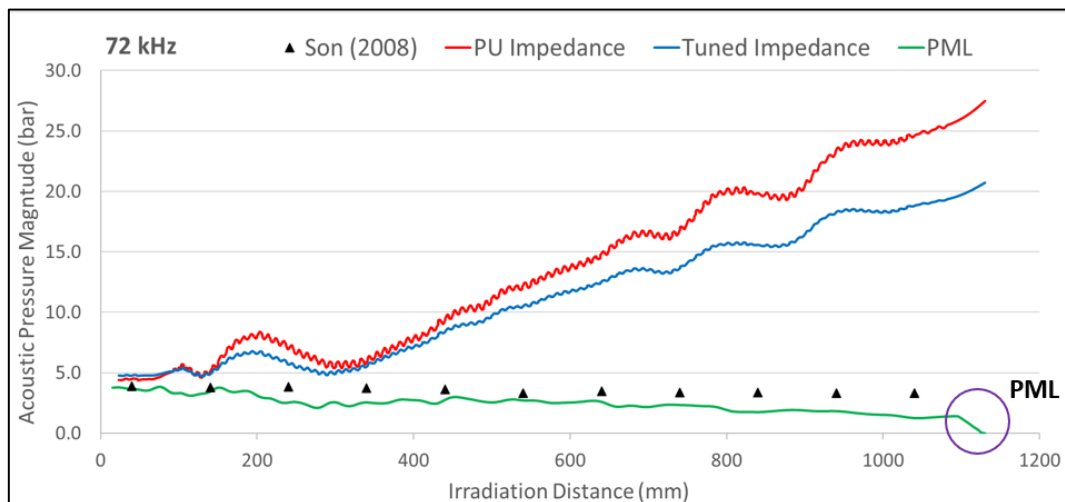


Figure 4.14: Comparison of acoustic pressure magnitude profiles for three boundary conditions against hydrophone measurements, solved for CP, $n = 1 \times 10^{10} \text{ m}^{-3}$.

It was noted that the strong reflection effects were mainly observed in the 72 kHz, $n = 1 \times 10^{10} \text{ m}^{-3}$ case. Nevertheless, the above observations revealed a key consideration for the modelling strategy. If the acoustic absorbents implemented in the physical system of Son et al. (2009) were perfect, then PML can be a viable approach. However, hydrophone measurement results showed otherwise, and that conditions enforced by the PML were too ideal to approximate the real system. When applied to other simulation cases, it was noted that the PML approach clearly underestimated the pressure profiles. Figure 4.15 shows an example for the 35 kHz pure-liquid case. Even with no explicit attenuation, the magnitude calculated by the pure-liquid model was found to be significantly lower than the empirical data. This finding strongly suggests that there is still a significant degree of reflection in the physical experiments, even with the use of acoustic absorbents. Thus, wall reflections should not be completely neglected in the simulations.

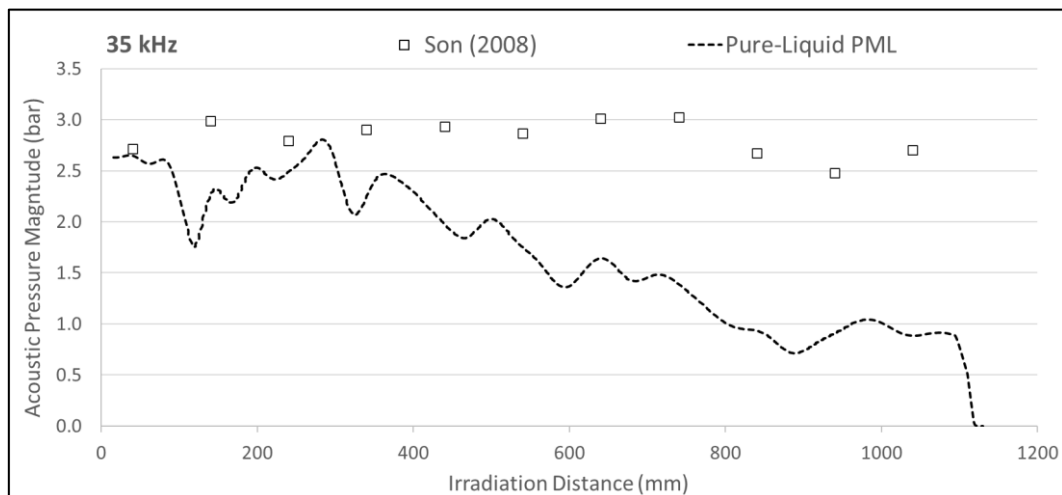


Figure 4.15: The results of the 35 kHz pure-liquid case simulated using PML to represent the absorbent boundaries against hydrophone measurements.

The comprehensive discussion on absorbent boundaries highlighted an important limitation for this investigation and possibly other validation studies. This limitation was caused by the inability to perfectly model the reflection effects in the simulation. Interestingly, similar studies in the past only briefly considered the issue of boundary reflections on the accuracy of pressure verification (Louisnard, 2012a; Trujillo, 2020). It was speculated that the uncertainties caused by reflection behaviour were less obvious in smaller geometries. It can be argued that the issue of reflection becomes significantly important at large scales due to the interaction between model geometry and standing wave behaviour. This topic shall be discussed in-depth in Case Study 4.

Extensive investigation of the various methods of modelling the absorbent boundaries in the simulations showed that the PU-impedance approach can cause a slight overprediction for certain cases, whereas PML vastly underestimated wall reflections. For subsequent acoustic pressure verification in this case study, the simulations were solved using the PU-impedance approach outlined in the methodology in Section 4.1.1.3. It was acknowledged that this introduces a degree of uncertainty into the pressure verification results. However, the approach was found to be the best compromise between perfectly reflecting boundaries and PML. In light of the limitations discussed, it should be noted that the validation results are strictly qualitative, but extremely valuable for an understudied area of sonoreactor acoustics.

4.1.2.5 Pressure Magnitude Validation for Linear Models

The measurements of Son et al. (2009) were reported in terms of pressure intensity I_{ac} (W/m²) to study cavitation activity. In this study, the measurements were converted into acoustic pressure magnitudes using Eqn. (87).

$$I_{ac} = \frac{|P|^2}{2\rho_l c_l} \quad (87)$$

Since the acoustic pressure models are linear, the use of the Dirichlet pressure boundary at the transducer normalised any errors introduced by hydrophone dimensions. Son et al. (2009) noted that the size of the probe exceeded the studied wavelengths, which led to measurements being taken as spatial averages. This effect was artificially introduced into the simulation results by plotting the simulated pressure profiles as a rolling average based on the diameter of the probe.

Analysis of pressure field validation results can be separated into low-frequency cases (35 and 72 kHz) and high-frequency cases (110 and 170 kHz). The data of Son et al. (2009) showed very little attenuation for the low-frequency cases, while the high-frequency cases showed obvious propagation losses. Figure 4.16 plots the simulation results of the 35 kHz system, where the pure-liquid model and the $n = 1 \times 10^{10} \text{ m}^{-3}$ CP simulation predicted pressure magnitudes that compared well with the empirical data. The results were found to be interesting for two reasons. First, the results of the pure-liquid model exhibited remarkable agreement with the empirical measurements. It showed the best agreement of all 35 kHz cases, with an averaged relative error of 11 % from the hydrophone measurements. This was found to be surprising, as the general consensus in recent research suggests that the pure-liquid model is unsuitable for

sonoreactor analysis, as it was noted to overpredict the pressure magnitude (Jamshidi et al., 2012; Louisnard, 2012a; Sarac et al., 2020).

This unexpected performance of the pure-liquid model can easily be explained. The low bubbly-liquid attenuations reported by Son et al. (2009) suggest that the physical system approximated pure-liquid behaviour. Past studies often analysed the pure-liquid model in conjunction with idealised boundaries (Tudela et al., 2014), which led to unrealistic pressure magnitudes, as in Figure 4.9. In this study, the weakly reflecting impedance boundary circumvented the infinitely reflecting behaviour. Essentially, the good agreement of the pure-liquid model can be attributed to the low bubble attenuation in the studied system, and the minimised reflection behaviour at the wall boundaries. This main implication of this finding is that the viability of the pure-liquid model could be reconsidered. Given the correct conditions (low frequency, low bubble fraction and minimal reflection behaviour), the model can be a viable alternative for a quick and simple analysis.

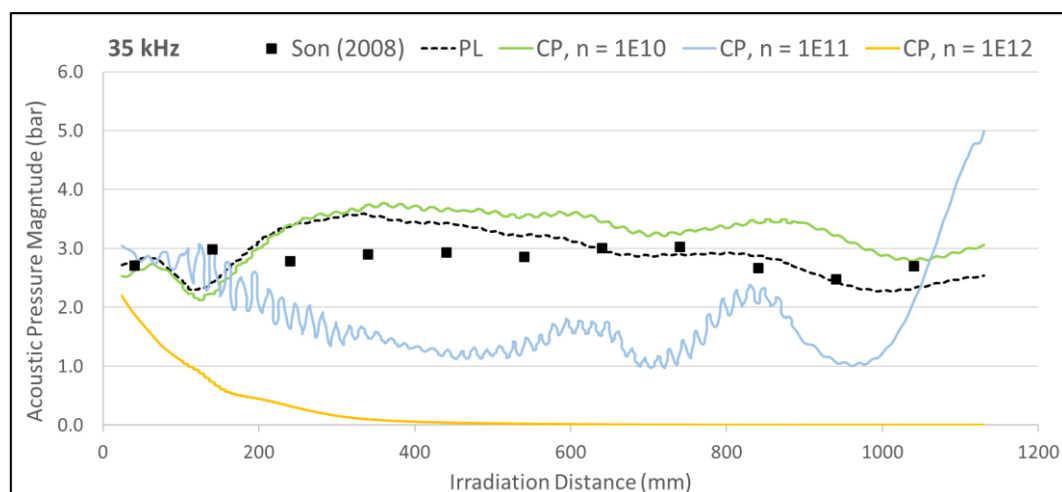


Figure 4.16: Absolute pressure comparison for the 35 kHz case against hydrophone measurements.

Figure 4.16 also shows that the linear CP model with $n = 1 \times 10^{10} \text{ m}^{-3}$ predicted on average a higher acoustic pressure magnitude over the pure-liquid model. This was unexpected considering that the attenuation of the linear CP model was higher. The results in Section 4.1.2.4 suggest that this was caused by increased reflection effects from impedance mismatch. Despite the slight deviation, the linear CP model managed to provide a relatively good approximation for hydrophone measurements at $n = 1 \times 10^{10} \text{ m}^{-3}$, with an averaged relative error of 19 %. On the other hand, the cases of $n = 1 \times 10^{11}$ and $1 \times 10^{12} \text{ m}^{-3}$ overestimated the attenuation, resulting in averaged relative error values of 38 and 90 %, respectively.

Part of the results for the 72 kHz system was discussed in the previous section. In particular, the unphysical overprediction in the simulation using the CP model at $n = 1 \times 10^{10} \text{ m}^{-3}$ resulted in a large averaged relative error of 281 %. Figure 4.17 compares the pressure profile for all simulated cases. Observations were found to be similar to 35 kHz simulations, where the pure-liquid model showed good agreement with hydrophone data at around 30 % averaged relative error, while the CP models show significant deviation due to wall reflection. Once again, the values of $n = 1 \times 10^{11} \text{ m}^{-3}$ and $n = 1 \times 10^{12} \text{ m}^{-3}$ overpredicted the attenuation behaviour of the system and resulted in a significant deviation from the hydrophone measurements (89 and 98 % relative error, respectively). It was noted that the pure-liquid model exhibited a markedly larger overprediction compared to the 35 kHz case. This trend was found to continue with increasing frequency, since the lack of attenuation in the pure-liquid approach would not be able to account for the dispersive nature of the system.

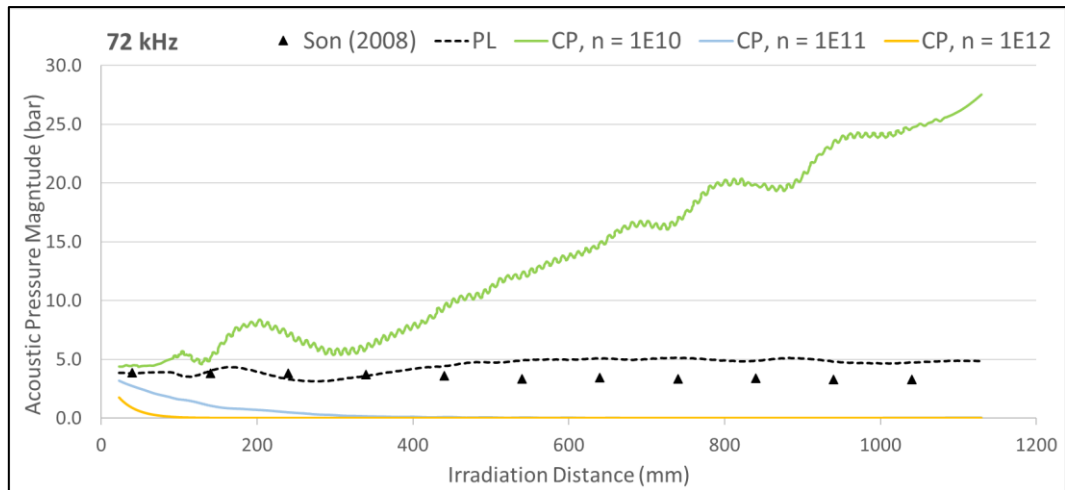


Figure 4.17: Absolute pressure comparison for the 72 kHz case against hydrophone measurements.

In the 110 and 170 kHz cases shown in Figure 4.18 and Figure 4.19, hydrophone measurements indicated clear attenuation behaviour. Thus, it was not surprising that the pure-liquid model overpredicted the pressure profile due to the lack of attenuation. In general, attenuation varies linearly to the square of frequency (Fox and Rock, 1941) and becomes more significant at higher frequencies. The results yielded 326 % and 96 % averaged relative error values for 110 and 170 kHz, respectively. For 110 kHz, the CP, $n = 1 \times 10^{10} \text{ m}^{-3}$ case showed remarkable agreement in the first half of the geometry, while a severe deviation was observed in the second half. If only the first half of the geometry was considered, simulations managed to yield very good agreement with an averaged relative error of 8 %; however, the large deviations at the end of the geometry caused the error to increase to 126 %. This was likely caused by uncertainties related to internal reflection. This claim is supported by the propagation pattern shown in Figure 4.9 and Figure 4.11, which showed that reflection effects tend to concentrate at the end of the geometry.

The cases for $n = 1 \times 10^{11} \text{ m}^{-3}$ and $n = 1 \times 10^{12} \text{ m}^{-3}$ underpredicted of the pressure magnitude (avg. relative error of 96 and 99 %, respectively). For the 170 kHz case, the pure-liquid model markedly overpredicted the pressure profile with an averaged relative error of 96 %. The three bubble densities studied for the linear CP model also performed poorly with averaged relative errors of 84, 88 and 100 %, respectively.

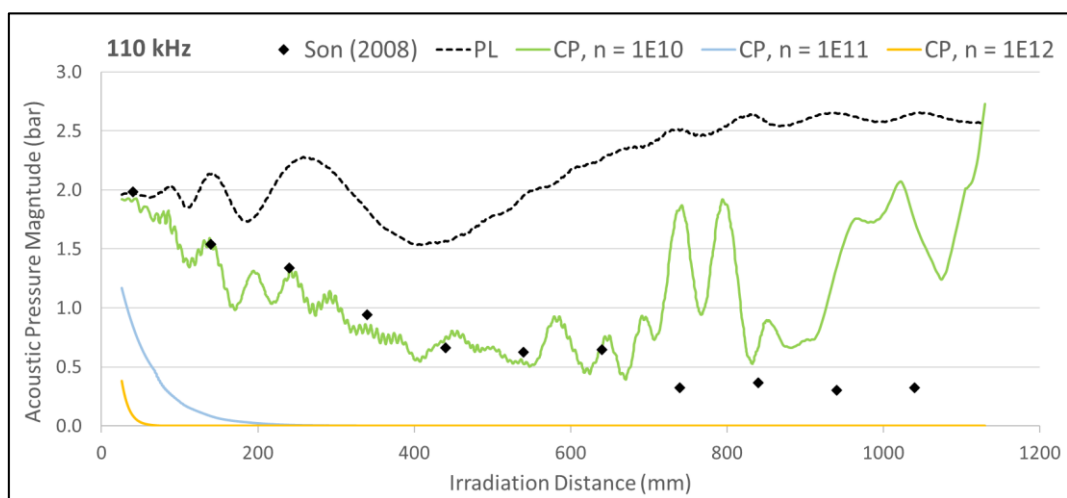


Figure 4.18: Absolute pressure comparison for the 110 kHz case against hydrophone measurements.

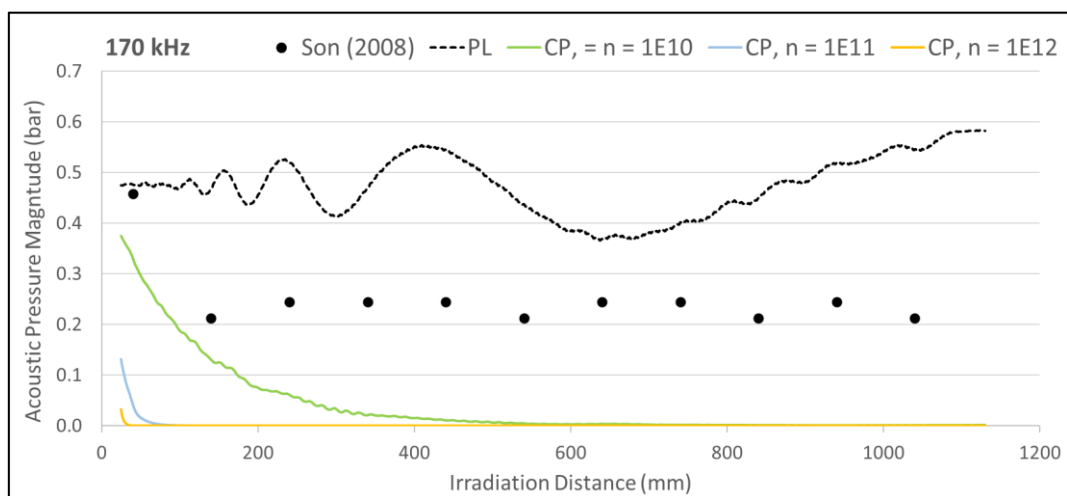


Figure 4.19: Absolute pressure comparison for the 170 kHz case against hydrophone measurements.

The results of this pressure validation study have shed light on another issue which needs to be further addressed. As discussed in Section 4.1.2.4, the effect of both the physical boundary in the experiment and the numerical boundary condition heavily influenced the quality of the results. The level of acoustic absorption at the walls of the sonoreactor was found to strongly affect the energy balance within the working fluid. The impact of this can be derived by analysing the standing wave and traveling wave contributions in the numerical solutions. The absolute pressure profiles obtained for the sonoreactor of Son et al. (2009) can be said to possess a strong travelling wave component even for the pure-liquid model. This was evident, based on the nodal pressure magnitude which greatly deviated from zero. This was found to be unsurprising as the wall boundaries were specified to be highly non-reflecting, which resulted in a magnitude imbalance between incident and reflected waves, as shown in Section 3.1.2.5 in Case Study 1.

4.1.2.6 The Effect of Bubble Density on the Results of the Linear CP Model

Hydrophone measurements for the 35 and 72 kHz cases showed low attenuation along the sonoreactor. This suggests that the bubbly-liquid attenuation, and subsequently the bubble fractions, were relatively low. This also explains the good agreement of the pure-liquid model with the hydrophone measurements in the 35 and 72 kHz cases. Current knowledge suggests that standing wave characteristics can affect the bubble field, where Bjerknes forces may cause an accumulation of coalescing bubbles near the antinodal regions of a sonoreactor (Metin et al., 1999; Metin, 2005). The antinode patterns observed from the simulations were found to be

weak. The inhibition of standing wave formation possibly reduced the bubble content in the working fluid. Son et al. (2009) commented that the liquid medium was fully degassed prior to the experiment, which further strengthened the above reasoning.

The lack of a proper method to specify the appropriate value of bubble density, n introduced uncertainties into the verification study. This is obvious in the pressure validation results predicted by the linear CP model using three arbitrary bubble density values. The reason for assuming a range of arbitrary magnitudes for n was the lack of a reliable method to characterise the bubble field in the studied system. A simple method to obtain a more suitable value for n is to reference the attenuation values measured in the original study of Son et al. (2009). The analytical dispersion relation of the linear CP model allowed the corresponding bubble density magnitude to be determined for each reported attenuation value, and the results are plotted in Table 4.7. The corresponding bubble densities obtained using this method lie around a magnitude of $1 \times 10^9 \text{ m}^{-3}$, which is one magnitude lower than the investigated range of $1 \times 10^{10} - 1 \times 10^{12} \text{ m}^{-3}$. Given this finding, the simulated acoustic pressure fields were also investigated using experimentally tuned bubble density magnitudes.

Table 4.7: Experimentally tuned bubble density magnitude determined from reported attenuation values, using the linear CP model with $R_0 = 5 \text{ um}$.

Frequency (kHz)	Son et al. (2008)		
	α , (Np/m)	n , ($1/\text{m}^3$)	c_{eff} , (m/s)
35	0.10	3.89E+09	1462.37
72	0.18	1.57E+09	1473.34
110	0.23	7.81E+08	1477.13
170	N/A	-	-

Figure 4.20 shows the results of the tuned CP model for the three frequencies. Son et al. (2009) did not report on an attenuation value for the 170 kHz case, and hence it was omitted. The 35 kHz case and the 72 kHz case showed distinct improvements over previous results. This is evident in the improved values of averaged relative error of 11 and 20 %, respectively. However, the tuned bubble density failed to improve the predictions for the 110 kHz case, as a vast overprediction of the pressure profile remained (260 % rel. error). Despite using a tuned bubble density parameter, there is still a significant deviation from the hydrophone measurements for the 110 kHz case. This result suggests that a well-approximated value of attenuation is not sufficient to fully model the studied sonoreactor. The exact reason for this remains unclear, but it was hypothesised that this could be a combination of factors such as acoustic reflection effects, geometry and interference patterns, and errors in hydrophone measurements. It was suggested that future studies should attempt to isolate these potential factors and investigate their effects in a strongly controlled experiment.

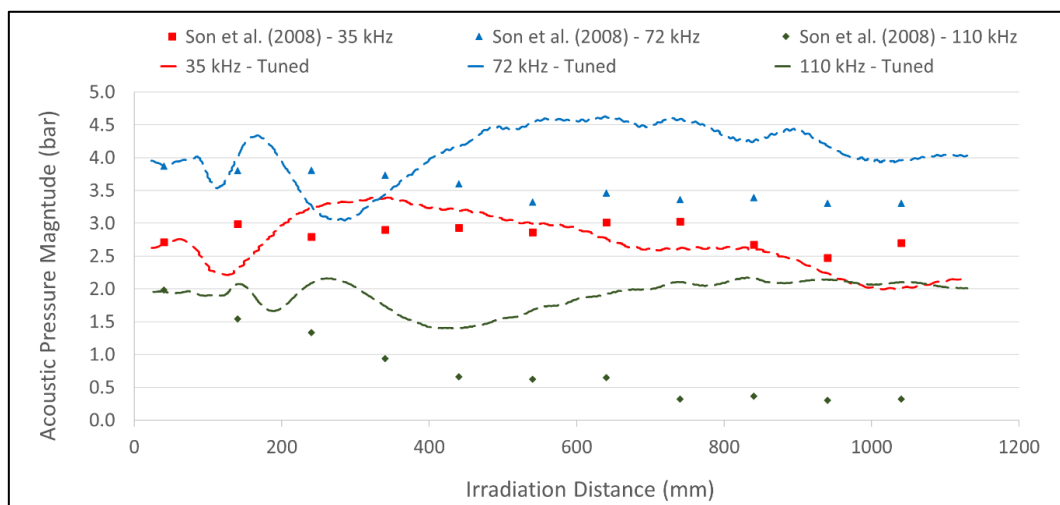


Figure 4.20: Results of the linear CP model solved with tuned bubble density parameters from attenuation measurements, compared against hydrophone measurements.

4.1.2.7 *Preliminary Investigations Involving Nonlinear Models*

The performance of nonlinear acoustic pressure models was not investigated using a full 2D simulation in this study, as attempts revealed that the NH and nonlinear CP models were unable to achieve convergence in the large geometry. The reason for the numerical instability was found to be unclear; but analysis of the convergence curves revealed oscillating behaviour which suggested the lack of a stable solution for the nonlinear problem (Fish and Belytschko, 2007). In light of this, it can be argued that a 2D simulation was unnecessary, as preliminary tests strongly showed that the model predictions greatly deviated from the hydrophone measurements.

The preliminary investigation was carried out using 1D test cases to represent the propagation axis along the length of the sonoreactor. The NH model and the nonlinear CP model were simulated for the 35 kHz and 72 kHz cases. The methods of setting up the NH model followed Trujillo (2020), while the methods of Jamshidi et al. (2012) and Fang et al. (2018) were used for the nonlinear CP model. Due to difficulties in converging the 35 kHz case using the NH model, even in a 1D model, the relative tolerance of the solver was relaxed from 0.001 (0.1% error) to 0.01 (1% error) to obtain the solution. The 1D pressure profiles for the NH and nonlinear CP models are presented in Figure 4.21. The overprediction of the bubbly-liquid attenuation relative to the hydrophone measurements was noted to be obvious for both models. The averaged relative errors for the NH model were found to be 71 and 83 % for the 35 and 72 kHz cases; while the nonlinear CP model yielded values of 83 and 96 %.

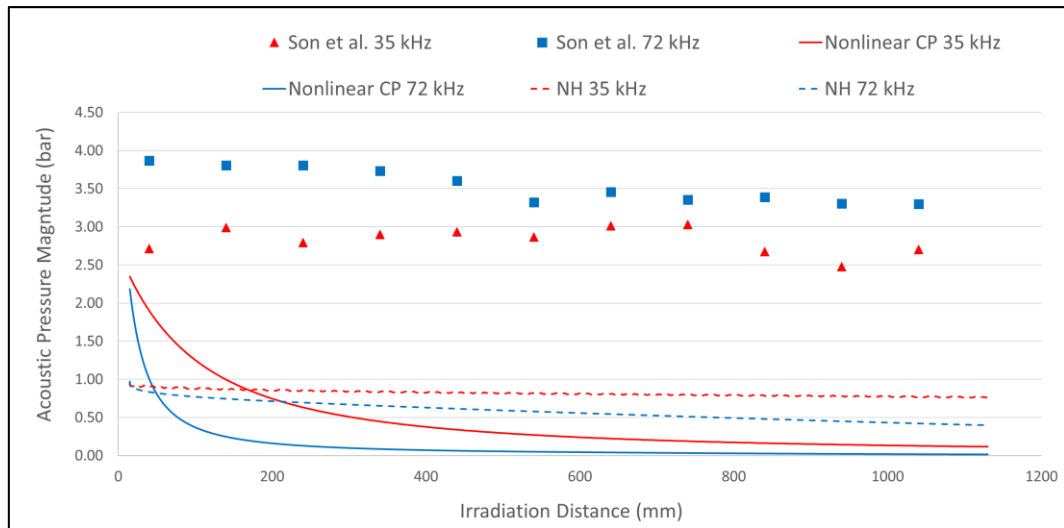


Figure 4.21: Absolute pressure profiles predicted by the nonlinear CP and NH ($1 \times 10^{10} \text{ m}^{-3}$) models and the empirical measurements, compared against hydrophone measurements.

Scrutiny of the attenuation values predicted by the nonlinear models revealed that they are up to four magnitudes higher than those measured by Son et al. (2009). Interestingly, the large attenuation values compared well with those reported in literature (Louisnard, 2012a; Jamshidi and Brenner, 2013). This finding was found to be interesting, as it challenged the viability of these models in ultrasonic baths. Since past works only validated these models in small-scale sonoreactors (Jamshidi et al., 2012; Louisnard, 2012a; Fang et al., 2018; Delacour et al., 2020; Sarac et al., 2020), these current observations offered a new perspective on model performance.

The principal mechanism of the nonlinear models is the pressure-dependent attenuation, which allows the model to predict a higher attenuation at higher local pressure magnitudes. Current results suggest that when the model is applied for more uniform cavitating systems such as ultrasonic baths, the model overpredicts the attenuation due to differences in working fluid / bubble field properties. Model development is still in its early stages and based on simplifying assumptions (Dähnke

and Keil, 1999; Louisnard, 2010). It should also be considered that they were developed mainly for strongly cavitating sonotrode systems (Louisnard, 2012a; Jamshidi and Brenner, 2013; Fang et al., 2018; Trujillo, 2018). This can be a plausible explanation for the large deviations observed in the 1D test cases, since the attenuation observed under ultrasonic horns was reported to be significantly stronger (Campos-Pozuelo et al., 2005).

These findings suggest that there are still large knowledge gaps that need to be addressed for nonlinear models. The results of Trujillo (2020) also suggested problems of overestimating attenuation for the NH model, as the bubble density required to match the pressure profile under an ultrasonic horn was found to be much lower than conventional values. To fully characterise the deviations exhibited by the nonlinear models would require an in-depth analysis on various factors ranging from the validity of model assumptions to the technical implementation of the simulation. The matter was deemed outside the scope of this work and shall be left for future work.

4.2 Case Study 4: The Effect of Geometry on Antinode Characterisation

Antinode validation of sonoreactors can be used to provide insights on the phase-speed reduction caused by bubble fields (Wijngaarden, 1968; Servant et al., 2000). Theoretically, this would result in shorter wavelengths and is henceforth referred as the ‘wavelength-shortening effect’. This effect was clearly observed in the SCL images of Case Study 5. It was noted that similar observations were rarely reported in past works, which was suspected to be due to the small geometries used. It was hypothesised that sonoreactor geometry significantly affects the ability to detect wavelength-shortening in antinode validation results. This hypothesis was tested in this case study in two parts. First, the effect of varying phase-speed deviation on the antinode predictions of a small-scale simulation was compared against known validation results. Next, a theoretical analysis was conducted to consider the relationship between the geometry, wavelength, and the detection of wavelength-shortening. This case study also characterised the minimum geometry-to-wavelength ratio, D_S/λ , required to show the wavelength-shortening effect in qualitative studies.

4.2.1 Defining the D_S/λ Parameter

Studies have shown that the reactor geometry and its associated wave reflection behaviour can significantly affect the pressure field (Yasui et al., 2007; Rashwan et al., 2020). In addition, the wavelength governs the characteristics of a standing wave and subsequently the location of antinodes within a sonoreactor. For this investigation, a new dimensionless ratio, D_S/λ , was introduced. The parameter D_S was defined as the effective length of a sonoreactor, which is the distance that a wave has to travel before

reflecting and potentially forming a standing wave. In a simple 1D waveguide problem, it was set as the distance between an emitting surface and its opposing reflecting surface. As a system approaches a 1D waveguide, the dimensionless parameter D_S/λ would better characterise its standing wave.

4.2.2 Heuristic Approach: Revisiting the Klíma et al. (2007) Validation Study

It was hypothesised that antinode validation studies carried out in systems with low D_S/λ values may not fully capture phase speed deviation effects. A numerical demonstration was used to show that the antinode prediction of a system with low D_S/λ would not change significantly even at large phase speed deviations. For this case, the validation result of Klíma et al. (2007) was selected for their detailed experimental set-up. The study considered a sonotrode-beaker set-up at 20 kHz. The effective length measured from the surface of the sonotrode to the floor of the beaker was reported to be 0.077 m. The D_S/λ value calculated for the studied system is 1. The pure-liquid Helmholtz model was solved for water ($c_l = 1500$ m/s, $\rho_l = 998$ kg/m³). Figure 4.22 (a) shows the validation result of Klíma et al. (2007), where they reported that the formation of bubble structures at the antinodes coincided well with the high-pressure regions predicted in their simulation. To investigate the effect of phase speed deviation on the solution, Figure 4.22 (b) – (g) presents the cases solved using arbitrary phase speeds with varying degrees of deviation from $c_l = 1500$ m/s. Other simulation parameters were unchanged. The plots of the solution used a normalised scale to highlight the antinode predictions. The results clearly showed that even with phase speed / wavelength deviations of up to +20%, Figure 4.22 (g) can be argued to show

qualitative agreement with the experimental observation in Figure 4.22 (a). Figure 4.22 (b) and (c) also compared well with the experimental observations of Klíma et al. (2007), as the high-pressure regions coincided with the 3 cavitation clouds highlighted by the blue arrows.

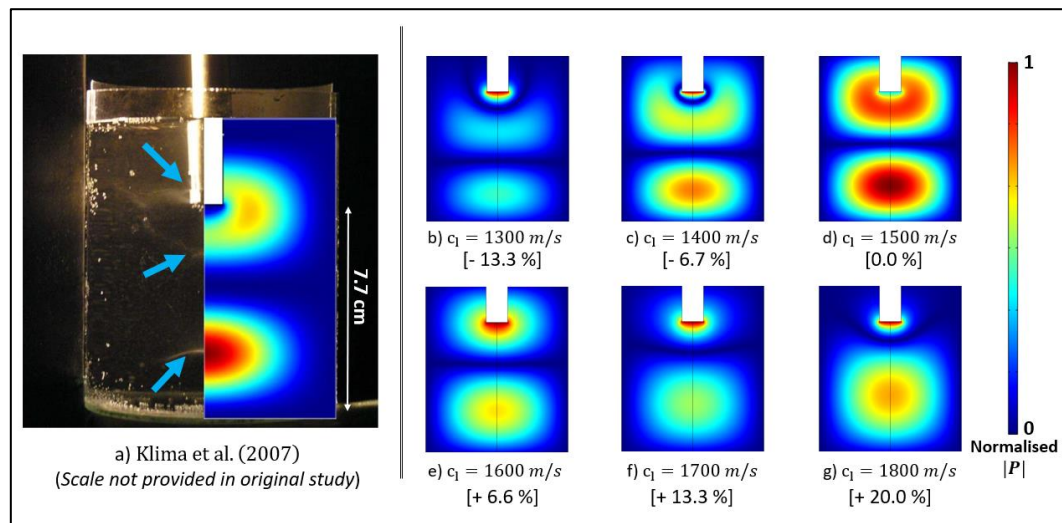


Figure 4.22: The antinode validation results of Klíma et al. (2007), compared against a series of simulation results using arbitrary phase speeds. [Image in (a) is Reprinted from: *Ultrasonics Sonochemistry* 14, Klíma, J., Frias-Ferrer, A., González-García, J., Ludvík, J., Sáez, V., Iniesta, J., *Optimisation of 20 kHz sonoreactor geometry on the basis of numerical simulation of local ultrasonic intensity and qualitative comparison with experimental results*. 19–28, Copyright (2007), with permission from Elsevier]

The above results led to two key points for discussion. First, it showed that even if there is a large reduction in phase speed by bubbly liquids, the effect on antinode locations would not be obvious if D_S/λ is small. This finding was found to support the main hypothesis of this study, and explained why previous studies did not distinctly observe wavelength-shortening effects in smaller systems (Lewis et al., 2007; Hussain and Janajreh, 2017; Tangsopa and Thongsri, 2019). To elaborate, antinode validation results were mainly evaluated by comparing the antinodal regions in the simulations

with experimental visual data (foil maps and SCL). Results mainly considered the number and location of antinodes. Unless the number of antinodes in the experiments was found to deviate significantly from the simulations (due to changes in wavelength), the phase-speed prediction error cannot be clearly detected.

The second point of discussion relates to the use of antinode measurements to validate the performance of acoustic pressure models. A well-posed antinode validation result can provide important insights on the combined effects of phase speed prediction and reflection behaviour in a sonoreactor. With the growing popularity of bubbly-liquid models, it can be used to validate the performance of modelling strategies. However, the results in Figure 4.22 suggest that antinode validation studies conducted with low D_S/λ should not be used to validate the phase speed prediction mechanism for bubbly-liquid models. It was clearly shown that the validation study of Klíma et al. (2007) compared well with simulations solved with clear phase speed deviations. This implies that small D_S/λ antinode validation studies cannot adequately characterise prediction errors in the acoustic pressure model, and could lead to incorrect conclusions regarding the validity of the phase-speed prediction mechanisms of the studied model.

4.2.3 Analysis of the D_S/λ Parameter

A theoretical analysis was performed to quantitatively analyse the relationship between the D_S/λ value and the condition that allows the phase speed deviation to be detected in an antinode validation study. For the analysis, the term ‘validation point’ was defined. The term ‘validation point’ refers to a region with a high acoustic

pressure magnitude relative to its surroundings. In experimental observations, validation points refer to visual aspects that represent cavitation zones, such as eroded regions in foil mapping and areas of high luminance in SCL. In simulation results, validation points refer to the local antinodal regions predicted by the acoustic pressure model. In qualitative antinode validation studies, the validation points from experimental observations are compared against those predicted by simulation results to evaluate the performance of the acoustic model.

The behaviour of standing waves in relation to the D_S/λ parameter was also established. A pure-liquid homogeneous Helmholtz equation with constant phase speed [Eqn. (11)] was considered for this analysis. For a 1D geometry, the general solution can be written as (Ginsberg, 2018):

$$P(x) = B_1 e^{-ikx} + B_2 e^{ikx} \quad (88)$$

The solution depends on the wavenumber k (containing phase speed and attenuation information) and the arbitrary coefficients B_1 and B_2 (dependent on boundary conditions). Thus, the characteristics of a standing wave depend on both the wavelength and the boundary conditions.

To characterise the behaviour of a 1D standing wave at the boundaries, a 1D monoharmonic system with an arbitrary effective length D_S of 20 units was considered. A D_S/λ value of 1 was used, which corresponded to a wavelength of 20 units. The parameter h , defined as the half-wavelength $\lambda/2$, governs the separation between adjacent nodes and antinodes in a pure standing wave. The potential standing wave patterns that could form within the example geometry are illustrated using pressure magnitude plots, $|P|$ in Figure 4.23. Since the geometry fits two half-

wavelengths, the pure standing wave would have a minimum of two antinodes, corresponding to two validation points as shown in Figure 4.23 (a). However, this would only occur when at least one of the boundaries is a pure node (zero pressure at the edge). Instead, most systems tend to exhibit one more validation point, which occurs when the boundaries exhibit a nonzero pressure. This was found to change the shape of the standing wave, forming 3 validation points in the system. For the example geometry, Figure 4.23 (b) shows the case where the left and right boundaries were set as pure antinodes. Based on anecdotal observations, it was postulated that systems are more likely to exhibit the behaviour in Figure 4.23 (c), where the boundaries are neither pure nodes nor pure antinodes. In this case, the number of validation points remains to be three. Since the qualitative nature of foil mapping and SCL results makes it difficult to know if a validation point is a pure antinode, both cases in Figure 4.23 (b) and Figure 4.23 (c) would yield three validation points when analysed.

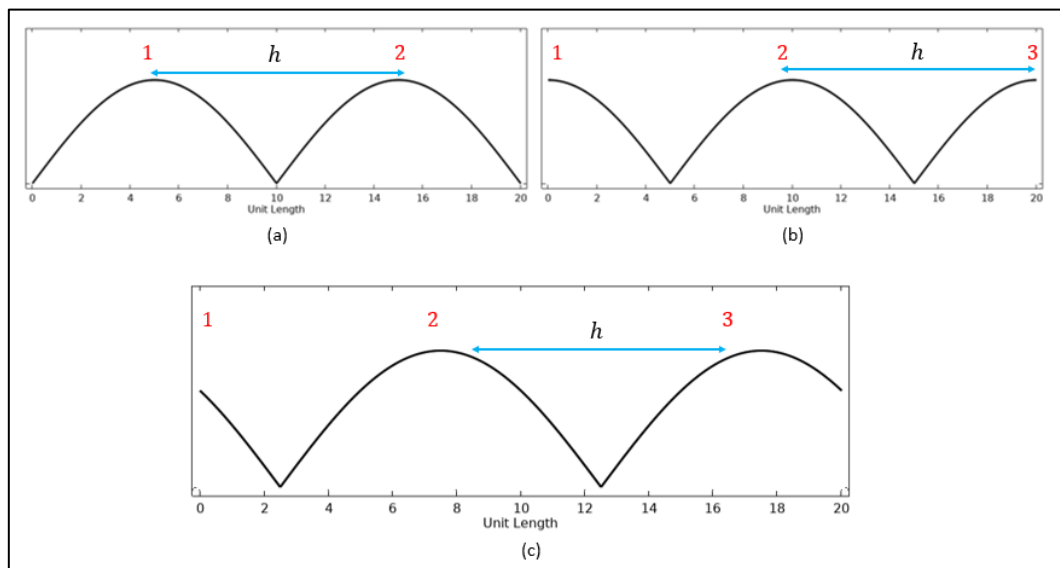


Figure 4.23: Depiction of an ideal standing wave model with constant wavelength, validation points numbered in red: (a) Pure node at boundary; (b) Pure antinode at boundary; (c) Neither a pure node nor pure antinode at the boundary.

From the simple standing wave model above, it was shown that the lowest possible number of validation points for a system is $2D_S/\lambda$ (rounded up). This occurs when a node lies on the boundary [Figure 4.23 (a)]. However, heuristics suggest that it is more likely for the standing wave to exhibit the behaviours depicted in Figure 4.23 (b) or (c), forming $(2D_S/\lambda + 1)$ validation points. In this study, this behaviour was used to predict the number of validation points for a certain wavelength and geometry.

Assuming that standing waves would result in $(2D_S/\lambda + 1)$ validation points, the phase speed prediction error was related to the D_S/λ parameter. The following analysis only considered the wavelength-shortening effect due to the reduction of phase speed in bubbly liquids. An obvious indication of a reduction in phase speed is the formation of additional validation points in the geometry as a result of the reduced half-wavelength. To elaborate, a system which showed more validation points than that predicted by a pure-liquid approximation would strongly indicate the presence of wavelength-shortening.

It was hypothesised that systems with large D_S/λ values are more likely to form an additional validation point when the wavelength-shortening effect is present. This is best explained using the graphical example shown in Figure 4.24. Consider a small geometry depicted in Figure 4.24 (a); a small reduction in wavelength would not significantly change the qualitative result in terms of the number of validation points, despite wavelength-shortening effects. On the contrary, a qualitative study conducted using the large geometry of Figure 4.24 (b) would be able to capture the wavelength-shortening effect in the form of an additional validation point.

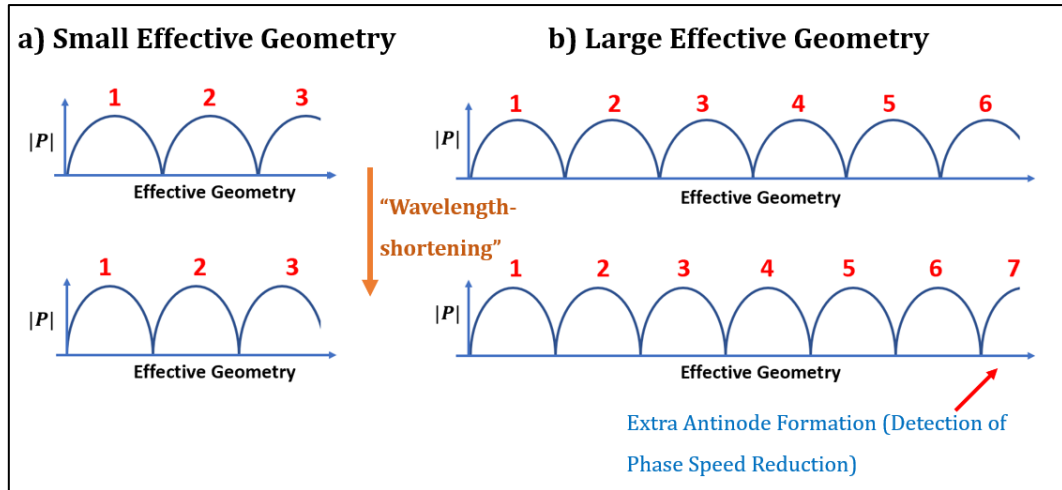


Figure 4.24: Graphical explanation on the effect of larger effective geometry on the detectability of 'wavelength-shortening' in the form of an extra validation point.

Since the relationship between phase speed and wavelength is linear, it is intuitive to use the wavelength λ and the half-wavelength h in the following analysis. It should also be noted that the wavelength-shortening effect is referenced from the pure-liquid phase speed. Consider an unreduced pure-liquid half-wavelength h , and a phase-speed/wavelength reduction factor f_e which has an upper limit at unity. A system that experiences a phase-speed reduction by a factor of f_e would exhibit a reduced half-wavelength of hf_e . In order for this wavelength deviation to manifest in one or more validation points in the geometry, as shown in Figure 4.24 (b), the total accumulated error across the geometry must exceed hf_e . This condition results in at least one additional validation point. Mathematically, this can be written as:

$$D_S(1 - f_e) > hf_e \quad (89)$$

Writing the relation in terms of wavelength λ and rearranging the inequality results in:

$$\frac{D_S}{\lambda} > \left(\frac{f_e}{2(1 - f_e)} \right) \quad (90)$$

Figure 4.25 plots the relation between the detection threshold for the additional validation point, and the corresponding D_S/λ requirement defined in Eqn. (90). Based on the defined relation, for a phase speed or wavelength reduction of 20 % ($f_e = 0.8$) to be detected as an extra validation point, D_S/λ should at least be greater than 2. For a 20 kHz system, this would require an effective geometry greater than 0.15 m.

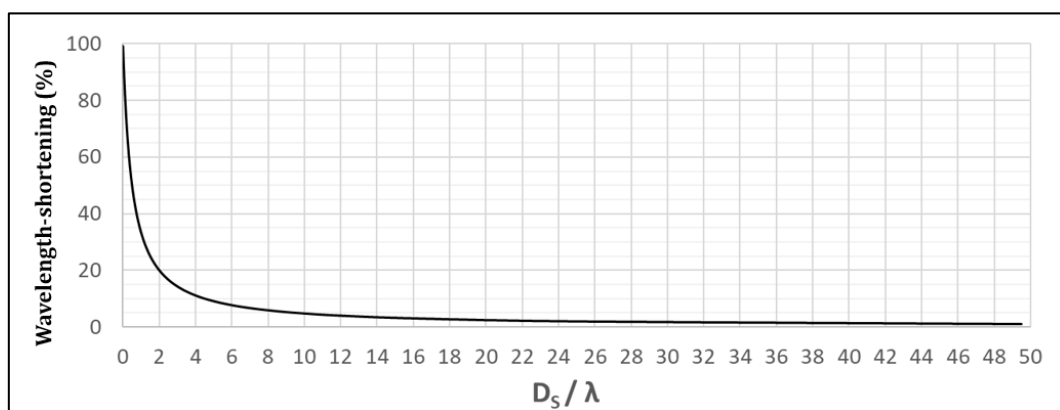


Figure 4.25: The relation between the D_S/λ parameter and its corresponding threshold to successfully capture wavelength-shortening effects in the form of a validation point.

For a more intuitive explanation, Figure 4.25 suggests that if the D_S/λ of the studied system is 2, a phase speed deviation of < 20% would result in the same number of validation points as the pure-liquid case. Interestingly, to capture a 1% reduction in phase speed, one would require a D_S/λ value more than 49.5 (c.a. 3.7 m @ 20 kHz). This was noted to be not practical, since attenuation would become a dominant factor at such lengths and standing wave formation may not occur.

Regarding the results presented in Figure 4.25, several important caveats were identified. First, it was noted that Figure 4.25 was calculated on the premise that at least one additional validation point should form in the geometry. It should be noted

that phase speed deviations can be detected by other means, such as measuring the distance between validation points using image processing software. Such methods could quantify wavelength reduction without relying on qualitative validation points. Second, it should also be considered that an additional validation point can also be observed from the boundary mechanism outlined in Figure 4.23. This aspect becomes important if the system exhibits a characteristic shown in Figure 4.23 (a). An example is the case of Klíma et al. (2007) in Figure 4.22, the original study tuned the geometry to approximate the antinode formation of Figure 4.23 (a). This becomes clear when one observes that the region under the horn in Figure 4.22 (a) is a nodal region (blue). The extra validation point formed in Figure 4.22 (b) and (c) is caused by a shift in boundary behaviour from Figure 4.23 (a) to Figure 4.23 (c), and not by the accumulation of wavelength-shortening error. This highlights the shortcoming of the simple model proposed in Eqn. (89), in which it does not account for the possibility of additional validation points forming due to boundary behaviour.

The presented analysis was performed for a waveguide assuming pure standing wave formation. In practice, acoustic pressure fields are often much more complex. It was noted that, while the derivation was conducted using a pure standing wave, the applicability of the model for systems with a combination of standing and travelling waves is not affected. This is because the model is strictly constructed upon the wavelength of the working fluid, which is strictly dependent on the phase speed. However, it should be noted that systems with dominant travelling wave contribution may not exhibit clear validation points during experiment measurement. Similarly, the presented discussions were also applicable for more complex reactor configurations such as flow-through reactors. Although the presence of a flow field within the

sonoreactor can affect the distribution of the bubbles (and subsequently the medium properties), current studies tend to treat the pressure field to be independent from the fluid velocity (Louisnard, 2017).

Nevertheless, the proposed D_S/λ parameter should strictly be treated as a rough approximation to improve the accuracy of validation studies. One possible use of the D_S/λ parameter is to characterise confidence levels of antinode validation results. The finding also suggests that simulation frameworks that had been validated at a certain D_S/λ , should provide the same performance for other systems with similar or less D_S/λ . The only consideration is that the medium properties (notably the bubble fraction) should be similar between the two systems, and that other factors such as boundary effects in Figure 4.23 (a) should not be present.

4.2.4 Compilation of the D_S/λ Parameter in Past Studies

During the course of this research, the D_S/λ values for the systems studied in past works were compiled and tabulated in Table 4.8. The information was found to be useful for comparing systems with similar D_S/λ values. Some liberty was taken when determining the effective length of systems with complex geometries. Table 4.8 only considered studies that have explicitly validated simulation results against experimental antinode characterisation.

It was found that most of the antinode validation studies in past works had been carried out using small geometries with relatively large wavelengths (low frequencies), which was characterised with low D_S/λ values. Table 4.8 shows that the sonoreactors in most studies have $D_S/\lambda < 4$. The compiled information also shows the lack of large-

scale validation studies, with reference to the compiled effective geometries used in past works. This information highlights the key knowledge gaps addressed in this work, and established a strong need to perform larger-scale validation studies. This should not be limited to evaluating bubbly-liquid models in terms of phase-speed prediction mechanisms, but also to develop and reveal important heuristics and practical know-how when simulating large geometries. This issue should be addressed if sonoreactor simulations are to be used as a design tool for commercial and industrial designs.

Lastly, it should be noted that while the D_S/λ values can be increased by using a higher operating frequency, the approach is limited to a certain frequency threshold. This is because antinode verification methods such as foil mapping and SCL become unpractical when the frequency is too high, as the short wavelength makes it difficult to distinctly identify the validation points (Yasui et al., 2007).

Table 4.8: Compilation of past antinode validation works and their calculated D_S/λ values.

Author(s)	Validation Method	Studied System	A. P. Model	f (kHz)	D_S (mm)	D_S/λ
Campos-Pozuelo et al., (2005)	Pressure Probe; Bubble Structure	Sonotrode Vessel	NW	20	150	2.0
Sáez et al., (2005)	Foil Map, Thermal Map	Ultrasonic Cell	PL	20	41	0.6
Klíma et al., (2007)	HD Photography	Sonotrode - Beaker	PL	20	77	1.0
Wang and Yao, (2013)	HD Photography	Sonotrode Vessel	PL	20	163	2.2
Wei and Weavers, (2016)	Pressure Probe	Sonotrode Vessel	PL	20	340	4.6
Dähnke, et al., (1999b)	Pressure Probe	Ultrasonic Bath	NW	23	90	1.4
Sarac et al., (2020)	Pressure Probe	Ultrasonic Bath	NH	27	60	1.1
Laborde et al., (1998)	Foil Map	Floor Irradiated Cylindrical Reactor	LW	28	120	2.3
Servant et al., (2001a)	Foil Map	Floor Irradiated Cylindrical Reactor	NW	28	107	2.0
Zhang et al., (2018)	Foil Map	Ultrasonic Bath	PL	28	180	3.4
Hussain and Janajreh, (2017)	Foil Map	Floor Irradiated Cylindrical Reactor	CP	28	80	1.5
Tangsopa and Thongsri, (2019)	Foil Map	Ultrasonic Bath	PL	28	200	3.8
Lais et al., (2018)	Pigment Cleaning	Ultrasonic Pipe Cleaning	LW	40	50	1.4
Delacour et al., (2020)	SCL	Microreactor	NH	40	40	1.1
Lewis et al., (2007)	Foil Map	Ultrasonic Bath	PL	44	c.a. 50	1.5
Yasui et al., (2007)	SCL	Floor Irradiated Cylindrical Reactor	PL	100	139	9.4

*LW = Linear Wave Equation, NW = Nonlinear Wave Equation, CAF = Caflisch Model, PL = Pure-Liquid Helmholtz Model, CP = Commander and Prosperetti Model, NH = Nonlinear Helmholtz Model

4.3 Case Study 5: Antinode Prediction in Large Sonoreactor

This case study focused on the phase-speed prediction aspect of the pure-liquid, linear CP, and NH models in a 16.5-L hexagonal sonoreactor previously reported by Tiong et al. (2017a). Antinode validation was carried out using SCL images. It was hypothesised that the properties of the linear CP model would give a good approximation for the uniform standing wave patterns observed in the studied system. The pure-liquid model was solved without attenuation, whereas the bubbly-liquid models were assumed to be monodisperse and solved for three bubble density magnitudes. This study revealed valuable insights into the effectiveness of popular frequency domain models in predicting the phase speed in large ultrasonic baths.

4.3.1 Methods: Experimental Data

4.3.1.1 *Physical Characteristics of the Sonoreactor*

The hexagonal sonoreactor involved in this case study had been reported in past literature (Manickam et al., 2014; Tiong et al., 2017a). The 16.5 L sonoreactor (*Sonictron, Malaysia*) possesses six vertical interior surfaces fitted with wall transducers, with each opposing wall having the same operating frequency. The sonoreactor is capable of operating at 28, 40 and 70 kHz which corresponds to D_S/λ values of 4.6, 6.6 and 11.5 respectively. The design power for each frequency was reported to be 300 W. A simplified model illustrating the key geometrical dimensions of the sonoreactor is shown in Figure 4.26 (a). Figure 4.26 (b) outlines the position of the transducers corresponding to each operating frequency from a top view perspective. All images depicting the hexagonal geometry followed this orientation to

ensure consistency. It should be noted that the representation of the wall transducers in Figure 4.26 (b) is merely a schematic and should not be taken to scale.

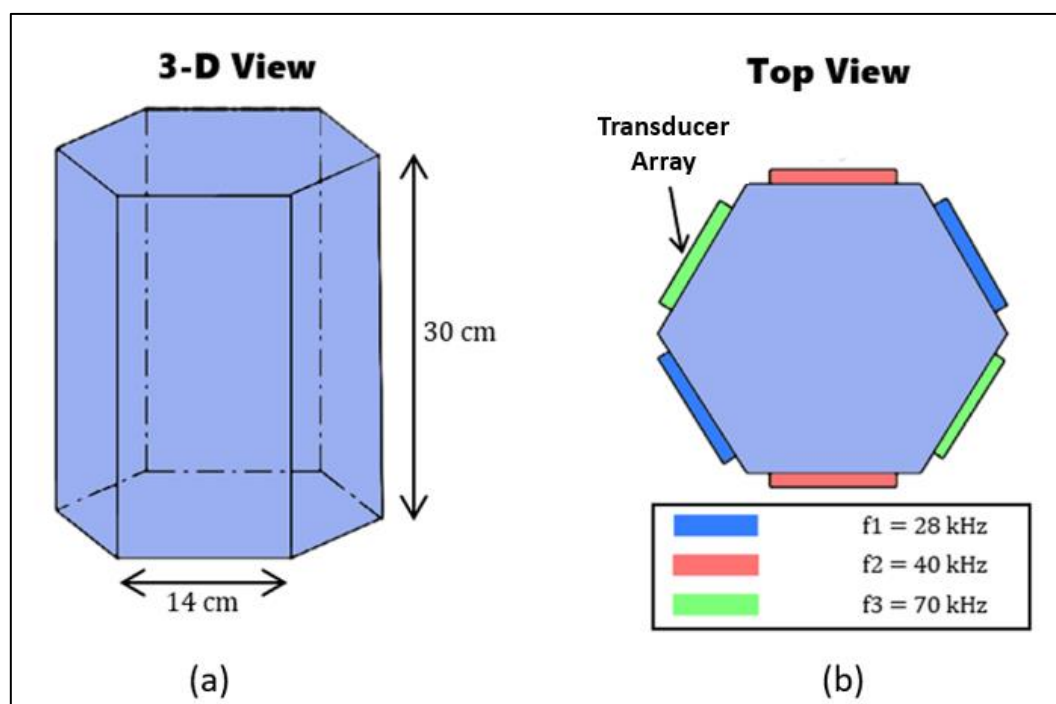


Figure 4.26: (a) Physical representation of the dimensions of the hexagonal sonoreactor; (b) Top view schematic showing the orientation of the transducers corresponding to each frequency.

4.3.1.2 Sonochemiluminescence (SCL) Data

The sonochemiluminescence (SCL) images used in this validation study are part of a data set that was published by Tiong et al. (2017b). Luminol was used as the chemiluminescence agent. Due to the mechanical design of the sonoreactor, the only way to obtain the SCL images was from a top view perspective, as shown in Figure 4.27 (b). Photography was carried out using a digital, single lens reflex camera (dSLR, Nikon D5100) with an exposure time of 30 seconds. To minimise optical noise, the images were captured in a dark environment. This was achieved by shielding the vessel with

a black cardboard box. Multiple images were taken for each case to ensure that steady-state behaviour was characterised. Raw SCL images were preconditioned using the image processing software, ImageJ. First, background measurements were subtracted using a dark frame image without any SCL activity. Next, the pixel noise was reduced using a Gaussian blur filter using the 'Smoothen' function of the software. The contrast was also adjusted to a saturated pixel value of 6%, which allowed the standing wave patterns to appear more distinct. To facilitate better alignment for comparison, the edges of the hexagonal geometry were detected and highlighted using ImageJ. Lastly, the 'Plot Profile' function of the software was used to extract luminance profiles for quantitative data.

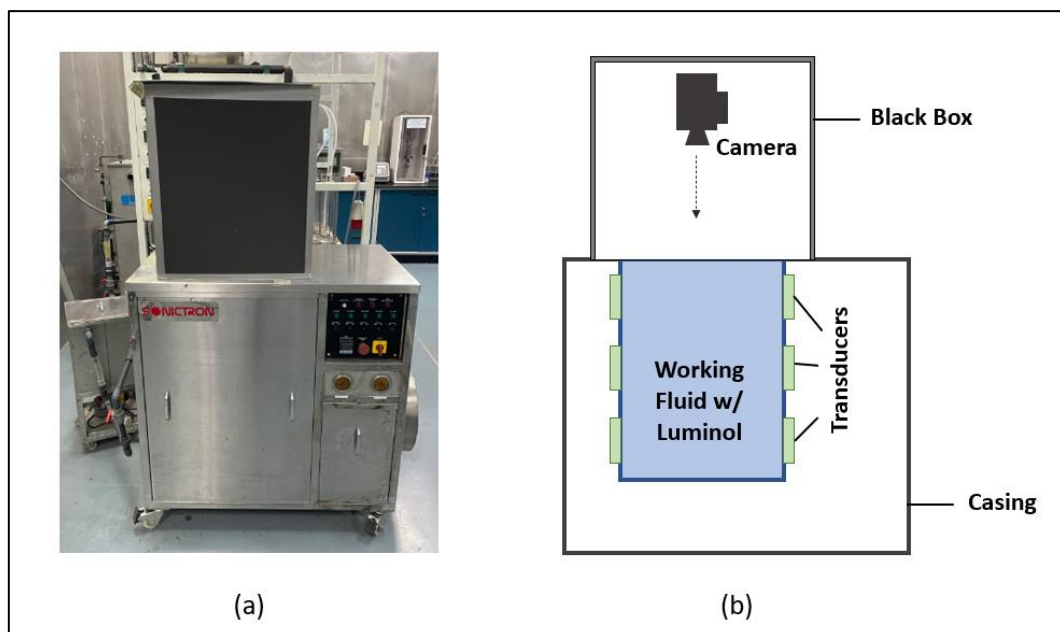


Figure 4.27: (a) Image showing the physical sonoreactor; (b) The schematic describing the method by which the SCL images were captured.

4.3.2 Methods: Numerical Simulation

4.3.2.1 Acoustic Pressure Models and Simulation Parameters

Three acoustic pressure models were validated against SCL standing wave data. The pure-liquid model was solved without attenuation, whereas the linear CP and NH models were formulated using identical bubble field characteristics. Implementations of the pure-liquid [Eqn. (12)] and linear CP [Eqn. (23)] models were identical to Case Study 3 [Section 4.1.1.1] and will be omitted for conciseness. For the NH model, the real part of k_c^2 adopted the approach of Louisnard (2012a), while the imaginary part was calculated using a more efficient formulation of Trujillo (2018) [Section 2.6.1.3]. The bubble ODE system used to calculate the interpolation curves used the Keller-Miksis equation in Eqn. (51), ideal gas model in Eqn. (53) and the heat transfer model of Preston et al. (2007) in Eqn. (60). The contribution of water vapour was neglected according to the reasoning in Section 2.7.2.3.

The bubble field was assumed to be monodisperse for both bubbly-liquid models with R_0 of 5 μm . Three magnitudes of bubble density n (1×10^{10} , 1×10^{11} , $1 \times 10^{12} \text{ m}^{-3}$) were assumed similar to Case Study 3. The gasses within the bubbles were assumed to exhibit ideal gas behaviour, and the properties resembled those of air. The liquid density, surface tension, and viscosity were assumed to be constant. The physical parameters used in this investigation are listed in Table 4.9. The acoustic pressure models were solved using the *Coefficient Form PDE* module in COMSOL, while the bubble ODE calculations were solved using the *ode15s* function in MATLAB. The methods used to solve for the bubble ODE system referenced the comprehensive work of Pandit et al. (2021).

Table 4.9: Physical properties (25°C) used in Case Study 5.

Parameter	Value	Unit	Description
D_g	2.19×10^{-5}	m^2/s	Diffusivity of gas
c_l	1481	m/s	Speed of sound in water
γ_l	1.41	-	Adiabatic index for air
K_T	24.35×10^{-3}	W/m.K	Thermal conductivity of gas
μ_l	0.001	Pa.s	Dynamic viscosity of liquid
p_∞	101325	Pa	Ambient pressure
R_{gas}	8.3145	J/mol.K	Gas constant
ρ_l	997	kg/m^3	Density of liquid
σ_l	0.0725	N/m	Surface tension of liquid

4.3.2.2 Boundary Conditions

The specification of boundary conditions was straightforward, with a Dirichlet pressure boundary used for the active walls of the operating frequency, and a sound-hard boundary for the non-vibrating passive walls. Table 4.10 tabulates the Dirichlet pressure P_{tr} used for each studied frequency. The values were calculated from calorimetric measurements by Tiong et al. (2017a) using the relation in Eqn. (84).

Table 4.10: Calorimetry data for the calculation of Dirichlet transducer boundary condition for single-frequency simulations (Tiong et al., 2017a).

Frequency (kHz)	Power, O_m (W)	Total Surface Area, A_{tr} (m^2)	$P_{Tr,28}$ (bar)	$P_{Tr,40}$ (bar)	$P_{Tr,70}$ (bar)
28	215.90	0.083	0.89	-	-
40	207.10	0.083	-	0.87	-
70	283.10	0.083	-	-	1.01

4.3.2.3 Geometry and Meshing Considerations

A full hexagonal 2D geometry was used to model the sonoreactor. Free triangular elements were used, and the mesh size was determined from the acoustic pressure model that was being solved. Mesh adjustments were simple for the analytical pure-liquid and linear CP models and a refinement curve similar to Section 4.1.2.2 was used. In contrast, the nonlinear nature of the NH model posed an interesting challenge. Since phase speed is a function of local pressure, regions with a higher local pressure magnitude would technically require a smaller mesh. For this study, a blanket solution was used by setting the mesh size to account for the lowest possible phase speed determined from the limits of the interpolation curves. In hindsight, this was inefficient, as FEM meshing techniques such as adaptive mesh refinement would be preferred. Nevertheless, this decision does not affect the accuracy of the simulation results, but only the solution time. Figure 4.28 (a) shows an example of the free triangular mesh generated for hexagonal geometry (pure liquid, 28 kHz simulation), while Figure 4.28 (b) outlines the boundary orientation for each active frequency.

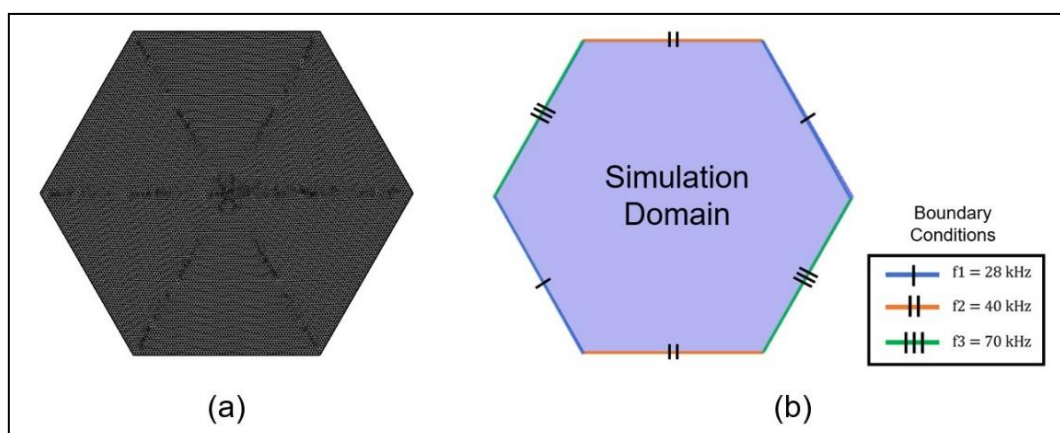


Figure 4.28: (a) Mesh for the pure liquid of the 28 kHz simulation with 229,241 degrees of freedom; (b) Orientation of the boundary conditions of single-frequency operations.

4.3.3 Results and Discussion

4.3.3.1 Modelling Strategy

This study argues that a 2D model was sufficient for the purpose of this study. This was supported by the SCL data shown in Section 4.3.3.2 that suggest strong plane-wave characteristics. The results of Figure 3.23 in Case Study 2 [Section 3.2.3] showed that the dynamics of the vibrating walls can be approximated using the Dirichlet pressure boundary conditions. This simplifying step was shown to be justifiable if the region of interest lies near the centre of the geometry. In this study, the Dirichlet pressure boundary conditions were specified from calorimetry measurements, which had been shown in Case Study 3 [Section 4.1.2.1] to better represent the effective energy emission into the working fluid.

The decision to model inactive walls as sound-hard boundaries was a simplifying assumption. A simple calculation of the reflection coefficient using the acoustic properties of 304 stainless steel ($\rho_{s,s} = 7930 \text{ kg/m}^3$, $c_{s,s} = 5790 \text{ m/s}$) using Eqn. (85) gives a reflection coefficient of around 0.9, which slightly deviated from a perfectly reflecting boundary. However, to avoid uncertainties related to impedance mismatch when using bubbly-liquid models, as in Case Study 3 [Section 4.1.2.4], the sound-hard boundary was used. As the analyses were focused near the centre of the geometry, the impact of this decision on the main findings was found to be small. Figure 4.29 supports this claim by plotting the antinode patterns of different passive boundaries for the 28 kHz case, solved using the pure-liquid model. The standing wave characteristics near the centre showed nearly identical results, with little difference between the impedance and the sound-hard boundary condition.

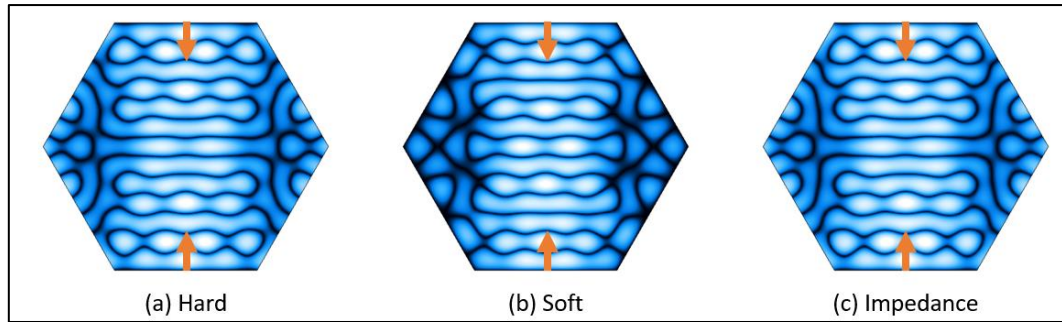


Figure 4.29: Effect of boundary conditions on predicted standing wave characteristics: (a) Sound-hard; (b) Sound-soft; (c) Impedance of stainless steel. Arrows represent the emitting walls.

Constant physical properties were assumed in the simulations because the reactor was kept at a constant temperature of 25°C by cooling (Tiong et al., 2017a). The original study also revealed that the temperature change within the system was relatively small, with a maximum temperature increase of 15°C per hour. Since the SCL images were obtained within a short time frame, it was deemed that the use of constant physical properties at a constant temperature was sufficient to represent the physical system. The design of the physical hexagonal sonoreactor also enhanced standing wave formation by emitting ultrasonic waves from opposite walls. Such conditions strengthened the standing wave characteristics of the pressure field, which was important to increase confidence in the antinode verification results. The transducer arrays on each wall were noted to be driven using the same ultrasonic generator to match the phase of oscillation. This was found to be important because it allowed both vibrating walls to be simulated using the same Dirichlet boundary condition in the same frequency-domain simulation⁴.

⁴ If there is a phase mismatch between the opposing vibrating walls, the Dirichlet boundaries would need to be corrected for phase difference.

4.3.3.2 SCL Characterisation

The presented SCL dataset was used not only for this case study, but also in Case Studies 6 and 7. Therefore, it is important to discuss the quality of the dataset. Figure 4.30 shows examples of SCL images obtained for single-frequency operations at 28, 40, and 70 kHz, respectively. The captured standing wave characteristics, represented by the bright and dark bands, were noted to be quite distinct, especially for the 40 kHz case. Slight visual smearing was observed in the SCL images, which was hypothesised to be the combined result of fluid motion and long-exposure photography. To reduce the impact of transient effects on the verification study, multiple images were taken and the image with the best representation of the distinct standing wave was selected.

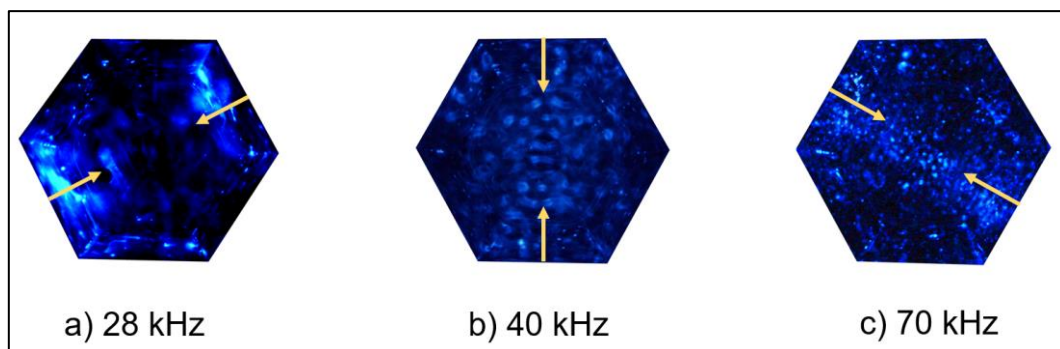


Figure 4.30: SCL results used in this work: (a) 28 kHz; (b) 40 kHz; (c) 70 kHz. Design power of 300 W and arrows show the ultrasound emitting walls.

A region of strong luminance was observed near the emitting walls for the 28 kHz case in Figure 4.30 (a). One possibility is to attribute this observation to the ‘shielding effect’ (Moussatov et al., 2003; Klíma et al., 2007). It was possible that the lower frequency of the 28 kHz transducers generated a higher local intensity near the walls due to the higher displacement amplitude, which resulted in said observation. The validity of SCL

visual data near the edges was also found to be prone to errors and uncertainties. The most prominent being the effect of the reflecting metal walls, which led to unreliable luminance data near the edges. Figure 4.31 shows an enlarged SCL image for the 40 kHz case. It is unclear whether the luminance data in the regions circled in red were a product of SCL or a result of reflection from the metal walls. To exclude possible errors caused by this uncertainty, the analysis in this work was restricted to the region of interest near the centre of the geometry (highlighted in yellow).

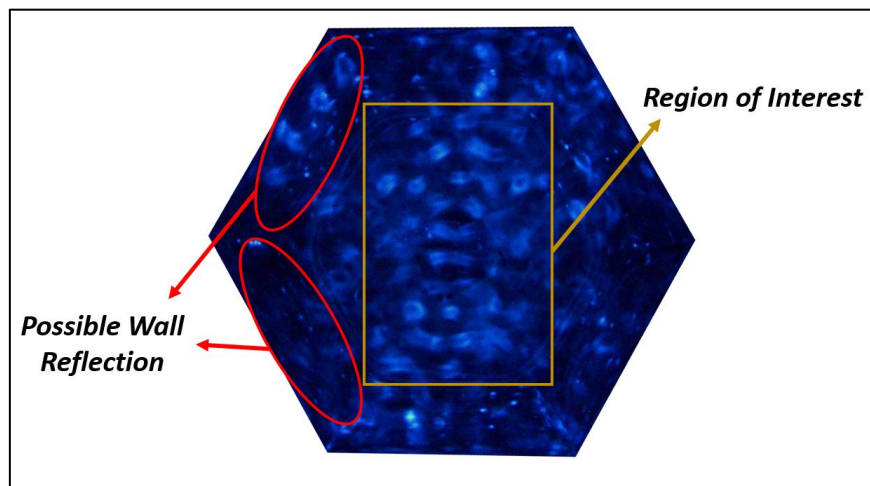


Figure 4.31: Example of possible visual errors metal wall reflection, and the region of interest used for antinode validation.

Another reason to focus on the results near the centre of the geometry is related to optical distortion. The image of the standing wave was essentially transmitted from the volume of liquid, past the water-air interface, and into the camera lens. As refraction is minimum at normal incidence and increases with the incidence angle, the representation of the standing waves was considered to be more accurate near the centre of the geometry.

Other considerations were also addressed using image processing techniques (Jähne, 2004). In this investigation, quantitative measurements had to be obtained from the SCL images, notably for the investigations in Chapter 5. Therefore, the integrity of the geometric data in the SCL images was confirmed, and possible sources of error were addressed. Lens effects such as barrel and pincushion distortion were determined to be negligible by verifying that the edges in the images are straight⁵ (Jähne, 2004). It was assumed that the pinhole camera model is valid, as it is for most conventional cameras (Forsyth and Ponce, 2002). The main concern was noted to be human error, where the camera position may have slightly deviated from the intended angle of capture for each experimental set-up, which can lead to perspective distortion and vignetting.

To obtain a measure of perspective distortion, the standard deviation of the edges of the hexagonal sonoreactor was analysed. Refraction effects were neglected because the edges of the metal vessel were not submerged. The edges of the hexagonal geometry were measured to be exactly 140 mm for the physical sonoreactor. The pixel deviation for all six edges was used to quantify the error from perspective distortion by analysing the difference in pixel length captured for each edge. The edge detection function in ImageJ was used, and the uncertainties were quantified in terms of standard error. With reference to the SCL data used in this study, the length-scale of 140 mm corresponded to pixel values of 1381.5 ± 13.8 , 1373.7 ± 13.2 , and 1376.7 ± 8.8 , for the 28, 40, and 70 kHz case, respectively. These results suggest that the

⁵ Generally, lens distortion manifests by 'bending' straight lines. A good example is the curved perspective of wide-angle photography. By verifying that the edges of the hexagonal geometry are straight allows a confident claim that the lens distortion effect is negligible.

perspective distortion error is very small, and the geometrical integrity of the hexagonal geometry was largely preserved. For the quantitative measurements in this work, the mean pixel length was set as the reference scale of 140 mm.

4.3.3.3 *Acoustic Pressure Solution of the Pure-Liquid Model*

Figure 4.32 shows the 2D absolute pressure field solved using the pure-liquid model for the three investigated frequencies. The large overprediction in terms of pressure magnitudes is evident in the colour scales. This outcome was expected due to the lack of attenuation and the specification of perfectly reflecting boundaries for all six hexagonal edges. The same conditions resulted in strong standing wave characteristics for all frequencies. Considering that the Dirichlet boundaries were only around 1 bar, these pressure magnitude predictions of up to 34 bar can be argued to be unrealistic. An interesting observation is the magnitude of the 40 kHz system, which is noticeably higher than the other two cases despite having similar Dirichlet pressure specifications [Table 4.10]. This observation coincides with the 40 kHz SCL results, which also showed higher luminance and clearer standing waves. Further analysis in Chapter 5 [Section 5.4.4.6] suggests that this was caused by constructive interference. The pure-liquid model was included in this study, as it had been reported to show good antinode predictions in previous work (Lewis et al., 2007; Xu et al., 2013; Tangsopa and Thongsri, 2019). It was included in this study to reconfirm these findings in systems with larger D_s/λ ; which had been determined to be 4.6, 6.6, and 11.5 respectively, for the 28, 40, and 70 kHz system.

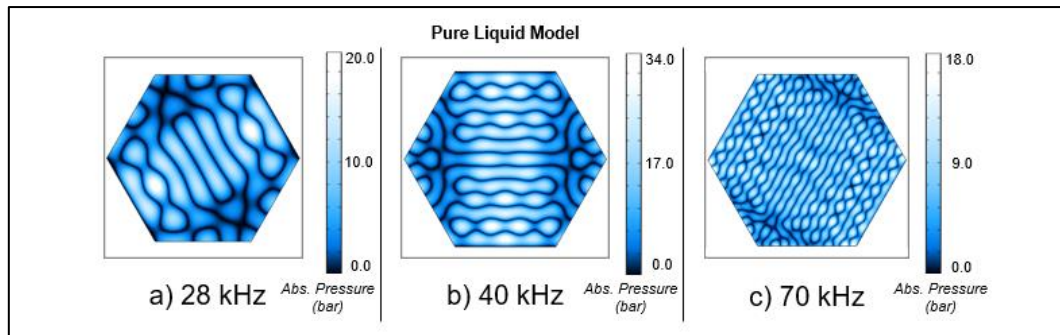


Figure 4.32: The absolute acoustic pressure fields predicted by the pure-liquid model for the three studied frequencies.

4.3.3.4 Acoustic Pressure Solution of the CP Model

The linear CP model was specified as a monodisperse model with a uniform bubble density n . There are two main reasons for adopting this formulation. First, it was argued that the linear variation of the CP model holds promising prospects in the characterisation of ultrasonic baths. This claim was made based on the assumption that ultrasonic baths exhibit uniform and well-distributed acoustic behaviour, as observed in previous studies (Kumar et al., 2007; Son et al., 2009; Tangsopa and Thongsri, 2019). The well-distributed luminescence activity in the SCL results in Figure 4.30 also supported this claim. The other reason was to facilitate a controlled comparison with the NH model, which had been gaining popularity in sonoreactor acoustics. This allowed a clearer comparison in terms of acoustic pressure prediction mechanisms for the two bubbly-liquid models. The meshing considerations for the linear CP model used the same strategy reported in Case Study 3, where the effective phase speed was used to refine the mesh [Section 4.1.2.2].

Figure 4.33 shows the absolute pressure fields solved using three different magnitudes of n . It was noted that there was neither sufficient data nor reliable methods in literature to confidently specify the value of the bubble density n for the studied

system. Thus, three magnitudes of n were parametrically tested, similar to Case Study 3. This topic was identified as a key knowledge gap for the adoption of bubbly-liquid models and will be addressed in Chapter 5. In terms of acoustic pressure magnitude, the solutions of the linear CP model yield lower predictions compared to those of the pure-liquid model. This observation, albeit qualitative, conformed to the findings of previous works (Jamshidi et al., 2012; Louisnard, 2012a). The lack of hydrophone measurement data for the hexagonal sonoreactor restricts further analysis of the results.

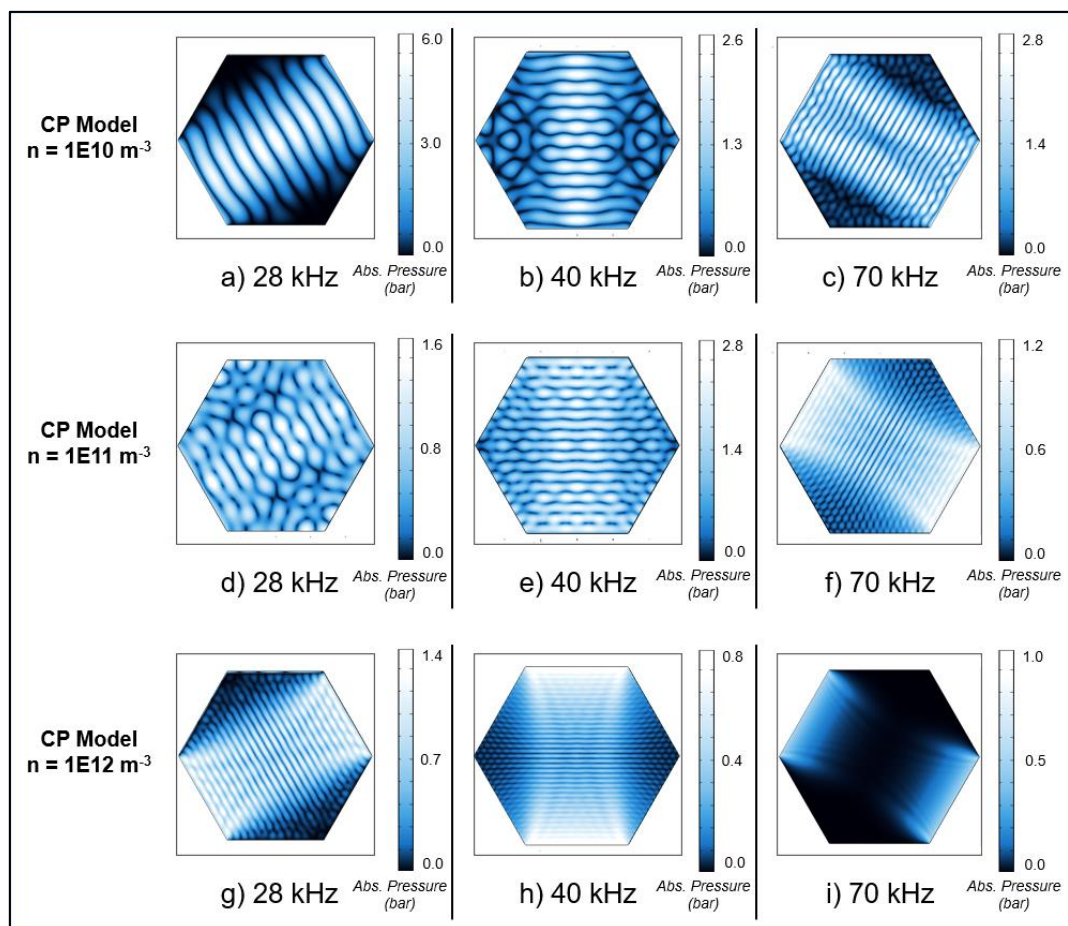


Figure 4.33: Absolute acoustic pressure fields predicted by the linear CP model for three frequencies at different bubble density magnitudes.

An interesting observation in Figure 4.33 is the drastic reduction in the predicted wavelength with increasing magnitude of n . As shown in Table 4.5, the linear CP model predicted lower effective phase speeds as n was increased. It was also shown that increasing n resulted in a higher attenuation for the entire domain. Thus, the observations in Figure 4.33 were expected. The results highlight the strong dependence of the simulation results on the specified bubble density n . The work of Dogan and Popov (2016) noted that the highly sensitive phase-speed prediction of the linear CP model is a disadvantage, as it can lead to unrealistic results. However, this study argues that the model is viable and preferred for bath-type configurations if the uncertainties around n can be addressed.

The linear CP model predicts an analytical phase speed and attenuation, which allowed the characteristics of the solution to be easily plotted and analysed. The variation of the real and imaginary parts of the wavenumber k_c against n is shown in Figure 4.34 (a). The phase speed ratio that quantifies phase-speed reduction against the pure liquid phase speed, c_{eff}/c_l is also plotted against bubble fraction in Figure 4.34 (b). It was noted that these characteristic curves can be used as a tool for empirical tuning, which was proposed as a solution to address uncertainties revolving around n . This potential improvement for the modelling strategy is demonstrated in Case Study 6 [Section 5.3].

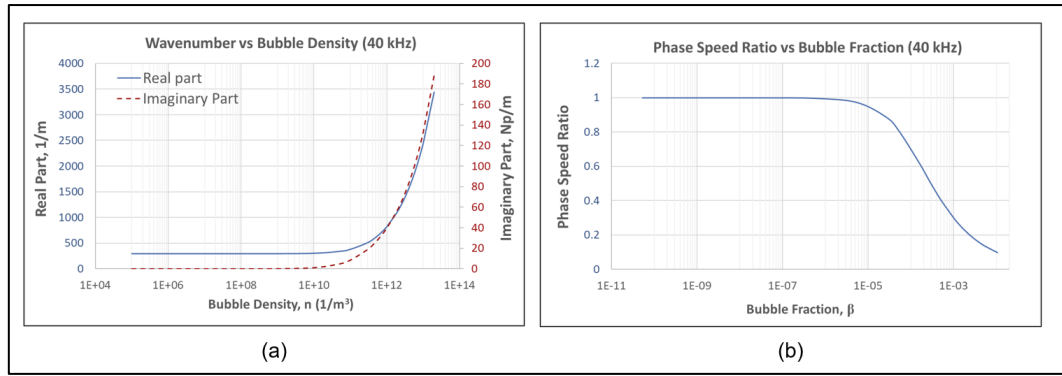


Figure 4.34: (a) Semi-log plot of the real and imaginary parts of the analytical wavenumber against bubble density; (b) Variation of the phase speed ratio against bubble fraction. Obtained using linear CP model with 5 μm equilibrium radius and 40 kHz.

4.3.3.5 Acoustic Pressure Solution of the NH Model

The NH model uses interpolation curves to represent the acoustic property of the working fluid (Louisnard, 2012a; Trujillo, 2018). Figure 4.35 shows examples of the attenuation interpolation curves used in this study. The calculated attenuation curves were in agreement with those reported in previous studies that used similar bubble characteristics (Louisnard, 2012a; Jamshidi and Brenner, 2013; Dogan and Popov, 2016; Trujillo, 2018). The attenuation predicted by the NH model in Figure 4.34 was found to increase sharply around the Blake threshold (Blake et al., 1999). For 5 μm bubbles, the Blake threshold was calculated to be 1.05 bar using:

$$P_{blake} = p_0 \left(1 + \left(\frac{4}{27} \frac{S^3}{1+S} \right)^{0.5} \right) \quad (91)$$

where the dimensionless Laplace tension $S = 2\sigma/(p_0 R_0)$.

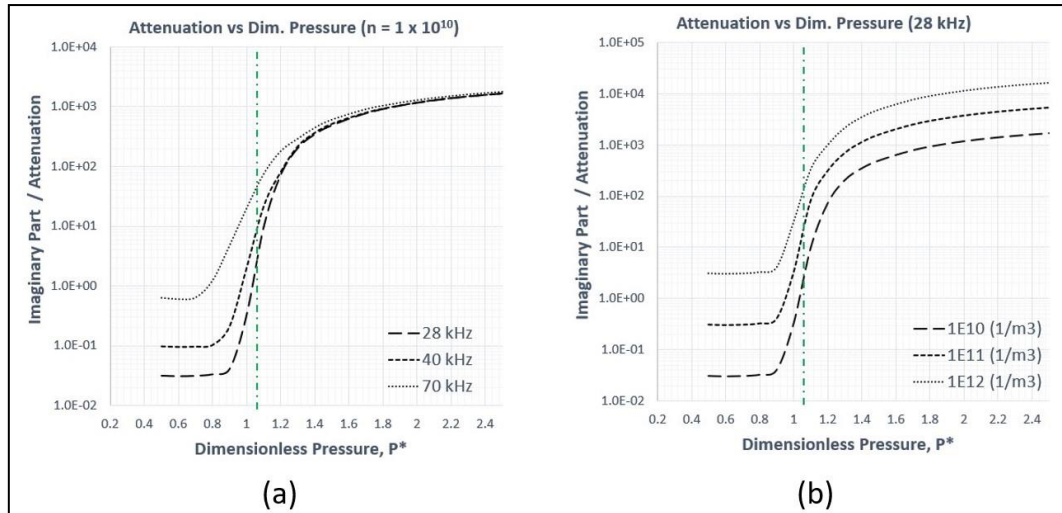


Figure 4.35: (a) Semi-log plot of attenuation as a function of dimensionless pressure for 28, 40 and 70 kHz; (b) Semi-log plot of 28 kHz attenuation as a function of dimensionless pressure at studied bubble densities. Vertical line represents Blake threshold at 1.05 bar.

Figure 4.35 (a) showed that attenuation increased with frequency just before the Blake threshold, and tends toward a linear approximation above it. In the simulations, this linear behaviour was used to extrapolate the wavenumber when P^* exceeds the upper limits of the interpolation curve. The effects of frequency on attenuation were found to be quite small for the range of studied frequencies. A case can be made that the effect of frequency is only important when resonance effects are significant, as discussed by Jamshidi et al. (2012). In this study, the range of resonance frequencies for an equilibrium bubble of $R_0 = 5 \mu\text{m}$ was approximated to be around 791 – 795 kHz (Commander and Prosperetti, 1989), which explained the reduced impact of frequency on the attenuation curves. In Figure 4.35 (b), the attenuation was noted to increase with higher bubble density magnitudes. This linear behaviour was expected since the model approximates the bulk attenuation by multiplying the dissipation of a single bubble by the bubble density in Eqn. (32).

Figure 4.36 shows the simulation results of the nonlinear Helmholtz model. The results showed lower acoustic pressure magnitudes compared to those of the pure-liquid and linear CP models due to the higher attenuation predictions. This observation is consistent with the results of pressure verification in Case Study 3. Similar to the linear CP case, three magnitudes of bubble density n were tested. As expected, the results showed that increasing the bubble density increased attenuation prediction, evident in the dimmer standing waves in Figure 4.36 (g), (h) and (i).

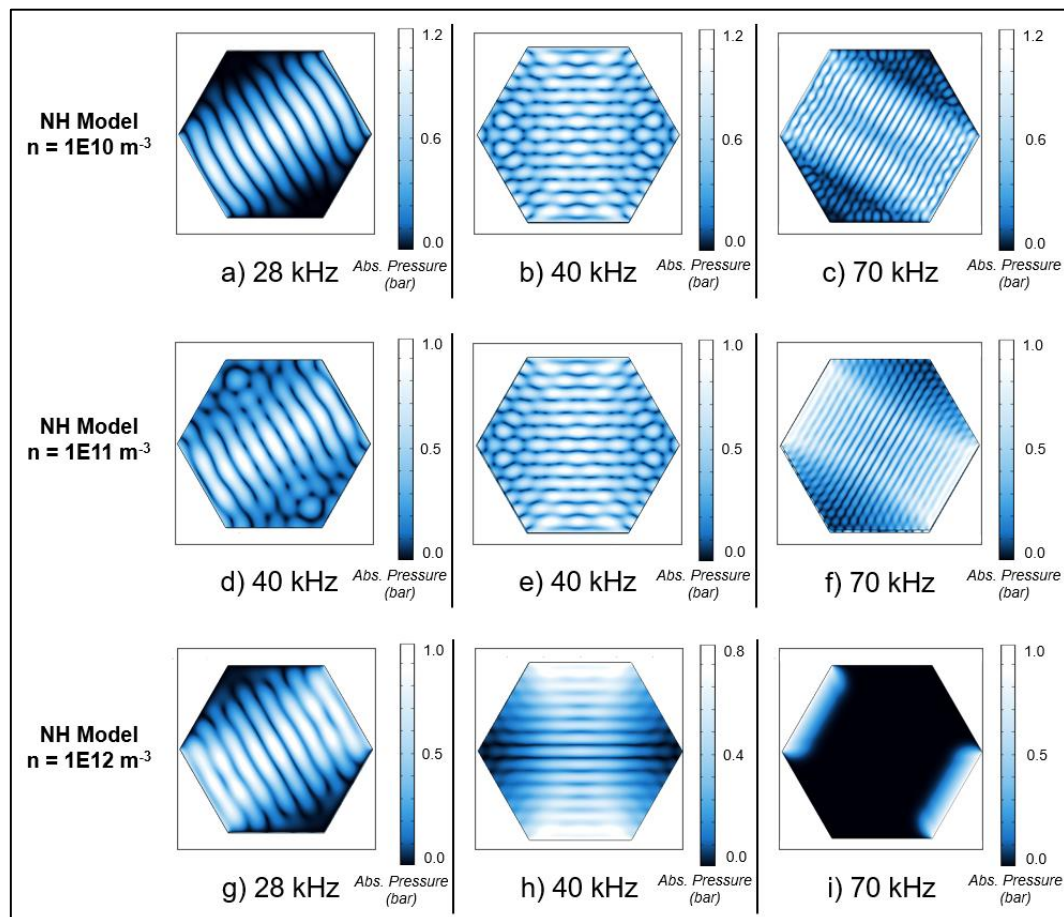


Figure 4.36: The absolute acoustic pressure fields predicted by the NH model for three frequencies at different bubble density magnitudes.

A notable drawback of the model was discovered during the solution phase. Numerical instability was observed when solving the NH model. In Case Study 3, it was reported that the NH model was unable to reach the required convergence error threshold of 0.1% [Section 4.1.2.7]. This issue was not encountered in this study. However, preliminary tests revealed that the speed of convergence depends on the quality of the interpolation curves. The NH interpolation curves in this study were obtained for a P^* interval of 0.1, with the exception of the region around the Blake threshold, where this interval was halved to account for the steep gradients shown in Figure 4.35. The dissipation interpolation curves were explicitly solved up to a P^* value of 2.5, in which higher values would result in difficulties in obtaining satisfactory solutions for the bubble dynamics, similar to the findings of Trujillo (2020). The implementation of the dissipation curves in the simulation software used a piecewise cubic interpolation function. Linear extrapolation was used for data points above the upper limit of the interpolation curve.

Out of all the studied frequencies, it was also noted that the 70 kHz cases took the largest number of nonlinear iterations to converge. On average, successful cases were found to converge within 60 iterations, even with $n = 1 \times 10^{12} \text{ m}^{-3}$. Additional test cases revealed that the quality of the mesh had a negligible effect on the convergence of the solver. This is shown in Figure 4.37, which describes the effect of mesh fineness (degrees-of-freedom, d.o.f.) on the convergence speed of the NH model solved for the 70 kHz, $1 \times 10^{10} \text{ m}^{-3}$ case. It was noted from the convergence plots that increasing the d.o.f. did not affect the number of iterations required to converge the simulation. This is clearly seen in Figure 4.37, where the number of iterations was found to be 45 for all three test cases.

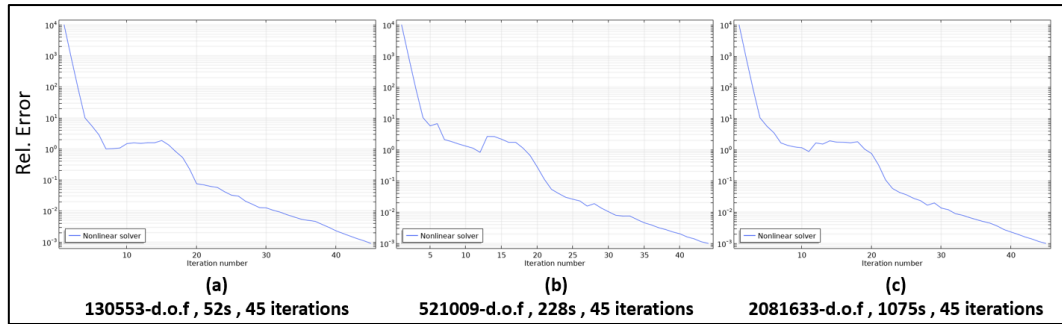


Figure 4.37: Three convergence plots of the nonlinear solver, for the NH simulations for the 70 kHz case with $n = 1 \times 10^{10} \text{ m}^{-3}$. The degree of freedom (mesh fineness), solution time, and number of iterations are shown for each case.

4.3.3.6 Qualitative Verification Results

A qualitative comparison was made to compare the standing wave patterns predicted by the studied models with the SCL images. Figure 4.38 describes the region of interest considered for the comparison. Due to uncertainties related to luminance data near the edges, the qualitative analysis only considered the rectangular region of interest ($182 \times 70 \text{ mm}$) along the propagation axis, as shown in Figure 4.38 (a). Figure 4.38 (b) shows an example of the investigated solver region of interest for the 40 kHz SCL image.

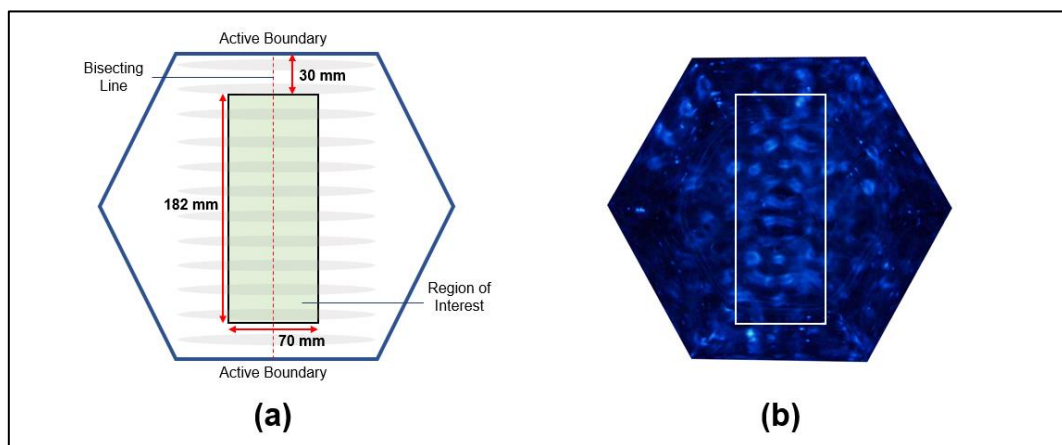


Figure 4.38: (a) Graphical description of the defined region of interest; (b) Example of the region of interest in the 40 kHz SCL image.

The region of interest defined in Figure 4.38 was cropped for all SCL images and absolute pressure plots. Figure 4.39 compares the regions of interest for the 28 kHz case. Standing wave formation cannot be distinctly identified for the 28 kHz SCL images, even with extensive image processing, as seen in Figure 4.39 (a). This result was previously discussed in Section 4.3.3.2. The presence of the ‘shielding effect’ near the vibrating walls was suspected to be the main reason, although there is no evidence to support this claim. However, several interesting observations can be made regarding the simulation results. The results in Figure 4.39 show an interesting result between the two bubbly-liquid models. The results of the linear CP model in Figure 4.39 (c), (d), and (e) clearly predicted the wavelength-shortening phenomenon when the bubble density was increased. On the other hand, the results of the NH model in Figure 4.39 (f), (g), and (h) resulted in qualitatively similar standing waves when the bubble density was increased. This result was found to be interesting since both models were solved using the same bubble field characteristics.

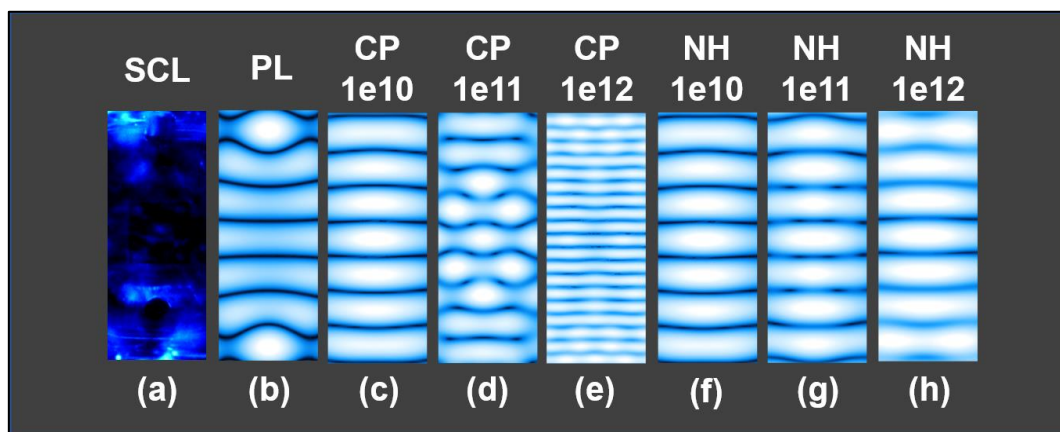


Figure 4.39: Qualitative comparison for the 28 kHz standing wave characteristics between the SCL image (a) and the investigated simulations (b) - (h).

It was hypothesised that the lack of obvious wavelength-shortening prediction in the NH model results was caused by the pressure-dependent wavenumber. To support the hypothesis, the variation of the wavenumber squared, k_c^2 predicted by the NH model was plotted and shown in Figure 4.40. Figure 4.40 shows the real and imaginary parts of the wavenumber squared along the propagation axis for the 70 kHz case, obtained from the solution of the NH model. The axes on the left represents the acoustic pressure magnitude, while the axes on the right show the complex components of the wavenumber squared.

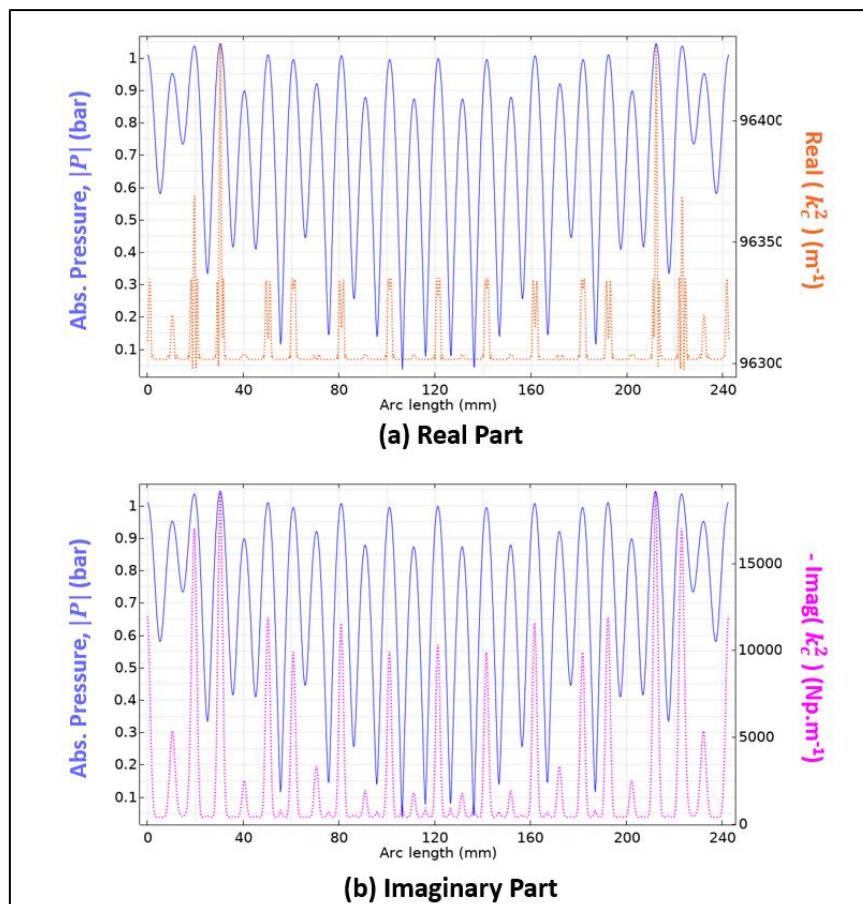


Figure 4.40: Real and imaginary parts of k_c^2 predicted by the NH model for the 70 kHz case, at $n = 1 \times 10^{10} \text{ m}^{-3}$.

It can be seen that the NH model only predicted high wavenumber values (which correspond to higher phase-speed reduction and attenuation) locally near the antinodes. Large spikes in k_c^2 were noted when the local pressure magnitude is near or above the Blake threshold of 1.05 bar. The acoustic pressure magnitudes predicted by the NH model for the studied system were mostly below the Blake threshold. Naturally, the wavenumber predictions converged to lower values, which led to the wavelength-shortening effect to be less distinct. This result outlines the difference between the prediction mechanism of the linear CP and the NH model. The linear CP model treats the entire working fluid as a uniform bubbly liquid. On the other hand, the NH model uses the Blake threshold to determine the magnitude of the bubbly-liquid effect using the wavenumber, which governs the phase-speed prediction.

Figure 4.41 compares the region of interest for the 40 kHz case. The SCL image of the 40 kHz case in Figure 4.41 (a) was found to show the clearest standing wave pattern of the three studied frequencies, for which yellow lines were added to mark the antinodes to facilitate a better qualitative analysis. The pure-liquid model was found to predict wavelengths that are longer than those of the SCL image. This observation is strong evidence for the need to consider bubble-field effects (which cause phase-speed reduction) in sonoreactor acoustics. Without the consideration of bubbles in the acoustic field of the sonoreactor, it will not be possible to characterise the phase speed-reduction effect. Interestingly, little emphasis had been placed on this topic in previous works. Analysis in Case Study 4 [Section 4.2] suggested that this is due to the small values of D_s/λ used, which did not clearly capture wavelength-shortening effects.

The prediction of phase-speed reduction is clear in the results of the linear CP model in Figure 4.41 (b), (c), and (d), albeit with noticeable deviations from the SCL observations in Figure 4.41 (a). A clearer representation of this deviation is shown by plotting the normalised luminance along the centre of each cropped image in Figure 4.42. The 1D profiles represent a normalised luminance value, in which the peaks can be used to approximately determine the antinode locations. Purple dashed lines were added to mark the antinodes captured in the SCL image. It was noted that the antinode separations are approximately uniform from the SCL luminance profile. This supports the assumption that the phase speed (and possibly the acoustic property) of the medium is uniform. This improved the viability of the linear CP model to characterise the sonoreactor, as the model assumes uniform acoustic properties in the domain. The results in Figure 4.42 show that the distances between the antinodes captured in the SCL image are longer than those of the CP, $n = 1 \times 10^{10} \text{ m}^{-3}$ case, but shorter than those of the $n = 1 \times 10^{11} \text{ m}^{-3}$ case. This finding suggests that the value of n that best characterises the bubble field of the 40 kHz system lies within the two values.

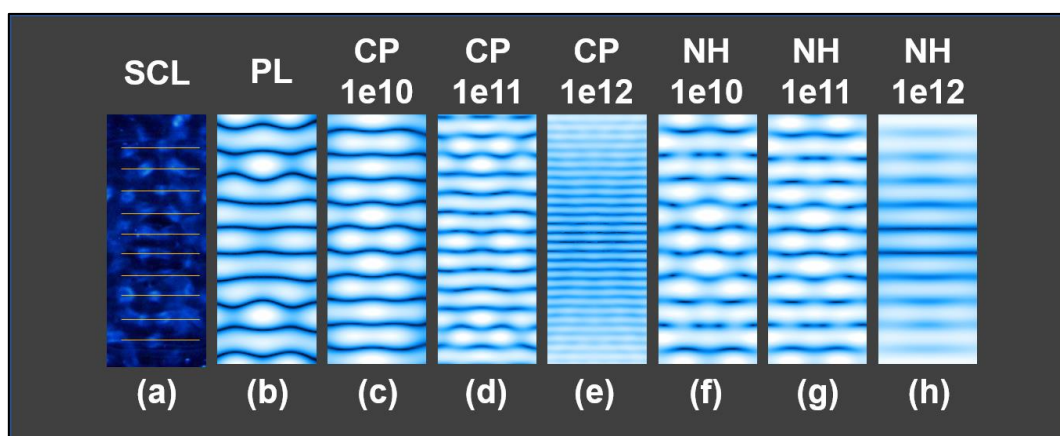


Figure 4.41: Qualitative comparison for the 40 kHz standing wave characteristics between the SCL image (a) and the investigated simulations (b) - (h).

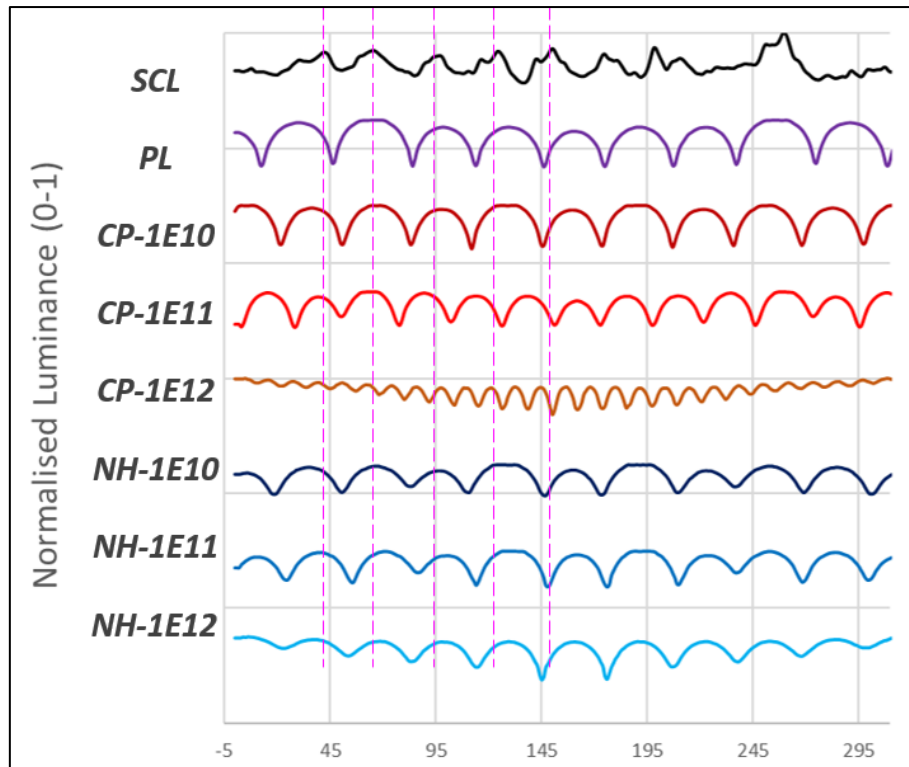


Figure 4.42: Normalised luminance profile plotted for the centre of the regions of interest for the 40 kHz case. Dashed lines mark the approximated locations of the SCL antinodes.

Comparisons involving the predictions of the NH model were less straightforward, as the phase speed varied across the simulation domain. Interestingly, the results in Figure 4.42 suggest that the antinode predictions of the NH model were similar to those of the pure-liquid model, albeit with slight deviations. This result was expected since the model only predicted a significant phase-speed reduction for regions that exhibit pressure magnitudes close to the Blake threshold, as shown in Figure 4.40. The NH model was found to predict some degree of phase-speed reduction, which is evident in Figure 4.42. Analysis of the edges of the profiles noted phase differences compared to the pure-liquid case, showing the presence of phase speed changes.

Figure 4.43 shows the side-by-side comparison for the 70 kHz case, and the normalised luminance profiles are plotted in Figure 4.44. The qualitative analysis of the antinode

prediction results yields findings similar to the 40 kHz case; however, the standing wave observed in the 70 kHz SCL image is less consistent in terms of antinode spacing. The thinner antinodal bands also made it difficult to clearly identify standing wave patterns. This increased the degree of uncertainty for the results of the verification study. It is clear from Figure 4.43 (e) and (h) that when the bubble density magnitude $n = 1 \times 10^{12} \text{ m}^{-3}$, both the linear CP and NH models over-predicted the attenuation, which eliminated any standing wave formation in the simulations. The pure-liquid model once again predicted a wavelength that was longer than that of the SCL image, and the wavelength-shortening effect was clearly found for three simulated cases of the linear CP model.

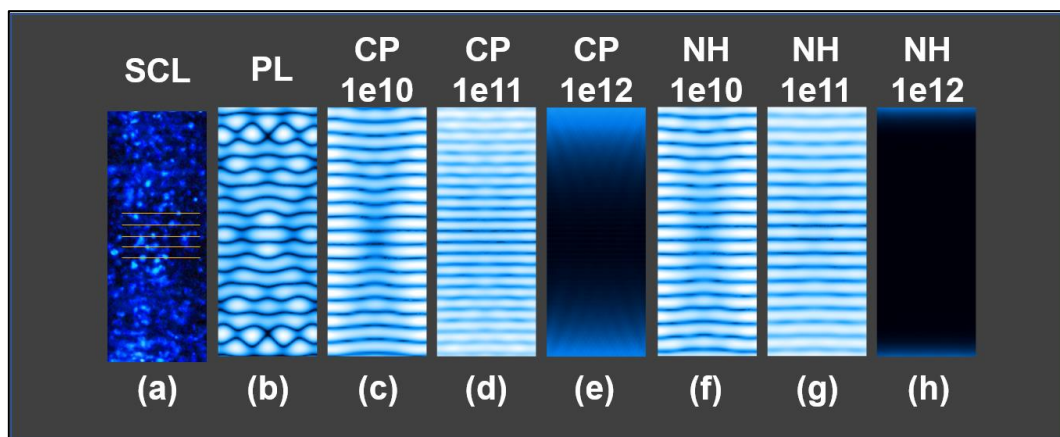


Figure 4.43: Qualitative comparison for the 70 kHz standing wave characteristics between the SCL image (a) and the investigated simulations (b) - (h).

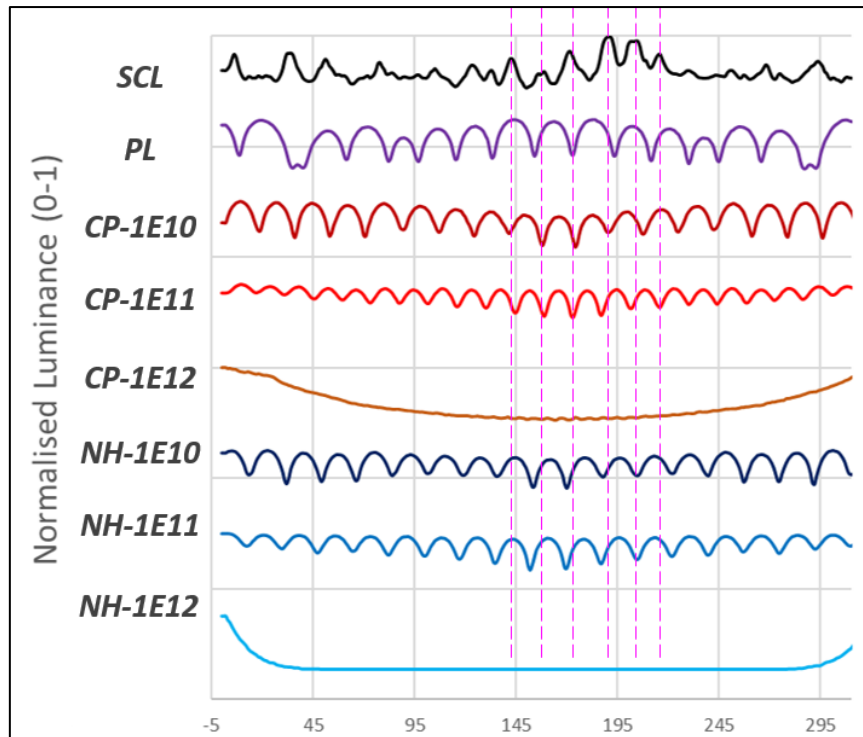


Figure 4.44: Normalised luminance profile plotted for the centre of the regions of interest for the 70 kHz case. Dashed lines mark the approximate locations of the SCL antinodes.

The antinode verification results yield several important findings. The following discussion is based on the 40 and 70 kHz cases, as the standing wave characteristics of the 28 kHz case were deemed insufficient for a confident analysis. For the pure-liquid approach, the antinode verification results showed that the model deviated from the SCL observations, as the predicted wavelengths were observed to be slightly larger. This is an expected outcome, as the pure-liquid model used did not account for any changes in phase speed due to bubbly-liquid effects.

The linear CP model managed to account for a uniform decrease in wavelength across the simulation domain. The characteristics of the solution predicted by the linear CP model strongly suggest that it is suitable for characterising systems that exhibit very uniform acoustic behaviours. For the bath-type configuration used for this work, this

is supported by the consistent antinodal separation observed in the SCL standing waves. Quantitative characterisation in Chapter 5 yields further information on this claim, as the antinode separations for the 40 and 70 kHz standing waves were noted to give a coefficient of deviation of 17 % and 21 % from the mean value. Nevertheless, the model still showed significant deviation in terms of wavelength prediction. It was hypothesised that deviations of the linear CP model from the SCL data were caused by an inaccurate specification of the bubble density n , rather than inaccuracies of the model itself.

Standing wave predictions of the NH model also resulted in qualitative deviation for the 40 and 70 kHz cases. Unlike the linear CP model, the more complex wavenumber prediction mechanism of the NH model made it difficult to pinpoint the exact reasons for the observations. The wavenumber squared k_c^2 that governs the phase speed prediction is nonlinear, as shown in Figure 4.40. This nonlinear mechanism is a complex result derived from energy balances of bubble dynamics (Louisnard, 2010; Trujillo, 2018). It remains unclear whether the deviations observed for the NH model can be attributed to inaccuracies in bubble field characterisation or caused by other factors. Currently, the validation efforts for the NH model were insufficient to fully understand the reliability of the model, particularly for large-scale sonoreactors. There was also sufficient reason to doubt the accuracy of the wavenumber prediction of the NH model, as it had not yet been fully validated under controlled conditions. Thus, limited remarks were made on the performance of the NH model.

The findings presented in this case study yielded important insights on not only the antinode prediction aspects of the studied models, but also on the methods involved

in the validation study. It should be emphasised that the orientation of the transducers in the hexagonal sonoreactor greatly enhanced standing wave contribution. This led to clearer antinodal regions to be captured in the SCL images. If such orientation was not used in large-scale validation, the travelling wave component would likely be dominant, leading to SCL images that shows streaming patterns (Choi et al., 2019). Last but not least, the findings presented in this case study would be applicable even in the presence of fluid flow, such as in a large flow-through sonoreactor. In general, given that the flow magnitude is relatively low and exhibits laminar characteristics, the pressure field can be modelled independently from the velocity field (Louisnard, 2017). It was strongly believed that the knowledge gained from this case study strongly contributed to the development of sonoreactor modelling strategies for large-scale applications, while also uncovered important knowledge gaps that should be addressed in the future.

4.4 Concluding Remarks for Chapter 4

Chapter 4 presented a comprehensive investigation into the performance of current acoustic pressure models in large ultrasonic baths. Pressure and antinode validation studies were presented in Case Studies 3 and 5 respectively, while Case Study 4 showed that the effect of geometry should be an important consideration when analysing antinode validation results.

Case Study 3 validated acoustic pressure models using hydrophone measurements for a 252 L bath-type sonoreactor. The pure-liquid model showed good agreement at lower frequency cases (35 and 72 kHz), but failed to account for increased attenuation

at higher frequencies (110 and 170 kHz) due to the lack of an explicit attenuation mechanism. The linear CP model showed mixed results. The model was found to exhibit the best performance at $n = 1 \times 10^{10} \text{ m}^{-3}$ except for the 72 kHz case due to the effects of internal reflection. The model was found to be strongly dependent on the bubble density specification n . This became evident when the agreement of the model was greatly improved upon tuning the bubble density. For the NH and nonlinear CP models, only preliminary insights were obtained from 1D simulations. Results suggested that current implementations of the nonlinear models overtuned the attenuation mechanism for the case of bath-type sonoreactors. This was evident in the significantly larger attenuations predicted by the models.

A major limitation encountered in Case Study 3 was the size of the model geometry, which limited the investigation to simplified simulation strategies. Future studies should address this by using better simulation hardware or by exploring more efficient simulation strategies. Another important limitation concerns the inability to properly model the effects of internal wall reflection. This greatly affected the validation results for the linear CP model. Both the PU-impedance and the matched-impedance methods failed to eliminate unrealistic pressure magnitude predictions of the 72 kHz, $n = 1 \times 10^{10} \text{ m}^{-3}$ case, while PML results were found to be too ideal for real systems. Current findings suggested a complex acoustic behaviour resulting from the effective phase speed, geometry, constructive interference, and reflection at the boundaries. It was noted that these effects should be minimised or eliminated in future studies to improve confidence in the results. One suggestion is to use very large geometries (open tanks) where reflection effects can be neglected.

Case Study 4 presents an interesting discussion on the effect of the geometry-to-wavelength ratio, D_S/λ , on the qualitative result of antinode validation studies such as SCL and foil mapping. The presented heuristic demonstration showed that even when the acoustic pressure field of a probe-beaker system ($D_S/\lambda = 1$) was solved using phase speed deviations of up to 20 %, the result still managed to yield qualitative agreement with experimental observations. The findings strongly showed that the effect of phase-speed reduction by bubbly liquids cannot be clearly captured by antinode characterisation methods in studies with small D_S/λ , both in simulations and experiments. The results also support the hypothesis which stated that the effect of wavelength-shortening in sonoreactors can be better detected if D_S/λ is large.

Based on extensive discussion on the topic, it was suggested that validation of phase speed mechanisms for acoustic pressure models should be done using large D_S/λ to minimise uncertainty. This claim was supported using an idealised 1D standing wave model which can be used to approximate the D_S/λ required to clearly the wavelength-shortening effect. Nonetheless, the model was noted to possess several key limitations, such as the neglect of boundary effects and the assumption of a pure standing wave. These limitations should be addressed in future work, and the model should be validated against physical test systems to better understand the effect of D_S/λ on antinode validation.

In **Case Study 5**, a comprehensive antinode validation was performed using SCL images obtained for a hexagonal sonoreactor. Observations suggested that phase-speed reduction in the bubbly liquid is significant. Validation results for the pure-liquid model outlined clear deviations in terms of antinode prediction due to neglecting

phase-speed reduction effects. The findings strongly suggest the need to account for phase-speed reduction when considering large sonoreactors to reduce antinode prediction errors. Among the studied models, the linear CP model best represented the phase-speed reduction effect observed in the SCL images, evident in the uniform wavelength reduction across the geometry. Similar to Case Study 3, the bubble density parameter n was noted to greatly affect the simulation results. It was suggested that the quality of the solution can be improved by tuning for a more suitable value for n . In contrast, the solutions of the NH model were less straightforward. The wavenumber predictions depended not only on the local pressure magnitude, but also on the Blake threshold and bubble field parameters. This made targeted analysis difficult and was left for future work. The results suggested that the NH model slightly underestimated the average phase-speed reduction. However, it remains unclear whether it was caused by inaccuracies in the model or by other factors. Based on these results, it was suggested that the linear CP model exhibited the strongest prospects in properly characterise the studied sonoreactor.

A key limitation of this study was the restricted region of analysis due to uncertainties in the SCL data. Future work should focus on obtaining higher-quality antinode validation data by employing strongly controlled test systems. Another limitation relates to data acquisition as SCL images were restricted to a 2D top-down perspective. Future work should consider the effect of sonoreactor depth on acoustical and optical reflections in the system. Last but not least, the uncertainties around the specification of bubble density parameter n in the bubbly-liquid models should be addressed. This was outlined as a key topic and was addressed in the subsequent chapter.

Chapter 5: Bubble Field and Multi-Frequency Considerations

Chapter 5 of this thesis documents the research efforts to further improve current modelling strategies by building upon knowledge gained from previous case studies. The linear CP model had shown promising potential in both validation studies presented in Chapter 4. However, model performance was found to be strongly affected by uncertainties related to bubble field parameters. The findings of Case Studies 3 and 5 strongly suggested the need to further address a key limitation related to the lack of a reliable method to specify the bubble field parameters. Thus, an in-depth review of this problem was carried out, and a potential solution was proposed. Additionally, it was also noted that the technology of multi-frequency power ultrasound had become increasingly popular within sonochemistry research. Thus, it was investigated whether the linear CP model could be extended to such use cases.

To achieve the above objective, the chapter begins by critically reviewing the topic of bubble field characterisation to identify current strategies used for bubble field characterisation in literature. This is followed by a theoretical derivation process to propose a novel semi-empirical approach for bubble field characterisation in large ultrasonic baths. The proposed strategy is subsequently demonstrated in Case Study 6. Last but not least, Case Study 7 presents an extensive investigation on the use of the linear CP framework for the modelling of multi-frequency acoustic pressure fields in a preliminary investigation.

5.1 Literature Review on Bubble Characterisation Strategies

The relationship between the acoustic pressure field and the bubble field in a sonoreactor is a well-researched topic (Metin et al., 1999; Metin, 2005). From a numerical modelling standpoint, a full model of the bubble field is a very complex problem and remains an active field of research (Ashokkumar, 2011; Naudé and Ellis, 2011; Sander et al., 2014; Pokhrel et al., 2016). For the bubbly-liquid models studied in this work, the problem was simplified using period-averaged properties and bubble field assumptions [Section 2.7.1]. In Case Studies 3 and 5, the specification of bubble field parameters mainly referenced past literature. In light of this, it was observed that current methods involve a significant degree of uncertainty, notably for the specification of β and n . This knowledge gap is a major problem for the applicability of bubbly-liquid models because the parameters strongly affect the accuracy of the solution as shown in previous validation results. This section presents an in-depth review to further shed light on this matter, with the goal of understanding current limitations, and to propose a novel solution in the subsequent section.

5.1.1 Experimental Measurements for Sonoreactor Bubble Fields

Data from experimental measurements of cavitation bubble fields are crucial to facilitate better modelling decisions. They also serve as important references when developing strategies for bubbly-liquid models. The measurement of cavitation bubble fields is an active field of research that spans multiple techniques. Table 5.1 summarised the relevant findings available in literature. Direct measurements of the bubble field mostly relied on optical techniques such as laser diffraction, X-ray, and

high-speed photography to obtain data. However, data resolution was found to be restricted by the detection limits of optical tools (Lee et al., 2005). Indirect methods such as the pulsed-ultrasound-sonochemiluminescence (PU-SCL) technique address this limitation by calculating bubble field properties using established mathematical models.

Table 5.1: Compilation of bubble measurements reported for cavitating systems in past works.

Author(s)	Description	Notable Results
Burdin et al., (1999)	<ul style="list-style-type: none"> • 20 kHz • LD and PD • Sonotrode in glass vessel 	<ul style="list-style-type: none"> • LD Sauter mean radius = 3.8 μm • PD Sauter mean radius = 5.0 μm • Bubble fraction noted to reduce with distance from the horn, in the magnitude of 1×10^{-5}.
Mettin et al., (1999)	<ul style="list-style-type: none"> • 20 kHz • Photography • Rectangular sonoreactor 	<ul style="list-style-type: none"> • Radius of 3.0 – 40.0 μm reported • No bubbles measured above 70.0 μm radius • Radius < 5.0 μm cannot be detected • Based on K-M bubble dynamics, equilibrium radius calculated reported to be around 1.0 – 5.0 μm
Tsochatzidis et al., (2001)	<ul style="list-style-type: none"> • 20 kHz • PD • Sonotrode in tank 	<ul style="list-style-type: none"> • Arithmetic mean radius = 3.3 μm • Sauter mean radius = 5.3 μm • Mostly considered bubble velocity measurements
Burdin et al., (2002)	<ul style="list-style-type: none"> • 20 kHz • LD and PD • Sonotrode in glass vessel 	<ul style="list-style-type: none"> • Three different methodologies were studied, and it was reported that the bubble radius is around 5 μm for the 20 kHz system • Bubble fraction reported around 1×10^{-4}
Avvaru and Pandit, (2009)	<ul style="list-style-type: none"> • 20 kHz • Hydrophone – FFT 	<ul style="list-style-type: none"> • Used the Minneart equation to infer bubble equilibrium radius based on broadband

	<ul style="list-style-type: none"> • <i>Ultrasonic bath</i> 	<ul style="list-style-type: none"> • <i>measurements, reported mean radius of 50-80 μm.</i> • <i>Unfortunately, the use of linear resonant models is often inaccurate, as pointed out by (Metin, Luther and Lauterborn, 1999)</i>
Kuroyama et al., (2011)	<ul style="list-style-type: none"> • <i>50 kHz</i> • <i>Optical Spectrometer</i> • <i>Floor irradiated glass cell (bath)</i> 	<ul style="list-style-type: none"> • <i>Mean radius reported to be around 2.5 μm.</i> • <i>Should be noted that the margin of uncertainty is quite large.</i>
Cairós and Mettin, (2017)	<ul style="list-style-type: none"> • <i>23 and 36.5 kHz</i> • <i>SL</i> • <i>Cavitation in Xenon saturated phosphoric acid</i> 	<ul style="list-style-type: none"> • <i>Largest radii reported up to 75.0 – 240.0 μm (23 kHz) and 50.0 – 80.0 μm (36.5 kHz), which is 1 – 10% of total bubbles.</i> • <i>23 kHz data was found to be modelled well using equilibrium radius of 36.7 μm.</i>
Reuter et al., (2019)	<ul style="list-style-type: none"> • <i>27.5 kHz</i> • <i>High-speed imaging</i> • <i>Floor irradiated sonoreactor (bath)</i> 	<ul style="list-style-type: none"> • <i>Informative study on the measurement of bubble sizes for difference bubble structure formations.</i> • <i>Despite vast differences in study conditions, the measured bubble sizes are reported to be in the range of 2 – 4 μm.</i>
Kuroyama, (2021)	<ul style="list-style-type: none"> • <i>27 kHz</i> • <i>Stroboscopic Imaging</i> • <i>Sonotrode in Vessel (horn)</i> 	<ul style="list-style-type: none"> • <i>Reported the bubble size profile below a sonotrode</i> • <i>Bubble size decreases with distance from sonotrode</i> • <i>Size ranges from 10 – 60 μm.</i>
Labouret and Frohly, (2002)	<ul style="list-style-type: none"> • <i>308 kHz</i> • <i>Void rate dissipation</i> • <i>Resonant electro-magnetic cavity (microreactor)</i> 	<ul style="list-style-type: none"> • <i>Bubble radius reported to be in range of 9.5 – 29.5 μm.</i> • <i>Bubble fraction during irradiation reported to be in the magnitude of 3E-4.</i> • <i>Variation covers a range of irradiation power and irradiation time.</i>

Lee et al., (2005)	<ul style="list-style-type: none"> • 525 kHz • PU-SL (configuration unclear) 	<ul style="list-style-type: none"> • Bubble equilibrium radius reported to be in range of 2.8 – 3.7 μm. • Time taken for bubble to dissolve reported to be around 400 ms.
Iida et al., (2010)	<ul style="list-style-type: none"> • 443 kHz • LD • Floor irradiated glass vessel (bath) 	<ul style="list-style-type: none"> • Parametric study covering a range of irradiation power and irradiation time. • Mean radius reported to be within range of 7.5 – 27.0 μm.
Xu et al., (2017)	<ul style="list-style-type: none"> • 1.2 and 5 MHz • Bubble dissolution • High-frequency focused ultrasound 	<ul style="list-style-type: none"> • Parametric study over several irradiation power and irradiation time. • Average bubble radius reported to be within 1 – 5 μm range.
Pflieger et al., (2021)	<ul style="list-style-type: none"> • 362 kHz • PU – SL • Glass sonoreactor 	<ul style="list-style-type: none"> • Equilibrium radius reported to be around 3 μm.

*LD = Laser Diffraction, PD = Phase Doppler Technique, PU = Pulsed Ultrasound, SL = Sonoluminescence, SCL = Sonochemiluminescence, FFT = Fast Fourier Transform

Most studies focused on bubble-radii measurements, which were commonly reported in terms of a Sauter or arithmetic mean. The reported values for a wide investigated range of frequencies were similar, although smaller measurements were observed at higher frequencies. The mean radii were reported to be within the range of 1-10 μm . Some studies also explicitly reported the value of equilibrium bubble radii, usually in the range of 1-5 μm (Mettin et al., 1999; Lee et al., 2005; Pflieger et al., 2021). On the contrary, data for the bubble fraction β or the bubble density n were found to be rare. Notable studies that have provided data for bubble fraction are those of Burdin et al.

(1999, 2002), who reported values measured near sonotrodes to be in the magnitude of 1×10^{-5} to $1 \times 10^{-4} \text{ m}^{-3}$. Although the values were referenced in previous simulation works (Louisnard, 2012a; Jamshidi and Brenner, 2013; Fang et al., 2018), this study argues that they are at best an approximation due to the small sample size.

Most of the measurements summarised in Table 5.1 were carried out for small-scale systems, primarily using horn-type configurations. The lack of data for larger, bath-type systems is once again a matter of concern, since there is little evidence which supports extending small-scale data for larger geometries. Current knowledge suggests that the bubble field characteristics of horn- and bath-type sonoreactors are noticeably different (Mettin et al., 1999; Žnidarčič et al., 2015; Ma et al., 2017; Reuter et al., 2019). In light of this, there is little choice in this work but to rely on educated assumptions and extrapolated data until further information is available.

5.1.2 Bubble Field Characterisation Strategies in Past Works

Table 5.2 presents a compilation of the values used to characterise the parameters R_0 , n and β in past simulation works. Specifications for R_0 were found to lie within the range of values reported in Table 5.1. Additionally, earlier studies favoured the polydisperse radii specification, while the simpler monodisperse assumption is more popular recently. The impact of this choice has not yet been fully explored, and shall be discussed in Section 5.1.2.1.

Table 5.2: Compilation of bubble field parameters used in past numerical investigations.

Author(s)	Study Description	Bubble Characterisation Parameters			Remarks
		β	R_0	n	
Dahlem et al., (1999)	Exp. Valid. w/ Dosimetry; Sonotrode-Beaker; 20 kHz; 300 and 1000 W	0.01	3 – 3000 μm Polydisp. (Gaussian)	-	Linear CP model
Dähnke and Keil, (1999)	Theoretical Design w/ Simulation; Cylindrical Vessel w/ Floor Transducer; 20 kHz and 50 kHz; Variable power.	Nonlinear n ; $\beta = f(P)$; [1E-4 to 1E-1]; Upper $ P $ 5 MPa and 10 MPa	100 – 3000 μm Polydisp. (Gaussian)	-	Wave eqn.
Dähnke et al., (1999b);	Exp. Valid. w/ sonotrode; Ultrasonic Tank w/ Floor Transducer, 23 kHz	Nonlinear n ; $\beta = f(P)$; $1\text{E-}4 < \beta < 1\text{E-}1$; $P_{Bl} < P < 50$ MPa	5 – 3000 μm Polydisp. (Gaussian)	-	w/ attenuation calculated from nonlinear CP model
Servant et al., (2000; 2001; 2003),	Exp. Valid. w/ SCL; Foil Test; Sarvazyan Method; Cylindrical Reactor w/ Floor Transducer; 28, 200, 477, 540 kHz	Nonlinear n ; $\beta = f(P)$; Unspecified range	1 – 1000 μm Polydisp. (Gaussian)	-	
Jamshidi et al., (2012)	Theoretical Design w/ Simulation; Sonotrode Microreactor; 10 – 30 kHz; 20, 110, 200 W	Nonlinear n ; $\beta = f(P)$; $\beta = 2 \times 1\text{E-}9 P $; 1 bar < $ P $ < 50 MPa	150 μm Monodisp.	-	Compared PL, linear CP, and nonlinear CP models.
Louisnard, (2012a)	Valid. w/ Bubble Data; Theoretical 1D Simulation	$\beta = 5\text{E-}5$	5 μm Monodisp.	9.5E10 m^{-3}	NH model (Louisnard formulation)
Jordens et al., (2013)	Theoretical Design w/ Simulation; Microchannel Reactor; 20 kHz; 30 W	Nonlinear n ; $\beta = f(P)$; $\beta = 2 \times 1\text{E-}9 P $; 1 bar < $ P $ < 100 bar	Minneart Eqn. Estimation: $R = 3/f$ Monodisp.	-	Nonlinear CP model
Dogan and Popov, (2016)	Theoretical Model Testing; Custom Sonoreactor Bath; 20 kHz	Parametric β ; 1E-5, 5E-5, 2E-4	5 μm Monodisp.	-	Compared linear CP vs NH model (Jamshidi formulation)
Lebon et al., (2017)	Exp. Valid. w/ Design; Sonotrode - Beaker	-	1-10 μm Polydisp.	1E11 m^{-3}	First-order N-S w/ bubble attenuation

Hussain and Janajreh, (2017; 2018)	<i>Theoretical Design w/ Simulation; Custom Horn Sonoreactor; 20 kHz; 100W</i>	<i>Nonlinear n; $\beta = f(P)$; $\beta = 2 \times 1E-9 P$; $P_{Bl} < P < 100$ MPa</i>	<i>Minneart Eqn. Estimation: $R = 3/f$</i>	-	
Fang et al., (2018)	<i>Streaming Study w/ PIV; Sonotrode – Beaker System; 20 kHz; 240 W</i>	<i>Nonlinear n; $\beta = f(P)$; $\beta = 2 \times 1E-9 P$</i>	<i>200 μm Monodisp.</i>	-	<i>Nonlinear CP model</i>
Lebon et al., (2019)	<i>Streaming Study w/ PIV; Sonotrode – Tank System; 20kHz</i>	<i>$\beta = 1E-5; 1E-4; 1E-3$; If $P_{Bl} < P$</i>	<i>5 μm Monodisp.</i>	-	
Trujillo, (2018; 2020)	<i>Model Validation w/ Bubble Data; Pressure Valid.; 20 kHz; Sonotrode – Beaker System</i>	-	<i>3 μm Monodisp.</i>	<i>3E7 – 3E8 m⁻³</i>	<i>NH model (Trujillo formulation)</i>
Chen et al., (2021)	<i>Streaming Study w/ PIV; Ultrasonic Tank System</i>	-	<i>5 μm Monodisp.</i>	<i>5E9 m⁻³</i>	

With reference to Table 5.2, the choice of bubbly-liquid model was found to be related to the specification of bubble parameters. Those that involved the linear CP and NH models tend to treat n or β as a constant, while the nonlinear n specification forms the basis for the nonlinear CP model and its variants. The popularity of the nonlinear n approach is interesting considering that it was developed based on simplified assumptions by Dähnke et al. (1999a).

It is clear that the range of values used for n and β varied greatly across studies, which was hypothesised to be the result of limited experimental data. Most recent studies specified n within the magnitudes of $1 \times 10^8 - 1 \times 10^{11} \text{ m}^{-3}$ (a similar range was used in Case Studies 3 and 5). The uncertainties surrounding the bubble-field parameters had also been commented upon by several authors. Servant et al. (2001b) noted that

one should exercise caution when adapting data that did not explicitly report the bubble equilibrium radius. Recent studies also explicitly highlighted the difficulties of specifying a reliable value for the bubble fraction or bubble density (Delacour et al., 2020; Sarac et al., 2020; Trujillo, 2020).

5.1.2.1 *Monodisperse vs. Polydisperse Approach for Bubbly-Liquid Models*

A brief discussion provided on the specification of the radii distribution for R_0 shall be provided. The following only considered the CP model, since a polydisperse NH model remains an unexplored problem, which is left as a suggestion for future work. The linearisation efforts of Commander and Prosperetti (1989) yield two wavenumber formulations for the CP model. The monodisperse formulation previously introduced in Section 2.5.1:

$$k_c^2 = \frac{\omega^2}{c_l^2} + 4\pi \frac{\omega^2 R_0 n}{\omega_0^2 - \omega^2 + 2ib\omega} \quad (23)$$

and the polydisperse formulation that accounts for a radii distribution for R_0 :

$$k_c^2 = \frac{\omega^2}{c_l^2} + 4\pi \int_0^\infty \frac{\omega^2 R_0 n(R_0)}{\omega_0^2 - \omega^2 + 2ib\omega} dR_0 \quad (92)$$

Although both formulations had been used in the past, there is surprisingly little discussion about the impact of this choice. The following presents a simple analysis, which attempts to show that current implementations of the polydisperse formulation in literature (Dähnke et al., 1999a; Servant et al., 2000) are similar to the monodisperse assumption.

The CP dispersion relation is just a variation of a linear scattering model proposed by Foldy (1945), who postulated that the acoustic wavenumber for stable bubble fields can be generalised as:

$$k_c^2 = \frac{\omega^2}{c_l^2} + 4\pi G = \frac{\omega^2}{c_l^2} + 4\pi[M(\mathbf{r}, R_0)N(\mathbf{r}, R_0)] \quad (93)$$

The parameter G relates to the dissipation per unit volume. It is the product of the bubble scattering function $M(\mathbf{r}, R_0)$ and the bubble distribution $N(\mathbf{r}, R_0)$. Equating the monodisperse assumption in Eqn. (23) to Foldy's generalised formulation yields the following:

$$G_{mono} = M(\mathbf{r}, R_0)N(\mathbf{r}, R_0) = \frac{\omega^2 R_0 n}{\omega_0^2 - \omega^2 + 2ib\omega} \quad (94)$$

The bubble dissipation factor $M(\mathbf{r}, R_0)$ and the bubble distribution $N(\mathbf{r}, R_0)$ corresponds to:

$$M(R_0(\mathbf{r})) = \frac{\omega^2 R_0}{\omega_0^2 - \omega^2 + 2ib\omega} \quad (95)$$

$$N(R_0(\mathbf{r})) = n \quad (96)$$

$M(R_0(\mathbf{r}))$ can be interpreted as the dissipation effect of a single bubble with equilibrium radius R_0 . Multiplying this factor by the density of bubbles with the same R_0 (in this case, n) gives the total dissipation per unit volume. Since R_0 is a constant, the dissipation factor M_{R_0} is also constant. Thus, for the monodisperse assumption, the dissipation per unit volume G_{mono} depends on the local bubble density n . The specification of n is usually done using two methods. A spatially constant bubble density assumption, $N(R_0(\mathbf{r})) = \text{constant}$, yields the simplest characterisation of the bubble field which results in an analytical CP wavenumber. On the other hand, the

bubble density can also be a function of space, $N(R_0(\mathbf{r})) = n(\mathbf{r})$. In bubbly-liquid models, this results in inhomogeneous dissipation effects in the domain.

A similar analysis can be done for the polydisperse formulation in Eqn. (92). It is instructive to note that the equilibrium radius takes the form of a time-averaged polydispersity, which is the result of the continuity assumption [Section 2.4]. Essentially, the average contribution of multiple equilibrium radii is considered for a *single point in the domain*⁶. Although the expression for $M(\mathbf{r}, R_0)$ and $N(\mathbf{r}, R_0)$ is similar to the monodisperse case, the main difference lies in how the total dissipation effect per unit volume, G_{poly} is defined. The polydisperse CP formulation requires the contribution of each equilibrium radius to be summed:

$$G_{poly} = \text{sum}[M(\mathbf{r}, R_0)N(\mathbf{r}, R_0)] = \int_0^\infty \frac{\omega^2 R_0 n(R_0)}{\omega_0^2 - \omega^2 + 2ib\omega} dR_0 \quad (97)$$

It is clear that this approach added an additional layer of complexity for the bubble field characterisation, since the bubble density is now a function of both space and equilibrium radius, $n(\mathbf{r}, R_0)$. If $n(\mathbf{r}, R_0)$ is assumed to be spatially constant, then the following condition would also have to be satisfied:

$$n(\mathbf{r}) = \int_0^\infty n(R_0) dR_0 = \text{constant} \quad (98)$$

Realistically speaking, the bubble equilibrium radii in real systems are undeniably polydisperse in nature, as reported by the studies compiled in Table 5.1. An important distinction to be made is that empirical evidence only suggests spatial polydispersity

⁶ Instead of multiple bubble radii existing at a single infinitesimal point in space, the expression instead considers a time-averaged contribution of multiple bubble sizes (e.g. average contribution of various bubble sizes passing through a single point in space).

and not time-averaged polydispersity. A case can be made that spatial polydispersity and time-averaged polydispersity are equivalent only when perfect mixing is achieved in the bubble field⁷. This could be the case for small, horn-type configurations where strong mixing effects had been observed (Tiong et al., 2019). The complexity further increases if one considers that the radii distribution can also be fixed in space (constant polydispersity) or vary as a function of space (spatial polydispersity). There are several suggestions in which spatial polydispersity could be implemented; however, many of them remain impractical within the scope of this work and are left for future discussions. Only constant polydispersity methods had been applied in sonoreactor simulations. The studies of Dähnke et al. (1999a, 1999b) and Servant et al. (2000) characterised R_0 as a fixed Gaussian distribution. The approach was inspired by the work of Commander and Prosperetti (1989) who used a truncated distribution:

$$n(R_0) = C_b \exp \left[-\frac{(R_0 - R_{0,mean})^2}{\sigma_B^2} \right], \quad R_{0,min} < R < R_{0,max} \quad (99)$$

The method involves specifying a mean bubble equilibrium radius $R_{0,mean}$, and a standard deviation σ_B^2 . The distribution was truncated at $R_{0,min}$ and $R_{0,max}$ and a tuning parameter C_b is necessary to satisfy bubble fraction specifications such as Eqn. (98). Further scrutiny revealed that this approach is not much different from the monodisperse assumption. To elaborate, if the radii distribution is fixed, then $G_{poly}/n(\mathbf{r})$ is essentially a constant. Thus, the total dissipation per volume for both methods varies linearly with the spatial bubble density n . A graphical representation

⁷ Under perfect mixing conditions, all bubble radii in the domain can be assumed to travel through all space coordinates when view from a time-averaged perspective.

of this argument is shown in Figure 5.1. The main difference is that the constant polydisperse approach relies on a scattering function calculated for a *fixed bubble group* instead of a *single bubble*. Thus, the Gaussian radii specification can be thought to be analogous to a monodisperse assumption, specified using an *effective equilibrium radius* representing the dissipation of a group of bubbles.

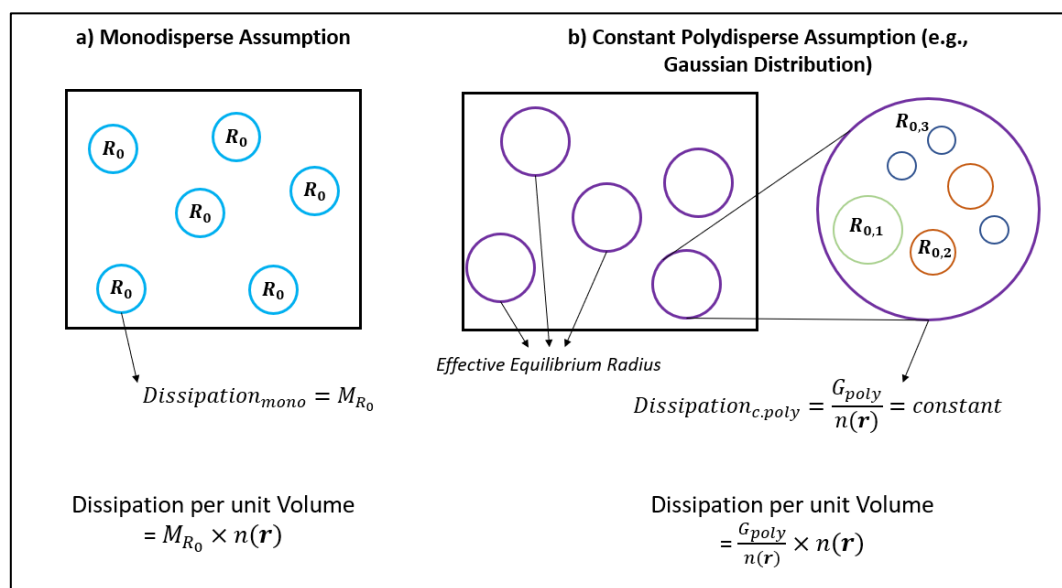


Figure 5.1: Graphical explanation depicting the similarities between the constant polydisperse approach and the monodisperse approach.

Based on this heuristic analysis, it is argued that there is currently little incentive to use the spatially constant polydisperse approach over the much simpler monodisperse assumption. Coincidentally, recent applications of the CP model opted for the latter, albeit with limited discourse on this matter (Fang et al., 2018; Hussain and Janajreh, 2017, 2018). This argument also justifies the constant equilibrium radius used in Case Studies 3 and 5.

On paper, a polydisperse formulation can better approximate real bubble fields. However, its implementation in bubbly-liquid models remains understudied. Additionally, given that there are larger sources of uncertainties, such as bubble density specifications, it is not clear whether the added accuracy would be significant. However, with developments in bubble measurement and modelling studies, it is expected that the polydisperse formulation will become increasingly feasible in the future.

5.1.2.2 Uniform vs. Pressure-Dependent Bubble Density

The simplest approach specifies n as a constant, which assumes that the bubble distribution is perfectly uniform. This assumption was used in Case Studies 3 and 5. This study argues that this simplified assumption of uniform bubble distribution is applicable when considering bath-type configurations. This claim is supported by the uniform SCL activity observed in Case Study 5, which can be related to the distribution of cavitation bubbles in the system (Sutkar and Gogate, 2009).

Another common specification for the bubble density was proposed by Dähnke et al. (1999a) in light of limited experimental data. In their work, the bubble fraction / bubble density was specified as a function of acoustic pressure magnitude, $|P|$. From a modelling perspective, this method incurs a large numerical cost since it introduces nonlinearity into the bubbly-liquid model (Jamshidi et al., 2012). However, it allowed the CP model to exhibit mechanisms similar to the NH model, where attenuation is 'self-regulating'. This causes the bubbly-liquid model to predict larger attenuation in regions with higher pressure magnitudes.

The perceived motivation behind the nonlinear n approach is attributed to the common observation that high-pressure regions tend to result in stronger cavitation behaviour, which translates to larger bubble fractions. Alternatively, one could also attribute the increased bubble density to Bjerknes motion towards antinodal regions (Mettin et al., 1997). Even then, there remains the problem of accurately defining the relation between bubble density and pressure magnitude. Currently, most studies adopted the original assumption of Dähnke et al. (1999a) who assumed a linear relationship by allocating $\beta = 0.1$ to a pressure magnitude of 500 bar (Jamshidi et al., 2012; Fang et al., 2018). Similar to the NH model, current evidence suggests that the attenuation predicted by the nonlinear CP approach is overtuned, as shown in Case Study 3. Although the errors from the overtuned attenuation may not be obvious when modelling sonotrodes, the results in Case Study 3 suggest that the linear relationship between n and $|P|$ requires further fine-tuning if it is to be used for large-scale baths.

5.1.2.3 Piecewise Specification of Bubble Density / Fraction

Another commonly adopted strategy proposed to characterise the bubble field was also first used in the simulation work of Dähnke et al. (1999a). The piecewise specification defines an additional characteristic for β or n which can be mathematically represented as:

$$n = \begin{cases} n, & \text{if } |P| > P_B \\ 0, & \text{if } |P| < P_B \end{cases} \quad (100)$$

The parameter P_B is the Blake threshold which is a minimum theoretical pressure to achieve transient cavitation (Blake et al., 1999). The piecewise condition was noted to

be quite popular in past works (Servant et al., 2000; Louisnard, 2012a; Jamshidi et al., 2012; Hussain and Janajreh, 2017). This work argues against the applicability of this assumption, as it strongly contradicts observations obtained from bubble field experiments reviewed in Section 5.1. The specification essentially constrains β or n to be zero when the local pressure magnitude is below the Blake threshold P_B . A simple review of experimental measurements reported by the studies in Table 5.1 revealed that this is unlikely, as physical bubbles do not simply disappear if the pressure magnitude falls below a specific threshold.

The specification was hypothesised to be a result of contradicting interpretations for the purpose of bubbly-liquid models. The piecewise assumption would be valid if one considers the bubbly-liquid model to only account for cavitating transient bubbles. From this perspective, the ‘vanishing’ of bubbles below the Blake threshold is applicable. Instead, this study argues that the bubbly-liquid models serve as an approximation to model the effects of both stable and transient bubbles in the sonoreactor. Even in the absence of transient cavitation, the effect of stable bubbles on the acoustic field is significant, and thus must be included. Other arguments include considerations for numerical stability, since the piecewise specification would cause a strong discontinuity in the wavenumber due to setting the bubble fraction to zero. Based on these arguments, the piecewise specification was not used in the modelling strategies of this work.

5.2 Derivation of the Semi-Empirical CP Method

The results of Case Studies 3 and 5 have highlighted the promising potential of the linear CP model as a suitable choice for the modelling of large-scale sonoreactor acoustics. However, there is still a need to address uncertainties related to the specification of bubble field parameters, notably the bubble density n . To address this limitation, an attempt to improve the linear CP modelling strategy was developed and proposed by considering a semi-empirical approach.

5.2.1 Reviewing Empirical Tuning Practices in Sonoreactor Acoustics

The phrase ‘empirical tuning’ henceforth constitutes a justified and educated manipulation of certain aspects of a simulation model against an experimental benchmark. Semi-empirical models are common in acoustics, especially in the field of atmospheric and ocean acoustics to characterise complex changes in acoustic properties (Ginsberg, 2018; Yu et al., 2021). The prospects of empirical methods in sonoreactor acoustics constitute an interesting discussion. Currently, it can be argued that empirical tuning is necessary to obtain some of the required physical properties of the bubble field, as current developments suggest that the knowledge gaps outlined in Sections 5.1 and 5.1.2 would not be resolved in the near future. The urgency that prompted this suggestion was the impact of bubble-field parameters on the simulation results. This section presents a well-defined framework for a semi-empirical approach which can be easily reproduced in future studies.

Historically, attempts to circumvent the uncertainties surrounding the specification of n and β using empirical tuning methods had been published. Vanhille and Campos-

Pozuelo (2005) tuned the value of n against hydrophone profiles obtained for a probe-beaker system for a simplified inhomogeneous wave equation model. The work of Yasui et al. (2007) also roughly determined the attenuation magnitude for a pure-liquid model by qualitatively comparing simulation results against SCL images. Recently, Trujillo (2020) adopted a similar approach as Campos-Pozuelo et al. (2005), where the NH model was parametrically solved for a range of n and compared against hydrophone measurements. The characterisation study of Delacour et al. (2020) also tuned the bubble fraction β in the NH model by matching the pressure magnitude predicted at the centre of the sonoreactor to a hydrophone measurement.

It is interesting to note that all the above works tuned either β or n against pressure measurements, except the work of Yasui et al. (2007). Several comments are provided on this matter. Assuming that the goal is to characterise the acoustic property of the bubbly liquid, this work argues that using acoustic pressure as a tuning reference is not preferred. The main problem stems from the fact that the acoustic pressure field prediction is not a sole function of the acoustic property, but also the boundary conditions, geometry, mesh, and solver configuration. Figure 5.2 shows the dependencies within the framework of an acoustic pressure simulation. It is clear that by tuning the acoustic pressure solution against hydrophone measurements, one risks ‘tuning over’ the need to properly model other variables, which could compromise simulation integrity. Instead, it is suggested that empirical tuning should be restricted to measurements that depend solely on the acoustic property of the working fluid, such as the wavelength. This is because the wavelength is strictly a function of the sound speed. Based on this idea, the following section presents a semi-empirical

approach, which involves tuning the bubble density parameter from wavelength measurements.

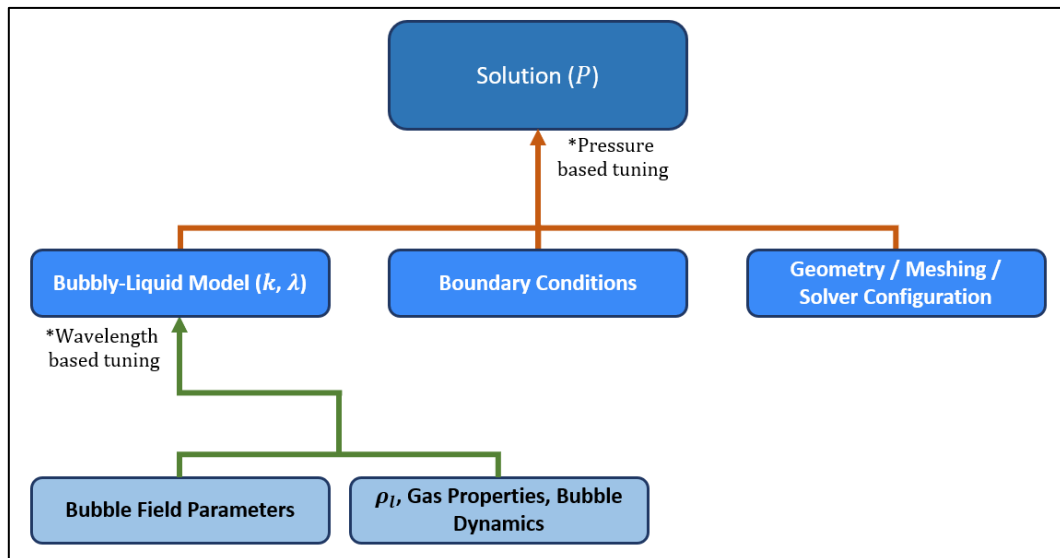


Figure 5.2: Representation of the dependencies within an acoustic pressure simulation framework.

5.2.2 Establishing the Basis of the Semi-Empirical Characterisation Approach

It is proposed that the value of the bubble density, n can be determined from empirical wavelength observations. The scope of this method is restricted to the characterisation of simple bath-type configurations with strong standing wave characteristics, for which the reason shall be made clear. The full semi-empirical characterisation method consists of two main steps. The first step involves the tuning of the bubble density parameter n , and the second step uses the tuned n to solve the acoustic pressure model. The proposed method depends on the theoretical foundations of the monodisperse linear CP model, and thus all associated assumptions

of the model are inherited. Another key prerequisite is that reliable wavelength measurements should be obtainable for the system of interest.

5.2.2.1 Key Assumptions of the Proposed Framework

The assumption of the monodisperse linear CP model is reiterated:

- The bubble liquid behaves as a continuum.
- Acoustic bubble behaviour approximated using linearised bubble dynamics.
- The monodisperse assumption is applicable for R_0 .
- The bubble distribution is perfectly uniform in space, so n is constant.
- The liquid is incompressible, thus ρ_l is constant.
- The properties of the gas within the bubbles resemble those of air.

The analytical dispersion relation of the linear CP model is important for the proposed tuning method. Previous results in Case Studies 3 and 5 had shown that the model offered a good balance between practicality and reliability when considering large-scale ultrasonic baths. It was also noted to be sensitive, yet predictable, to changes in bubble-field parameters, which was found to be a useful property for tuning. The CP model was also more comprehensively validated within its range of applications by Commander and Prosperetti (1989), as opposed to the newer NH model.

5.2.2.2 Establishing the λ -Tuning Strategy for Bubble Density n

Several ways of obtaining the bubble density n for a sonoreactor were considered in this work. A straightforward bubble field measurement using the methods discussed in Section 5.1 can be impractical if one considers large sonoreactors. However, if the

bubble field can be assumed to be uniform and homogeneous, the average phase speed can be related to n using the dispersion relation of the linear CP model. Interestingly, this concept had been applied in commercial bubble field measurement tools (Duraismami et al., 1998). The problem with obtaining the average phase speed is that most conventional methods require acoustic measurements. While they work well in stable bubbly liquids (e.g. aerated tanks), it was hypothesised that their use in sonoreactors is limited by cavitation noise. Large broadbands reported by hydrophone measurements in sonoreactors support this claim (Campos-Pozuelo et al., 2005; Avvaru and Pandit, 2009; Yasuda et al., 2018).

Instead of measuring the phase speed in the working fluid, it is proposed that wavelength measurements are obtained and then related to the phase speed. The wavelength and phase speed are related using the simple equation (Pierce, 1989):

$$\lambda = \frac{c_l}{f} \quad (101)$$

Methods that allow the wavelength to be determined, such as SCL and foil mapping, are already well established in sonoreactor research [Section 1.2.2.1]. Case Study 4 already introduced the variable h which is the half-wavelength. The measurement for h can be obtained from SCL and foil mapping results. The main caveat is that reliable measurements for h can only be obtained if distinct and uniform standing wave characteristics can be observed.

5.2.2.3 Relating λ to n Using the CP Dispersion Relation

The monodisperse, linear CP model allows the working fluid to be characterised using a single phase-speed, which can be related to wavelength measurements in Eqn. (101).

The dispersion relation of the model in Eqn. (23) also allow the value of λ to be directly related to a corresponding value of n . For the complex valued wavenumber k_c , the predicted phase speed can be obtained from the real part of the wavenumber (Commander and Prosperetti, 1989):

$$c_c = \frac{\omega}{\text{real}(k_c)} \quad (102)$$

A useful way to visualise this relationship is to plot the phase speed and wavelength as a function of bubble density, as shown in Figure 5.3. The data shown were plotted using the physical properties in Table 4.9 used in Case Study 5 for the 40 kHz system. The plot clearly established how the wavelength measurement can be related to a corresponding value of bubble density.

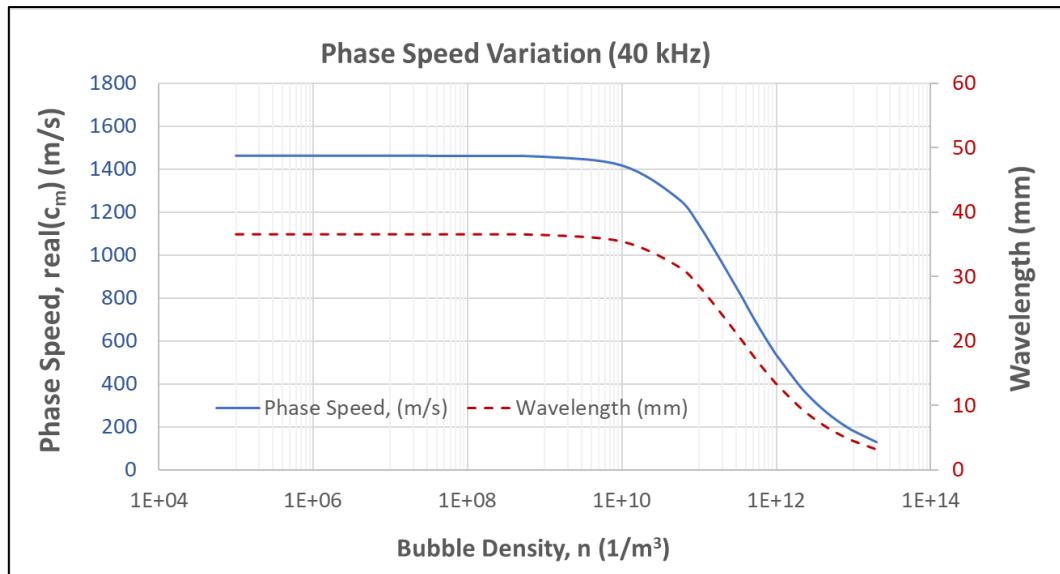


Figure 5.3: Relationship between the phase speed and wavelength as a function of the uniform bubble density, plotted at 40 kHz and bubble radius of $5 \mu\text{m}$.

5.2.2.4 Procedure for the Proposed Semi-Empirical Approach

It is henceforth summarised the procedure for applying the semi-empirical approach:

1. Standing wave data are obtained for the sonoreactor of interest, using methods such as SCL and foil mapping.
2. Obtain the measurements for the wavelength as twice the distance between the antinodal points in the standing wave ($\lambda = 2h$).
3. The corresponding value for n is determined using the dispersion relation of the monodisperse linear CP model using interpolation plots (Figure 5.3).
4. Lastly, solve the sonoreactor acoustics model along with other modelling aspects (boundary conditions, meshes, etc.) using the linear CP model and the tuned bubble density.

5.3 Case Study 6: Demonstrating the Semi-Empirical Tuning Approach

This short study briefly demonstrates and discusses the λ -tuning approach proposed in the previous section. The hexagonal sonoreactor investigated in Case Study 5 shall be used for this purpose. Previously in Case Study 5, the results revealed that the linear CP model suffered from uncertainties surrounding the bubble density parameter, which led to deviations from the experimental observation. In the following demonstration, this issue is shown to be addressed using the λ -tuning approach.

5.3.1 Methodology

The same hexagonal sonoreactor studied in Case Study 5 was used. The strong standing wave characteristics previously observed in the SCL images in Figure 4.30 were found to be suitable for the wavelength measurements. The uniform characteristics of standing waves also support the assumptions of the λ -tuning approach. The methods followed the procedure outlined in Section 5.2.2.4 . The average wavelength for each frequency was extracted from SCL images using the image processing software, ImageJ. After smoothing and establishing the reference scale, the 'Plot Profile' function was used to quantify the distances between the luminance peaks of standing waves that correspond to bright bands in the SCL images. The wavelength was taken as twice the average distance between peaks, as:

$$\lambda_{SCL} = 2h_{SCL} \quad (103)$$

The corresponding tuned phase speed was determined from:

$$c_{SCL} = \lambda_{SCL, f_i} \times f_i \quad (104)$$

Acoustic pressure simulations were performed using the monodisperse linear CP model and followed the same strategy presented in Case Study 5 [Section 4.3.2]. The complete procedure for this demonstration is graphically summarised in Figure 5.4. Only the 40 kHz and 70 kHz cases were considered due to the lack of a distinct standing wave pattern for the 28 kHz SCL images.

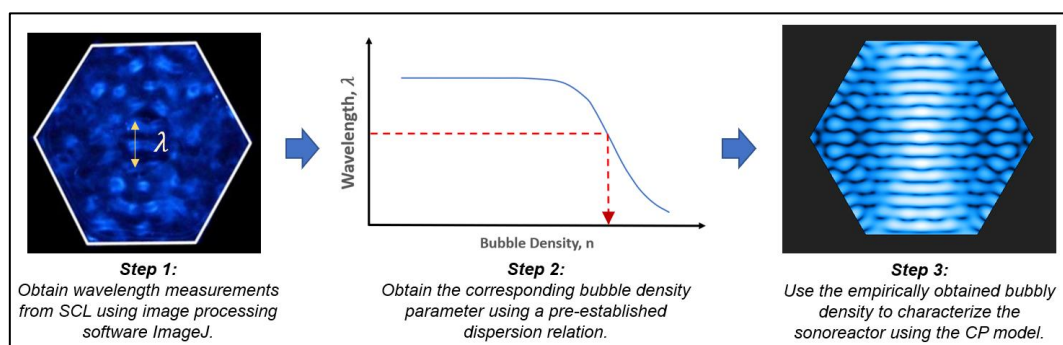


Figure 5.4: Graphical description of the proposed semi-empirical approach to characterise the hexagonal sonoreactor using SCL image data.

5.3.2 Results and Discussion

5.3.2.1 Wavelength Measurement from SCL Images

The value of h_{SCL} was determined as an averaged value from well-formed SCL standing waves. Figure 5.5 describes the measurement process for the 40 and 70 kHz standing wave. After image processing for noise reduction and contrast adjustment, a luminosity profile was extracted from the region of interest, as shown by the yellow lines in Figure 5.5 (a). The luminance profile was defined parallel to the direction of wave propagation to minimise error. The luminosity profiles plot the brightness of the pixels as shown in Figure 5.5 (b). The ‘peaks’ of the luminosity profile were used to

quantify the distance between the bright bands, allowing h_{SCL} to be averaged across the region of interest.

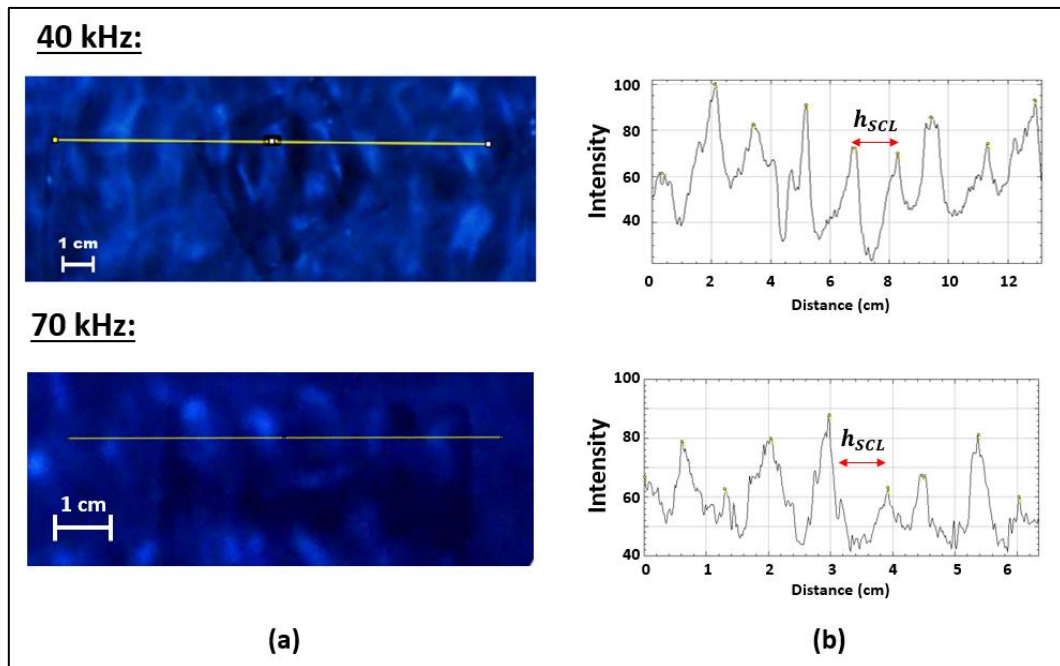


Figure 5.5: The wavelength measurement process: (a) Distinct and uniform standing waves for the 40 and 70 kHz case; (b) Normalised luminosity plots.

Note that the standing wave pattern (and subsequently h_{SCL}) was not perfectly uniform, which was to be expected for a real system. With reference to Table 5.3, the mean values of h_{SCL} measured for the 40 and 70 kHz systems were noted to be 1.57 and 0.94 cm, respectively. These values correspond to wavelengths of 3.14 and 1.87 cm. The luminosity plots in Figure 5.5 (b) showed that the distance between the antinodes were consistent within the regions of interest. For the 40 kHz case, the variance was found to be 0.06 cm² while the coefficient of variation is 17 % across 8 measurements. On the other hand, the 70 kHz case exhibits a variance of 0.04 cm² and a coefficient of variation of 21 % across 9 measurements. The measurements

revealed a wavelength-shortening effect of 15.1 % and 11.4 % for the 40 and 70 kHz cases, which correspond to reduced phase speeds of 1256 and 1309 m/s respectively.

Table 5.3: Averaged wavelength measurements from SCL images compared to theoretical pure-liquid wavelength.

Frequency (kHz)	Avg. Wavelength, λ_{SCL} (cm)	Theoretical Wavelength, $\lambda = \frac{c_l}{f}$ (cm)	Difference (%)
28	N/A*	5.29	N/A*
40	3.14	3.70	-15.12
70	1.87	2.12	-11.43

* Data unavailable due to lack of clear standing wave patterns in the 28 kHz case.

5.3.2.2 Empirical Tuning of the Bubble Density Parameter

The measured wavelength was used to determine the corresponding value of n using the dispersion relation in Figure 5.3. The empirically determined bubble density magnitude for the 40 kHz case is $n = 6.04 \times 10^{10} \text{ m}^{-3}$, while the 70 kHz system resulted in a value of $n = 4.31 \times 10^{10} \text{ m}^{-3}$. Interestingly, the difference between the values of n determined for both frequencies was relatively small. Furthermore, it is also remarkable that the values compared well with the common range of magnitudes used in recent bubbly-liquid studies (Delacour et al., 2020; Sarac et al., 2020; Trujillo, 2020; Chen et al., 2021). As shown in Table 5.2, recent works had used R_0 values within 3-10 μm , and the bubble density magnitudes within 1×10^9 to $1 \times 10^{11} \text{ m}^{-3}$. The findings of this case study support the use of these simulation parameters for bath-type systems.

The reported values of n were calculated for an equilibrium bubble radius of 5 μm , as assumed in Case Study 5. With reference to the CP dispersion relation, the effect of the equilibrium radius R_0 on the λ -tuning approach was also studied. Figure 5.6 illustrates the effect of the R_0 on the phase speed predicted for a range of n . It was noted that a larger R_0 would result in a larger phase-speed reduction for the same bubble density. The formulation of the dispersion relation described by Eqns. (23) - (28) revealed a rather complex dependency on R_0 . In contrast n has a more linear effect on the dispersion relation, the parameter R_0 not only determines the effect of resonance, but also the individual contributions of viscous, thermal, and radiation damping (Commander and Prosperetti, 1989). The main takeaway from this result is that the bubble-field parameters should not be considered separately, but instead the entire specification has to be evaluated as a whole when compared between studies.

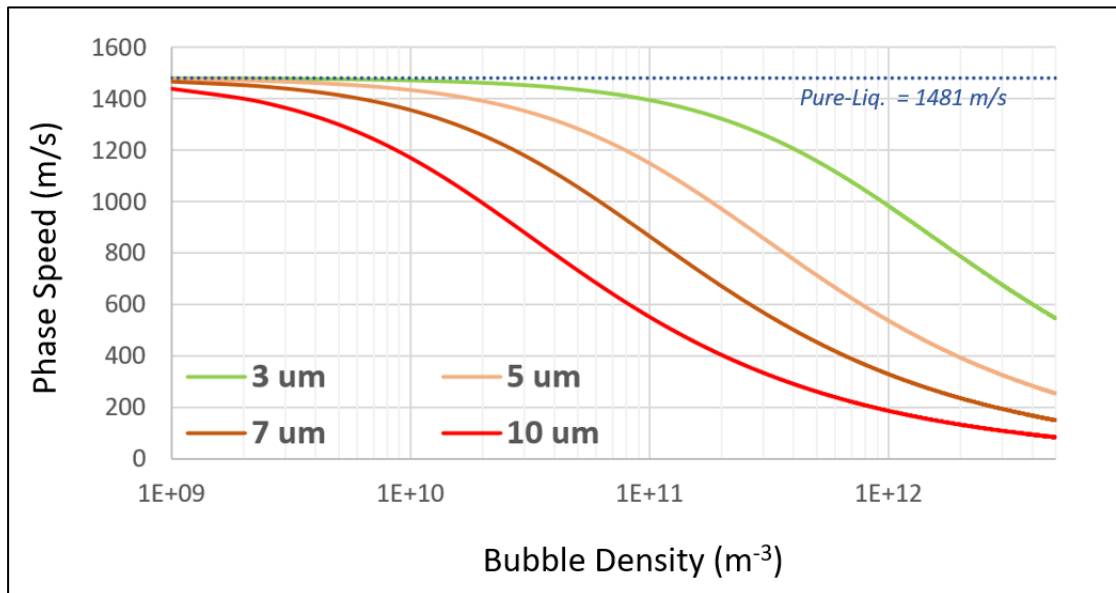


Figure 5.6: The effect of different equilibrium bubble radii on the relationship between the bubbly-liquid phase speed and the bubble density.

5.3.2.3 Sonoreactor Characterisation Using Tuned Bubble Density

An obvious concern with regard to the tuning of n is that it may invalidate the integrity of the simulation. It is reiterated that the wavelength is solely a function of the acoustic property. The acoustic pressure field solutions would still depend on other factors, such as the performance of the bubbly-liquid model, boundary conditions, and mesh quality. In fact, it was argued that the tuning method would allow other aspects of the bubbly-liquid model to be better studied since the uncertainties related to bubble field parameters can be addressed. Furthermore, characterisation methods such as SCL or foil mapping can provide a better bulk representation of the working fluid, as opposed to using pressure measurements at a single point (Delacour et al., 2020) or a single profile (Trujillo, 2020). This consideration becomes particularly important in models that assumed uniform bubble fields, such as recent applications of the linear CP and NH models [Table 5.2]. Additionally, such methods were well established among researcher, further improving its accessibility.

Figure 5.7 shows the 40 kHz acoustic pressure field of the hexagonal sonoreactor simulated using the tuned value of $n = 6.04 \times 10^{10} \text{ m}^{-3}$. The qualitative agreement of the antinode prediction across the standing wave compared well with the SCL data. Although slight deviations can be observed, the standing wave was approximately uniform across the geometry. This agreement supports the viability of the monodisperse linear CP model for the characterisation of the standing wave in the studied sonoreactor. The observation also suggests that the previously observed deviations in Case Study 5 were the result of incorrectly specifying the bubble field parameters. For the 70 kHz case validated in Figure 5.8, the simulation results solved using a tuned value of $n = 4.31 \times 10^{10} \text{ m}^{-3}$ were found to be less conclusive due to the

thinner standing wave patterns in the SCL image. It was noted that future studies should explore more reliable methods to capture the experimental antinode at higher frequencies.

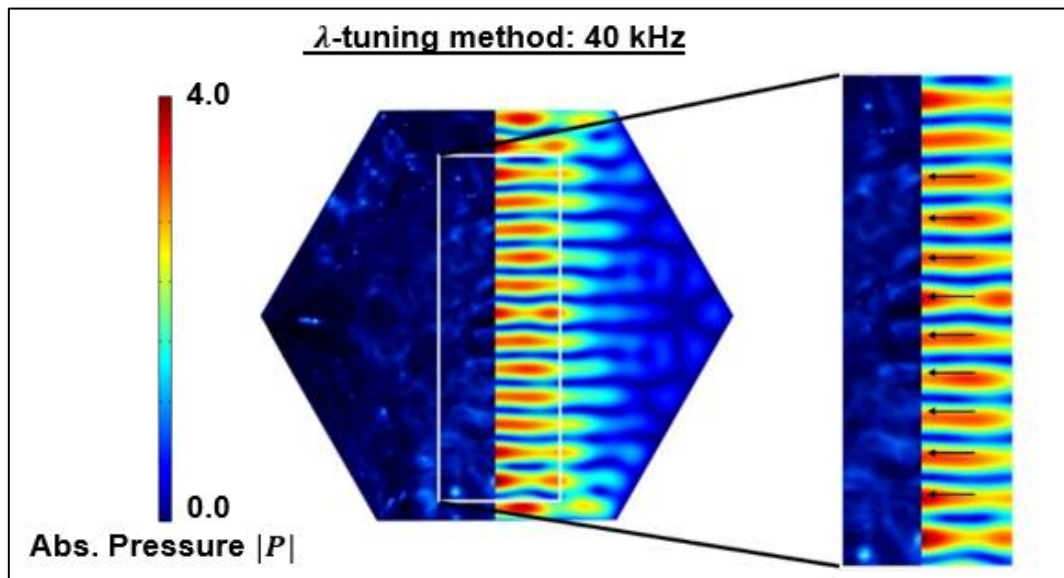


Figure 5.7: The comparison of the antinode prediction of the monodisperse linear CP model using a tuned bubble parameter of $n = 6.04 \times 10^{10} \text{ m}^{-3}$ for the 40 kHz case.

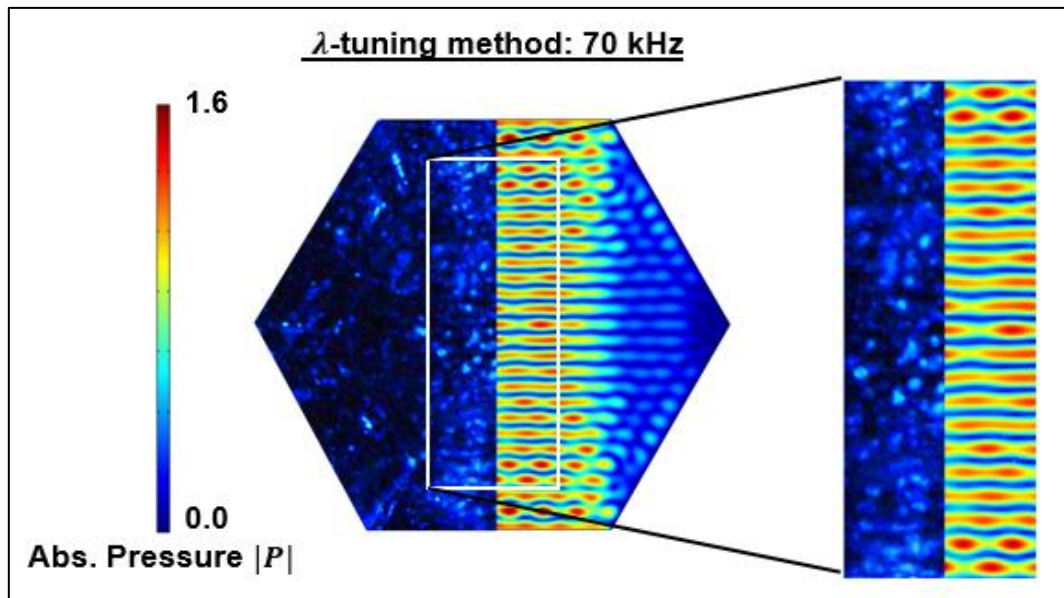


Figure 5.8: The comparison of the antinode prediction of the monodisperse linear CP model using a tuned bubble parameter of $n = 4.31 \times 10^{10} \text{ m}^{-3}$ for the 70 kHz case.

Despite the promising outlook, it was noted that there was much room for improvement. Current results only showed experimental agreement in terms of standing wave (phase speed) predictions. Pressure magnitude validation was omitted due to the lack of hydrophone measurements for the hexagonal sonoreactor. The λ -tuning approach was also based on the theoretical foundations of the monodisperse linear CP model. This led to certain restrictions on its applicability, which can be considered a key limitation. In particular, the approach was noted to be restricted to systems that comply with the key assumptions outlined in Section 5.2.2.1.

Nonetheless, the results suggested that the proposed approach can be viable if the assumptions are obeyed. Based on observations from previous antinode characterisation works (Lewis et al., 2007; Tangsopa and Thongsri, 2019), a case can be made that conventional bath-type configurations approximate the key assumptions well. In contrast, past observations for sonotrode configurations (Dahlem et al., 1999; Vanhille and Campos-Pozuelo, 2006; Žnidarčič et al., 2014) suggest that the assumption of bubble field uniformity would be violated due to the large gradients in bubble field distribution.

While the need to perform experimental measurements was noted to be a drawback of the λ -tuning approach, this additional step was argued to be a reasonable cost to improve the accuracy and practicality of the linear CP model. Taking into account the large knowledge gaps that currently limit bubble field characterisation efforts, the proposed approach was able to strike a good balance between accuracy and practicality. Ultimately, the application of this method for a larger sample size of sonoreactors is required to provide key insights for its viability. It is also possible that,

with enough empirical data, a consolidated databank for bubble field characteristics could be created to serve as a reference for future simulation work. Until better methods are developed for the purpose of characterisation of the bubble field in large sonoreactors, the λ -tuning approach was argued to be a promising alternative to bypass the uncertainties of bubble field characterisation.

5.4 Case Study 7: Preliminary Investigation for Multi-Frequency Systems

A notable rising trend in the field of sonoreactor and power ultrasound research is the application of multi-frequency systems. There have been an increasing number of studies that reported better performance for multi-frequency operations as opposed to mono-frequency sonoreactors (Brotchie et al., 2008; Son et al., 2010). These findings were supported by higher cavitation potential measurements in experiments (Avvaru and Pandit, 2008; Guédra et al., 2015) and stronger cavitation dynamics in theoretical studies (Suo et al., 2018; Ye et al., 2019). The increased popularity of multi-frequency ultrasound also raised interests in the simulation and design of multi-frequency sonoreactors (Matafonova and Batoev, 2020; Wongwuttanasatian and Jookjantra, 2020; Wang et al., 2021).

Literature review identified several key knowledge gaps that need to be addressed. The biggest problem remains to be the lack of modelling strategies, as past developments mainly considered mono-frequency systems. When considering multi-frequency systems, frequency-domain models face a key limitation due to the assumption of periodicity [Section 2.2]. Thus, a conventional approach to simulate multi-frequency systems is to use a time-domain model. There were only two known works that considered multi-frequency acoustic pressure fields in sonoreactors. The first is an early study published by Servant et al. (2003), who very briefly commented on the topic. Using a modified Caflisch equation, their study solved for the 3D time-dependent pressure fields of multi-frequency systems in a 1-L sonoreactor. However, the discussion and validation of the accuracy of their results were limited. Another recent study by Tangsopa and Thongsri (2021) used the pure-liquid model to optimise

an ultrasonic cleaning tank. They noted that the multi-frequency time-domain simulations took 16 times longer to solve compared to frequency-domain simulations of single-frequency cases. Their findings showed that the time-domain strategy was more resource intensive, which was supported by the results in Case Study 1.

Although they are a straightforward solution to the problem, time-domain methods present a glaring number of drawbacks and challenges. As suggested by the results in Case Study 1, stricter solver tuning, longer simulation times, and larger memory requirements make the approach less desirable compared to frequency domain counterparts. Furthermore, nonlinear bubbly-liquid models in the time domain were found to be prone to numerical blow-up [Figure 2.1] and other instabilities (Louisnard, 1998). Compared to frequency-domain models, dispersive behaviour such as attenuation is also harder to mathematically implement (Ginsberg, 2018). This is clear in the work of Dähnke et al. (1999a), who went to great lengths to incorporate the CP dispersion relation into a wave equation. Lastly, transient bubbly-liquid models are very demanding for large geometries. The modified wave equation proposed by Dähnke et al. (1999a) remains the most practical approach to this day for the consideration of ultrasonic baths. Other time-domain models such as variations of the Caflisch (Caflisch et al., 1985), Westervelt (Doinikov et al., 2013) and Korteweg–de Vries–Burgers (KdVB) equations were considered. However, these models are still restricted to 1D simulations (Kanagawa et al., 2021) or are only applicable for very low amplitudes and small geometries (Tejedor-Sastre and Vanhille, 2017).

In light of this, a simplified method of approximating the multi-frequency acoustic pressure based on acoustic theory was proposed. Studies on waves and signals used

frequency-domain methods to characterise time-domain problems, even in nonharmonic cases (Prinn, 2021). Similarly, if the acoustic behaviour in the sonoreactor satisfies linear wave theory, the sum of frequency-domain solutions can be a good prediction for the multi-frequency response. In this study, the frequency-domain solutions were used to characterise a multi-frequency sonoreactor using the root-mean-squared pressure based on Parseval's theorem (Ginsberg, 2018). This study argues that this approach can be used as a preliminary characterisation technique to circumvent the difficulties of time-domain models in the early design and optimisation stages.

This study also extended the semi-empirical CP model demonstrated in Case Study 6 to address multi-frequency acoustic pressure fields. For the consideration of multi-frequency attenuation, a linear and nonlinear strategy were studied. This investigation consists of three main parts. First, the theory involved in the proposed method is presented and the assumptions are outlined and discussed. The second part involves evaluating the performance of the method against multi-frequency SCL standing wave patterns obtained from the hexagonal sonoreactor. A total of three dual-frequency cases and one triple-frequency case were studied. Lastly, several aspects related to multi-frequency attenuation and pressure field characterisation are discussed.

5.4.1 Theoretical Derivation

The relationship between the multi-frequency acoustic pressure $p_T(\mathbf{r}, t)$ to the frequency-domain solutions, $P(\mathbf{r})$ is presented. Consider a space domain (\mathbf{r}) which experiences two sinusoidal time-harmonic pressure fields p_1 and p_2 at angular frequencies of ω_1 and ω_2 respectively:

$$p_1(\mathbf{r}, t) = \Re[P_1(\mathbf{r})e^{i\omega_1 t}] \quad (105)$$

$$p_2(\mathbf{r}, t) = \Re[P_2(\mathbf{r})e^{i\omega_2 t}] \quad (106)$$

The space-dependent pressure amplitudes $P_1(\mathbf{r})$ and $P_2(\mathbf{r})$ can be obtained by solving the Helmholtz equation for each harmonic:

$$\nabla^2 P_1(\mathbf{r}) + k_1^2 P_1(\mathbf{r}) = 0 \quad (107)$$

$$\nabla^2 P_2(\mathbf{r}) + k_2^2 P_2(\mathbf{r}) = 0 \quad (108)$$

An important assumption is that the system obeys linear wave theory (Ginsberg, 2018), where the superposition principle allows the total pressure, p_T to be written as the sum of two pressure fields:

$$p_T(\mathbf{r}, t) = p_1(\mathbf{r}, t) + p_2(\mathbf{r}, t) = \frac{1}{2} (P_1(\mathbf{r})e^{i\omega_1 t} + P_2(\mathbf{r})e^{i\omega_2 t} + c. c.) \quad (109)$$

where *c. c.* denotes the complex conjugates. The time-averaged mean-squared value of $p_T(\mathbf{r}, t)$ can be directly obtained using Parseval's theorem, where P_m represents the frequency-domain solution for the m^{th} harmonic:

$$(\overline{p_T})^2 = \frac{1}{2} \sum_{m=1}^M |P_m|^2 = \frac{1}{2} (|P_1|^2 + |P_2|^2) \quad (110)$$

It is also assumed that the steady-state time-averaged acoustic pressure in the sonoreactor can be interpreted as the root-mean-squared pressure. This can be written for two harmonics as follows:

$$P_{rms}(\mathbf{r}) = \sqrt{\frac{1}{2}(|P_1|^2 + |P_2|^2)} \quad (111)$$

A generalised formulation for more than two harmonics is:

$$P_{rms}(\mathbf{r}) = \sqrt{\frac{1}{2}\sum_{m=1}^M |P_m|^2} \quad (112)$$

It is clear from Eqn. (111) and (112) that $P_{rms}(\mathbf{r})$ is a function of space, calculated directly from the frequency-domain solutions P_m . This is valid if the total pressure does not depend on the phase of the components⁸.

5.4.2 Modification of the CP Model for Multi-Frequency Considerations

The lack of information on the approximation of multi-frequency bubbly-liquid effects in the frequency domain presents a significant challenge. This matter has yet to be explored in literature. The methods used in this study take inspiration from the work of Dähnke et al. (1999a), who modified a frequency-domain model to approximate acoustic behaviour in their transient simulations. It is imperative to state that the following methods are preliminary and based on simplifying assumptions.

⁸ This is also commonly known as incoherent waves, as opposed to coherent waves where the phase difference between components can affect the sum of the solution (Ginsberg, 2018).

5.4.2.1 Semi-Empirical Monodisperse Linear CP Model

Initial investigations in this case study used a linear CP model to characterise the acoustic pressure fields of the individual harmonics. The method followed the procedures demonstrated in Case Study 6. The specifications of the bubble field parameters warrant an interesting discussion. Previously, the λ -tuning approach had been suggested to be able to provide a good estimation of the bubble density parameter n . In this investigation, the approach was adopted with a slight modification to account for multi-frequency effects. It was assumed that the multi-frequency bubbly liquid in the hexagonal sonoreactor can be approximated using the acoustic properties averaged from single frequency measurements in Case Study 6. This was done to use the same acoustic property to characterise the entire working fluid, instead of using different properties for each harmonic. Since the working fluid was simultaneously irradiated by multiple frequencies, it makes sense that all harmonics were travelling through the same acoustic domain, and thus should be simulated using the same acoustic properties.

5.4.2.2 Consideration of Nonlinear Attenuation

This investigation also considered the nonlinear CP approach presented in Section 5.1.2.2. An attempt to incorporate the mechanisms of the NH model led to several challenging issues that were unable to be resolved, and thus were left for future work. It was hypothesised that incorporation of the NH model would require re-establishing the entire theoretical foundation using multi-frequency bubble dynamics, which was noted to be out of the current scope.

The nonlinear CP formulation was adopted by applying only the nonlinear mechanism on the imaginary part of the wavenumber. The real part of the wavenumber (the propagation wavenumber κ) was assumed to be constant in space for all simulated frequencies. The main reason for this implementation was to ensure numerical stability and consistency. Preliminary tests using a full nonlinear CP model for the multi-frequency simulation would fail to achieve convergence even after rigorous solver tuning. It was also noted that the convergence of the simulations showed strong sensitivity to the changes in simulation geometry. Scrutiny of the convergence plots strongly suggested that this was caused by the nonlinear phase speed similar to that discussed in Sections 4.1.2.7 and 4.3.3.5.

The formulation of multi-frequency bubbly-liquid attenuation was challenging because of the strong dependence of bubble attenuation on the frequency and the lack of information in literature. Even within the restricted framework of quasilinear sonoreactor acoustics, the number of knowledge gaps is large and could not be fully explored within this work. For this work, the attenuation mechanism was simplified to serve as an exploratory investigation on this matter. In multi-frequency systems, the pressure fields share the same spatial domain. Thus, it makes sense to model the attenuation using a single bubble field. It was assumed that the bubbly-liquid attenuation can be characterised by using the frequency loading of the dominant harmonic (brightest standing wave) observed from the SCL images. Clearly, this is an oversimplification of the matter. However, there is yet to be a more suitable alternative due to the limited knowledge on this matter.

Another key assumption was to consider the nonlinear attenuation as a function of the local root-mean-squared pressure (effective pressure). A modified variation of the nonlinear formulation presented by Dähnke et al. (1999a) was used. The method assumes a linear relationship between the bubble fraction β and the local absolute pressure $|P|$ as:

$$\beta = X|P| \quad (113)$$

For a monodisperse system, X can be written as:

$$X = \frac{\beta}{|P|} = \frac{4\pi n R_0^3}{3|P|} \quad (114)$$

In this investigation, the linear relationship specified for the bubble fraction was assumed to depend on the effective pressure, $\beta = f(P_{rms}(\mathbf{r}))$. The modified relationship can then be written as:

$$\beta = 2 \times 10^{-9} P_{rms} \quad (115)$$

For a monodisperse system, the relationship can also be written in terms of bubble density parameter n as:

$$n(\mathbf{r}) = \frac{6 \times 10^{-9} P_{rms}}{4\pi R_0^3} \quad (116)$$

Outside of the above modifications to account for multi-frequency effects, the framework of the nonlinear CP model used in this study followed past investigations. The value of the linear coefficient $X = 2 \times 10^{-9} Pa^{-1}$ directly referenced past literature (Jamshidi et al., 2012; Fang et al., 2018). In this study, the piecewise condition of n was not considered, according to the reasoning presented in Section 5.1.2.3.

5.4.3 Methodology

5.4.3.1 Multi-Frequency SCL and Calorimetry Data

In this investigation, the same sonoreactor from Case Study 5 was used (Manickam et al., 2014; Tiong et al., 2017b). Figure 5.9 shows a simplified representation of the sonoreactor and defines the orientation of the frequencies associated with the pressure-emitting walls used in subsequent discussions.

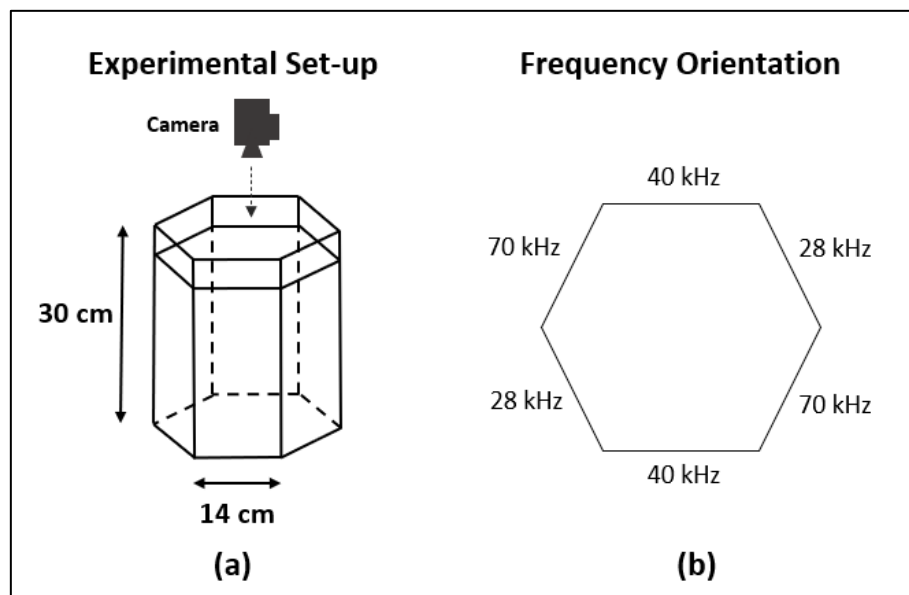


Figure 5.9: (a) Visual representation of the hexagonal sonoreactor dimensions; (b) Orientation of the frequencies involved.

The acquisition and pre-processing methods of SCL images were described in Case Study 5 and omitted here. Calorimetry data for the specification of pressure boundaries are shown in Table 5.4. The pressure magnitude values were obtained under the assumption that the pressure intensity is equally distributed across the entire emitting wall of the sonoreactor.

Table 5.4: Calorimetry data for the calculation of Dirichlet transducer boundary condition for multi-frequency simulations (Tiong et al., 2017a).

Frequency (kHz)	Power, O_M (W)	Total Surface Area, A_s (m ²)	$P_{Tr,28}$ (bar)	$P_{Tr,40}$ (bar)	$P_{Tr,70}$ (bar)
28 + 40	403.7	0.165	0.86	0.86	-
28 + 70	528.5	0.165	0.98	-	0.98
40 + 70	446.8	0.165	-	0.90	0.90
28 + 40 + 70	657.3	0.248	0.89	0.89	0.89

5.4.3.2 Numerical Simulation

All acoustic pressure simulations were carried out using 2D models with full-scale geometry in the frequency domain. Only harmonics that correspond to the frequencies of active transducers in the multi-frequency system were considered (e.g., only 28 and 40 kHz harmonics were simulated for the 28-40 kHz operation). The frequency response of other harmonics in the system, such as cavitation broadbands (Avvaru and Pandit, 2009), were not considered. Streaming effects were also assumed to be negligible, based on the minimal streaming activity observed in the SCL data. The meshing step essentially followed Case Study 5. Pressure-emitting boundary conditions for the simulated harmonics were specified in terms of Dirichlet pressure from the calorimetry data in Table 5.4. In contrast to Case Study 5, sound-soft boundaries were used to represent inactive walls. This was done to ensure numerical consistency with the Dirichlet pressure-emitting boundaries. The previous results in Case Study 5 [Figure 4.29] confirmed that the differences are minimal and do not affect the key observations of this study. The physical parameters used for the multi-frequency simulations are listed in Table 5.5. All parameters were assumed to be constant in the domain, and the gas within the bubbles was modelled using properties of air. All properties were taken at standard values at 25°C. For the investigation using

the linear CP model, an equilibrium bubble radius of 5 μm was used. The value of the bubble density n used in this study referenced the λ -tuning results for single-frequency operations in Section 5.3.2.1.

Table 5.5: Physical properties (25°C) used in Case Study 7.

Parameter	Value	Unit	Description
D_g	2.19×10^{-5}	m^2/s	Diffusivity of air within bubble
c_l	1481	m/s	Speed of sound in pure water
γ_l	1.41	-	Adiabatic index for air
μ_l	0.001	$\text{Pa}\cdot\text{s}$	Dynamic viscosity of water
ρ_l	997	kg/m^3	Density of water
σ_l	0.0725	N/m	Surface tension of water

In the second half of this study, an exploratory investigation was carried out using a modified nonlinear CP model outlined in Section 5.4.2.2. The propagation wavenumber was assumed to be a constant tuned phase speed of $c_{avg} = 1277.5 \text{ m/s}$ for all simulated harmonics. It was also assumed that the dispersive nature of the studied system is negligible, which was supported by simulation results. For the nonlinear attenuation, it was assumed that the attenuation curve can be approximated using the dominant harmonic. The 28-40, 40-70, and 28-40-70 kHz cases were characterised using the 40 kHz attenuation curve, while the 28 kHz was assumed to be dominant in the 28-70 kHz case. The following outlined the steps involved for the multi-frequency nonlinear CP approach:

1. Bubble density magnitudes were obtained for a range of root-mean-squared pressures using Eqn. (116). Monodisperse CP attenuation curves were prepared.
2. Frequency domain simulations were performed for each harmonic to obtain their corresponding frequency domain solutions.
3. The root-mean-squared pressure field, $P_{rms}(\mathbf{r})$ was calculated from time-harmonic solutions using Eqn. (112).
4. The bubble density field $n(\mathbf{r})$ and by extension the attenuation field $\alpha(\mathbf{r})$ in the simulation domain was determined from $P_{rms}(\mathbf{r})$ based on the attenuation curve prepared in Step 1.
5. Steps 2 to 4 were iterated until the nonlinear pressure and attenuation fields achieved convergence.

To better represent the iteration loop of the modified nonlinear CP approach, a graphical representation is provided in Figure 5.10.

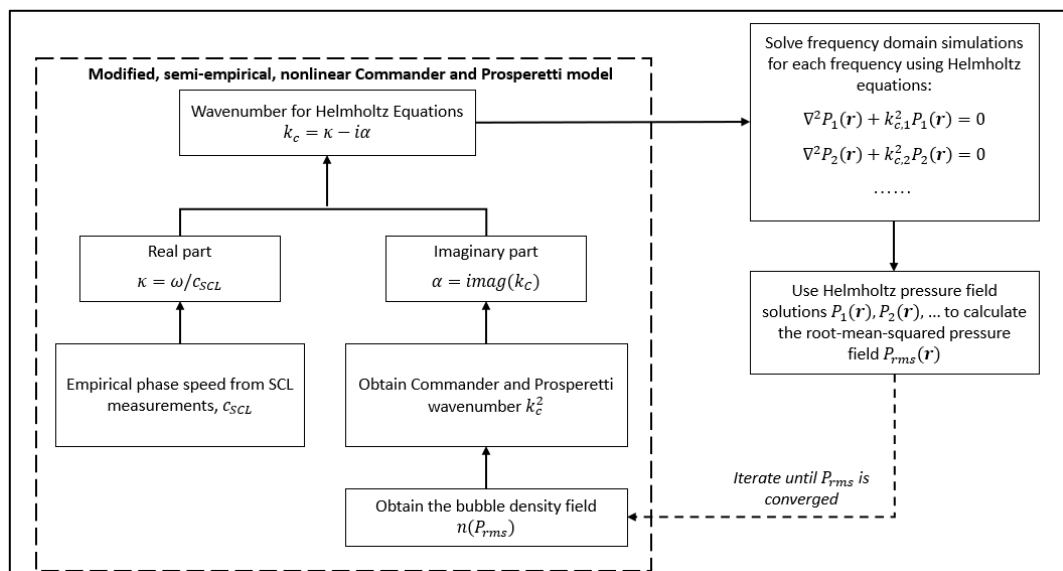


Figure 5.10: Graphical representation of the nonlinear CP iteration loop.

5.4.4 Results and Discussion

5.4.4.1 Analysis of Multi-Frequency SCL Images

Figure 5.11 depicts the top-down SCL images captured for four multi-frequency configurations of the studied sonoreactor. The frequency combinations considered in this study were 28-40, 28-70, 40-70, and 28-40-70 kHz. The presence of standing wave patterns was found to be more distinct compared to single-frequency cases in Case Study 5. Similar to Case Study 5, a focus was placed on the region of interest near the centre of the reactor, as data near the edges suffer from uncertainties caused by metal wall reflections. With reference to Figure 5.11 (a), (c), and (d), 40 kHz standing waves were observed to be most distinct and dominant, followed by 28 kHz standing waves. Standing waves of 70 kHz were dim for all images and could not be distinctively characterised, with the only exception being the 28-70 kHz shown in Figure 5.11 (b).

5.4.4.2 Linear CP Approach

Bubble field characterisation for the multi-frequency operation brought up several interesting considerations. When applying the linear CP approach, the main challenge lies in the question of whether to simulate each frequency using the same value of n . Realistically, all harmonics share the same bubble field. The problem remains in obtaining the value of n that characterises this behaviour. One possibility was to tune the value of n for each multi-frequency operation. However, the multi-frequency SCL images contain the superposition of multiple standing waves, which made the luminosity plots quite unreliable for multi-frequency tuning.

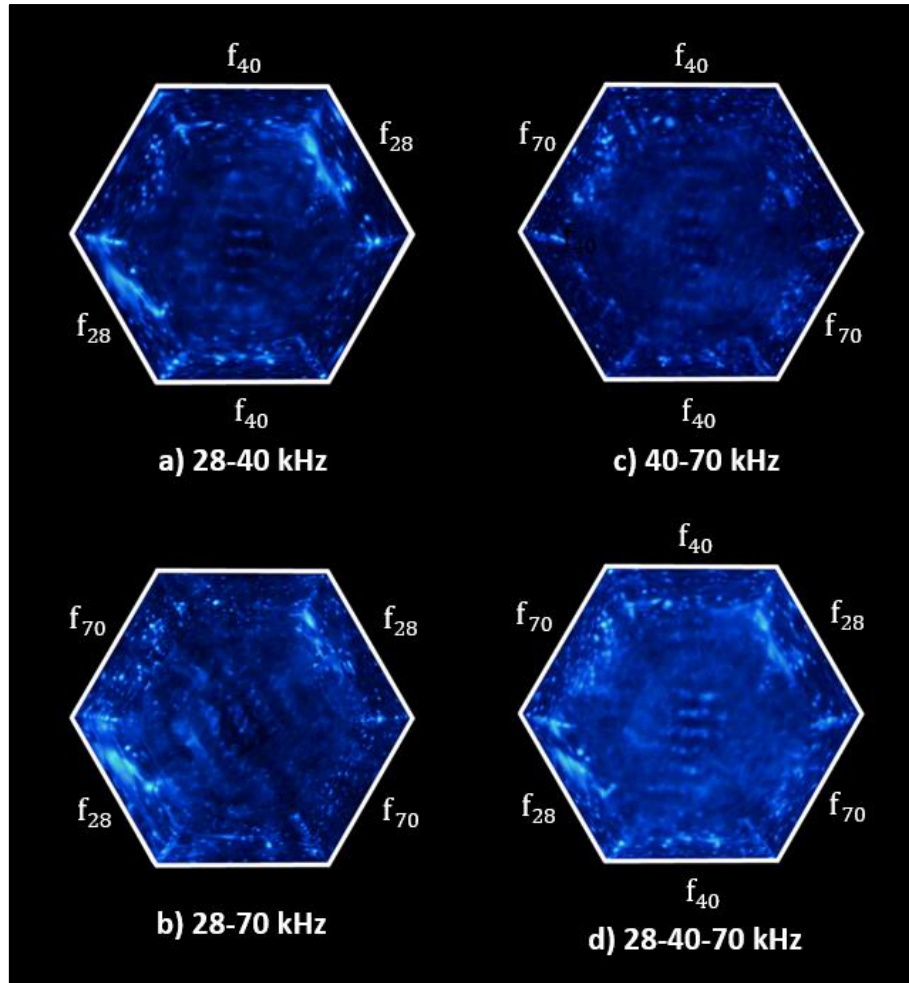


Figure 5.11: SCL images of multi-frequency combinations; with design power of 600 W for dual-frequency and 900 W for tri-frequency.

Alternatively, it was noted that the n tuned from single frequency operations did not exhibit significant differences between the 40 and 70 kHz operation. Thus, it was hypothesised that an averaged value of n approximated from previous measurements would be able to characterise the multi-frequency system. Table 5.6 summarises the acoustic properties of the bubbly liquid for each considered harmonic. A value of $n = 5.2 \times 10^{10} \text{ m}^{-3}$ was assumed. This value was obtained by taking the average bubble density measured from single frequency operation in Case Study 6. As shown later, this assumption resulted in surprisingly good agreement in terms of antinode comparisons.

Table 5.6: Bubble field parameters used for each harmonic in the multi-frequency simulation.

Frequency (kHz)	Equi. Bubble Rad. R_0 (μm)	Uniform Bubble Density, n (m^{-3})	Phase Speed c_{bl} (m/s)	Att. Coeff. α (Np/m)
28			1278.1	0.75
40	5	5.2×10^{10}	1277.8	1.535
70			1276.5	4.89

Figure 5.12 shows the root-mean-squared pressure field predicted for the four frequency combinations using the linear CP approach. The dominance of the 40 kHz standing wave is apparent. Subsequent investigations in Section 5.4.4.4 suggest that this was caused by constructive interference. It will also be shown in Section 5.4.4.4 that the predicted antinodes show remarkable agreement with the SCL images. This was interesting as these results support the hypothesis that the averaged value of $n = 5.2 \times 10^{10} \text{ m}^{-3}$ can be used to approximate the multi-frequency bubble field.

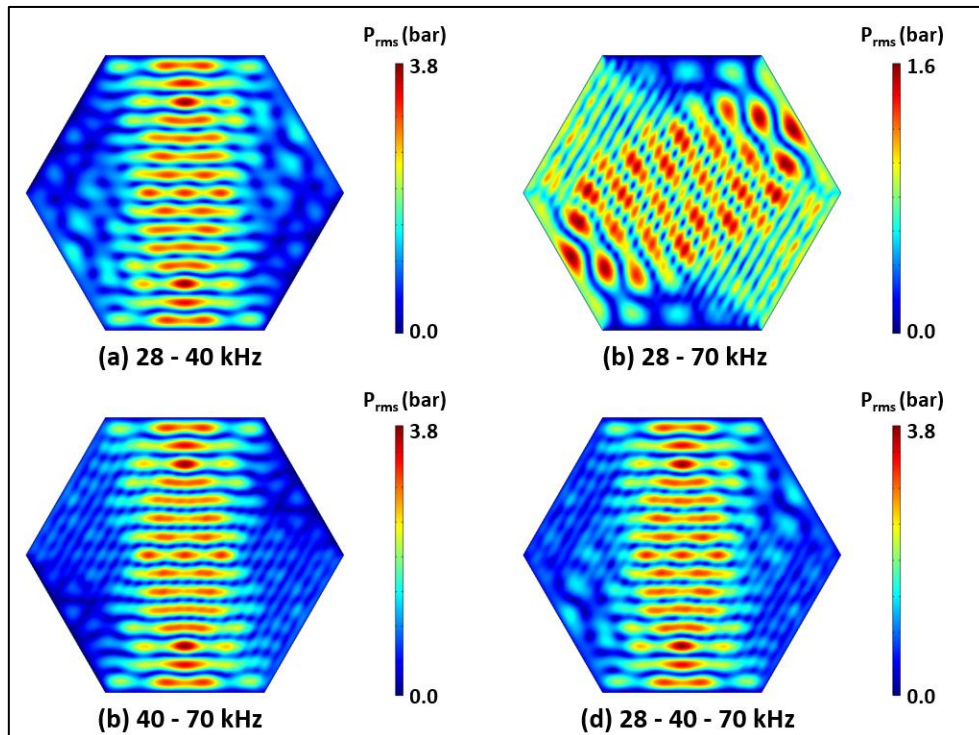


Figure 5.12: RMS acoustic pressure solved using the linear CP approach.

5.4.4.3 *Nonlinear CP Approach*

A different perspective was explored for the modelling strategy of multi-frequency attenuation by considering a nonlinear CP approach. This approach assumed bubble density to vary with the local effective pressure magnitude. The motivation was to explore key concepts that might be useful for future work, such as incorporating pressure-dependent attenuation strategies. The implementation of the nonlinear CP and NH models was found to be similar during the course of this work. The ultimate goal of this approach is to establish a modelling strategy that depends on a wavenumber derived from multi-frequency bubble dynamics.

The propagation wavenumber was assumed to be constant for all harmonics at $c_{bl} = 1277.5$ m/s. This value was averaged from Table 5.6 as it had been shown to give a good approximation of the phase speed. Naturally, this assumes that the real and imaginary parts can be considered separately. This approach is comparable to studies that assumed the pure liquid phase speed but considered separate attenuation effects (Yasui et al., 2007; Rashwan et al., 2020). The assumption was used to simplify the modelling strategy, and future studies should attempt to investigate a more comprehensive approach based on theoretical derivation. Figure 5.13 shows the root-mean-squared pressure field solved using the nonlinear CP approach. From the perspective of phase speed prediction, the standing wave profiles observed were similar to those obtained using the linear CP approach in Figure 5.12. This was expected because the values of the phase speeds used were similar. The key differences were found to be the lower pressure magnitudes predicted by the stronger attenuation, which changed the scaling of the colour legend.

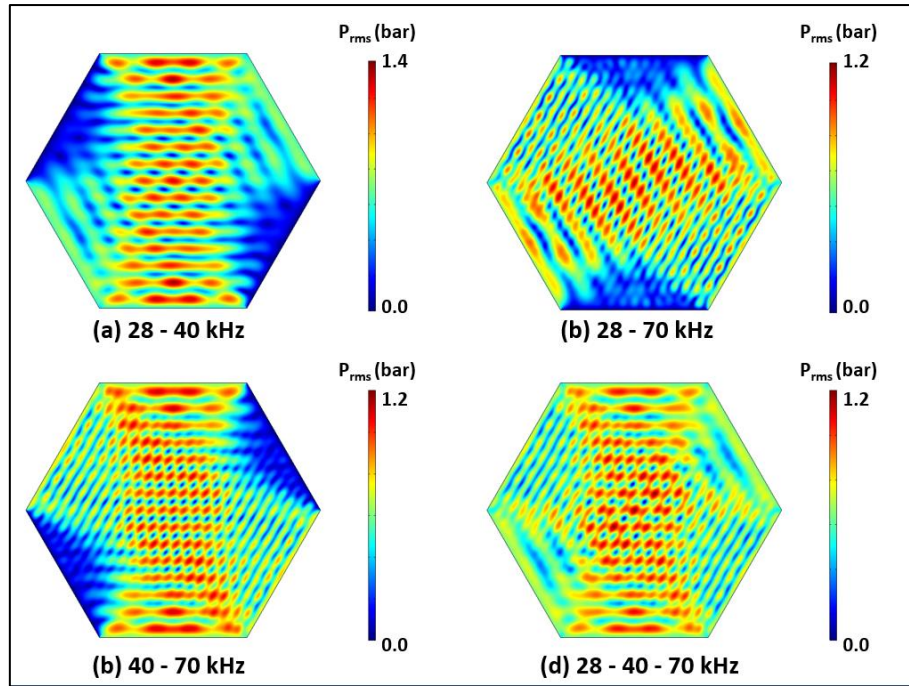


Figure 5.13: Plots of the root-mean-squared acoustic pressure solved for the four multi-frequency cases using the nonlinear CP approach.

The nonlinear CP attenuation mechanism used in this study was based on methods discussed in Section 5.1.2.2, where a linear relation was used for the pressure-dependent bubble density. For this study, the incorporation of the pressure dependent bubble density, $n(|P|)$, also drew inspiration from the NH model by using an interpolation curve to reduce the load on the nonlinear solver. Figure 5.14 plots the pressure-dependent bubble density parameter n and the corresponding attenuation coefficient plotted against P_{rms} . Since the CP dispersion relation is essentially monoharmonic, the 40 kHz attenuation curve was assumed for the 28-40, 40-70, and 28-40-70 kHz cases, while the 28 kHz attenuation was assumed in the 28-70 kHz simulation. One could consider this to be an extension of the concept first demonstrated in the work of Dähnke et al. (1999a). Naturally, the approach is a major simplification and should be considered as a novel exploration of this concept. The

linear CP and nonlinear CP methods ultimately explored two different strategies of modelling multi-frequency attenuation. As implied, the key differences relate to the linearity of the model as graphically described in Figure 5.15. The linear CP model assumed that the harmonic fields are strictly independent, and the attenuation is a function of separate frequencies in the bubble field. This allowed the attenuation to be defined independently for each harmonic using the dispersion relation. The only constraint that was imposed is that all harmonics share the same local bubble field.

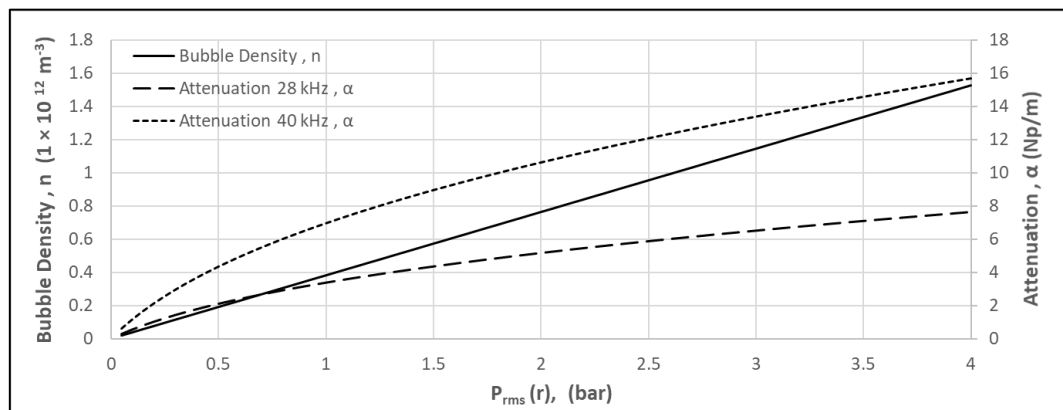


Figure 5.14: Bubble density (left axis) and its associated attenuation magnitude (right axis) plotted as a function of root-mean-squared pressure for the harmonic fields of 28 and 40 kHz.

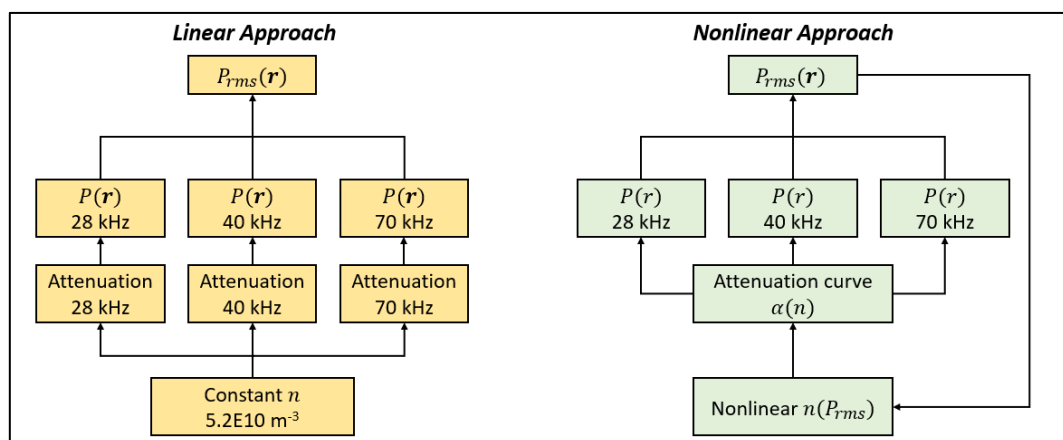


Figure 5.15: Attenuation mechanism of the linear and nonlinear approach in this investigation.

The nonlinear CP approach explored the idea that energy dissipation at a local point in space affects all harmonics. The validity of this assumption in relation to the dispersive nature of the working fluid remains to be investigated. The approach also assumes that the individual harmonic fields are nonlinearly related, for which the extent of this heuristic modification on the integrity of the framework is unknown. The lack of experimental data to verify this matter restricts the current discussion. In light of this, this work mainly considered the numerical aspects of the results.

5.4.4.4 *Antinodal Verification of Standing Wave Profiles*

The simulation outputs were compared with SCL images. Considering that both the linear and nonlinear methods yield similar standing wave profiles, the following verification study used the results of the latter. The smaller contrast between different harmonics allowed for better observation of the composite standing wave pattern.

Figure 5.16 (a) shows the superimposition of the simulated effective pressure field $P_{rms}(\mathbf{r})$ onto one of the SCL images for the 28-40 kHz case. A magnified view of the region of interest is shown in Figure 5.16 (b), where it can be seen that the high $P_{rms}(\mathbf{r})$ regions aligned well with bright SCL bands captured for the standing wave of 40 kHz. Figure 5.17 shows another image that better captured the 28 kHz standing wave, where it can be seen that the 28 kHz standing waves exhibit similar agreement, albeit with dimmer and less obvious bands.

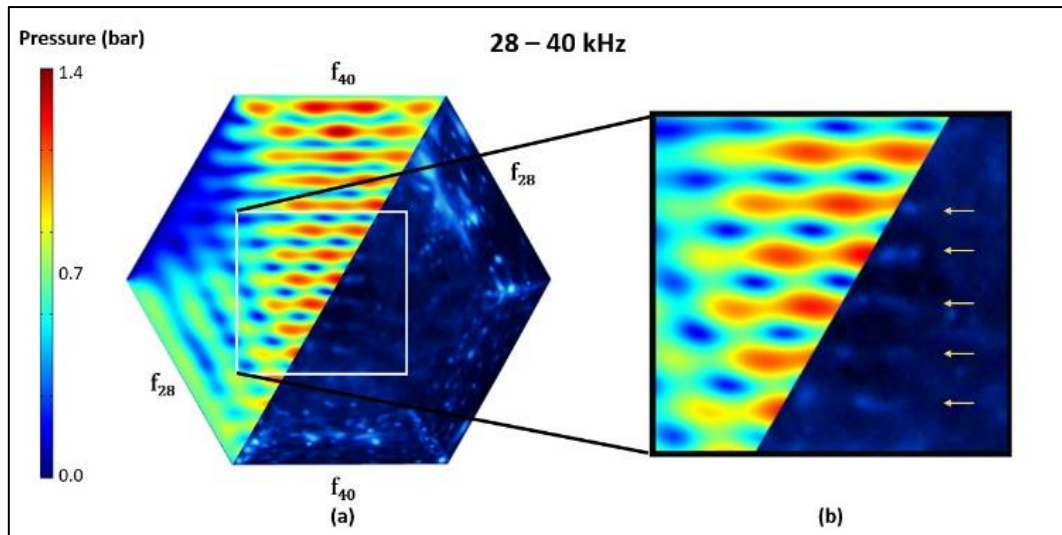


Figure 5.16: (a) Comparison between $P_{rms}(r)$ predicted from simulation and SCL data for the 28 – 40 kHz case, (b) Region of interest showing the agreement of the 40 kHz standing wave.

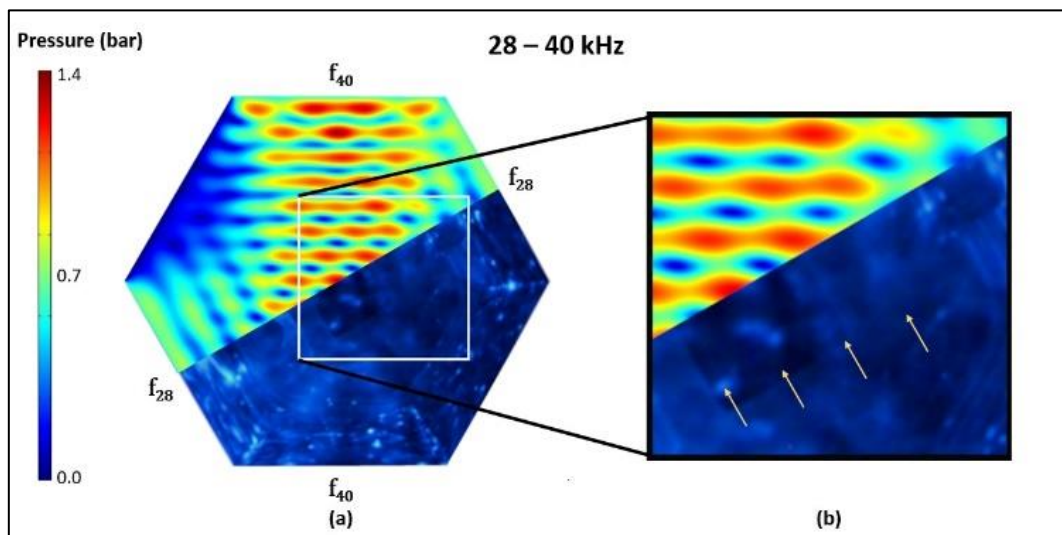


Figure 5.17: (a) Comparison between $P_{rms}(r)$ predicted from simulation and SCL data for the case of 28-40 kHz case; (b) Region of interest showing the agreement of the 28 kHz standing wave.

The results for the 40-70 kHz dual-frequency case were less conclusive. SCL bands were significantly dimmer compared to other frequency combinations, and the standing waves were less distinct. The low intensity of the 70 kHz standing wave made it indistinguishable from the surrounding visual noise, and thus qualitative comparison

was limited. However, a detailed inspection revealed that the 40 kHz standing wave bands agreed well with the simulated antinode locations, as shown in Figure 5.18 (b).

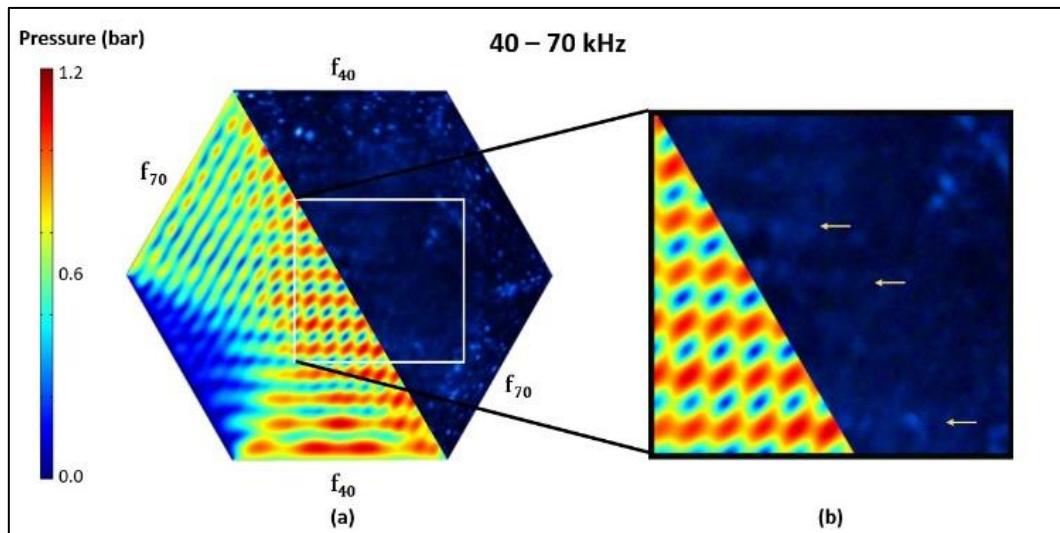


Figure 5.18: (a) Comparison between $P_{rms}(r)$ predicted from simulation and SCL data for the 40 – 70 kHz case; (b) Region of interest showing the weak agreement of the 40 kHz standing wave.

Compared to the previous two cases, where a single standing wave dominates, the 28-70 kHz SCL images managed to yield clear dual-frequency standing waves. Figure 5.19 (b) shows a very clear superimposition between the 28 and 70 kHz standing waves. The 28 kHz bands in Figure 5.20 were also much more distinct, arguably more than the single frequency cases shown in Case Study 5. Comparison results in Figure 5.19 and Figure 5.20 showed the best agreement between simulation and SCL of all studied cases. It is worth noting that this was an unexpected observation, as the 70 kHz SCL standing wave formations in previous cases were difficult to be characterised. It was hypothesised that the good characterisation in this case was due to the larger frequency difference. However. The exact mechanism that led to this observation

remains unclear. Current knowledge suggests that it could be related to multi-frequency synergistic effects in cavitation studies (Suo et al., 2018).

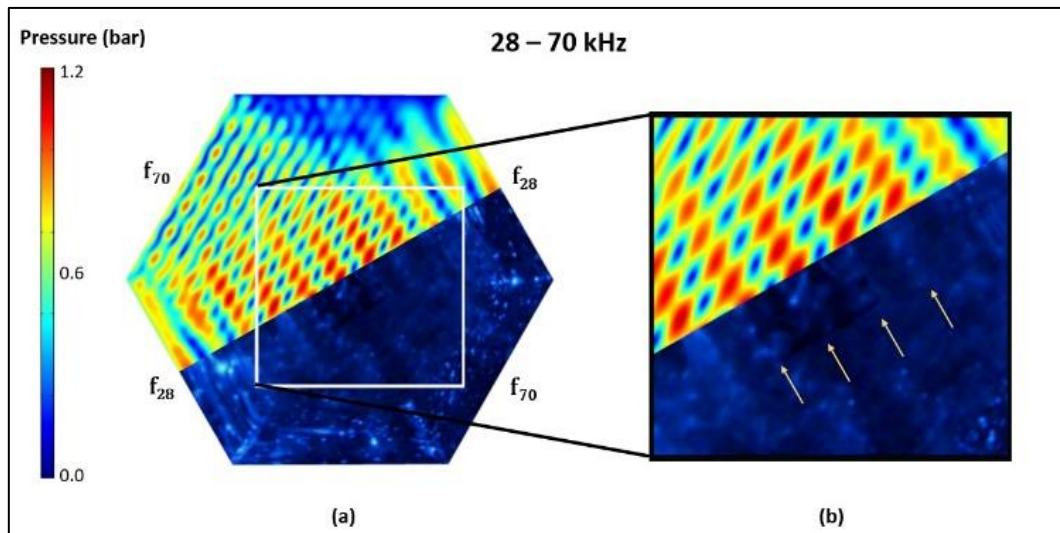


Figure 5.19: (a) Comparison between $P_{rms}(r)$ predicted from simulation and SCL data for the 28 – 70 kHz case superimposed along the 28 kHz standing wave; (b) Region of interest showing very good agreement.

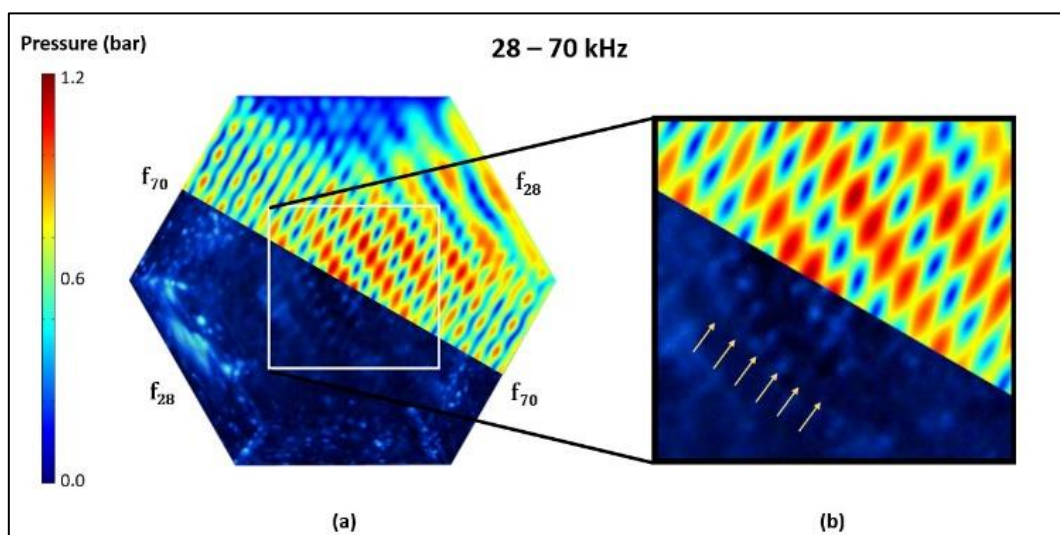


Figure 5.20: (a) Comparison between $P_{rms}(r)$ predicted from simulation and SCL data for the 28 – 70 kHz case; (b) Region of interest showing very good agreement for the fine 70 kHz wave patterns.

Tri-frequency SCL images showed 40 kHz standing waves to be the most dominant, followed by 28 kHz and 70 kHz. The results in Figure 5.21 and Figure 5.22 reconfirmed previous findings in dual-frequency cases where standing wave patterns coincided well with the SCL data, notably with a clear dominance of the 40 kHz standing waves.

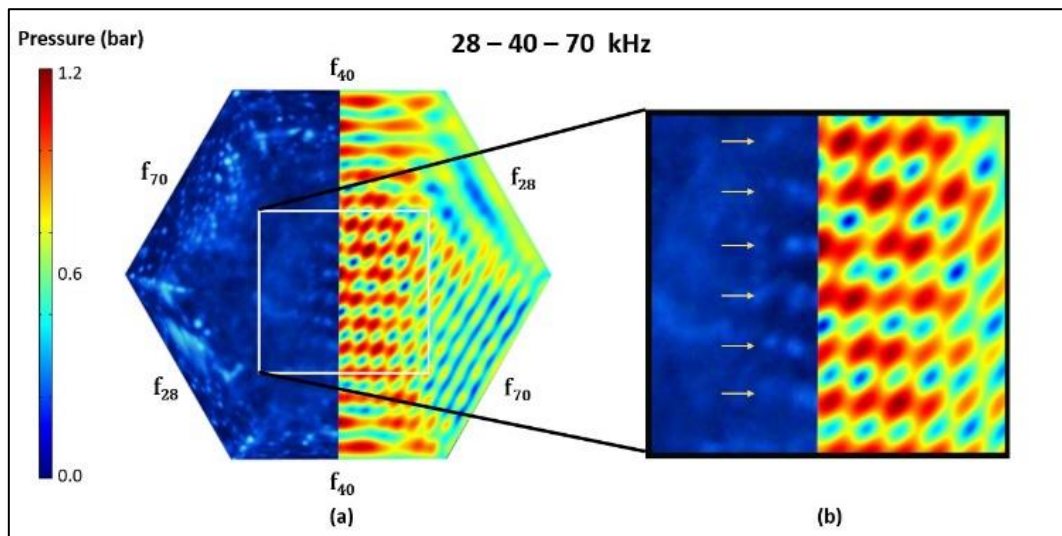


Figure 5.21: (a) Comparison between $P_{rms}(r)$ predicted from simulation and SCL data for the tri-frequency case; (b) Region of interest comparing the 40 kHz standing wave.

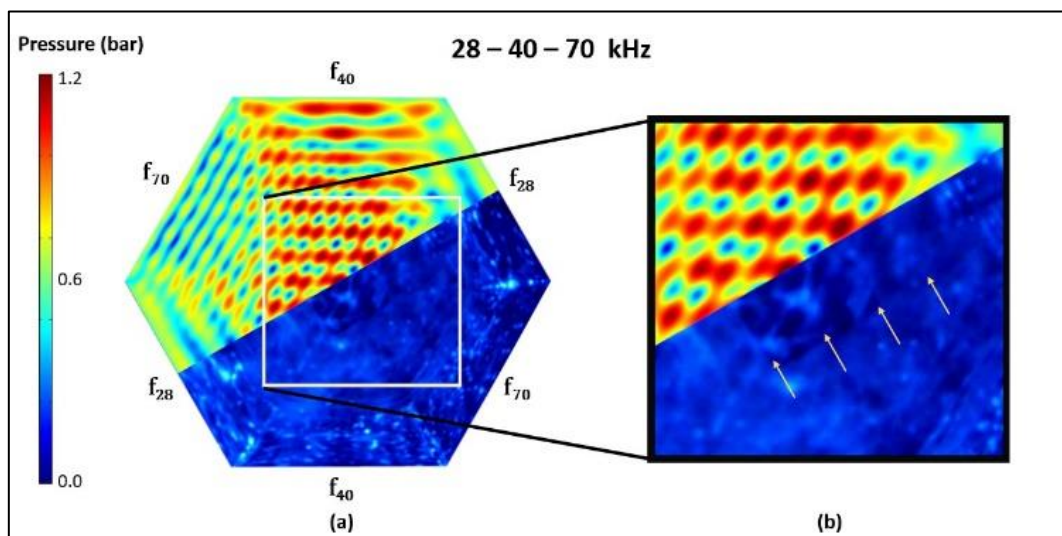


Figure 5.22: (a) Comparison between $P_{rms}(r)$ predicted from simulation and SCL data for the tri-frequency case; (b) Region of interest comparing the 28 kHz standing wave.

The characterisation of multi-frequency composite standing waves in sonoreactors at this scale has yet to be reported in literature. The results presented in this case study provided valuable insights to the behaviour of multi-frequency standing waves in large sonoreactors. The strong agreement in the results suggests that the multi-frequency standing wave patterns can be characterised by linear superposition of frequency-domain solutions. This is an interesting finding because studies on multi-frequency sonoreactor acoustics had predominantly focused on nonlinear effects using time-domain models (Tejedor-Sastre and Vanhille, 2017; Zhang et al., 2017). It should, of course, be noted that previous works only considered horn-type configurations or very small geometries.

The good agreement observed across multiple antinode comparison images suggests that future modelling strategies for bath-type configuration should account for the possibility of a more linear acoustic behaviour. The implication of this is significant, as it suggests that the use of resource intensive time-domain models to characterise multi-frequency sonoreactors can be circumvented. This would greatly improve the efficiency of the design and optimisation process for multi-frequency sonoreactors. The good agreements also strongly support the characterisation method used to predict standing waves in the simulations, which is the linear CP model. This result further supports the hypothesis that the linear CP model is capable of providing good characterisation of bath-type sonoreactors.

Another finding that further supports the applicability of the linear CP model is that the phase speed tuned from Case Study 6 managed to correctly characterise the acoustic behaviour. The agreement for all three studied frequencies using a single

bubble density ($5.2 \times 10^{10} \text{ m}^{-3}$), which approximately corresponds to a phase speed of 1277.5 m/s, is an interesting finding. The results further support the viability of the λ -tuning approach. The finding also suggests that the acoustic property of the working fluid does not change significantly between single- and multi-frequency operations. Additionally, the results also imply that the working fluid exhibits similar acoustic behaviour for all three frequencies, and dispersive effects in the bubbly-liquid are weak. Nevertheless, it is proposed that further investigation on this matter should be carried out using a larger sample size of bath-type sonoreactors, before strong conclusions can be drawn.

5.4.4.5 Interpretation of the Multi-Frequency Pressure Field

The lack of hydrophone measurements to validate the attenuation mechanism of the model limited the following section to a theoretical discussion. Nevertheless, the interpretation of the multi-frequency results presents several points of discussion. In monoharmonic studies, cavitation activity can be interpreted using the absolute acoustic pressure field, $|P|$. The same rationale was not suitable for multi-frequency systems, since the domain experiences multiple pressure fields simultaneously. The total pressure is dependent on the phase differences between harmonics and is no longer sinusoidal. In this case study, it was assumed that the potential for cavitation activity can be characterised using the root-mean-squared pressure $P_{rms}(\mathbf{r})$, which can be interpreted as the effective pressure (Ginsberg, 2018). It is of interest to compare this method to interpreting the cavitation potential using the sum of absolute pressures, or the maximum achievable local pressure magnitude:

$$P_{max}(\mathbf{r}) = \sum abs(P(\mathbf{r})_i) \quad (117)$$

To illustrate the two ideas, Figure 5.23 graphically describes the pressure variation at a *single point in space* experiencing three harmonic acoustic pressure fields oscillating at their respective amplitudes of $P_1(\mathbf{r})$, $P_2(\mathbf{r})$ and $P_3(\mathbf{r})$. The total pressure $p_{total}(\mathbf{r}, t)$ is the sum of the three harmonics, and it is clear that it is no longer sinusoidal. The difference between the root-mean-squared pressure $P_{rms}(\mathbf{r})$ and the maximum achievable magnitude $P_{max}(\mathbf{r})$ is graphically represented. Figure 5.24 plots the same pressure profiles in terms of their absolute value. The absolute total pressure clearly shows the point where the sum of three harmonics reached their highest pressure-potential, which is essentially $P_{max}(\mathbf{r})$. Figure 5.24 shows that $P_{rms}(\mathbf{r})$ better represents the variation of local pressure across time, $|p_{total}|$. Furthermore, it is shown in Figure 5.24 that using $P_{max}(\mathbf{r})$ is less representative of the mean transient behaviour, as it only characterises the acoustic pressure at a specific time.

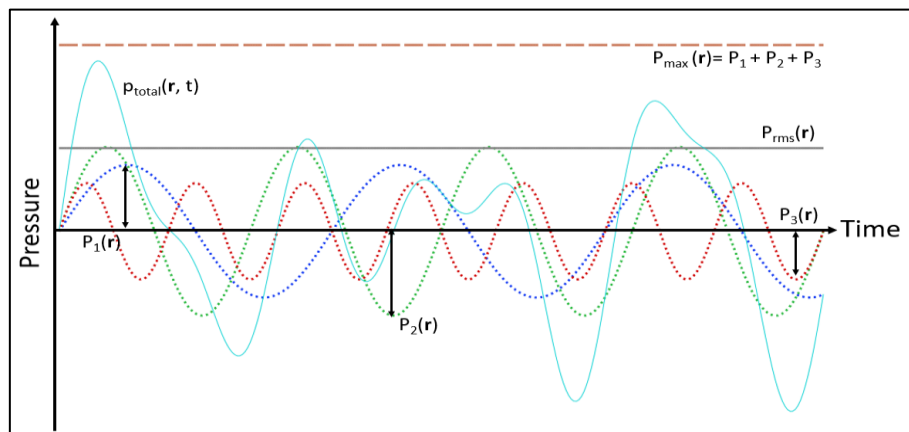


Figure 5.23: Illustration comparing $P_{rms}(\mathbf{r})$ (horizontal solid line) and $P_{max}(\mathbf{r})$ (horizontal dotted line). The fine-dotted curves represent different frequencies oscillating at magnitudes $P_1(\mathbf{r})$, $P_2(\mathbf{r})$ and $P_3(\mathbf{r})$, and $p_{total}(\mathbf{r}, t)$ is the sum of pressure (solid curve).

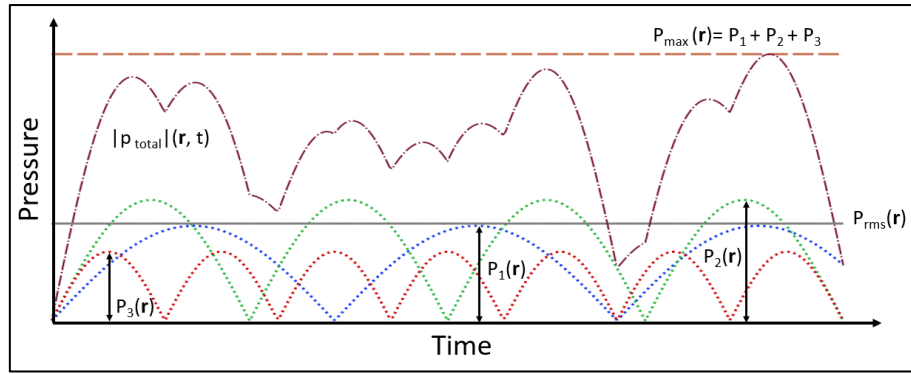


Figure 5.24: The graphical representation in Figure 5.23 plotted in terms of absolute pressure.

To extend this discussion to include the simulation results, the peak values in the domain for both $P_{rms}(\mathbf{r})$ and $P_{max}(\mathbf{r})$ are tabulated in Table 5.7. It should be noted that only the nonlinear CP attenuation model was considered. It is clear that the problem with using $P_{max}(\mathbf{r})$ is that the magnitude becomes larger as the number of summed frequencies increases. One could see how using $P_{max}(\mathbf{r})$ to characterise cavitation potential can lead to overprediction when considering many harmonics.

Table 5.7: Comparison between peak values of RMS pressure and Maximum pressure for frequency combinations.

Simulation	Peak root-mean-squared pressure, $P_{rms,peak}$ (bar)	Peak maximum pressure, $P_{max,peak}$ (bar)
28 – 40	1.365	2.478
28 – 70	1.358	2.715
40 – 70	1.121	2.203
28 – 40 – 70	1.185	3.168

Investigations were also extended to consider the effects of $P_{max}(\mathbf{r})$ and $P_{rms}(\mathbf{r})$ on the nonlinear attenuation mechanism. To visualise how the use of $P_{max}(\mathbf{r})$ instead of

$P_{rms}(\mathbf{r})$ in Eqn. (112) would differ from the current methods, a simulation of the triple-frequency set-up was carried out by setting:

$$\beta = 2 \times 10^{-9} P_{max}(\mathbf{r}) \quad (118)$$

The results are summarised in Figure 5.25. It is clear that the pressure fields predicted for Case 2 were significantly lower than those for Case 1. This was caused by the dependence of attenuation on $P_{max}(\mathbf{r})$. The spatial plot of $P_{max}(\mathbf{r})$ in Figure 5.25 (b) and (d) yields similar observations. Qualitatively, it is interesting to note that Figure 5.25 (a) best represents the standing wave characteristics observed in the SCL image in Figure 5.11 (d). In particular, the dominance and shape of the 40 kHz standing wave compared well with the tri-frequency SCL images in Figure 5.21 and Figure 5.22.

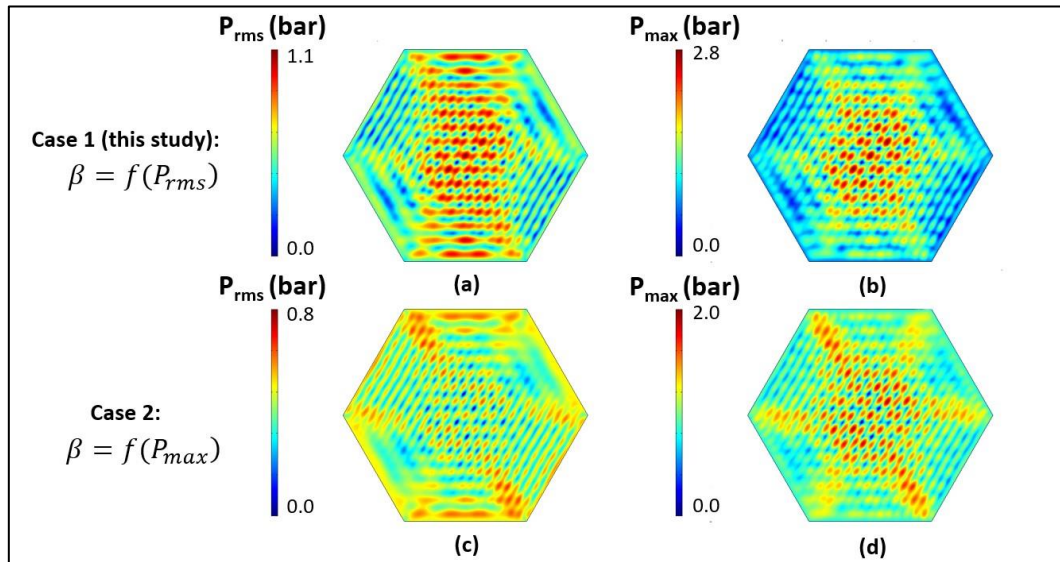


Figure 5.25: Case study on two different interpretations of the acoustic pressure magnitude for the tri-frequency case: Pressure field characterised using $P_{rms}(\mathbf{r})$ (a and c); Pressure field characterised using $P_{max}(\mathbf{r})$ (b and d).

5.4.4.6 Analysis of the Multi-Frequency Standing Wave Characteristics

In this work, the dominance of the 40 kHz standing waves over the 28 and 70 kHz standing waves was clearly observed in the SCL images. Figure 5.26 plots the individual harmonics simulated for the triple frequency operation using the nonlinear approach. Even in the simulations, it is evident that the 40 kHz harmonic showed higher absolute pressure magnitudes. A plausible reason for this observation is the effect of geometry on the interference patterns for each operating frequency.

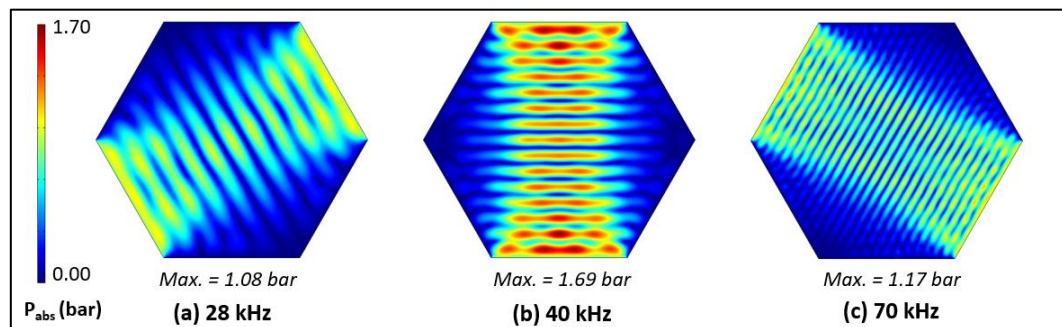


Figure 5.26: Simulated single frequency components for the triple frequency case. Image (a), (b) and (c) represents the 28, 40 and 70 kHz frequency-domain absolute pressure. Results are plotted using a shared colour legend.

The different wavelengths for each harmonic can result in various degrees of constructive / destructive interference due to differences in phase. For the physical hexagonal sonoreactor used in this study, the 40 kHz standing wave was found to experience stronger constructive interference over the other two harmonics. This is shown by simulating the same system using different sizes of hexagonal geometry. Figure 5.27 shows the maximum pressure magnitude calculated for each frequency component as the side length of the hexagonal geometry was varied from 10 to 20 cm.

By varying the side length, the distance between two opposing transducers changes in the hexagonal geometry, resulting in different interference behaviours.

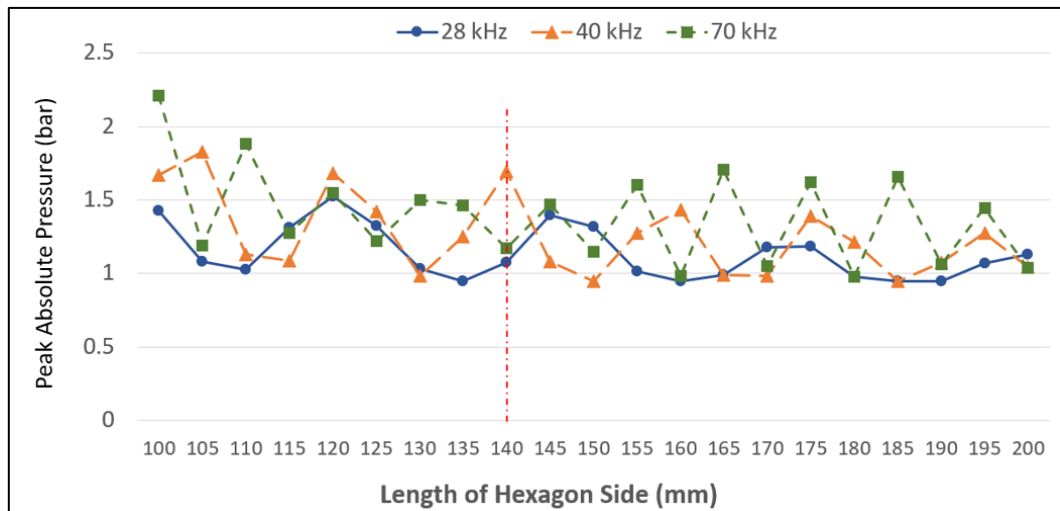


Figure 5.27: Peak absolute pressure for 28, 40 and 70 kHz with increasing hexagonal sonoreactor sizes. The physical sonoreactor used in this work has a side length of 140 mm, marked as the vertical line.

It was observed that the peak absolute pressures exhibit a slight downward trend as the size of the reactor increased because attenuation effects became greater with propagation length. Figure 5.27 shows an oscillating pattern for the pressure magnitude as the dominance of constructive and destructive interference effects alternated with changes in the effective geometry. The physical hexagonal sonoreactor used in this work has a side length of 140 mm, where it can be clearly shown that the 40 kHz frequency experiences strong constructive interference effects. On the other hand, the 70 kHz standing wave was noted to experience strong destructive interference, and the 28 kHz case was noted to be neither. These findings explain the dominance of 40 kHz standing waves observed in the SCL images. The

results also shed light on the observations in Figure 5.19 and Figure 5.20 where the composite standing wave of 28 and 70 kHz was found to be very distinct. Results suggests that the observation was caused by their similar peak pressures. The results presented in Figure 5.27 were also noted to be useful for the optimisation of similar systems.

5.5 Concluding Remarks for Chapter 5

In Chapter 5, a series of investigations and discussions were presented to address current limitations surrounding the linear CP model. An in-depth review on the topic of bubbly-liquid characterisation was conducted, and a novel semi-empirical approach for determining the bubble density parameter was derived and proposed.

Case Study 6 demonstrated the proposed semi-empirical approach and validated antinode prediction results using existing SCL data. The proposed λ -tuning method was argued to be a better alternative to hydrophone tuning methods, and was shown to provide a simple way to circumvent the uncertainties of bubble field characterisation while preserving the integrity of the simulation framework, while also using fewer resources. Validation results were positive, where the tuned bubble densities improved antinode characterisation results in the simulations. Despite promising prospects, several limitations need to be addressed to improve confidence in the method. This includes validation studies for pressure magnitude prediction and the consideration of more complex geometries. The strict assumptions imposed upon the approach also restricted its applicability for horn-type configurations.

Case Study 7 presented a novel exploratory investigation on the concept of characterising multi-frequency pressure fields using frequency-domain simulations. The investigation was the first to characterise multi-frequency sonoreactors at such scales. The linear and nonlinear CP methods were considered under monodisperse conditions, and modified to account for multi-frequency effects. Multi-frequency validation results using SCL showed that standing wave profiles exhibit remarkable agreement. The observations strongly support the viability of the CP model. The results also supported the hypothesis which stated that the multi-frequency pressure field can be characterised using linear superposition and Parseval's theorem. This outcome suggests that the novel modelling strategy can be a promising substitute for transient methods, while offering faster solution time, lower memory consumption, and more streamlined simulation strategies.

The SCL verification results also suggested that the use of a single phase speed to characterise multi-frequency systems to be viable. The study also presented an in-depth discussion on the potential simulation strategies that can be applied to multi-frequency systems. This included the use of a root-mean-squared pressure for cavitation modelling and attenuation modelling for composite pressure fields. Nevertheless, current prospects remain preliminary, as future work had to be done to consider a wider range of configurations and conditions. It was suggested that future studies should consider more experimental validation, as the lack of hydrophone measurements was noted to be a key limitation.

Chapter 6: Conclusions and Future Work

6.1 Key Contributions

The aim of this research is to identify, validate, and improve modelling strategies for large-scale sonoreactors. The scope of this work focused on the performance of frequency-domain modelling strategies in bath-type sonoreactors, specifically for the pure-liquid, linear CP, and NH models in FEM simulations. Compared to horn-type configurations which dominated current literature, bath-type sonoreactors remain to be understudied. This research project reports several in-depth investigations on the topic of modelling in large, bath-type sonoreactors. Across the seven case studies reported in this thesis, the key contributions of this work can be summarised under three main topics.

The first key contribution pertains to the topic of the wavelength-shortening effect. In Case Study 5, the wavelength-shortening effect was systematically documented in the SCL images obtained for the hexagonal sonoreactor. This finding was noted to be important, as the effect had not been experimentally characterised in past literature which used smaller geometries. The reduction of phase speed and subsequent wavelength shortening in sonoreactors was found to be an important consideration when modelling sonoreactor behaviour, evident in Case Studies 4, 5, 6 and 7. The work in Case Study 4 comprehensively analysed the importance of considering geometric properties when applying traditional antinode validation methods. The implications on past and current antinode validation results were also discussed, notably when used for the validation of modelling strategies. In Case Studies 5, the prediction of the wavelength shortening effect was shown to be strongly tied to the bubble density term in bubbly-liquid models. The work in Case Studies 6 and 7 improved current

modelling strategies in terms of predicting the wavelength shortening effect. This was achieved using the λ – tuning method developed in Chapter 5.

The pressure and antinode validation results in Case Studies 3 and 5 revealed important information on the performance of popular modelling strategies in bath-type sonoreactors. In-depth comparison of the pure-liquid, linear CP, and NH models was noted to be useful for future modelling efforts. The validation results strongly suggested that bath-type configurations can be modelled using simpler linear models; in contrast to horn-type configurations which required much comprehensive acoustic and numerical considerations. This claim was further supported by the applicability of linear superposition for the multi-frequency sonoreactor, which showed remarkable agreement in Case Study 7. These insights were found to be useful, as they support the use of more efficient strategies to model bath-type sonoreactors.

In addition to the performance of acoustic pressure models, this work also provided useful information on other aspects of sonoreactor modelling. In particular, the large geometries involved required simplified representations to be explored. The resource requirements highlighted in Case Studies 1 and 3 were found to be useful for future reference. The results of Case Study 2 revealed interesting numerical behaviour exhibited by acoustic boundary conditions in FEM simulations which should be considered in modelling strategies. Furthermore, the need to consider the effective acoustic properties when solving bubbly-liquid models was highlighted.

Chapter 5 of this work presented an in-depth consideration on the topic of bubble field characterisation for bubbly-liquid models. This work revealed a large knowledge gap regarding the applicability of current bubbly-liquid models, which was caused by

the lack of data for bubble density. A novel method to address this knowledge gap was presented in the form of the λ -tuning method, albeit only with limited applicability. Last but not least, the preliminary idea presented in Case Study 7 showed promising prospects in light of remarkable antinode validation results. It was found that the proposed methods can significantly simplify the modelling process of multi-frequency bath-type sonoreactors.

6.2 Summary of Case Studies

Case Study 1 showed that frequency-domain models compared well with time-domain models in terms of antinode prediction, but showed slight deviations in terms of pressure magnitude prediction. The deviations in pressure magnitude were shown to be caused by idealised conditions of the test simulation, which led to periodic phase-cancelling behaviour. **Case Study 2** showed that Dirichlet boundary conditions can be used to model sonoreactor walls in Case Studies 5, 6 and 7. Results showed that the added accuracy of a fully coupled simulation was not significant for the regions of interest investigated in this work. Interestingly, test cases also revealed that Neumann boundary conditions behave differently depending on the size of the boundary, mesh, and shape function. The uncertainties caused by this behaviour should be considered in future studies.

Case Study 3 validated the pure-liquid, linear CP, and NH models using hydrophone measurements for a large ultrasonic bath. Results for the pure-liquid model suggest that it can be considered for systems with low attenuation and negligible reflection effects. At high-frequencies and idealised wall reflections, the model risks predicting

unrealistic pressure magnitudes. The linear CP model yielded mixed results, as performance was strongly dependent on the bubble density. Tuning the bubble density yielded significant improvements for the pressure predictions. The result highlighted the need to focus on improving the bubble field characterisation aspect of bubbly-liquid models. 1D validation of the NH and nonlinear CP models suggested that current implementations overpredict the attenuation in bath-type systems. The investigation also brought attention to a key concern regarding pressure validation studies. Tests using several wall boundary types coupled with the linear CP model suggest a complex behaviour resulting from the effective phase speed, geometry, constructive interference, and boundary reflection which could affect result quality.

Case Study 4 reported a novel investigation on the effect of the geometry-to-wavelength ratio, D_S/λ , on the qualitative result of antinode validation studies. The study identified the importance of geometry and scale in existing antinode validation methods. This issue becomes an important issue when studying large-scale sonoreactors. Both heuristic and theoretical analyses presented strong evidence that the effect of phase-speed reduction by bubbly liquids cannot be clearly captured by antinode characterisation methods if the studies were conducted with a small D_S/λ . The findings provide a good explanation for the lack of wavelength-shortening observations in past studies. Additionally, results also implied against the use of small-scale antinode measurements to validate acoustic pressure models. The study involved the development of a simple idealised model which was used to approximate the geometry threshold in which the wavelength-shortening effect can be captured as additional validation points. The proposed model was noted to be a useful metric for

comparing and characterising antinode validation results between sonoreactors of different geometries.

Case Study 5 reported an antinode validation study for a hexagonal bath-type sonoreactor using SCL data. Validation was carried out at frequencies of 28, 40 and 70 kHz with D_S/λ values of 4.6, 6.6 and 11.5 respectively. The SCL images strongly showed the presence of wavelength-shortening, notably for the standing wave of 40 kHz. This finding was deemed important as it was yet to be documented in literature due to the lack of comprehensive large-scale validation. The pure-liquid model overpredicted the wavelength due to the neglect of bubbly-liquid effects. The linear CP model was able to clearly characterise phase-speed reduction in the simulation results. The predicted wavelength reduction was uniform across the domain, similar to that observed in the SCL results. Similar to Case Study 3, the performance of the linear CP model was strongly dependent on the bubble density specifications. Limited discussion can be made for the NH model due to its complex wavelength prediction mechanism. Antinode validation results showed that the model underestimated the average phase-speed reduction in the studied system, but the main causes were unclear.

Case Study 6 demonstrated the λ -tuning approach derived in Chapter 5 to characterise the bubble density parameter for the hexagonal sonoreactor. The approach managed to circumvent the uncertainties related to bubble field data and better preserved the integrity of the simulation framework. Antinode validation results using SCL images showed remarkable agreement which strongly supported the validity of the proposed approach. The λ -tuning method was identified to be a

promising tool to support current simulation strategies until better bubble density data can be made available for sonoreactors. A key limitation of the approach is that it was developed using heuristics and simplifying assumptions. Further tests such as hydrophone validation were suggested to further confirm its viability.

Case Study 7 explored a novel concept for characterising multi-frequency sonoreactors using frequency-domain models. The assumption of linear superposition was used to approximate the multi-frequency solution. The linear and nonlinear CP models were modified using several key assumptions to predict multi-frequency pressure fields. Antinode verification results showed remarkable agreement for the composite standing waves, which suggest that the strategy can be a promising substitute for transient methods when tackling multi-frequency problems. This was an important discovery, as the proposed method was noted to be more efficient compared to transient methods. Nevertheless, prospects remained to be strongly preliminary, as future work needs to be done to study a wider range of configurations and conditions. The multi-frequency validation results also further supported the viability of the CP model for the characterisation of bath-type configurations, consistent with findings in Case Study 5 and 6. Ancillary simulations also revealed the effect of geometry on standing wave magnitudes of each harmonic, which explained the dominance of the 40 kHz standing wave in both SCL and simulation results.

6.3 Future Work

Several knowledge gaps were identified and suggested for future work:

First, future work should further validate the acoustic pressure models by addressing the limitations encountered in this project. In particular, the acoustic pressure validation study can be improved by considering a more controlled experimental set-up to limit the effects of wall reflection on the acoustic pressure. In terms of antinode validation studies, future work should consider investigating the wavelength-shortening effect in more sonoreactor systems to better understand its effects on sonoreactor acoustics. The lack of hydrophone measurement data for the hexagonal sonoreactor used in this work should also be addressed, and additional validation should be carried out using the obtained measurements. If possible, a full 3D simulation model could also be considered in future investigations. In general, the acoustic pressure models should also be validated for a larger number of systems to strengthen the findings of this work.

The consideration of empirical methods to characterise the bubble field parameters required for the bubbly-liquid models also presents an interesting topic for future research. In this work, the λ -tuning method had shown to be promising in terms of characterising a suitable bubble density parameter for the hexagonal sonoreactor. Additional tests should be performed to investigate the viability of the proposed method in more sonoreactor systems. Future work should also consider extending the proposed idea to consider more wavelength measurement methods (e.g., foil maps) or to improve the dispersion relation used to relate the wavelength to the bubble density.

Last but not least, the idea of characterising the acoustic pressure of a multi-frequency system using frequency-domain models based on linear superposition was shown to be promising in Case Study 7. However, further validation in terms of pressure prediction is still required. There is also a large knowledge gap on the topic of modelling multi-frequency attenuation effects using bubble dynamics. The use of more comprehensive wavenumber predictions similar to the NH model can be considered to improve the proposed method.

References

Ando, E., Kagawa, Y., 1989. Finite element simulation for the design of an ultrasonic cleaning tank. *Electron Commun Jpn* 72, 43-57.

Ando, K., Colonius, T., Brennen, C.E., 2009. Improvement of acoustic theory of ultrasonic waves in dilute bubbly liquids. *J Acoust Soc Am* 126, EL69–EL74.

Asakura, Y., Yasuda, K., 2021. Frequency and power dependence of the sonochemical reaction. *Ultrason Sonochem* 81, 105858.

Asakura, Y., Yasuda, K., Kato, D., Kojima, Y., Koda, S., 2008. Development of a large sonochemical reactor at a high frequency. *Chem Eng J* 139, 339–343.

Ashokkumar, M., 2011. The characterization of acoustic cavitation bubbles - An overview. *Ultrason Sonochem* 18, 864–872.

Ashokkumar, M., Lee, J., Kentish, S., Grieser, F., 2007. Bubbles in an acoustic field: An overview. *Ultrason Sonochem* 14, 470–475.

Avvaru, B., Pandit, A. B., 2009. Oscillating bubble concentration and its size distribution using acoustic emission spectra. *Ultrason Sonochem* 16, 105–115.

Avvaru, B., Pandit, A.B., 2008. Experimental investigation of cavitation bubble dynamics under multi-frequency system. *Ultrason Sonochem* 15, 578–589.

Bandelin, J., Lippert, T., Drewes, J.E., Koch, K., 2020. Assessment of sonotrode and tube reactors for ultrasonic pre-treatment of two different sewage sludge types. *Ultrason Sonochem* 64.

Barthès, M., Mazue, G., Bonnet, D., Viennet, R., Hihn, J.Y., Bailly, Y., 2015. Characterization of the activity of ultrasound emitted in a perpendicular liquid flow using Particle Image Velocimetry (PIV) and electrochemical mass transfer measurements. *Ultrasonics* 59, 72–78.

Beckwith, C., Djambazov, G., Pericleous, K., Subroto, T., Eskin, D.G., Roberts, D., Skalicky, I., Tzanakis, I., 2021. Multiphysics modelling of ultrasonic melt treatment in the hot-top and launder during direct-chill casting: Path to indirect microstructure simulation. *Metals (Basel)* 11.

Berenger, J.-P., 1994. A perfectly matched layer for the absorption of electromagnetic waves. *J Comput Phys* 114, 185–200.

Bjerknes, V.F.K., 1906. *Bjerknes, Fields of Force*, Columbia University Press. Columbia University Press, New York.

Blake, J.R., Keen, G.S., Tong, R.P., Wilson, M., 1999. Acoustic cavitation: The fluid dynamics of non-spherical bubbles. *Philos. Trans. Royal Soc. A: Mathematical, Physical and Engineering Sciences* 357, 251–267.

Brotchie, A., Grieser, F., Ashokkumar, M., 2008. Sonochemistry and Sonoluminescence under Dual-Frequency Ultrasound Irradiation in the Presence of Water-Soluble Solutes. *J Phys Chem C* 112, 10247–10250.

Burdin, F., Guiraud, P., Wilhelm, A., Delmas, H., 2002. Implementation of the Laser Diffraction Technique for Acoustic Cavitation Bubble Investigations. *Part Part Syst Charact* 19, 73–83.

Burdin, F., Tsochatzidis, N.A., Guiraud, P., Wilhelm, A.M., Delmas, H., 1999. Characterisation of the acoustic cavitation cloud by two laser techniques. *Ultrason Sonochem* 6, 43–51.

Caflich, R.E., Miksis, M.J., Papanicolaou, G.C., Ting, L., 1985a. Effective equations for wave propagation in bubbly liquids. *J Fluid Mech* 153, 259–273.

Caflich, R.E., Miksis, M.J., Papanicolaou, G.C., Ting, L., 1985b. Wave propagation in bubbly liquids at finite volume fraction. *J Fluid Mech* 160, 1–14.

Cairós, C., Mettin, R., 2017. Simultaneous high-speed recording of sonoluminescence and bubble dynamics in multibubble fields. *Phys Rev Lett* 118, 64301.

Campos-Pozuelo, C., Granger, C., Vanhille, C., Moussatov, A., Dubus, B., 2005. Experimental and theoretical investigation of the mean acoustic pressure in the cavitation field. *Ultrason Sonochem* 12, 79–84.

Carstensen, E.L., Foldy, L.L., 1947. Propagation of Sound Through a Liquid Containing Bubbles. *J Acoust Soc Am* 19, 481–501.

Chai, Y., Bathe, K.-J., 2020. Transient wave propagation in inhomogeneous media with enriched overlapping triangular elements. *Comput Struct* 237, 106273.

Chai, Y., Zhang, Y., 2020. Transient Wave Propagation Dynamics with Edge-Based Smoothed Finite Element Method and Bathe Time Integration Technique. *Math Probl Eng* 2020, 7180489.

Chen, X., Jiao, Q., Tan, X., Wang, W., 2021. Numerical simulation of ultrasonic enhancement by acoustic streaming and thermal effect on mass transfer through a new computation model. *Int J Heat Mass Transf* 171.

Chen, Y.-C., 2011. A comparative assessment of classification methods for resonance frequency prediction of Langevin piezoelectric transducers. *Appl Math Model* 35, 3334–3344.

J. Choi, J. Khim, B. Neppolian, Y. Son, 2019. Enhancement of sonochemical oxidation reactions using air sparging in a 36 kHz sonoreactor, *Ultrason Sonochem* 51, 412-418.

Chu, J.K., Tiong, T.J., Chong, S., Asli, U.A., 2022. Investigation on different time-harmonic models using FEM for the prediction of acoustic pressure fields in a pilot-scale sonoreactor. *Chem Eng Sci* 247, 116912.

Church, C.C., Carstensen, E.L., 2001. "Stable" inertial cavitation. *Ultrasound Med Biol* 27, 1435–1437.

Commander, K.W., Prosperetti, A., 1989. Linear pressure waves in bubbly liquids: Comparison between theory and experiments. *J Acoust Soc Am* 85, 732–746.

COMSOL AB, 2018. *COMSOL Multiphysics Reference Guide*. Stockholm.

Courant, R., Friedrichs, K., Lewy, H., 1928. Über die partiellen Differenzgleichungen der mathematischen Physik. *Math Ann* 100, 32–74.

Csoka, L., Katekhaye, S.N., Gogate, P.R., 2011. Comparison of cavitation activity in different configurations of sonochemical reactors using model reaction supported with theoretical simulations. *Chem Eng J* 178, 384–390.

Dahlem, O., Reisse, J., Halloin, V., 1999. The radially vibrating horn: A scaling-up possibility for sonochemical reactions. *Chem Eng Sci* 54, 2829–2838.

Dähnke, S., Swamy, K.M., Keil, F.J., 1999a. Modeling of three-dimensional pressure fields in sonochemical reactors with an inhomogeneous density distribution of cavitation bubbles. *Ultrason Sonochem* 6, 31–41.

Dähnke, S., Swamy, K.M., Keil, F.J., 1999b. A comparative study on the modeling of sound pressure field distributions in a sonoreactor with experimental investigation. *Ultrason Sonochem* 6, 221–226.

Dähnke, S.W., Keil, F.J., 1999. Modeling of linear pressure fields in sonochemical reactors considering an inhomogeneous density distribution of cavitation bubbles. *Chem Eng Sci* 54, 2865–2872.

DeAngelis, D.A., Schulze, G.W., 2016. Performance of PZT8 Versus PZT4 Piezoceramic Materials in Ultrasonic Transducers. *Phys Procedia* 87, 85–92.

Delacour, C., Stephens, D.S., Lutz, C., Mettin, R., Kuhn, S., 2020. Design and Characterization of a Scaled-up Ultrasonic Flow Reactor. *Org Process Res Dev* 24, 2085–2093.

Deuflhard, P., 1974. A modified Newton method for the solution of ill-conditioned systems of nonlinear equations with application to multiple shooting. *Numer Math (Heidelb)* 22, 289–315.

Dogan, H., Popov, V., 2016. Numerical simulation of the nonlinear ultrasonic pressure wave propagation in a cavitating bubbly liquid inside a sonochemical reactor. *Ultrason Sonochem* 30, 87–97.

Doinikov, A., Novell, A., Bouakaz, A., Calmon, P., 2013. The Westervelt equation for nonlinear propagation: Numerical simulations and experimental validation of ultrasonic fields produced by array transducers, in: *2013 IEEE International Ultrasonics Symposium (IUS)*. pp. 608–610.

Duraiswami, R., Prabhukumar, S., Chahine, G.L., 1998. Bubble counting using an inverse acoustic scattering method. *J Acoust Soc Am* 104, 2699–2717.

Eckart, C., 1948. Vortices and streams caused by sound waves. *Physical Review* 73, 68–76.

Fang, Y., Yamamoto, T., Komarov, S., 2018. Cavitation and acoustic streaming generated by different sonotrode tips. *Ultrason Sonochem* 48, 79–87.

Fish, J., Belytschko, T., 2007. *A First Course in Finite Elements*.

Flynn, H.G., 1964. *Physics of Acoustic Cavitation*, Academic Press.

Foldy, L.L., 1945. The multiple scattering of waves. I. General theory of isotropic scattering by randomly distributed scatterers. *Phys Rev* 67, 107–119.

Forsyth, D.A., Ponce, J., 2002. *Computer Vision: A Modern Approach*. Prentice Hall Professional Technical Reference.

Fox, F.E., Rock, G.D., 1941. Ultrasonic Absorption in Water. *J Acoust Soc Am* 12, 505–510.

Fuster, D., Conoir, J.M., Colonius, T., 2014. Effect of direct bubble-bubble interactions on linear-wave propagation in bubbly liquids. *Phys Rev E Stat Nonlin Soft Matter Phys* 90, 63010.

Fuster, D., Montel, F., 2015. Mass transfer effects on linear wave propagation in diluted bubbly liquids. *J Fluid Mech* 779, 598–621.

Gholami, P., Khataee, A., Soltani, R.D.C., Bhatnagar, A., 2019. A review on carbon-based materials for heterogeneous sonocatalysis: Fundamentals, properties and applications. *Ultrason Sonochem* 58, 104681.

Ginsberg, J.H., 2018. *Acoustics-A Textbook for Engineers and Physicists*, 1st ed. Springer International Publishing.

Glasse, R.T., 1981. Finite-time blow-up for solutions of nonlinear wave equations. *Math Z* 177, 323–340.

Gogate, P.R., Sutkar, V.S., Pandit, A.B., 2011. Sonochemical reactors: Important design and scale up considerations with a special emphasis on heterogeneous systems. *Chem Eng J* 166, 1066–1082.

Guédra, M., Inserra, C., Gilles, B., Béra, J.-C., 2015. Numerical investigations of single bubble oscillations generated by a dual frequency excitation. *J Phys Conf Ser* 656, 12019.

Guo, Y., Yang, X., Li, G., Dong, B., Chen, L., 2019. Effect of ultrasonic intensification on synthesis of nano-sized particles with an impinging jet reactor. *Powder Technol.* 354.

Helton, J., 2012. Numerical Methods in Engineering and Science. *Technometrics* 29, 248–249.

Hunt, J.T., Knittel, M.R., Barach, D., 1974. Finite element approach to acoustic radiation from elastic structures. *J Acoust Soc Am* 55, 269–280.

Hussain, M.N., Janajreh, I., 2018. Acousto-chemical analysis in multi-transducer sonochemical reactors for biodiesel production. *Ultrason Sonochem* 40, 184–193.

Hussain, M.N., Janajreh, I., 2017. Numerical Simulation and Experimental Testing of Novel Sonochemical Reactor for Transesterification. *Waste Biomass Valorization* 8, 1733–1747.

Huttunen, T., Malinen, M., Kaipio, J.P., White, P.J., Hynynen, K., 2005. A full-wave Helmholtz model for continuous-wave ultrasound transmission. *IEEE Trans Ultrason Ferroelectr Freq Control* 52, 397–409.

Ihlenburg, F., Babuška, I., 1995. Finite element solution of the Helmholtz equation with high wave number Part I: The h-version of the FEM. *Computers and Mathematics with Applications* 30, 9–37.

Iida, Y., Ashokkumar, M., Tuziuti, T., Kozuka, T., Yasui, K., Towata, A., Lee, J., 2010. Bubble population phenomena in sonochemical reactor: I Estimation of bubble size distribution and its number density with pulsed sonication – Laser diffraction method. *Ultrason Sonochem* 17, 473–479.

Islam, M.H., Burheim, O.S., Pollet, B.G., 2019a. Sonochemical and sonoelectrochemical production of hydrogen. *Ultrason Sonochem* 51, 533–555.

Islam, M.H., Paul, M.T.Y., Burheim, O.S., Pollet, B.G., 2019b. Recent developments in the sonoelectrochemical synthesis of nanomaterials. *Ultrason Sonochem* 59, 104711.

Iula, A., Vazquez, F., Pappalardo, M., Gallego, J.A., 2002. Finite element three-dimensional analysis of the vibrational behaviour of the Langevin-type transducer. *Ultrasonics* 40, 513–517.

Jähne, B., 2004. *Practical Handbook on Image Processing for Scientific and Technical Applications*, Second Edition.

Jamshidi, R., Brenner, G., 2013. Dissipation of ultrasonic wave propagation in bubbly liquids considering the effect of compressibility to the first order of acoustical Mach number. *Ultrasonics* 53, 842–848. <https://doi.org/10.1016/j.ultras.2012.12.004>

Jamshidi, R., Pohl, B., Peuker, U.A., Brenner, G., 2012. Numerical investigation of sonochemical reactors considering the effect of inhomogeneous bubble clouds on ultrasonic wave propagation. *Chemical Engineering Journal* 189–190, 364–375.

Johnson, S.G., 2010. Notes on Perfectly Matched Layers (PMLs) [WWW Document]. URL: <https://math.mit.edu/~stevenj/18.369/spring09/pml.pdf>

Jordens, J., Honings, A., Degève, J., Braeken, L., Gerven, T. Van, 2013. Investigation of design parameters in ultrasound reactors with confined channels. *Ultrason Sonochem* 20, 1345–1352.

Kanagawa, T., Ayukai, T., Kawame, T., Ishitsuka, R., 2021. Weakly nonlinear theory on pressure waves in bubbly liquids with a weak polydispersity. *Int J Multiph Flow* 142, 103622.

Kargl, S.G., 2002. Effective medium approach to linear acoustics in bubbly liquids. *J Acoust Soc Am* 111, 168–173.

Keller, J.B., Miksis, M., 1998. Bubble oscillations of large amplitude. *J Acoust Soc Am* 68, 628–633.

Kinsler, L.E., Frey, A.R., Coppens, A.B., Sanders, J. V., 1982. *Fundamentals of Acoustics*, 3rd ed. John Wiley and Sons.

Kiss, A.A., Geertman, R., Wierschem, M., Skiborowski, M., Gielen, B., Jordens, J., John, J.J., van Gerven, T., 2018. Ultrasound-assisted emerging technologies for chemical processes. *J Chem Technol Biotechnol* 93, 1219–1227.

Klíma, J., Frias-Ferrer, A., González-García, J., Ludvík, J., Sáez, V., Iniesta, J., 2007. Optimisation of 20 kHz sonoreactor geometry on the basis of numerical simulation of local ultrasonic intensity and qualitative comparison with experimental results. *Ultrason Sonochem* 14, 19–28.

Kumar, A., Gogate, P.R., Pandit, A.B., 2007. Mapping the efficacy of new designs for large scale sonochemical reactors. *Ultrason Sonochem* 14, 538–544.

Kuroyama, T., 2021. Number density of bubbles under ultrasonic horn measured from stroboscopic images. *Jpn J Appl Phys* 60.

Kuroyama, T., Ebihara, T., Mizutani, K., Ohbuchi, T., 2011. Experimental study on measurement of acoustic cavitation bubbles in spatial frequency domain using optical spectrometer. *Jpn J Appl Phys* 50, 07HE05.

Laborde, J.L., Bouyer, C., Caltagirone, J.P., Gérard, A., 1998. Acoustic cavitation field prediction at low and high frequency ultrasounds. *Ultrasonics* 36, 581–587.

Labouret, S., Frohly, J., 2002. Bubble size distribution estimation via void rate dissipation in gas saturated liquid. Application to ultrasonic cavitation bubble fields. *EPJ Appl. Phys* 19, 39–54.

Lais, H., Lowe, P.S., Gan, T.H., Wrobel, L.C., 2018. Numerical modelling of acoustic pressure fields to optimize the ultrasonic cleaning technique for cylinders. *Ultrason Sonochem* 45, 7–16.

Lebon, G.S.B., Tzanakis, I., Djambazov, G., Pericleous, K., Eskin, D.G., 2017. Numerical modelling of ultrasonic waves in a bubbly Newtonian liquid using a high-order acoustic cavitation model. *Ultrason Sonochem* 37, 660–668.

Lebon, G.S.B., Tzanakis, I., Pericleous, K., Eskin, D., 2018. Experimental and numerical investigation of acoustic pressures in different liquids. *Ultrason Sonochem* 42, 411–421.

Lebon, G.S.B., Salloum-Abou-Jaoude, G., Eskin, D., Tzanakis, I., Pericleous, K., Jarry, P., 2019a. Numerical modelling of acoustic streaming during the ultrasonic melt treatment of direct-chill (DC) casting. *Ultrason Sonochem* 54, 171–182.

Lebon, G.S.B., Tzanakis, I., Pericleous, K., Eskin, D., Grant, P.S., 2019b. Ultrasonic liquid metal processing: The essential role of cavitation bubbles in controlling acoustic streaming. *Ultrason Sonochem* 55, 243–255.

Lee, J., Ashokkumar, M., Kentish, S., Grieser, F., 2005. Determination of the size distribution of sonoluminescence bubbles in a pulsed acoustic field. *J Am Chem Soc* 127, 16810–16811.

Leighton, T., 1994. *The Acoustic Bubble*

Lewis, J.P., Gardner, S., Corp, I., 2007. A 2D finite element analysis of an ultrasonic cleaning vessel: Results and comparisons. *International Journal of Modelling and Simulation* 27, 181–185.

Ley, S.V., Low, C.M.R., 1989. Ultrasound in synthesis, *Journal of Organometallic Chemistry*. Springer-Verlag, Berlin.

Liu, Y.-N., Jin, D., Lu, X.-P., Han, P.-F., 2008. Study on degradation of dimethoate solution in ultrasonic airlift loop reactor. *Ultrason Sonochem* 15, 755–760.

Lorimer, J.P., Mason, T.J., 1987. Sonochemistry. Part 1 - The physical aspects. *Chem Soc Rev* 16, 239–274.

Louisnard, O., 2017. A viable method to predict acoustic streaming in presence of cavitation. *Ultrason Sonochem* 35, 518–524.

Louisnard, O., 1998. Contribution à l'étude de la propagation des ultrasons en milieu cavitant. Génie des procédés. Ecole des mines de Paris, Français.

Louisnard, O., 2012a. A simple model of ultrasound propagation in a cavitating liquid. Part I: Theory, nonlinear attenuation and traveling wave generation. *Ultrason Sonochem* 19, 66–76.

Louisnard, O., 2012b. A simple model of ultrasound propagation in a cavitating liquid. Part II: Primary Bjerknes force and bubble structures. *Ultrason Sonochem* 19, 56–65.

Louisnard, O., 2010. Nonlinear attenuation of sound waves by inertial cavitation bubbles. *Phys Procedia* 3, 735–742.

Louisnard, O., Gonzalez-Garcia, J., Tudela, I., Klíma, J., Saez, V., Vargas-Hernandez, Y., 2009. FEM simulation of a sono-reactor accounting for vibrations of the boundaries. *Ultrason Sonochem* 16, 250–259.

Ma, X., Huang, B., Wang, G., Zhang, M., 2017. Experimental investigation of conical bubble structure and acoustic flow structure in ultrasonic field. *Ultrason Sonochem* 34, 164–172.

Manickam, S., Zainal Abidin, N.-binti, Parthasarathy, S., Alzorqi, I., Ng, E.H., Tiong, T.J., Gomes, R.L., Ali, A., 2014. Role of H₂O₂ in the fluctuating patterns of COD (chemical oxygen demand) during the treatment of palm oil mill effluent (POME) using pilot scale triple frequency ultrasound cavitation reactor. *Ultrason Sonochem* 21, 1519–1526.

Markham, J.J., Beyer, R.T., Lindsay, R.B., 1951. Absorption of sound in fluids. *Rev Mod Phys* 23, 353–411.

Matafonova, G., Batoev, V., 2020. Dual-frequency ultrasound: Strengths and shortcomings to water treatment and disinfection. *Water Res* 182, 116016.

Mettin, R., 2005b. Bubble structures in acoustic cavitation, in: Doinikov, A.A. (Ed.), *Bubble and Particle Dynamics in Acoustic Fields: Modern Trends and Applications. Research Signpost*, Kerala, India, pp. 1–36.

Mettin, R., Akhatov, I., Parlitz, U., Ohl, C.D., Lauterborn, W., 1997. Bjerknes forces between small cavitation bubbles in a strong acoustic field, *Phys Rev E* 56, 2924-2931.

Mettin, R., Luther, S., Lauterborn, W., 1999. Bubble size distribution and structures in acoustic cavitation, in: 2nd Conf. on Applications of Power Ultrasound in Physical and Chemical Processing. pp. 125–129.

Mettin, R., Luther, S., Ohl, C.D., Lauterborn, W., 1999. Acoustic cavitation structures and simulations by a particle model. *Ultrason Sonochem* 6, 25–29.

Miksis, M.J., Ting, L., 1989. Effects of bubbly layers on wave propagation. *J Acoust Soc Am* 86, 2349–2358.

Miles, R., 2020. *Physical Approach to Engineering Acoustics*.

Minnaert, M., 1933. XVI. On musical air-bubbles and the sounds of running water. *Lond Edinb Dubl Phil Mag* 16, 235–248.

Modarres-Gheisari, S.M.M., Gavagsaz-Ghoachani, R., Malaki, M., Safarpour, P., Zandi, M., 2019. Ultrasonic nano-emulsification – A review. *Ultrason Sonochem* 52, 88–105.

Mohammadi, B., Safaiyan, A., Habibi, P., Moradi, G., 2021. Evaluation of the acoustic performance of polyurethane foams embedded with rock wool fibers at low-frequency range; design and construction. *Appl Acoust* 182, 108223.

Moholkar, V.S., Sable, S.P., Pandit, A.B., 2000. Mapping the cavitation intensity in an ultrasonic bath using the acoustic emission, *AIChE Journal*.

Moser, F., Jacobs, L.J., Qu, J., 1999. Modeling elastic wave propagation in waveguides with the finite element method. *NDT & E International* 32, 225–234.

Moussatov, A., Granger, C., Dubus, B., 2003. Cone-like bubble formation in ultrasonic cavitation field. *Ultrason Sonochem* 10, 191–195.

Naudé, C.F., Ellis, A.T., 2011. On the Mechanism of Cavitation Damage by Nonhemispherical Cavities Collapsing in Contact With a Solid Boundary. *Journal of Basic Engineering* 83, 648.

Noltingk, B.E., Neppiras, E.A., 1950. Cavitation produced by Ultrasonics. *Proceedings of the Physical Society. Section B* 63, 674–685.

O’Sullivan, J.J., Espinoza, C.J.U., Mihailova, O., Alberini, F., 2018. Characterisation of flow behaviour and velocity induced by ultrasound using particle image velocimetry (PIV): Effect of fluid rheology, acoustic intensity and transducer tip size. *Ultrason Sonochem* 48, 218–230.

Pandit, A.V., Sarvothaman, V.P., Ranade, V.V., 2021. Estimation of chemical and physical effects of cavitation by analysis of cavitating single bubble dynamics. *Ultrason Sonochem* 77, 105677.

Perincek, S., Uzgur, A.E., Duran, K., Dogan, A., Korlu, A.E., Bahtiyari, İ.M., 2009. Design parameter investigation of industrial size ultrasound textile treatment bath. *Ultrason Sonochem* 16, 184–189.

Pflieger, R., Bertolo, J., Gravier, L., Nikitenko, S.I., Ashokkumar, M., 2021. Impact of bubble coalescence in the determination of bubble sizes using a pulsed US technique: Part 1 – Argon bubbles in water. *Ultrason Sonochem* 73, 105532.

Pierce, A.D., 1989. *Acoustics: An Introduction to Its Physical Principles and Applications*. Acoustical Society of America.

Plesset, M.S., 1949. The dynamics of cavitation bubbles. *ASME J. Appl. Mech.* 16, 228–231.

Pokhrel, N., Vabbina, P.K., Pala, N., 2016. Sonochemistry: Science and Engineering. *Ultrason Sonochem* 29, 104–128.

Preston, A.T., Colonius, T., Brennen, C.E., 2007. A reduced-order model of diffusive effects on the dynamics of bubbles. *Physics of Fluids* 19, 123302.

Prikšaitis, J., Mažeika, L., Barauskas, R., Žukauskas, E., Kriščiūnas, A., 2015. Influence of the Numerical Dispersion Effects in the Modelling of Ultrasonic Measurements. *Phys Procedia* 70, 532–536.

Prinn, A.G., 2021. On Computing Impulse Responses from Frequency-Domain Finite Element Solutions. *J Theor Comput Acoust* 29, 2050024.

Prosperetti, A., 2015. The speed of sound in a gas–vapour bubbly liquid. *Interface Focus* 5, 20150024.

Prosperetti, A., 1977. Thermal effects and damping mechanisms in the forced radial oscillations of gas bubbles in liquids. *J Acoust Soc Am* 61, 17–27.

Prosperetti, A., 1975. Nonlinear oscillations of gas bubbles in liquids. Transient solutions and the connection between subharmonic signal and cavitation. *J Acoust Soc Am* 57, 810–821.

Rashwan, S.S., Dincer, I., Mohany, A., 2020. Investigation of acoustic and geometric effects on the sonoreactor performance. *Ultrason Sonochem* 68, 105174.

Rashwan, S.S., Mohany, A., Dincer, I., 2021. Development of efficient sonoreactor geometries for hydrogen production. *Int J Hydrogen Energy* 46, 15219–15240.

Rayleigh, L., 1917. VIII. *On the pressure developed in a liquid during the collapse of a spherical cavity*. *London Edinburgh Philos Mag J Sci* 34, 94–98.

Reuter, F., Lesnik, S., Ayaz-Bustami, K., Brenner, G., Mettin, R., 2019. Bubble size measurements in different acoustic cavitation structures: Filaments, clusters, and the acoustically cavitated jet. *Ultrason Sonochem* 55, 383–394.

Romdhane, M., Gadri, A., Contamine, F., Gourdon, C., Casamatta, G., 1997. Experimental study of the ultrasound attenuation in chemical reactors. *Ultrason Sonochem* 4, 235–243.

Sáez, V., Frías-Ferrer, A., Iniesta, J., González-García, J., Aldaz, A., Riera, E., 2005. Characterization of a 20 kHz sonoreactor. Part I: Analysis of mechanical effects by classical and numerical methods. *Ultrason Sonochem* 12, 59–65.

Sander, J.R.G., Zeiger, B.W., Suslick, K.S., 2014. Sonocrystallization and sonofragmentation. *Ultrason Sonochem* 21, 1908–1915.

Sarac, B.E., Stephens, D.S., Eisener, J., Rosselló, J.M., Mettin, R., 2020. Cavitation bubble dynamics and sonochemiluminescence activity inside sonicated submerged flow tubes. *Chem Eng Process: Process Intensif* 150.

Servant, G., Caltagirone, J.P., Gérard, A., Laborde, J.L., Hita, A., 2000. Numerical simulation of cavitation bubble dynamics induced by ultrasound waves in a high frequency reactor. *Ultrason Sonochem* 7, 217–227.

Servant, G., Laborde, J.L., Hita, A., Caltagirone, J.P., Gérard, A., 2001a. Spatio-temporal dynamics of cavitation bubble clouds in a low frequency reactor: Comparison between theoretical and experimental results. *Ultrason Sonochem* 8, 163–174.

Servant, G., Laborde, J.L., Hita, A., Caltagirone, J.P., Gérard, A., 2001b. On the use of ultrasound in chemistry: Modelling of sonoreactors. Determination of cavitation bubble emergence, bubble migration through time, fluid flow induced by the propagation of an ultrasound wave. Comparison of theoretical and experimental results, *American Society of Mechanical Engineers, Pressure Vessels and Piping Division (Publication) PVP 424*, pp. 13–26.

Servant, G., Laborde, J.L., Hita, A., Caltagirone, J.P., Gérard, A., 2003. On the interaction between ultrasound waves and bubble clouds in mono- and dual-frequency sonoreactors. *Ultrason Sonochem* 10, 347–355.

Seung, S., Kwak, H.-Y., 2017. Shock wave propagation in bubbly liquids at small gas volume fractions. *Journal of Mechanical Science and Technology* 31, 1223–1231.

Shao, Z.W., Le, Q.C., Cui, J.Z., Zhang, Z.Q., 2010. Numerical simulation of standing waves for ultrasonic purification of magnesium alloy melt. *Transactions of Nonferrous Metals Society of China (English Edition)* 20, s382–s387.

Singla, M., Sit, N., 2021. Application of ultrasound in combination with other technologies in food processing: A review. *Ultrason Sonochem* 73, 105506.

Son, Y., Lim, M., Khim, J., 2009. Investigation of acoustic cavitation energy in a large-scale sonoreactor. *Ultrason Sonochem* 16, 552–556.

Son, Y., Lim, M., Cui, M., Khim, J., 2010. Estimation of Sonochemical Reactions under Single and Dual Frequencies Based on Energy Analysis. *Jpn J Appl Phys* 49, 07HE02.

Son, Y., No, Y., Kim, J., 2020. Geometric and operational optimization of 20-kHz probe-type sonoreactor for enhancing sonochemical activity. *Ultrason Sonochem* 65, 105065.

Soto, G., Castro, A., Vechiatti, N., Iasi, F., Armas, A., Marcovich, N.E., Mosiewicki, M.A., 2017. Biobased porous acoustical absorbers made from polyurethane and waste tire particles. *Polym Test* 57, 42–51.

Subroto, T., Lebon, G.S.B., Eskin, D.G., Skalicky, I., Roberts, D., Tzanakis, I., Pericleous, K., 2021. Numerical modelling and experimental validation of the effect of ultrasonic melt treatment in a direct-chill cast AA6008 alloy billet. *J Mater Res Technol* 12, 1582–1596.

Suo, D., Govind, B., Zhang, S., Jing, Y., 2018. Numerical investigation of the inertial cavitation threshold under multi-frequency ultrasound. *Ultrason Sonochem* 41, 419–426.

Sutkar, V.S., Gogate, P.R., 2010. Mapping of cavitation activity in high frequency sonochemical reactor. *Chem Eng J* 158, 296–304.

Sutkar, V.S., Gogate, P.R., 2009. Design aspects of sonochemical reactors: Techniques for understanding cavitation activity distribution and effect of operating parameters. *Chem Eng J* 155, 26–36.

Sutkar, V.S., Gogate, P.R., Csoka, L., 2010. Theoretical prediction of cavitation activity distribution in sonochemical reactors. *Chem Eng J* 158, 290–295.

Tangsopa, W., Thongsri, J., 2021. A dual frequency ultrasonic cleaning tank developed by transient dynamic analysis. *Appl Sci (Switzerland)* 11, 1–20.

Tangsopa, W., Thongsri, J., 2019. Development of an industrial ultrasonic cleaning tank based on harmonic response analysis. *Ultrasonics* 91, 68–76.

Tejedor Sastre, M.T., Vanhille, C., 2017. Numerical models for the study of the nonlinear frequency mixing in two and three-dimensional resonant cavities filled with a bubbly liquid. *Ultrason Sonochem* 39, 597–610.

Thompson, L.L., 2006. A review of finite-element methods for time-harmonic acoustics. *J Acoust Soc Am* 119, 1315–1330.

Tian, Y., Liu, Z., Li, X., Zhang, L., Li, R., Jiang, R., Dong, F., 2018. The cavitation erosion of ultrasonic sonotrode during large-scale metallic casting: Experiment and simulation. *Ultrason Sonochem* 43, 29–37.

Tiong, T.J., Chandesa, T., Yap, Y.H., 2017a. Comparison of sonochemiluminescence images using image analysis techniques and identification of acoustic pressure fields via simulation. *Ultrason Sonochem* 36, 78–87.

Tiong, T.J., Liew, D.K.L., Gondipon, R.C., Wong, R.W., Loo, Y.L., Lok, M.S.T., Manickam, S., 2017b. Identification of active sonochemical zones in a triple frequency ultrasonic reactor via physical and chemical characterization techniques. *Ultrason Sonochem* 35, 569–576.

Tiong, T.J., Chu, J.K., Lim, L.Y., Tan, K.W., Hong Yap, Y., Asli, U.A., 2019. A computational and experimental study on acoustic pressure for ultrasonically formed oil-in-water emulsion. *Ultrason Sonochem* 56, 46–54.

Toegel, R., Gompf, B., Pecha, R., Lohse, D., 2000. Does Water Vapor Prevent Upscaling Sonoluminescence? *Phys Rev Lett* 85, 3165–3168.

Tonry, C.E.H., Djambazov, G., Dybalska, A., Griffiths, W.D., Beckwith, C., Bojarevics, V., Pericleous, K.A., 2020. Acoustic resonance for contactless ultrasonic cavitation in alloy melts. *Ultrason Sonochem* 63.

Trujillo, F.J., 2020. A strict formulation of a nonlinear Helmholtz equation for the propagation of sound in bubbly liquids. Part II: Application to ultrasonic cavitation. *Ultrason Sonochem* 65, 105056.

Trujillo, F.J., 2018. A strict formulation of a nonlinear Helmholtz equation for the propagation of sound in bubbly liquids. Part I: Theory and validation at low acoustic pressure amplitudes. *Ultrason Sonochem* 47, 75–98.

Tsochatzidis, N.A., Guiraud, P., Wilhelm, A.M., Delmas, H., 2001. Determination of velocity, size and concentration of ultrasonic cavitation bubbles by the phase-Doppler technique. *Chem Eng Sci* 56, 1831–1840.

Tudela, I., Sáez, V., Esclapez, M.D., Bonete, P., Harzali, H., Baillon, F., González-García, J., Louisnard, O., 2011. Study of the influence of transducer-electrode and electrode-wall gaps on the acoustic field inside a sonoelectrochemical reactor by FEM simulations. *Chem Eng J* 171, 81–91.

Tudela, I., Sáez, V., Esclapez, M.D., Díez-García, M.I., Bonete, P., González-García, J., 2014. Simulation of the spatial distribution of the acoustic pressure in sonochemical reactors with numerical methods: A review. *Ultrason Sonochem* 21, 909–919.

Wijngaarden, L., 1970. On the structure of shock waves in liquid-bubble mixtures. *Appl Sci Res* 22, 366–381.

Vanhille, C., Conde, C., Campos-Pozuelo, C., 2004. Finite-difference and finite-volume methods for nonlinear standing ultrasonic waves in fluid media. *Ultrasonics* 42, 315–318.

Vanhille, C., Campos-Pozuelo, C., 2005. Numerical and experimental analysis of strongly nonlinear standing acoustic waves in axisymmetric cavities. *Ultrasonics* 43, 652–660.

Vanhille, C., Campos-Pozuelo, C., 2009a. Numerical simulation of nonlinear ultrasonic standing waves in bubbly liquid. *Int J Nonlinear Sci Numer* 10, 751–757.

Vanhille, C., Campos-Pozuelo, C., 2009b. Nonlinear ultrasonic waves in bubbly liquids with nonhomogeneous bubble distribution: Numerical experiments. *Ultrason Sonochem* 16, 669–685.

Vanhille, C., Campos-Pozuelo, C., 2011. Nonlinear ultrasonic standing waves: Two-dimensional simulations in bubbly liquids. *Ultrason Sonochem* 18, 679–682.

Wang, Y.-C., Yao, M.-C., 2013. Realization of cavitation fields based on the acoustic resonance modes in an immersion-type sonochemical reactor. *Ultrason Sonochem* 20, 565–570.

Wang, Y.-Y., Yan, J.-K., Rashid, M.T., Ding, Y., Chikari, F., Huang, S., Ma, H., 2021. Dual-frequency sequential ultrasound thawing for improving the quality of quick-frozen

small yellow croaker and its possible mechanisms. *Innov Food Sci Emerg Technol.* 68, 102614.

Wei, Z., Weavers, L.K., 2016. Combining COMSOL modeling with acoustic pressure maps to design sono-reactors. *Ultrason Sonochem* 31, 490–498.

Wijngaarden, L.v., 1972. One-Dimensional Flow of Liquids Containing Small Gas Bubbles. *Annu Rev Fluid Mech* 4, 369–396.

Wijngaarden, L.v., 1968. On the equations of motion for mixtures of liquid and gas bubbles. *J Fluid Mech* 33, 465–474.

Wilson, P.S., Roy, R.A., Carey, W.M., 2005. Phase speed and attenuation in bubbly liquids inferred from impedance measurements near the individual bubble resonance frequency. *J Acoust Soc Am* 117, 1895–1910.

Wongwuttanasatian, T., Jookjantra, K., 2020. Effect of dual-frequency pulsed ultrasonic excitation and catalyst size for biodiesel production. *Renew Energy* 152, 1220–1226.

Xu, S., Zong, Y., Liu, X., Wan, M., 2017. Size distribution estimation of cavitation bubble cloud via bubbles dissolution using an ultrasound wide-beam method, AIP Conference Proceedings.

Xu, Z., Yasuda, K., Koda, S., 2013. Numerical simulation of liquid velocity distribution in a sonochemical reactor. *Ultrason Sonochem* 20, 452–459.

Yao, Y., Pan, Y., Liu, S., 2020. Power ultrasound and its applications: A state-of-the-art review. *Ultrason Sonochem* 62, 104722.

Yasuda, K., Nguyen, T.T., Asakura, Y., 2018. Measurement of distribution of broadband noise and sound pressures in sonochemical reactor. *Ultrason Sonochem* 43, 23–28.

Yasui, K., 2018. *Acoustic Cavitation and Bubble Dynamics*, 1st ed. Springer International Publishing.

Yasui, K., Kozuka, T., Tuziuti, T., Towata, A., Iida, Y., King, J., Macey, P., 2007. FEM calculation of an acoustic field in a sonochemical reactor. *Ultrason Sonochem* 14, 605–614.

Ye, L., Zhu, X., Liu, Y., 2019. Numerical study on dual-frequency ultrasonic enhancing cavitation effect based on bubble dynamic evolution. *Ultrason Sonochem* 59, 104744.

Young, F.R., 1989. *Cavitation*. McGraw-Hill, London; New York.

Yu, Y., Krynkin, A., Li, Z., Horoshenkov, K. V., 2021. Analytical and empirical models for the acoustic dispersion relations in partially filled water pipes. *Applied Acoustics* 179, 108076.

Zhang, Y., Zhang, Y., Li, S., 2017. Combination and simultaneous resonances of gas bubbles oscillating in liquids under dual-frequency acoustic excitation. *Ultrason Sonochem* 35, 431–439.

Zhang, Z., Gao, T., Liu, X., Li, D., Zhao, J., Lei, Y., Wang, Y., 2018. Influence of sound directions on acoustic field characteristics within a rectangle-shaped sonoreactor: Numerical simulation and experimental study. *Ultrason Sonochem* 42, 787–794.

Žnidarčič, A., Mettin, R., Cairós, C., Dular, M., 2014. Attached cavitation at a small diameter ultrasonic horn tip. *Phys Fluids* 26, 023304f.

Žnidarčič, A., Mettin, R., Dular, M., 2015. Modeling cavitation in a rapidly changing pressure field - Application to a small ultrasonic horn. *Ultrason Sonochem* 22, 482–492.